Class II Methanol Masers and Their Environment at High Resolution

by

Christopher John Phillips, B.Sc. (Hons.)

Submitted in fulfilment of the requirements
for the Degree of
Doctor of Philosophy

University of Tasmania
Hobart

Physics
Mathematics

Jan, 1998

Declaration

This thesis contains no material which has been accepted for the award of any other higher degree or graduate diploma in any tertiary institution. To the best of my knowledge and belief, this thesis contains no material previously published or written by another person, except where due reference has been made in the text of the thesis.

Christopher John Phillips

This thesis may be made available for loan and limited copying in accordance with the Copyright Act 1968.

Christopher John Phillips

Thesis Summary

Observations of the 6.7- and 12.2-GHz masing transitions of methanol by Norris *et al.* (1988; 1993) using the Australia Telescope Compact Array (ATCA) and the Parkes-Tidbinbilla Interferometer (PTI) found that for ten of the seventeen sources imaged the individual maser components had a linear spatial distribution. Many of the linear sources also had a velocity gradient along the source. This is in marked contrast to similar observations of OH and H_2O masers. Norris *et al.* interpreted this to be evidence of an edge-on circumstellar disc surrounding a young massive star.

The evolution of young massive stars is poorly understood, because the stars are surrounded by a cocoon of dust and dense molecular gas. Thus the direct detection of a disc around these stars would be a major step in understanding the dynamics of the formation of massive stars. In this thesis I have taken a sample of methanol sources and observed them using a variety of instruments and techniques to improve our understanding of these interesting objects and find further evidence to investigate the circumstellar disc model of linear methanol maser sources.

The sources imaged by Norris *et al.* were some of the brightest known methanol masers. In this thesis, I have used the ATCA to imaged a further ten methanol sources which have a more modest flux. All the methanol sources originally observed by Norris *et al.* have been reobserved either in this thesis or by Ellingsen *et al.* (1996a; 1998). As many of the maser sources have separate sites of emission separated by a few arcseconds to a few arcminutes , there are 45 maser sources which have now been observed at high resolution using the ATCA. Seventeen of these sources have a linear morphology. No difference in the properties of the linear and non-linear sources could be found.

Simultaneous observations of the 8.6 GHz continuum towards the methanol sources have been made for all the sources in the sample. Half of the methanol sources are associated with an ultra-compact HII (UCHII) region. The sources without UCHII regions may either be pre-main sequence, or are associated with a less massive embedded star.

The Anglo-Australian Telescope has been used to observed the 11.5 μm continuum emission associated with 35 of the maser sources. Nine of the sources were found to have detectable mid-infrared (MIR) emission. No correlation has been found between the the methanol and MIR luminosities. The observations were sensitive enough to detect embedded stars of spectral type B3 and above. That so few sources were found to have a MIR counterpart indicates that there are large variations in the circumstellar environment of the methanol sources.

A VLBI proper motion study at 6.7 and 12.2 GHz of a subsample of eight of

the linear sources has been started using the Australian VLBI network. If the lines do represent edge-on circumstellar discs then it should be possible to detect Keplerian rotation in 3 to 5 years.

The ATCA has been used to search for extragalactic 6.7-GHz methanol "megamasers" towards 87 galaxies selected on their *IRAS* colours and known OH megamaser galaxies. No methanol emission was found, with a typically detection limit of 15-40 mJy. This is surprising given the close association between Galactic OH and methanol masers.

Acknowledgments

There are many friends and colleagues to whom I am indebted to for their contributions to this thesis as well as the help, advice and friendship they have offered over the course of my PhD. I wish to express my sincere gratitude to my two supervisors, Prof. Peter McCulloch and Dr. Ray Norris. Their knowledge and sound understanding of the concepts of radio-astronomy and astrophysics have been invaluable for my own understanding. Ray's constant enthusiasm and advice has helped keep me focused, especially while writing this thesis.

I would also like to thank Dr. John Reynolds, Dr. Neil Killeen and Dr. Jim Caswell for patiently answering my many astronomical and data processing questions. The VLBI presented in Chapter 4 would not have been possible without the assistance of many people. These include Dr. John Reynolds, Dr. Tasso Tzioumis, Dr. Russell Gough, Dr. Edward King, Dr. Jim Lovell, Dr. Simon Ellingsen, Dr. Grant Gussie, Dave Rayner and David Legge. I am sure that there are other people who have also helped, whom I thank. In particular, I owe a lot to John Reynolds for his help scheduling and running the experiments and Dr. Warwick Wilson for his help using the fledgling S2 correlator.

The Mid-infrared observations presented in Chapter 3 were made in collaboration with Dr. Craig Smith using a camera built by him at ADFA. He very obligingly gave up his time to help us make the observations as well as doing all the data processing.

I would like to thank all the graduate students and staff in the Physics Department for their friendship and company. I would like to particularly thank Edward King, Jim and Jenny Lovell and Simon Ellingsen for their help and friendship both at work and socially. I have immensely appreciated the suggestions and advice Simon has had to offer which have done much to improve this thesis. Arguing the finer points of spectral-line interferometry with Simon has improved my understanding of this subject a lot, regardless of which one of us was right. Simon, along with Edward and Jim have collectively read drafts of the entire thesis at least twice and have never been rude about my spelling or grammar. Jim and Edward had the added the responsibility of ensuring I arrived at the church on my wedding day, a task they passed with flying colours.

Thank you to my parents who have been generous with their support both emotionally and financially while I have been at university. I am truly grateful for their love and support over this period particularly through some times which we have all found difficult. My father has patiently listened to me while I have tried to explain the many things which I was confused about and had not understood myself. He has also generously proofread the entire thesis.

Lastly I would like to thank my wife, Lisa, for her love and friendship. Her companionship has helped keep me sane and my head above water. She has also made a large sacrifice and suspended a promising career to come to the Netherlands with me, for which I am immensely grateful.

Contents

List of Tables

List of Figures

Chapter 1

Introduction

Massive stars play a vital role in the dynamics and evolution of a galaxy. They produce powerful stellar winds which deposit momentum and mechanical energy into the interstellar medium. They heat the surrounding molecular clouds and supply energy for endothermic chemical reactions, but eventually destroy their parent molecular cloud, halting further star formation. At the end of their lifetime (of the order of 10^6 yr) they violently explode as supernovae, enriching the region with heavy elements and producing a violent shock which is thought to trigger star-formation in neighboring molecular clouds. Understanding the formation and evolution of massive stars is important for understanding galaxies as a whole.

Massive stars form in the warm dense cores of molecular clouds, and so they are obscured at optical wavelengths by many magnitudes of extinction. As a consequence, their evolution is poorly understood. Newly formed O and B stars heat and ionize their environment, creating sources of infrared and radio emission. So investigations of massive stars rely on indirect observations of their effect on the immediate vicinity and usually consist of far-infrared (FIR) observations of thermal dust, and radio-wavelength observations of ionized hydrogen (HII) and molecular line emission from the gas cloud. Much of this work has consisted of low (spatial) resolution infrared and single-dish radio observations. Because of the small size ($\sim$1 arcsec) of the sources and the complexity of the star-forming regions, high resolution observations are needed to understand properly the dynamics of these objects.

1.1 Ultra-compact HII regions

Ultra-compact HII regions (UCHII) are small photo-ionized nebulae produced by O and B stars embedded in molecular gas and dust. They are characterized by having diameters less than 0.15 parsec (pc), high emission measures ($>10^6$ pc cm^{-6}) and high electron densities ($>10^3$ cm^{-3}) (Habing and Israel, 1979). From a VLA survey of 75 UCHII regions, Wood & Churchwell (1989b) classified the morphologies into five classes: spherical or unresolved (43%), cometary (20%), core-halo (16%), shell (4%) and irregular or multiply peaked (17%).

UCHII regions form when fusion begins in the cores of young stars with a

spectral type earlier than about B3. The flux of UV photons ionizes the circumstellar region which expands rapidly, but the rate of expansion quickly slows as the ionized volume increases. The initial ionized region forms over a timescale of a few years, so is essentially unobservable. The radius, r_i, of the initial "Strömgren Sphere" is expressed as:

$$r_i = \left(\frac{3S_*}{4\pi n_0^2 \beta_2} \right)^{1/3}, \tag{1.1}$$

where S_* is the flux of the ionizing photons, n_0 is the ambient density of the gas, and β_2 is the recombination coefficient and equals $\beta_2(T_e) = 2.6\times10^{-10} T_e^{-3/4} \mathrm{cm^3 s^{-1}}$, and T_e is the temperature of the ionized gas (Strömgren, 1939; De Pree *et al.*, 1995). The value of r_i depends on the density in which the star forms, $r_i \propto n_0^{-2/3}$, and the spectral type of the embedded star, $r_i \propto S_*^{1/3}$.

Once the Strömgren Sphere has formed, the ionized region is suddenly at 10^4 K while the surrounding region is at ~100 K, creating a pressure gradient. The newly formed UCHII region expands until pressure equilibrium has been achieved. The expansion of the UCHII regions follows the relation:

$$r(t) = r_i \left[1 + (7c_i t/4r_i)\right]^{4/7}, \tag{1.2}$$

where r_i is the initial Strömgren radius, c_i is the sound speed (10 km $\mathrm{s^{-1}}$) and t is the time in seconds.

The inferred lifetime of an UCHII region is approximately 10 per cent of the lifetime of the central OB star (see Section 3.1). However the simple model of UCHII evolution outlined above implies that the UCHII phase can only last ~1.7 per cent of an OB star's lifetime or a few times 10^4 years (Wood and Churchwell, 1989b). Expansion of the HII region must be inhibited in some way and several mechanisms have been proposed the explain this apparent paradox.

1.1.1 The bow shock model

Approximately 20 per cent of UCHII regions have a cometary morphology. Cometary HII regions have a limb-brightened parabolic shell with bright coma and a swept back tail of much lower surface brightness (van Buren *et al.*, 1990). A number of explanations of the morphology of cometary UCHII regions have been proposed, a summary is included in van Buren *et al.* (1990). Wood & Churchwell (1989b) and van Buren *et al.* (1990) have suggested that cometary UCHII regions are produced by OB stars with powerful stellar winds moving supersonically thorough molecular cloud cores. As the star moves though the molecular cloud at velocities exceeding the local sound speed (less than ~10 km $\mathrm{s^{-1}}$), the interaction of the star's stellar wind and the ambient cloud material produces a "bow-shock". The HII region becomes confined by the ram pressure of the molecular cloud. Theoretical modelling of the bow-shocks has been able to reproduce most observable cometary morphologies (van Buren *et al.*, 1990; Mac Low *et al.*, 1991). However, with velocities of the order of 10 km $\mathrm{s^{-1}}$, the embedded star would cross the molecular core in a timescale of 10^4 yr. van Buren *et al.* suggest that the star

may in fact cross numerous separate cloud cores in its lifetime, producing separate cometary HII regions in each.

A problem with this model is that only 20 per cent of UCHII regions have a cometary morphology, but if their lifetimes are greater they should represent the majority. Mac Low *et al.* (1991) suggest that unresolved and spherical UCHII regions could represent cometary HII regions coming towards the observer. Hollenbach *et al.* (1994) have criticized this model because they consider a high fraction of fast moving OB stars unlikely.

1.1.2 The champagne flow model

Tenorio-Tagle has suggested that some UCHII regions may be "champagne" HII regions (Tenorio-Tagle, 1979; Bodenheimer *et al.*, 1979; Yorke *et al.*, 1983). If a star forms near a density gradient in the molecular cloud (at the edge of the cloud for instance), then when the ionization front of the expanding HII region reaches the density gradient a "blow-out" of the ionized gas will occur, into the low density region. This will cause pressure confinement in the high density direction and the HII region will expand more slowly. A comparison of HII regions and CO cloud observations shows that the majority of HII regions are at the edge of molecular clouds (Israel, 1978).

The expected morphology of a champagne flow roughly matches that of the cometary UCHII regions, but van Buren *et al.* (1990) note that observed cometary compact HII regions are limb-brightened, which is rarely seen in champagne flow models. The champagne model also predicts that more objects should be seen at a later evolutionary stage, while the simulations which best match observed HII regions correspond to young objects.

1.1.3 Photo-evaporated molecular core model

Gaume *et al.* (1994; 1995) have made high sensitivity VLA observations of G 34.3+0.2 and Sgr B2. They find a velocity gradient in the H93α line emission perpendicular to the symmetry axis of a number of cometary HII regions. They claim that neither the bow-shock nor champagne flow models adequately explain these observations. They propose an "improved" champagne model, in which the exciting star photo-evaporates material off of the hot molecular core, which flows towards a region of lower density.

1.1.4 The circumstellar disc photo-ionization model

Hollenbach *et al.* (1994) have proposed that many UCHII regions are formed by the photo-ionization and photo-evaporation of a neutral accretion disc in orbit around an OB star. The dense ionized gas expands away from the star, but is replaced by new dense plasma which is photo-evaporated and photo-ionized from the neutral disc. Such discs follow naturally from most models of star formation and are expected to have masses of $\sim 0.3 M_*$ around young stars (Shu *et al.*, 1990). The UCHII region will persist as long as the disc survives, and lifetimes of $\geq 10^5$ yr

are achievable with a 2-10 $M_{\odot}$ disc. The disc will be optically thick at centimetre wavelengths with a spectral index of $\alpha = 0.6$ ($S_{\nu} \propto \nu^{0.6}$). However, as noted by De Pree *et al.* (1995), the spectral indices found by Wood & Churchwell (1989b) cover a much larger range. This model does not address the variety of UCHII morphologies observed.

1.1.5 The warm, dense molecular gas model

De Pree *et al.* (1995) have suggested a simple explanation to extend the lifetime of UCHII regions. Wood & Churchwell (1989b) assumed a molecular density of 10^5 cm^{-3} and a temperature of 25 K. De Pree *et al.* suggest that the molecular gas in which the OB stars form is denser and warmer than previously believed. Recent observations of Sgr B2 and G 10.47+0.03 support this with derived densities of $\sim 10^7$ cm^{-3} and 1.2×10^7 cm^{-3} and temperatures of 200 K and 75 K respectively (Hüttemeister *et al.*, 1993; Garay *et al.*, 1993). A higher initial density will result in a smaller initial Strömgren radius (Equation 1.1). Thus the expanding UCHII region will have a smaller diameter after a given period of time. The rate of expansion will also be less for a smaller sphere (Equation 1.2). Using the simple Strömgren model, UCHII region life-times of $\sim 10^5$ yr would be expected with a density of 10^7 cm^{-3}. Adding further support to this model, De Pree *et al.* found many UCHII regions in the literature with smaller radii than the expected initial Strömgren sphere, assuming a density of 10^5 cm^{-3}.

1.2 The IR properties of massive stars

As well as ionizing the surrounding gas, the embedded star heats the circumstellar dust which then radiates at FIR wavelengths. The properties of this emission and how it has been used to study massive star-formation is discussed in Chapter 3.

1.3 Molecular environment of massive stars

Because radio-wavelength observations can penetrate the obscuring dust in star forming regions, observations of molecular lines at these wavelengths can tell us much about the environment of the young star. Studies of the maser emission from OH and H_2O molecules has vastly improved our understanding of the physical conditions around young massive stars.

1.3.1 OH

The first astronomical maser was detected in 1965 by Weaver *et al.* (1965) who observed the 1665-MHz transition of OH. Perkins *et al.* (1966) suggested that the emission was the result of maser amplification. High resolution VLBI observations by Moran *et al.* of W3(OH) confirmed this, as the brightness temperatures of the individual components was too high to be explained by thermal processes. The association of OH with UCHII regions was recognized early on (Zuckerman *et al.*,

1965; Mezger *et al.*, 1967; Habing *et al.*, 1974), but not confirmed with high resolution (<1 arcsec) observations until 1980 (Reid *et al.*, 1980).

To explain the high molecular density thought to be needed to pump OH, Elitzur & de Jong (1978) suggested that OH maser spots are located in a compressed shell between the shock and ionization fronts of an expanding HII region. This theory is supported by the observations of Baart & Cohen (1985) who find that there is a general tendency for the OH masers to lie at a greater distance from more luminous OB stars. Bloemhof *et al.* (1996) find that the shape of the OH maser spots show a tendency to be elongated in a direction parallel to the shock front delineated by the HII region, and suggest that this supports this theory.

However this view is not uniformly held; Garay *et al.* (1985) find the majority of maser spots appear projected onto the most compact HII regions in a complex, with the probability of finding an OH maser spot highest towards the centre of the UCHII region. Gaume & Mutel (1987) make a similar finding and conclude that OH masers cannot be uniformly distributed in a shell around a central star. van Buren *et al.* (1990) have suggested that the OH masers lie in the shock-compressed flow around the ionized region in cometary bow-shocks.

Because OH is a paramagnetic molecule it is a powerful tool for studying astronomical magnetic fields. A typical magnetic field of a few milli-Gauss will split the OH spectral lines into left and right circular polarisations by an amount greater than the line's width (Elitzur, 1992). As the splitting is proportional to the strength of the magnetic field, this allows a direct measurement of the field to be made.

1.3.2 H_2O

Emission from the 22-GHz $6_{16}-5_{23}$ rotational transition of H_2O was first identified by Cheung *et al.* (1969) and quickly identified as masing. Like OH masers it is frequently associated with regions of active star-formation, but unlike OH, it is generally located near, but not coincident with, compact HII regions (Reid and Moran, 1988). Water masers are the brightest of all known masers, a single spectral feature in W49N has a luminosity of 0.1 $L_{\odot}$ (Walker *et al.*, 1982). The spatial morphology of H_2O masers is very complex with no overall structure. Most sources show strong low velocity features (within ± 10 km s^{-1} of the systemic velocity) as well as weak high velocity features (up to ± 250 km s^{-1} from the systemic velocity). Strelnitskii & Syunyaev (1973) proposed that the high velocity features represent high velocity ballistic flows. This has been confirmed by VLBI proper motion observations by Genzel *et al.* (1981b; 1981a). They found that the transverse motions of the the low velocity features are much larger than the motions of the high velocity features. This can be explained if all the features share the same kinematics, with the high velocity features coming towards the observer and the low velocity feature moving perpendicular. The masers are beamed perpendicular to the direction of motion, so the low velocity features are stronger. Mac Low & Elitzur (1992) have suggested that these systems are very young and show the very first stages of the formation of a jet.

1.4 Star formation

The processes of star formation are complex and cover 12 orders of magnitude in mass and linear scale. Not surprisingly, there is a wide variety of opinion on the details of the processes. The following summary is based on the models of Shu *et al.* (1987; 1993).

Giant molecular clouds (GMC) are the principal site of active star formation. In the first stage of star formation, cores develop within a molecular cloud. The clouds are supported against self-gravitation by a combination of the magnetic field and turbulent motions. Support of neutral components arises through friction generated when these components slip with respect to charged components. In a lightly ionized gas, the magnetic fields slowly leak out via ambipolar diffusion and eventually magnetic support is lost and the gas and dust slowly contract.

When the contracting core becomes sufficiently centrally concentrated the second stage of the process occurs and a protostar, with a surrounding disc, forms at the centre of the cloud core, which collapses from the inside out.

In the third stage, powerful winds break out along the rotation axis of the system, creating a bipolar outflow. These winds are triggered by the commencement of deuterium burning in the protostar. The bipolar outflows sweep up material over the poles into two outwardly expanding shells of gas and dust, reversing the infall. The angle subtended by the outflow opens and eventually halts all accretion onto the star, revealing a newly formed star with a circumstellar disc.

It is generally believed that different mechanisms are involved in the formation of high and low mass stars. High mass stars form when a large core in a GMC collapses, producing a tight group of stars formed more-or-less simultaneously. Low mass stars form independently from core collapses. If the mass of the cloud core is larger than a critical value, the self-gravitation of the core will overcome the magnetic support. However, for lower mass cores, collapse will not occur until the magnetic field has significantly decayed. The above description largely applies to the formation of low mass stars, and the formation of massive stars is more complex and less well understood.

The formation of discs is a natural consequence of the process of star formation. Most models have mass accretion onto the protostar occurring though a circumstellar disc. In recent years the existence of discs around young stellar objects has gained wide-scale acceptance, both theoretically (Shu *et al.*, 1990; Lin and Pringle, 1990; Yorke *et al.*, 1993; Aikawa *et al.*, 1997) and observationally using infrared and millimetre observations (Plambeck *et al.*, 1990; Beckwith *et al.*, 1990; Beckwith and Sargent, 1993; Sargent and Beckwith, 1994; Hillenbrand *et al.*, 1992; Mannings and Sargent, 1997). These have only dealt with low and intermediate mass stars, although it is a reasonable assumption to make that circumstellar discs play an intimate role in the formation of massive stars. Interestingly, considerations of the magnetic field suggest that for massive stars the formation of a disc may precede the formation of the protostar (McKee *et al.*, 1993). Cesaroni *et al.* (1997) have found evidence for a rotating disc around the very young massive star IRAS 20126+4104.

1.5 Methanol masers

Many lines of methanol have been observed in molecular clouds, due to its complex microwave spectrum and high abundance in molecular clouds. There are 294 transitions of methanol which have been detected astronomically between 834 MHz and 802 GHz (Lovas, 1992). The history and properties of methanol masers, up until 1991, has been reviewed by Menten (1991b) and a brief summary follows including more recent results.

1.5.1 Brief history

The first interstellar methanol maser was discovered in 1971 by Barrett *et al.* (1971) towards Orion-KL at 25.0 GHz. This was the only known masing transition of methanol until 1984 when Wilson *et al.* (1984; 1985) discovered two masing transitions of methanol at 23.1 and 20.0 GHz towards the star-forming region W3(OH). Since then many masing transition of methanol have been discovered. The discovery of the very strong and widespread methanol transitions at 12.2 GHz (Batrla *et al.*, 1987) and then at 6.7 GHz (Menten, 1991a) have triggered great interest in the properties of interstellar methanol masers.

1.5.2 Class I and Class II methanol masers

Methanol masers can be divided into two classes (Batrla *et al.*, 1987). Class I masers include transitions at 9.9, 25.0, 36.2, 44.1, 84.5, 95.2 and 146.6 GHz. They are characterized by being offset from HII regions and OH/H_2O sources by up to 1 parsec. They typically show narrow emission (Δv=0.3-0.7 km s^{-1}) and the spectra from different transitions at the same site are very similar. They are almost certainly collisionally pumped (Cragg *et al.*, 1992) and are thought to arise when mass outflows interact with ambient high density material (Plambeck and Menten, 1990).

Class II sources include transitions at 6.7, 12.2, 20.0, 23.1, 37.7, 38.3, 38.5 and 107.0 GHz. They are closely associated with UCHII regions and OH maser sources. Their spectrum is more complex than Class I sources with many components spread over a few km s^{-1}. The spectra of different transitions cover the same velocity range but show more variation than Class I masers.

Slysh *et al.* (1994) have used the Parkes radio telescope to search for the Class I 44.1-GHz methanol transition in the direction of Galactic HII, H_2O and 6.7-GHz methanol maser sources. Of the 44.1-GHz detections, 82 per cent also showed 6.7-GHz emission (the actual percentage is probably higher, as no 6.7-GHz observations have been made towards a number of the sources). Slysh *et al.* found a strong anti-correlation between the flux densities of the 6.7- and 44.1-GHz transitions. They suggest that Class I and Class II methanol masers come from the same volume of space and that strong emission from one class suppresses the emission from the other. However, the large size of the single dish beam at Parkes (1.5 arcmin, as only the inner 16 m of the dish is illuminated at 44 GHz) is roughly equivalent to the typical separation of 1 parsec for Class I sources. Without high

resolution (interferometric) observations at both transitions, the claim of Slysh *et al.* cannot be verified.

1.5.3 Pumping of methanol masers

It is generally agreed that Class I methanol masers are pumped by collisional excitation, followed by spontaneous radiative decay (Cragg *et al.*, 1992).

The pumping of Class II methanol masers is poorly understood, a situation not helped by the fact that details of the collisional excitation of methanol by molecular hydrogen are not known. In the model of Cragg *et al.* (1992) there exist two regimes: Class I masers appear when gas kinetic temperature is greater than the continuum temperature, while Class II masers appear when the kinetic temperature is less than the continuum temperature. The populated states in the two regimes are opposite, explaining why absorption of Class II transitions is seen towards Class I sources and vice-versa. Pumping of Class II masers is by sub-millimetre photons and the effects of collisional excitation are thought to be negligible. This model accounted for all known Class I and Class II masers at the time it was published but failed to predict the 107.0-GHz $3_1 - 4_0\mathrm{A}^+$ transition (Val'Tts *et al.*, 1995). This model could not produce brightness temperatures as high as those observed.

Sobolev *et al.* (1994; 1997b; 1997a) have expanded this model including the second and first torsionally excited states of the molecule, to account for the high brightness temperatures of the 6.7- and 12.2-GHz methanol transitions. This model can produce high brightness temperature emission for all known Class II transitions, and predicts a number of new candidate transitions. The basic elements of the model are that portions of methanol-rich gas amplify continuum radiation from the background HII region. The masers are pumped by warm dust, hotter than 150 K. The main findings of this model are that to produce strong masers:

(i) the masers must be beamed with $\varepsilon^{-1} > 3$.

(ii) the ratio of the methanol abundance to molecular hydrogen must be greater than 7×10^{-7}. This is much higher than the usual environment in molecular clouds.

(iii) high molecular hydrogen densities are required (greater than $3 \times 10^6\,\mathrm{cm}^{-3}$).

(iv) the gas kinetic temperatures must be less than 50 K.

1.5.4 Observations of methanol masers

As the 6.7-GHz transition of methanol is, on average, stronger that the 1.6-GHz transition of OH it is potentially more useful for studying star formation. Most observations of the 6.7- and 12.2-GHz transitions of methanol have been made using single dish instruments and a surprisingly small number of high resolution observations have been made. This is because the Australia Telescope Compact

Array (ATCA) and the Australian Long Baseline Array (LBA) are the only interferometers which can routinely observe the 6.7-GHz transition of methanol. The VLBA can observed the 12.2-GHz transition of methanol, but most methanol sources are in the Southern Hemisphere.

All early surveys for 12.2-GHz masers were targeted towards known star-formation regions or OH and H_2O masers, which trace star formation regions, and were very successful (Batrla *et al.*, 1987; Norris *et al.*, 1987; Kemball *et al.*, 1988; Koo *et al.*, 1988; Caswell *et al.*, 1993). These observations firmly established that methanol masers are found in star forming regions. Observations towards OH/IR sources failed to find any emission (Norris *et al.*, 1987; Koo *et al.*, 1988). Early searches for the 6.7-GHz transition towards star forming regions and OH masers were also successful (Menten, 1991a; Macleod and Gaylard, 1992; Gaylard and Macleod, 1993; Caswell *et al.*, 1995c). Searches for 6.7-GHz masers towards known 12.2-GHz sources (Macleod *et al.*, 1992) and vice-versa (Macleod *et al.*, 1993; Gaylard *et al.*, 1994; Caswell *et al.*, 1995b) showed that the two transitions are closely related. A number of surveys for 6.7-GHz methanol have been targeted towards colour selected *IRAS* sources and have been very successful(Schutte *et al.*, 1993; van der Walt *et al.*, 1995; van der Walt *et al.*, 1996; Walsh *et al.*, 1997), these surveys are discussed in Chapter 3. Using targeted surveys such as these, it is possible that an entire class of methanol masers not associated with star formation or OH masers may be missed. A fully sampled blind survey by Ellingsen *et al.* (1996b) and partially sampled blind survey by Caswell (1996b; 1996a) have found a large number of previously undetected methanol masers, but have not found the new masers to be associated with any other type of object. In fact, a large proportion of these masers are not associated with *any* known sources (Ellingsen, 1997 private communication).

The spectra of 6.7- and 12.2-GHz masers are quite similar, both in velocity and overall shape. The velocity ranges of the 12.2-GHz spectra are typically smaller than for the 6.7-GHz spectra (Caswell *et al.*, 1995b). The 6.7-GHz transition is, on average, stronger than the 12.2-GHz transition. The median ratio of the 6.7-GHz peak flux density to the 12.2-GHz peak flux density is 9 (Caswell *et al.*, 1995b). The 6.7-GHz transition is found towards most 1.6-GHz OH masers and is, on average, brighter than the OH, with a median ratio of the peak flux densities of 6 (Caswell *et al.*, 1995c). The OH spectra and methanol spectra have a similar velocity range.

Caswell *et al.* (1995a) found that most (75 per cent) 6.7- and 12.2-GHz methanol masers show little variability, which is in agreement with other observations (Catarzi *et al.*, 1993; Moscadelli and Catarzi, 1996), which suggests that the masers are, in general, saturated. Most masers which are variable have amplitude variations less than a factor of two and the separate spectral features often vary independently. Some features have been seen to flare and fade numerous times, while others vary quasi-periodically with a median period of 16 months (Caswell *et al.*, 1995a; Macleod and Gaylard, 1996). A small number of sources show significant variation on a time-scale of weeks (Macleod and Gaylard, 1996; Ellingsen 1996, private communication).

Few high resolution observations of methanol masers have been made. These

consist of a few VLBI observations (Menten *et al.*, 1988; McCutcheon *et al.*, 1988; Norris *et al.*, 1988; Menten *et al.*, 1992; Ellingsen, 1996; Norris *et al.*, 1998), which are discussed in Chapter 4, and ATCA observations, discussed below. One of the more important findings of the VLBI is that, in some cases, the 6.7- and 12.2-GHz maser components are coincident to within a few milli-arcsec. The main ATCA observations consist of the 6.7-GHz surveys by Caswell, mentioned above, observations of the 6.7-GHz maser emission and absorption in the molecular cloud complex Sgr B2 (Houghton and Whiteoak, 1995), comparison of the 6.7-GHz methanol maser positions to 1.6-GHz OH and 6.0-GHz excited OH (Caswell *et al.*, 1995d; Caswell, 1997), maps of the individual maser components (Norris *et al.*, 1993) and associated UCHII regions (Ellingsen *et al.*, 1996a). Work in progress includes ATCA followup observations of the single-dish surveys of Walsh *et al.* (1997) and Ellingsen *et al.* (1996b) (by the respective authors).

Comparison of the positions of 1.6-GHz OH and 6.7-GHz methanol show that they are coincident to within the errors of 1 arcsec. This confirms the close association between methanol and OH. The spatial resolution of these observations (particularly at 1.6-GHz) is not enough to test whether or not the masers come from the same region; comparisons of the individual component positions suggest they do not. Emission from 6.0-GHz excited OH is also coincident with the 6.7-GHz methanol and, interestingly, has a similar overall spatial morphology.

The ATCA observations of Norris *et al.* (1993) are of particular interest for this thesis. Ten out of 15 sources imaged showed a linear or curved structure. Remarkably, many of the linear sources also showed a monotonic or near monotonic velocity gradient along the source. This morphology was also seen in earlier Parkes Tidbinbilla Interferometer (PTI) observations at 12.2-GHz (Norris *et al.*, 1988). Norris *et al.* (1993; 1998) have suggested a model in which the linear maser sources delineate an edge-on circumstellar disc around a young massive star. Interestingly, Moscadelli & Catarzi (1996) have suggested the methanol maser source W48 is an edge-on disc, to explain the velocity dependence of the spectral intensity variations.

Observations of extra-galactic methanol masers are discussed in Chapter 5. The only known extra-galactic masers are 3 found in the Large Magellanic Cloud (Sinclair *et al.*, 1992; Ellingsen *et al.*, 1994a; Ellingsen *et al.*, 1994b; Beasley *et al.*, 1996).

1.6 Outline of the thesis

To understand the nature of methanol masers, and massive star-formation in general, high resolution observations are needed. Often, complex star forming regions such W3(OH) and NGC 6334F are studied in great detail, while other (simpler) regions are studied with less depth. This, and the limited amount of high-resolution observations of methanol masers, gives a wide scope for new observations. For this thesis, it was decided to take a moderate sized sample of methanol masers and study them in detail, with particular emphasis on critically evaluating the circumstellar disc model. The sample selection is described in Chapter 2, and includes the sources previously observed using the ATCA by Norris *et al.* (1993)

and a number of new sources which have not been observed at high resolution before.

The different high resolution observations carried out as part of this thesis are summarized below.

Chapter 2. The ATCA has been used to make simultaneous observations of the 6.7-GHz transition of Galactic methanol masers and the associated 8.6-GHz continuum. Half the masers are associated with an UCHII region. Reasons why the other half are not associated with a detected UCHII region are discussed. The morphology of the masers, and their positions relative to the associated UCHII regions are considered in view of the circumstellar disc model of methanol masers. This chapter is a reproduction of a paper accepted for publication in the *Monthly Notices of the Royal Astronomical Society.*

Chapter 3. The Anglo-Australian Telescope has been used to make sub-arcsec observations of the 11.5 μm continuum from dust in the regions of Galactic methanol masers. A critical analysis of the validity of *IRAS* associations with the maser sources is made on the basis of the mid-infrared detections (and limits) made. Reasons for the low detection rate are also discussed.

Chapter 4. A VLBI proper-motion experiment at 6.7- and 12.2-GHz has commenced on a sample of 8 methanol sources. It is too early to expect to see results from this experiment, but a portion of the data has been processed to make sure the experiment is viable. Simulations have shown that it will take 5 to 10 years to see proper-motions, assuming sources are edge-on discs.

Chapter 5. The ATCA has been used to search a large sample of *IRAS* luminous galaxies for 6.7-GHz methanol. The implications of the non-detections are discussed. This chapter is a reproduction of a paper which appeared in the *Monthly Notices of the Royal Astronomical Society*, volume 294 (1998).

Chapter 6. The investigations presented in this thesis and the major results are summarized and briefly discussed. Further observations which should be made are outlined.

Chapter 2

ATCA observations of methanol masers

C.J. Phillips,[1] R.P. Norris,[2] S.P. Ellingsen[1] and P.M. McCulloch[1]

[1] Department of Physics, University of Tasmania, GPO Box 252-21, Hobart, TAS 7001, Australia.

[2] CSIRO Australia Telescope National Facility, PO Box 76, Epping, NSW 2121, Australia.

2.1 Abstract

We have used the Australia Telescope Compact Array (ATCA) to make high-resolution images of the 6.7-GHz $5_1 \rightarrow 6_0$ A^+ maser transition of methanol towards 33 sources in the Galactic Plane. Including the results from 12 methanol sources in the literature we find 17 out of 45 sources have curved or linear morphology. Most of the 17 have a velocity gradient along the line, which is consistent with masers lying in an edge-on circumstellar disc surrounding a massive star. We also made simultaneous continuum observations of the sources at 8.6 GHz, in order to image any associated HII region. Twenty-five of the sources are associated with an ultra-compact HII region, with a detection limit of $\sim$0.5 mJy beam^{-1}. We argue that the methanol sources without an associated HII region represent less massive embedded stars, not an earlier stage in the lifetime of the star, as previously suggested.

2.2 Introduction

Observations of spectral lines associated with young massive stars at radio-wavelengths is one of the best ways of studying these objects; this is because the sources are obscured by the surrounding dust, making optical studies difficult or impossible. Interferometric observations of masing transitions are especially useful because of the accuracy with which the position and velocity of the individual maser components can be measured.

Observations of the common masing molecules, OH and H_2O, have yielded much information on the physical conditions of young star-forming regions. However, the masers typically have a complex morphology which is difficult to interpret. The strong and common $2_0 \rightarrow 3_{-1}$ E and $5_1 \rightarrow 6_0$ A^+ methanol transitions at 12.2 and 6.7 GHz (Batrla *et al.*, 1987; Menten, 1991a) add a third masing molecule to probe the regions around massive stars. These two transitions of methanol are frequently associated with OH and H_2O masers, which are themselves believed to be tracers of massive star formation and associated with ultra-compact HII (UCHII) regions (Reid and Moran, 1988). Because of this, methanol masers are also thought to be associated with UCHII regions, although this has only been confirmed for a small number of sources (Menten *et al.*, 1988; Ellingsen *et al.*, 1996a).

Norris *et al.* (1988; 1993) used the Parkes-Tidbinbilla Interferometer (PTI) at 12.2 GHz and the Australia Telescope Compact Array (ATCA) at 6.7 GHz to make high-resolution images of these two transitions of methanol. Ten of the 15 sources imaged using the ATCA had a linear or curved structure. Remarkably, many of the linear sources also showed a monotonic or near-monotonic velocity gradient along the source. The sources which were also imaged using the PTI showed a similar morphology at 12.2 GHz.

Norris *et al.* (1993; 1998) have suggested a model in which the linear maser sources delineate an edge-on circumstellar disc around a young massive star. Such discs are thought to be common around young stars (Lin and Pringle, 1990; Hillenbrand *et al.*, 1992; Hollenbach *et al.*, 1994). Other models such as shock-fronts or bipolar outflow can not easily explain the velocity gradients. Modelling of the sources by Norris *et al.* (1998) has shown that the velocity gradients are consistent with Keplerian motion around stars with masses in the range of 4 to 14 $M_\odot$.

If the masers are in a molecular disc around a young OB star, then the methanol emission would be expected to be coincident with the continuum emission assuming a simple HII morphology. To test this, Ellingsen *et al.* (1996a) imaged the continuum emission associated with four of the sources observed by Norris *et al.* (1993). Only two of the sources were associated with an UCHII region. One of these, G 339.878−1.252, has a linear structure and is aligned with a largely unresolved HII region, as predicted by the circumstellar disc model. The other, NGC 6334F, is offset from the peak of the HII region. Similar observations of a larger number sources are required to make any statistically significant conclusions.

In this paper we present high-resolution images of 10 methanol masers which have not previously been imaged. We also present high-resolution images of UCHII regions associated with these sources and with nine of the methanol sources previously imaged by Norris *et al.* Increasing the sample size of methanol masers imaged at high resolution will allow us to evaluate the circumstellar disc model of methanol masers more critically.

2.3 Observations

The sample of sources that we observed consists of:

- 10 sources from the single-dish survey by Caswell *et al.* (1995c), which had been discovered mainly by their association with known OH. We selected sources from Caswell *et al.* which had strong multiple components and had a declination south of -20°;
- 7 sources which had been previously imaged in methanol by Norris *et al.* (1993).

In addition, we have included for discussion and statistics a further 12 sources observed by Ellingsen *et al.* (1996a) and Ellingsen *et al.* (in preparation), and a further 16 methanol sources which happened to be in the fields of the observations of the 17 sources selected above. Nine of the sources observed by Ellingsen *et al.* have previously been observed by Norris *et al.* (1993). Thus we discuss a total of 45 sources in this paper. The sample, however, cannot be considered a representative sample because of the lack of rigid selection criteria.

The observations were made using the ATCA during observing sessions on 1994 August 25 and 26 and 1995 February 10 and 11 with the array in the 6A configuration, and on 1995 July 3 and 4 using the 6C configuration. The baselines range in length from 337 to 5939 m for 6A and 153 to 6000 m for 6C. The correlator was configured to record a 128-MHz band centred on 8.6 MHz and a 4-MHz band centred on 6.7 MHz simultaneously. The exact band centre for the spectral observations was 6669 or 6670 MHz depending on the LSR velocity of the source. For the continuum observations the band was centred on 8586 MHz in 1994 August and 1995 February and 8640 MHz in 1995 July. Dual orthogonal linear polarizations were recorded for both bands and averaged to form Stokes I after calibration. These observations allowed us to image simultaneously the $5_1 \rightarrow 6_0$ A^+ transition of methanol and any HII continuum associated with the maser sources. The 4-MHz band was divided into 1024 spectral channels, giving a velocity resolution of 0.35 km s^{-1} after Hanning smoothing. The FWHM of the primary beams of each antenna is approximately 8.4 and 6.5 arcmin at 6.7 and 8.6 GHz respectively, while the synthesised beam was typically 1.8×1.4 and 1.5×1.1 arcsec, depending on the declination of the source.

The observations were made by interleaving three program sources over the observing sessions of 11 to 14 h (except for the observations on 1995 July 3 where four sources were observed over 19 h). Each program source was observed for approximately 15 min with a 4-min observation of a calibrator source before and after each scan, giving a cycle time of slightly greater than 1 h.

The data were calibrated using the Astronomical Image Processing System (*AIPS*). PKS 1934-638 was used as the flux-density calibrator, with an assumed flux density of 3.92 and 2.84 Jy at 6.7 and 8.6 GHz respectively. Standard reduction techniques were applied to the spectral data (bandpass calibration, correction for the Doppler shift and continuum subtraction) and imaged using the *AIPS* package. Phase self-calibration using a point-source model was done on a

single channel of the data, generally the strongest maser component, and applied to the entire data set. As the maser peak flux density is strong and the maser spot size is small (in the order of a few milli-arcsec) (Ellingsen, 1996) this technique works very well. The absolute position of the maser sources was obtained by calibrating and imaging a single strong spectral feature (the feature used in the self-calibration step) using a standard secondary calibrator, before the phase self-calibration was applied. This position should be accurate to better than 0.3 arcsec.

After initial calibration using *AIPS*, the continuum data were self-calibrated using the Difmap (Shepherd, 1997) package. Both amplitude and phase self-calibration were applied to the stronger sources, while only phase self-calibration was used with the weaker sources. The final images were produced using *AIPS*. For many of the sources observed with the 6C configuration, the correlated flux density on the shortest baseline was very large because of confusion from extended, low-brightness-temperature emission in the primary beam. The amplitude dropped off very quickly with baseline and so this extended structure was not sampled well enough to image. To improve the sensitivity to compact structure, these short baselines were removed before imaging. This reduces the sensitivity to extended structure (greater than $\sim$17 arcsec).

The size of the maser clusters was found to be 0.5 - 1.5 arcsec in extent, comparable to the $\sim$1.5-arcsec synthesised beam of the ATCA at 6.7 GHz. However, as the individual maser spots are unresolved, with a scale size of a few milli-arcsec, we can measure relative spot positions to a much greater accuracy than the size of the synthesised beam. This is done by fitting a Gaussian model to the imaged data to find the peak position. In theory, this should give a positional accuracy of the order of $(B/(2 \times \mathrm{SNR}))$, where B is the size of the synthesised beam and SNR is the signal-to-noise ratio. For most of the sources observed, individual spectral features with fluxes greater than about 20 Jy were dynamic-range-limited with a maximum SNR typically of about 400 (this varied from 100 to 600 for the various sources). This technique fails if there are two features at the same velocity with a separation less than the size of the synthesised beam. In this case we measure the centroid of the two positions (weighted by the component flux density). Despite this limitation the sources which have been imaged using both the ATCA and VLBI show a very similar structure (Ellingsen, 1996; Phillips *et al.*, 1996; Norris *et al.*, 1998), and shows that for most components the ATCA positions have errors of between 10 and 50 milliarcsec (Section 4.5 has a detailed discussion on the accuracy of the ATCA images).

Alignment of methanol and UCHII positions

Phase corrections using a close secondary calibrator remove most phase variations caused by the atmosphere. However, as the calibrators are typically offset by 5 to 10 degrees from the source, there will be residual phase errors which will scale with frequency. These phase errors will contribute to the error in the absolute position of the source, and will cause a shift in the relative positions of the 6.7- and 8.6-GHz images as the phase errors will be different at the two frequencies.

To determine the position of the maser features with respect to the continuum, three techniques were used.

(i) No additional corrections were made to the positions of the sources, assuming the relative positional errors were small.

(ii) The line-free channels at 6.7 GHz were averaged and then imaged for sources with detectable HII emission at 6.7-GHz. Assuming spectral index effects are small, this should, give an accuracy similar to that achieved for the relative maser component positions, namely a few tens of milli-arcsec. However, the accuracy of the alignment is limited by the SNR which can be obtained for the 6.7-GHz image. The flux density of the UCHII regions is less at 6.7-GHz, the size of the synthesised beam is larger and the bandwidth of the observations is less. For weaker UCHII regions (16 mJy at 6.7-GHz) the positional error is around 80–160 mas, and around 30 mas for a stronger (160 mJy) source.

(iii) As the two frequencies were observed simultaneously, the phase corrections used to self-calibrate the spectral data can be scaled by the ratio of the frequencies and applied to the (non-self-calibrated) 8.6-GHz continuum data. This technique assumes that phase-calibration errors are dominated by the optical path length in the atmosphere, and that this path length is independent of frequency between 6.7 and 8.6 GHz. This will not work if the self-calibration phase corrections are large, because of phase-wrapping ambiguities. However, after secondary calibrator corrections were applied, the self-calibration corrections were quite small.

As the corrections applied during phase self-calibration were small (typically a few tens of degrees), the shift in the position of the source when applying self-calibration was also small, of the order of a few tens of milliarcsec. This is also equal to the shift when the phase corrections are scaled and applied from one frequency to the other.

The offset between the masers and the 8.6-GHz continuum when no corrections are made can be estimated by assuming an absolute positional accuracy of the ATCA of around 0.3 arcsec . If this error is dominated by phase errors due to the offset phase calibrator, then as both the 6.7- and 8.6-GHz data are subject to the same phase errors, the offset will be proportional to the ratio of the frequencies i.e. $(1 - 6.7/8.6) \times 0.3 = 66$ milliarcsec.

Thus, the positional corrections which are needed to align the masers and the 8.6-GHz continuum are quite small, and are of a similar size to the expected error in the positions due to thermal noise. Because of this it was decided that the alignment of the observations was not improved significantly by techniques (ii) or (iii) above, and the simple approach of (i) was used with a conservative alignment error of 100 milliarcsec between the methanol and UCHII region positions.

2.4 Results

Table 2.1 lists the methanol sources observed and the absolute position of the reference feature. Table 2.2 lists the 8.6-GHz flux density of associated HII regions and detection limits. Because of problems encountered in modelling extended, low-brightness-temperature emission, the detection limits vary significantly between sources.

Figs. 2.1 - 2.28 show the maser spectra, the maser component distribution and the associated 8.6-GHz continuum (if any) with the 6.7-GHz maser components overlayed. Also shown in these Figures is a velocity - major axis offset (v-a) diagram. This is produced by fitting a line to the maser components and plotting the velocity of the components as a function of the distance along the line. The line fitting was done using a least-squares technique, minimizing the distance of the points to the line. This was used because the usual technique of minimizing

Table 2.1: 6.7-GHz methanol masers observed using the ATCA. Masses are given only for sources with a linear v-a relationship and assume Keplerian motion. The distances are the near kinematic distance, unless noted otherwise in Section 4.1. The quoted velocities correspond to the component for which we have given a position (either the reference feature or the brightest component). The derived masses are very uncertain, as neither the distance to the source nor the size of the disc can be well determined.

Source Name	Right Ascension (J2000)	Declination (J2000)	Peak Flux Density (Jy)	Vel. LSR (km s^{-1})	Dist. (kpc)	Diam. (AU)	Mass $M_\odot$	Morphology
G 305 202+0 207	13·11:10.51	-62:34:38 9	27.7	-43 9	6.2	1612	4.1	Linear
G 305 208+0.206	13.11:13.72	-62:34:41.4	327.8	-38 3	6.2	4960	5.8	Elongated
G 305.247+0.245	13.11:32.45	-62:32.09.2	2.0	-32.1	2 7	189		Complex
G 308.918+0.123	13:43:01.75	-62:08.51.3	29.7	-54.5	5 2	1040		Linear
G 309.921+0.479	13:50:41.79	-61:35:10.1	540 2	-59.6	5 3	4240	9 6	Curved
G 316.640−0.087	14:44:18.38	-59:55:11.0	96.6	-19.7	1.3	585	5 4	Elongated
G 323.740−0.263	15:31:45.42	-56:30:50.5	2167.3	-51.2	3.3	1360	6 1	Linear
G 323.741−0.263	15.31.45.84	-56.30:50.6	3.6	-57.1	3 7	990		Complex
G 327.120+0.511	15:47·32.71	-53:52:38.5	73.6	-87.0	5.5	3300	14.7	Linear
G 327.402+0.445	15:49:19.33	-53·45:14 4	11 6	-75.3	4.8	2640	8.9	Linear
G 327.402+0.444	15:49:19.50	-53.45:13.9	92.0	-82 4	5.2	832	1.3	Linear
G 327.402+0 444E	15:49 19.72	-53.45:14.6	1.1	-74.0	4 7			Simple
G 328.236−0 547	15:57·58.27	-53.59:23.1	376.2	-44 6	3.0	2400	33.8	Double
G 328.254−0.532	15:57.59.73	-53:58:00.8	359.7	-37.4	2.6	2080	35.5	Double
G 331.132−0 244	16:10.59.74	-51·50:22.7	21.1	-85.5	5.2	3120	21.8	Linear
G 331.278−0.188	16:11·26.57	-51:41:57.1	109.2	-77.9	4.8	816		Elongated
G 335.726+0.191	16:29·27.37	-48.17:54.7	41.1	-44.4	3.2	1120	15.8	Double
G 335.789+0.174	16:29:47.33	-48.15:52.4	98.8	-47.5	3.4	1360		Linear
G 336.404−0.254	16:34:11 31	-48:06:27.6	0.5	-85.3	5.2	1040		Simple
G 336.409−0.257	16:34:13.17	-48:06:20.8	5.1	-85.6	5.2			Simple
G 336.410−0.256	16:34:13.18	-48.06.15.6	3.2	-93.2	5.5			Simple
G 336.433−0.262	16:34:20 18	-48.05.32.0	38.8	-93.4	5.6	840		Complex
G 337.612−0.060	16:38:09.51	-47:05.00.2	21.4	-43 1	3.3	1980	17.1	Elongated
G 337.632−0.079	16:38:19.10	-47:04·53.9	12.3	-56 8	4 0	560		Complex
G 337.703−0.054	16:38:29.10	-47:00.43.8	4.2	-44.2	3 4			Simple
G 337 705−0.053	16·38:29.61	-47:00:35.7	116.2	-54 7	3 9	5460	72.6	Linear
G 338.460−0.245	16.42:15.48	-46:34:18.7	68.1	-50 5	3 7	555		Elongated
G 340.785−0.096	16:50:14.87	-44:42·26 6	92.9	-107.0	6.2	5580		Complex
G 348 550−0.979S	17:19:20.41	-39:03:51 4	33.6	-9.9	2.2	2420		Curved
G 348.550−0.979N	17·19:20.45	-39:03.49.2	25 3	-20 1	2 2	440		Complex
G 353.410−0.360	17:30:26.17	-34.41:45.6	59 4	-20 2	3 9	624	0.5	Linear
G 9.621+0.196	18.06:14.66	-20.31:31 6	2736.0	1.2	2 0	700	9.9	Elongated
G 9.619+0.193	18:06·14.92	-20.31:43.7	43 8	5 4	2 0			Simple

Table 2.2: Continuum associated with the 6.7-GHz methanol masers. The upper limit for the sources without any detected continuum is four times the rms noise level in the image. The restoring beam size was typically about 1.4×1.1 arcsec.

Source Name	Peak Flux Density (mJy)	Integrated Flux Density (mJy)	Size (arcsec)	Size (AU × 10^3)	Relative Position to Methanol
G 305.202+0.207	<0.9				
G 305.208+0.206	<0.5				
G 305.247+0.245	<1.4				
G 308.918+0.123	28.4	167.1	12×12	62×62	Edge
G 309.921+0.479	350.9	676.2	1.6×1.4	8×7	Slightly offset
G 316.640−0.087	<0.4				
G 323.740−0.263	<0.2				
G 323.741−0.263	<0.2				
G 327.120+0.511	0.5	0.5	1.3×1.6	7×9	Slightly offset
G 327.402+0.445	59.4	101.3	1.2×1.9	6×9	Aligned
G 327.402+0.444	59.4	101.3	1.2×1.9	6×10	Edge
G 327.402+0.444E	<0.5				
G 328.236−0.547	24.3	27.7	1.1×1.3	3×4	Slightly offset
G 328.254−0.532	<0.6				
G 331.132−0.244	36.5	198.6	5×4	26×21	Edge
G 331.278−0.188	3.4	4.1	1.7×1.5	8×7	Aligned
G 335.726+0.191	<0.7				
G 335.789+0.174	<0.4				
G 336.404−0.254	<0.3				
G 336.409−0.257	0.3	0.4	1.0×1.3	5×7	Aligned
G 336.410−0.256	1.0	1.0	1.0×1.3	6×7	Aligned
G 336.433−0.262	<0.3				
G 337.612−0.060	<11.2				
G 337.632−0.079	17.2	65.2	2.2×3.0	9×12	Offset
G 337.703−0.054	<0.6				
G 337.705−0.053	157.5	191.9	1.2×1.6	5×6	Aligned
G 338.460−0.245	<0.3				
G 340.785−0.096	15.9	16.5	1.1×1.6	7×10	Aligned
G 348.550−0.979S	0.8	0.6	1.4×2.0	3×4	Slightly offset
G 348.550−0.979N	<0.5				
G 353.410−0.360	215.1	662.8	3×4	12×16	Slightly offset
G 9.621+0.196	3.1	5.7	2.2×2.5	4×5	Aligned
G 9.619+0.193	75.9	91.9	1.3×2.5	3×5	Slightly offset

the offset in the y-axis failed for the sources elongated in a north-south (y-axis) direction. We have produced a v-a diagram for non-linear sources using the same technique, but the line of best fit will be somewhat arbitrary. If there is a velocity gradient along the maser line, the components will lie on a line in the v-a diagram.

Table 2.4 lists the HII regions that were present in the primary beam of the observations, but without any associated methanol emission. Images of these sources are presented in Appendix A.

To improve the statistical significance of our analysis we have included in the discussion, 12 sources imaged by Ellingsen *et al.* (1996a) and Ellingsen *et al.* (in preparation) with similar observing parameters to the current observations. These sources are listed in Table 2.5 and the properties of these sources are briefly

Table 2.3: Derived parameters for the observed HII regions and the exciting stars associated with them. The values have been calculated following the techniques of Panagia & Walmsley (1978). These equations cannot be applied to extended sources, or very small sources.

Source	$n_e/10^4$ (cm^{-3})	EM/10^7 (pc cm^{-6})	$M_{HII}/10^{-3}$ ($M_\odot$)	U (pc cm^{-2})	Log N_L (s^{-1})	Spectral Type
G 305.202+0.207				<4.8	<45.78	<B0.5
G 305.208+0.206				<4.1	<45.58	<B1
G 305.247+0.245				<3.2	<45.26	<B1
G 308.918+0.123				24.5	47.91	O9.5
G 309.921+0.479	6.8	13.6	78.8	39.5	48.54	O7.5
G 316.640−0.087				<1.3	<44.04	<B3
G 318.949−0.193				<2.3	<44.83	<B2
G 323.740−0.263				<1.8	<44.49	<B2
G 323.741−0.263				<1.9	<44.59	<B2
G 327.120+0.511				3.6	45.40	B1
G 327.402+0.445	3.4	2.7	19.4	19.6	47.63	O9.5
G 327.402+0.444	3.2	2.7	23.7	20.7	47.70	O9.5
G 327.402+0.444E				<3.3	<45.31	<B1
G 328.236−0.547	6.6	3.1	1.1	9.3	46.65	B0.5
G 328.254−0.532				<2.3	<44.84	<B2
G 331.132−0.244				25.9	47.99	O9
G 331.278−0.188	1.9	0.4	1.4	6.7	46.23	B0.5
G 335.726+0.191				<2.8	<45.11	<B1
G 335.789+0.174				<2.5	<44.94	<B2
G 336.404−0.254				<3.0	<45.19	<B1
G 336.409−0.257				3.3	45.31	B1
G 336.410−0.256				4.6	45.74	B1
G 336.433−0.262				<3.2	<45.28	<B1
G 337.612−0.060				<7.3	<46.35	<B0.5
G 337.632−0.079	1.0	0.4	29.7	15.0	47.28	B0
G 337.703−0.054				<2.9	<45.13	<B1
G 337.705−0.053	9.5	11.4	8.6	21.1	47.72	O9.5
G 338.460−0.245				<2.3	<44.81	<B2
G 339.878−1.252	1.7	0.3	1.1	6.0	46.07	B0.5
G 340.785−0.096	13.4	10.9	1.3	12.7	47.06	B0
G 348.550−0.979S	15.6	2.2	0.0	2.1	44.71	B2
G 348.550−0.979N				<2.0	<44.66	<B2
NGC 6334F	7.6	14.7	57.0	36.8	48.45	O7.5
NGC 6634F−NW				<5.0	<45.85	<B0.5
G 351.445+0.660				<3.5	<45.36	<B1
G 353.410−0.360	3.8	5.1	74.1	32.0	48.26	O8.5
G 9.621+0.196	0.7	0.1	1.0	4.2	45.62	B1
G 9.619+0.193	6.7	3.6	1.5	10.6	46.82	B0

Table 2.4: Continuum sources detected with no associated 6.7-GHz methanol.

Source Name	Right Ascension (J2000)	Declination (J2000)	Peak Flux Density (mJy)	Integrated Flux Density (mJy)
G 305.199+0.206	13:11:08.73	-62:34:42.8	10.3	195.0
G 323.744−0.253	15:31:44.13	-56:30:13.3	1.6	123.3
G 327.131+0.526	15:47:32.48	-53:51:31.4	17.3	18.4
G 327.176+0.514	15:47:50.04	-53:50:24.1	7.7	16.8
G 327.107+0.493	15:47:33.11	-53:53:55.7	1.3	1.4
G 328.238−0.549	15:57:59.26	-53:59:25.2	8.4	9.2
G 331.128−0.246	16:10:58.72	-51:50:29.9	10.1	143.2
G 331.278−0.189	16:11:26.68	-51:41:58.9	10.5	16.6
G 335.772+0.143	16:29:51.24	-48:17:51.9	5.4	7.8
G 335.772+0.139	16:29:52.38	-48:18:02.6	1.6	1.3
G 336.442−0.260	16:34:21.99	-48:05:02.5	2.5	49.9
G 336.410−0.258	16:34:13.61	-48:06:20.5	9.4	30.0
G 338.461−0.258	16:42:19.08	-46:34:48.2	6.0	23.9
G 338.405−0.205	16:41:51.89	-46:35:12.8	49.5	621.7
G 348.530−0.972	17:19:15.07	-39:04:36.3	6.0	154.1
G 348.698−1.027	17:19:58.88	-38:58:15.7	5.5	35.2
G 9.622+0.198	18:06:14.35	-20:31:25.5	15.2	30.8

summarized in Section 2.5.

The total size of the sample of methanol masers with simultaneous UCHII observations is 45. These can be qualitatively characterized into five groups.

- ***Linear or curved:*** 17 of the sources have a simple linear morphology. Twelve of these linear sources also show a linear velocity trend across the line while the other five do not. For a number of the sources with a velocity gradient (e.g. G 327.120+0.511 and G 327.402+0.445), the components show a remarkably straight line in the v-a digram. Others (such as G 337.705−0.053) are not as well defined, but still show a definite trend in velocity.

- ***Elongated:*** 8 of the sources have the individual maser components significantly more extended in one direction than the other. These sources seem to be half way between the linear and the complex sources. Of these, 6 show a velocity gradient, while the other two do not.

- ***Pair:*** 3 of the sources consist of two clusters separated by 0.5 to 1.0 arcsec. In each case the cluster velocities differ by approximately 10 km s^{-1} and the individual clusters are elongated in a direction perpendicular to the line joining them.

- ***Complex:*** 10 of the sources have a complex structure. Of these sources two (G 305.247+0.245 and G 340.785−0.096) show some structure in the v-a diagram.

- ***Simple:*** 7 of the sources have a simple morphology with only one or two spectral components. All of these simple sources, except one (G 9.619+0.193), are quite weak with a peak flux density of less than 5 Jy.

Table 2.5: Methanol sources from Ellingsen *et al.* (1996b) and Ellingsen *et al.* (in preparation).

Source Name	Right Ascension (J2000)	Declination (J2000)	Peak Flux Density (Jy)	Vel. LSR (km s^{-1})	Morphology	Cont. Peak Flux Density (mJy)
G 318.949−0.193	15:00:55.33	-58:58:42.0	700	-34.7	Linear	<0.7
G 328.808+0.633	15:55:48.45	-52:43:06.6	240	-43.8	Linear	200.2
G 328.809+0.633	15:55:48.71	-52:43:05.7	53	-44.2	Simple	248.2
G 339.878−1.252	16:52:04.66	-46:08:34.2	1700	-38.7	Linear	5.6
G 345.003−0.224	17:05:11.23	-41:29:06.9	73	-26.2	Complex	176.2
G 345.003−0.223	17:05:10.89	-41:29:06.2	240	-22.5	Complex	<0.2
G 345.012+1.797	16:56:46.82	-40:14:08.9	31	-12.7	Linear	<0.7
G 345.010+1.792	16:56:47.58	-40:14:25.9	410	-18.0	Linear	178.5
NGC 6334F	17:20:53.37	-35:47:01.3	3300	-10.4	Elongated	536.4
NGC 6634F−NW	17:20:53.18	-35:46:59.3	1500	-11.2	Elongated	<6.3
G 351.445+0.660	17:20:54.61	-35:45:08.6	100	-9.2	Complex	<2.6
G 351.775−0.536	17:26:42.57	-36:09:17.6	230	1.3	Complex	10.7

We have classified 38 per cent of the sample as linear, 18 per cent are elongated, 22 per cent are complex, 7 per cent are pairs and 15 per cent are simple.

Of the 45 6.7-GHz methanol sources in this sample, 25 are associated with 8.6-GHz emission, presumably from an UCHII region. The typical 4-σ detection limit was 0.4 to 0.6 mJy $beam^{-1}$ for sources without any detected UCHII emission. These detection limits are given in Table 2.2. The peak flux density of the detected continuum ranges from 0.3 to 536 mJy $beam^{-1}$. The relationships of the methanol position to the UCHII region can be characterized into four groups.

- ***Aligned:*** 8 of the sources with associated continuum emission have the maser components aligned with the peak of the (unresolved) continuum emission.
- ***Slightly offset:*** 10 of the maser sources are offset 0.5 to 1.0 arcsec from the peak of the UCHII region. All but one of these continuum regions are unresolved or very slightly resolved.
- ***At edge:*** 3 of the sources are at the edge of the HII region. Two of these continuum sources are about 10 arcsec across and probably represent regions of multiple star-formation. The masers may be associated with compact cores which are not detected because of confusion with nearby extended HII emission.
- ***Offset:*** 2 of the sources are offset by 3.5 arcsec from an unresolved or partially resolved UCHII region. Assuming the near kinematic distance to these sources, this represents a linear separation of about 15,000 AU or 0.07 parsec. For these sources, the methanol source is unlikely to be directly associated with the detected HII region.

2.5 Individual sources

In the following section we briefly discuss the morphology of the methanol maser sources and their associated UCHII region. In particular, we consider whether the geometry of individual sources can be explained using the circumstellar disc model.

2.5.1 Kinematic distance

Unless otherwise noted, we have calculated the kinematic distance to the maser sources using the Galactic rotation model of Brand & Blitz (1993) assuming R_0=8.5 kpc and Θ_0=220 km s^{-1}. For many of the sources we can rule out the far-kinematic distance as this implies an unrealistic luminosity of the sources. For the sources for which we cannot rule out the far-kinematic distance, we note that the source is more likely to be at the near distance, as our sample is not flux-density-limited and the sources were chosen to have (relatively) strong peak flux densities. The assumed kinematic distances are listed in Table 2.1.

2.5.2 Modelling the discs

As discussed previously, one possible explanation for the linear sources which also show a line in the v-a diagram is that the maser emission comes from an edge-on disc around a massive young star. If the maser components are at a constant distance, r, from the central star, then the gradient of the line in the v-a diagram,

$$\frac{dv}{da} = \sqrt{GM/r^3}$$

where M is the mass of the star. If the disc is inclined the measured velocity gradient will decrease as the cosine of the inclination angle (Section 4.7.1), and the derived mass will be reduced by the square of the cosine. For modest inclination angles, this effect is quite small.

For the linear sources which show a velocity gradient, we have calculated the mass of the central star assuming the velocity gradient is caused by Keplerian rotation, assuming an edge-on disc. The derived masses are listed in Table 2.1. We have taken r to equal the maximum extent of the observed line, so the size of the disc will almost certainly be underestimated, as we do not know over what fraction of the disc the maser emission occurs. This, along with the effect of inclination, means the derived masses should be considered a lower limit. The masses also depend on the distance to the source which cannot be accurately measured.

2.5.3 Properties of the ionized gas

To calculate the physical properties of the UCHII regions associated with the methanol sources, we follow the technique of Panagia & Walmsley (1978). This technique assumes that the HII region is spherically symmetric, optically thin and

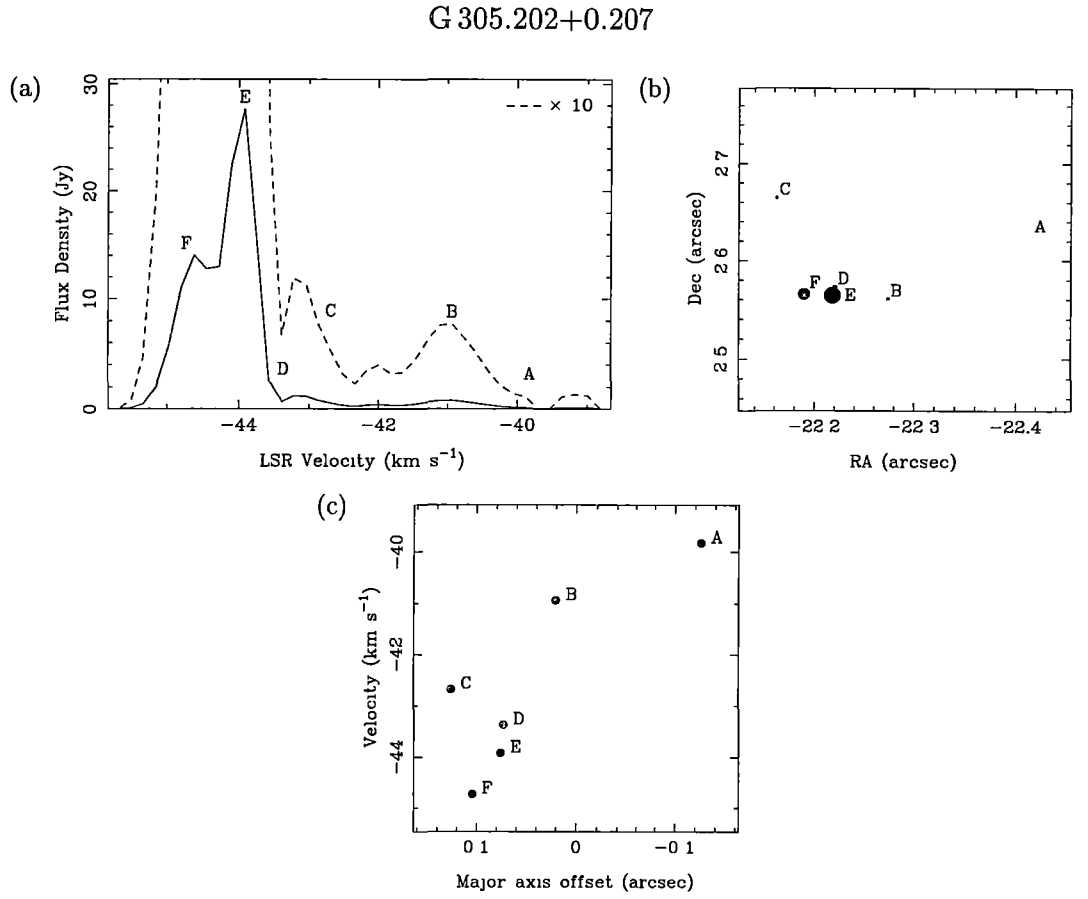

Figure 2.1: (a) Spectrum, (b) map and (c) position-major axis offset (v-a) diagram of G 305.202+0.207. The area of the solid circles (b) is proportional to the flux density of the component.

ignores effects such as absorption by dust. For sources which could be fitted with an elliptical Gaussian function we have used the equations of Panagia & Walmsley to calculate the electron density (n_e), emission measure (EM) and the mass of the ionized hydrogen ($M_{\rm HII}$). The excitation parameter (U) was obtained using equation (8) of Schraml & Mezger (1969) which was then used to derive the Lyman continuum photon flux ($N_{\rm L}$) and spectral class as derived in Panagia (1973). As U and $N_{\rm L}$ do not depend on the source geometry, we have calculated them for extended sources and an upper limit for sources without detectable continuum emission, assuming a 4-σ detection limit. The calculated parameters are shown in Table 2.3. For these calculations we have assumed an electron temperature of 10^4 K and He^+/H^+ abundance ratio of 0.1 (Wood and Churchwell, 1989b). We have included sources from Ellingsen *et al.* (1996b), as the values were calculated incorrectly.

Optical depth effects will reduce our estimate of the derived values. Wood & Churchwell (1989b) used the Panagia & Walmsley technique with a VLA UCHII region survey at 4.9 and 14.9 GHz and found that the values agreed to within a factor of 2. The absorption of UV photons by dust will reduce the ionizing

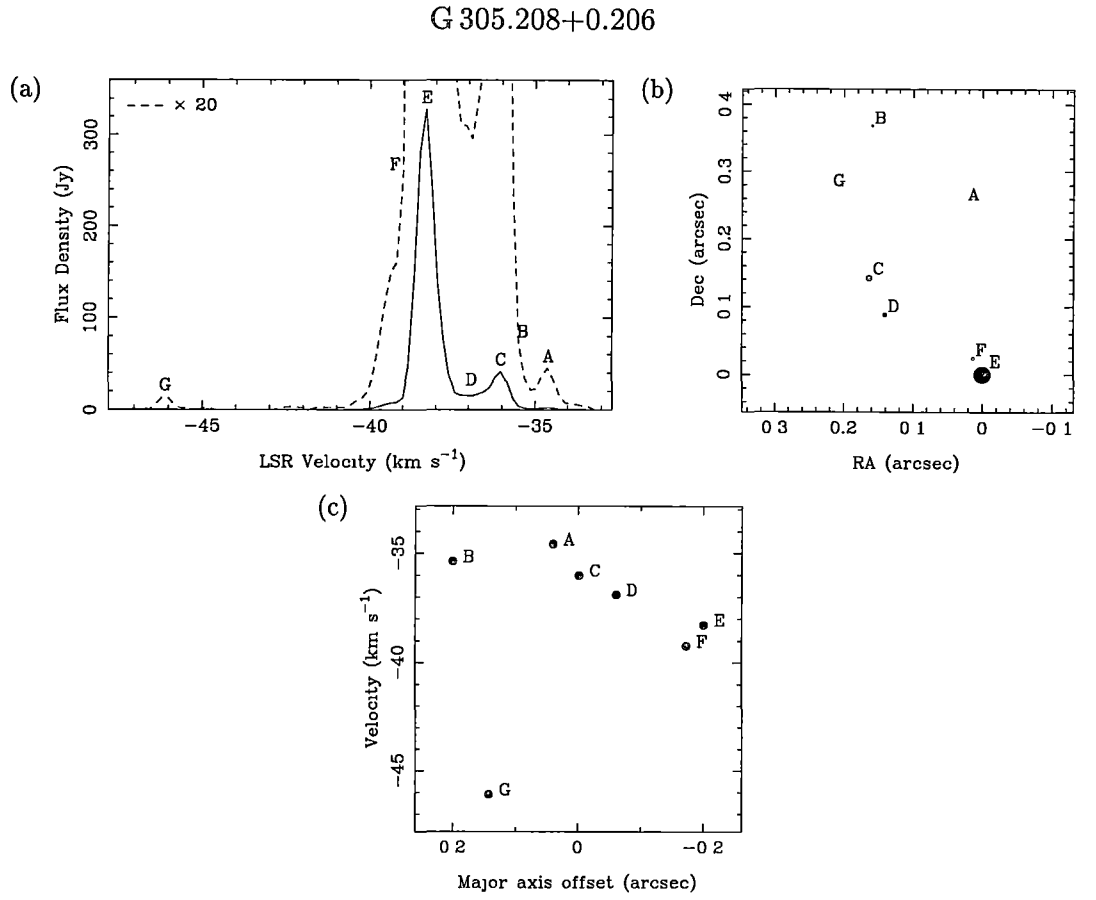

Figure 2.2: (a) Spectrum, (b) map and (c) v-a diagram of G 305.208+0.206.

potential of the embedded star, making the spectral types an underestimation depending on the magnitude of this effect. The fraction of UV photons absorbed by dust may be as high as 90 per cent (Wood and Churchwell, 1989b). Absorption of 90 per cent of UV photons would reduce the apparent spectral type by about one sub-class only. Another problem is that the HII region may be ionized by more than one embedded star. If this is the case the HII flux density will be dominated by the most massive, but the maser source is not necessarily associated with the largest star.

In the following notes we have grouped together sources that were close enough to observe from a single pointing centre.

G 305.202+0.207, G 305.208+0.206, G 305.247+0.245

The 6.7-GHz methanol spectrum and component maps for these three sources are shown in Figs. 2.1-2.3. G305.202+0.207 has been previously observed with the ATCA by Norris *et al.* (1993) and Caswell *et al.* (1995c) although no component map has been published. The source has a curved morphology with a velocity gradient, excluding component 'C'. The source is not associated with any continuum above a 4-σ limit of 0.9 mJy beam^{-1}, and is offset by 15 arcsec from an extended

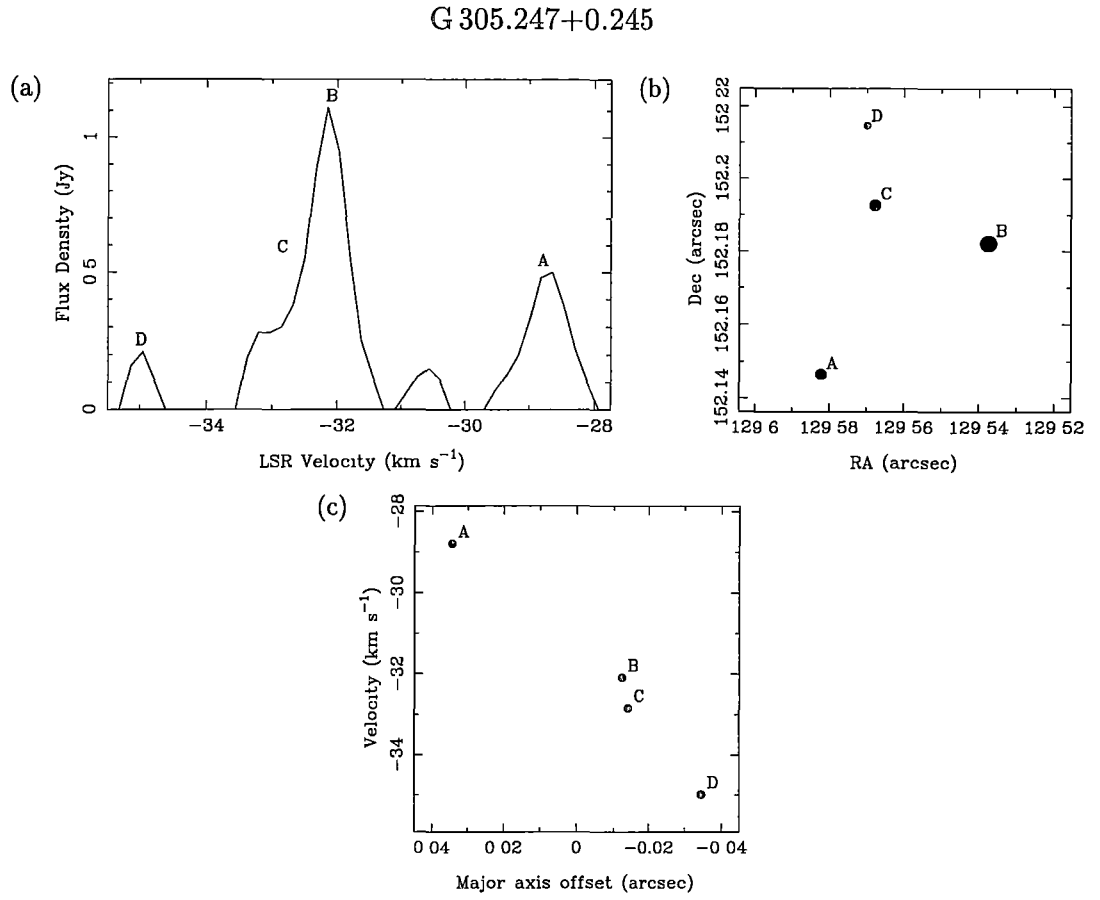

Figure 2.3: (a) Spectrum, (b) map and (c) v-a diagram of G 305.247+0.245. Although the source is complex, the v-a diagram is linear. This could be the result of a disk with a significant inclination angle.

(15×10 arcsec) HII region with an integrated flux density of 195 mJy.

Norris *et al.* (1993) presented a component map of G 305.208+0.206. The current observations are consistent to within the relative position errors (20 milliarcsec), but also show a number of new components. The source shows a curved morphology with a near-monotonic gradient (excluding 'G'). This source is not associated with any continuum emission with a flux density limit of 0.55 mJy beam^{-1}.

Caswell & Haynes (1987) suggest that the HII region offset from G 305.202+0.207 and G 305.208+0.206 is at a kinematic distance of 6.5 kpc (based on HI absorption). The far kinematic distance of G 305.208+0.206 is 6.2 kpc, while the kinematic distance to G 305.202+0.207 is 4.8 kpc with no ambiguity. As it is most likely that these sources come from the same region, we have adopted a kinematic distance of 6.2 kpc from both G 305.202+0.207 and G 305.208+0.206. This gives a source size of 1612 AU for G 305.202+0.207 and 4960 AU for G 305.208+0.206.

G 305.247+0.245 is separated from the first two sources by more than 3 arcmin. Although the component map is complex, the v-a diagram does show a clear velocity gradient. This could be result of a disk with a significant inclination

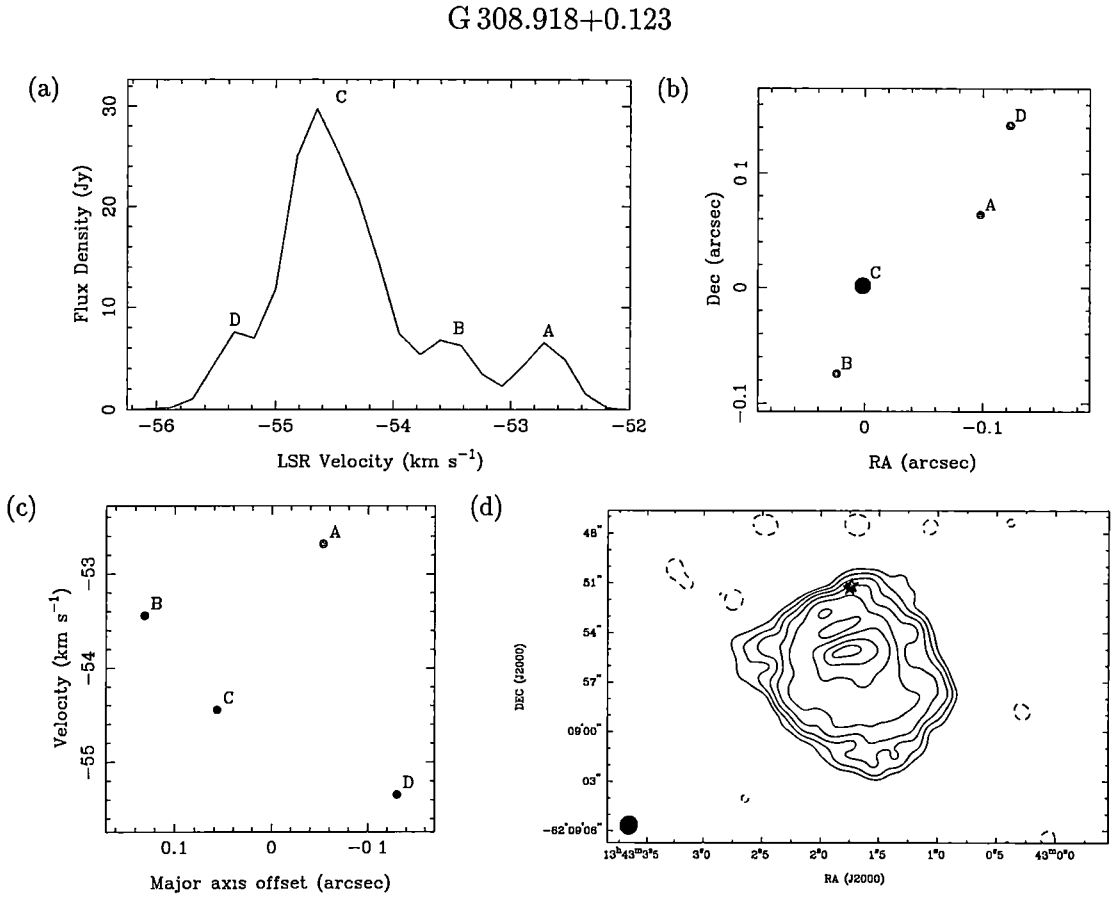

Figure 2.4: (a) Spectrum, (b) map and (c) v-a diagram of G 308.918+0.123. The area of the solid circles in (b) is proportional to the flux density of the component (d) Radio continuum image of G 308.918+0.123 at 8.6 GHz. The contours are at -1, 1, 2, 4, 8, 16, 32, 64 and 90 per cent of the peak flux density (28.4 mJy beam^{-1}). The integrated flux density of the source is 167.1 mJy. The positions of the methanol masers are indicated by stars. The size of the Gaussian restoring beam is 1.07×1.16 arcsec and is shown on the lower left of the plot. The clumpy morphology of the UCHII region suggests that there is more than one embedded star within the HII region.

angle. The source is sufficiently offset from the other two that we cannot select between the near and far kinematic distance. If we adopt the near distance of 2.7 kpc, the source has a linear extent of 190 AU.

G 308.918+0.123

The 6.7-GHz spectrum and map as well as the 8.6-GHz continuum are shown in Fig. 2.4. This is the first high-resolution image of the 6.7-GHz methanol emission. The maser components are in a line, though there is no clear velocity gradient along the source. The maser emission is located at the edge of a 15×15-arcsec HII region with an integrated flux density of 167 mJy. The shape and size of the HII region suggest that there is more than one embedded star and that the HII region is primarily ionized by a star not associated with the maser emission. This HII

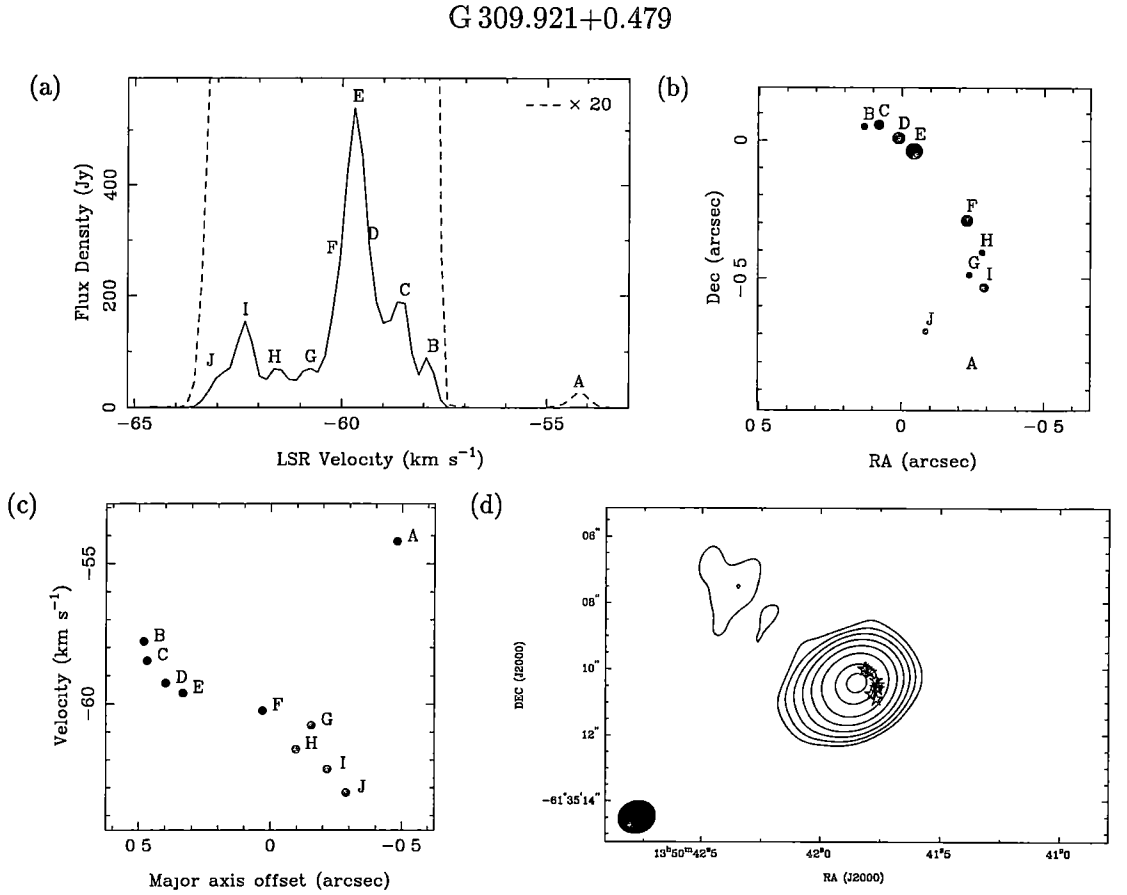

Figure 2.5: (a) Spectrum, (b) map and (c) v-a diagram of G 309.921+0.479. The areas of the solid circles in (b) is proportional to the flux density of the component. The curve of maser spots shows a velocity gradient, which implies a central mass of 9.6 $M_{\odot}$ assuming Keplerian motion. (d) Radio continuum image of G309.921+0.479 at 8.6 GHz. The contours are at -1, 1, 2, 4, 8, 16, 32, 64 and 90 per cent of the peak flux density (350.9 mJy beam^{-1}). The integrated flux density of the source is 676.2 mJy. The positions of the methanol masers are indicated by stars. The size of the Gaussian restoring beam is 0.99×1.20 arcsec and is shown on the lower left of the plot.

region has been previously imaged by Caswell *et al.* (1992) using the Molonglo Observatory Synthesis Telescope and they reported a 843-MHz flux density of 310 mJy. The kinematic distance to this source is 5.2 kpc (with no ambiguity) giving a source size of 1040 AU. The position of the maser source with respect to the HII region could indicate outflow from a central star, though the narrow velocity range of the source makes this seem unlikely. The flux density of the HII region indicates a spectral type of O8.5 for the embedded star although, as discussed above, this is probably not the star associated with the maser source.

G 309.921+0.479

The methanol spectrum and map, as well as the associated HII region, are shown in Fig. 2.5. The 6.7-GHz methanol emission has been previously imaged using

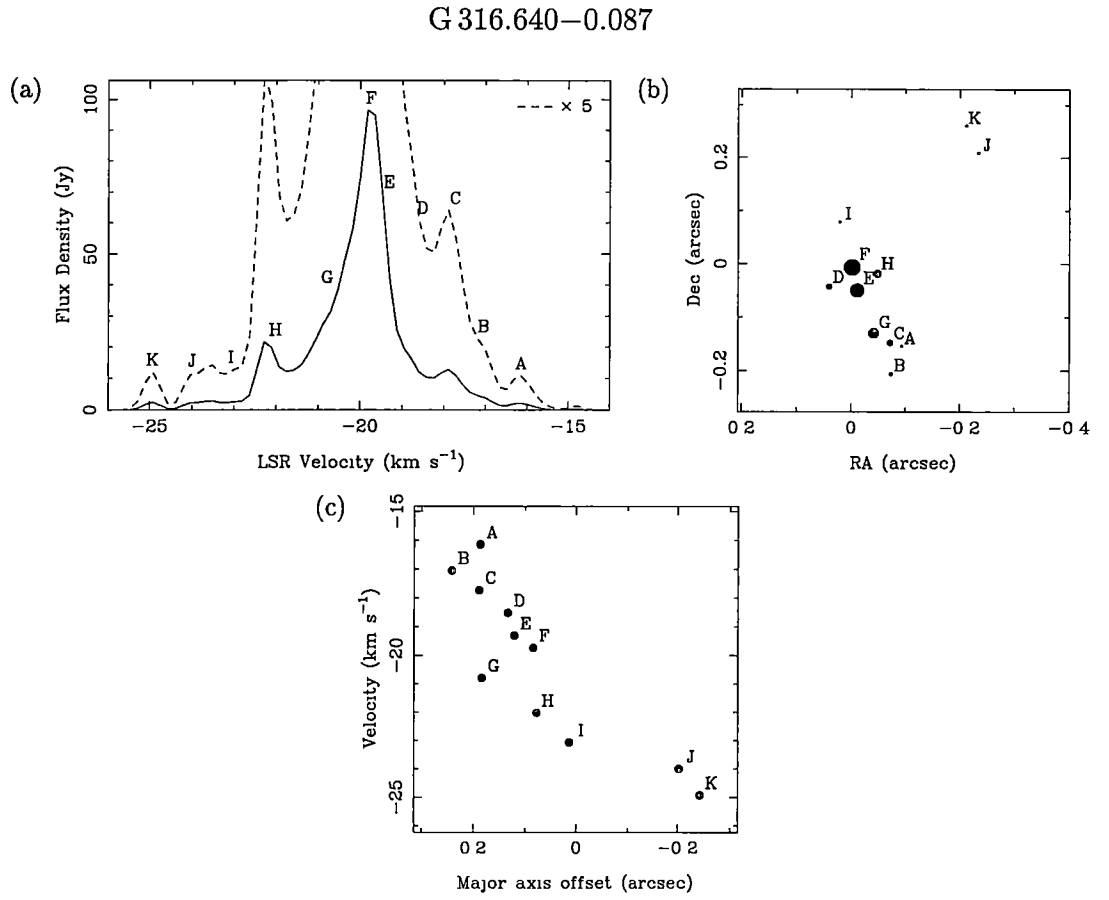

Figure 2.6: (a) Spectrum, (b) map and (c) v-a diagram of G 316.640−0.087. Although this source does not have a linear morphology, the v-a diagram does shows a velocity gradient, which implies a central mass of $5.4 M_{\odot}$ assuming Keplerian rotation.

the ATCA and using VLBI at 12.2-GHz by Norris *et al.* (1993; 1998), and is consistent with the current observations. The maser components lie on an arc with a clear velocity gradient along it, except for a single feature ('A') which is offset in velocity from the other features by 4 km s^{-1}. The maser components are offset by 0.75 arcsec from the peak of an almost unresolved HII region with an integrated flux density of 676 mJy. This continuum source was strong enough to image at 6.7 GHz and so the alignment of the methanol and continuum is better than 0.1 arcsec. Interestingly, the maser features seem to follow the contours of the continuum image. The maser source is the second brightest in the sample and is associated with the most luminous UCHII region. The kinematic distance to the source is 5.3 kpc with no ambiguity. This implies a source size of 4240 AU. The position of the maser components in relation to the UCHII region is better explained by a shock-front rather than by a circumstellar disc, though this does not explain the velocity gradient.

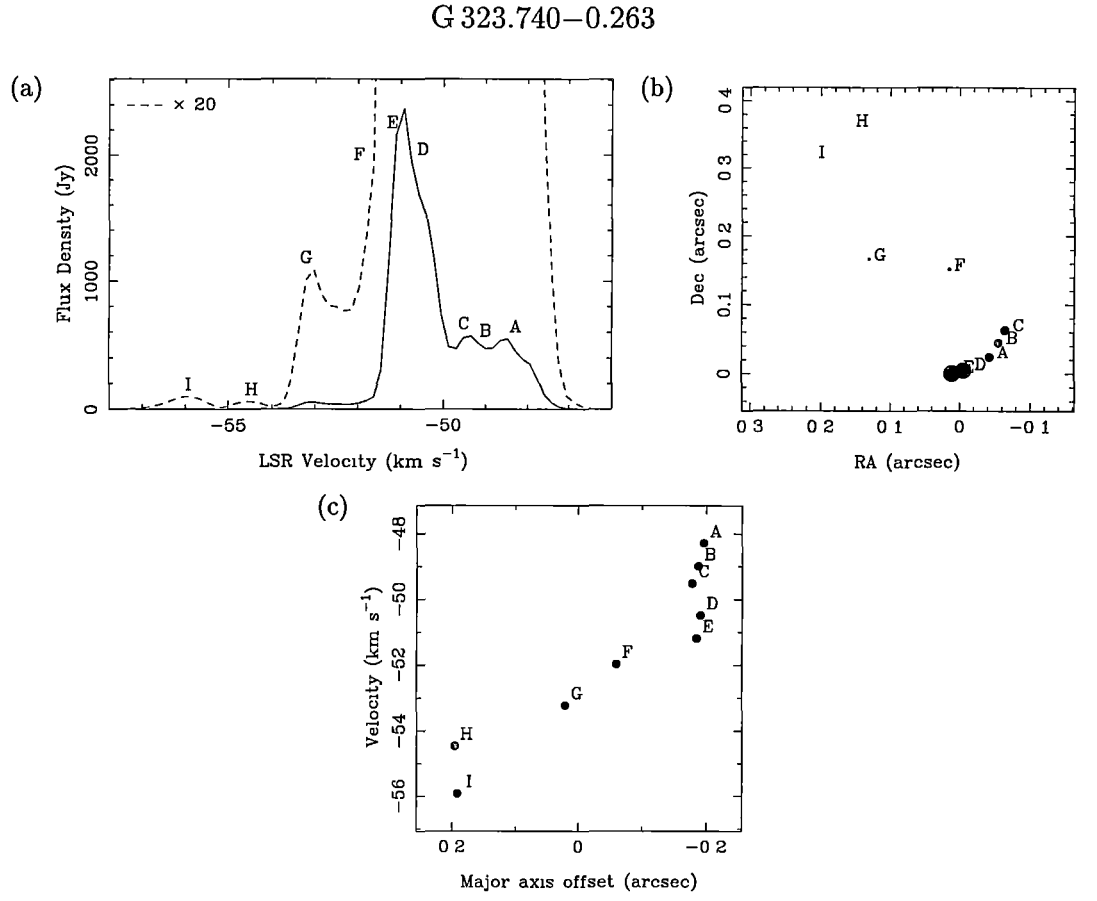

Figure 2.7: (a) Spectrum, (b) map and (c) v-a diagram for G 323.740−0.263. The velocity gradient implies Keplerian motion around a mass of 6.1 $M_{\odot}$.

G 316.640−0.087

The ATCA spectral-line image and 6.7-GHz spectrum are shown in Fig. 2.6. This is the first high-resolution image of the 6.7-GHz maser emission. The component distribution shows an elongated/curved morphology with a definite velocity gradient along the source, though it is not monotonic. The v-a diagram shows the velocity trend more clearly. We detected no continuum associated with this source, with a 4-σ flux density limit of 0.4 mJy beam^{-1}. Assuming the near kinematic distance of 1.3 kpc, the size of this source is 585 AU. The far kinematic distance of 11.0 kpc cannot be ruled out, though it would make this source one of the most luminous in this sample.

G 323.740−0.263 & G 323.741−0.263

The 6.7-GHz spectrum and image for these two sources are shown in Figs. 2.7 and 2.8. The two sources are separated by 3.5 arcsec and neither has any associated continuum with a 4-σ flux density limit of 0.2 mJy beam^{-1}.

The source G 323.740−0.263 has previously been named G 323.74−0.26, G 323.74−0.25 and G 323.77−0.21 (Norris *et al.*, 1993; McCutcheon *et al.*, 1988;

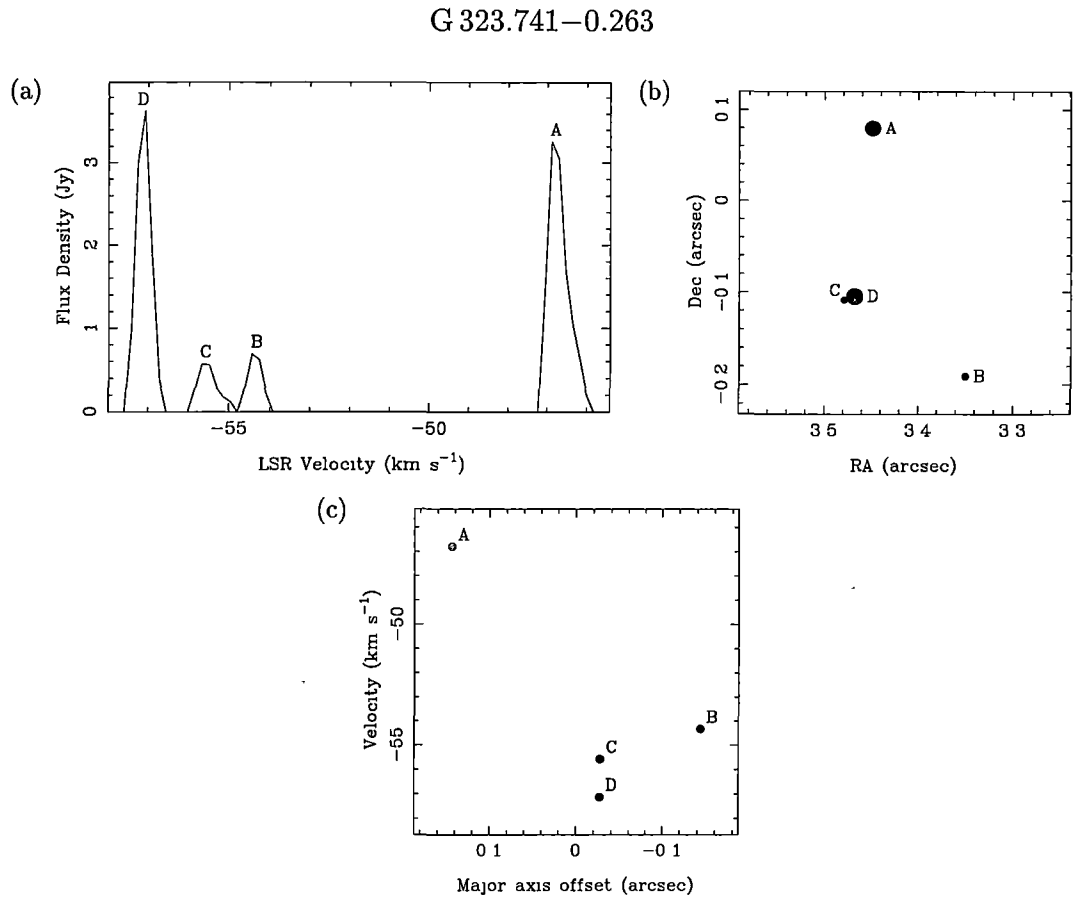

Figure 2.8: (a) Spectrum, (b) map and (c) v-a diagram for G 323.741−0.263

Macleod and Gaylard, 1992) and has been imaged at high resolution by Norris *et al.* The morphology of this source is rather unusual with the stronger components 'A' to 'E' forming a line (without a clear velocity gradient) while the weak and blue-shifted components 'F' to 'I' form another line, perpendicular to the first one. The v-a diagram shows that the second line does have a velocity gradient. One explanation of this is that the first, stronger, line delineates an edge-on disc, while the weak blue-shifted components are in outflow. The velocity gradient of the blue-shifted components does not support this view though, nor does the narrow velocity range of the components in the outflow region. Alternatively, the second line may delineate a thick disc and the line of stronger components represent a region in the disc which is particularly favorable to the maser pumping (such as a shock front). Another possibility is that this source is a binary system with two separate discs.

This source is almost certainly at the near kinematic distance of 3.4 kpc and is the most luminous in the sample. This implies a size of 1360 AU for the whole source, while the line in the south-west has an extent of 340 AU. The Keplerian mass in Table 2.1 assumes that the whole source represents an edge-on disc.

The source G 323.741−0.263 has not been reported before, probably because it is about 1000 times weaker than its counterpart. It also shows no clear spatial

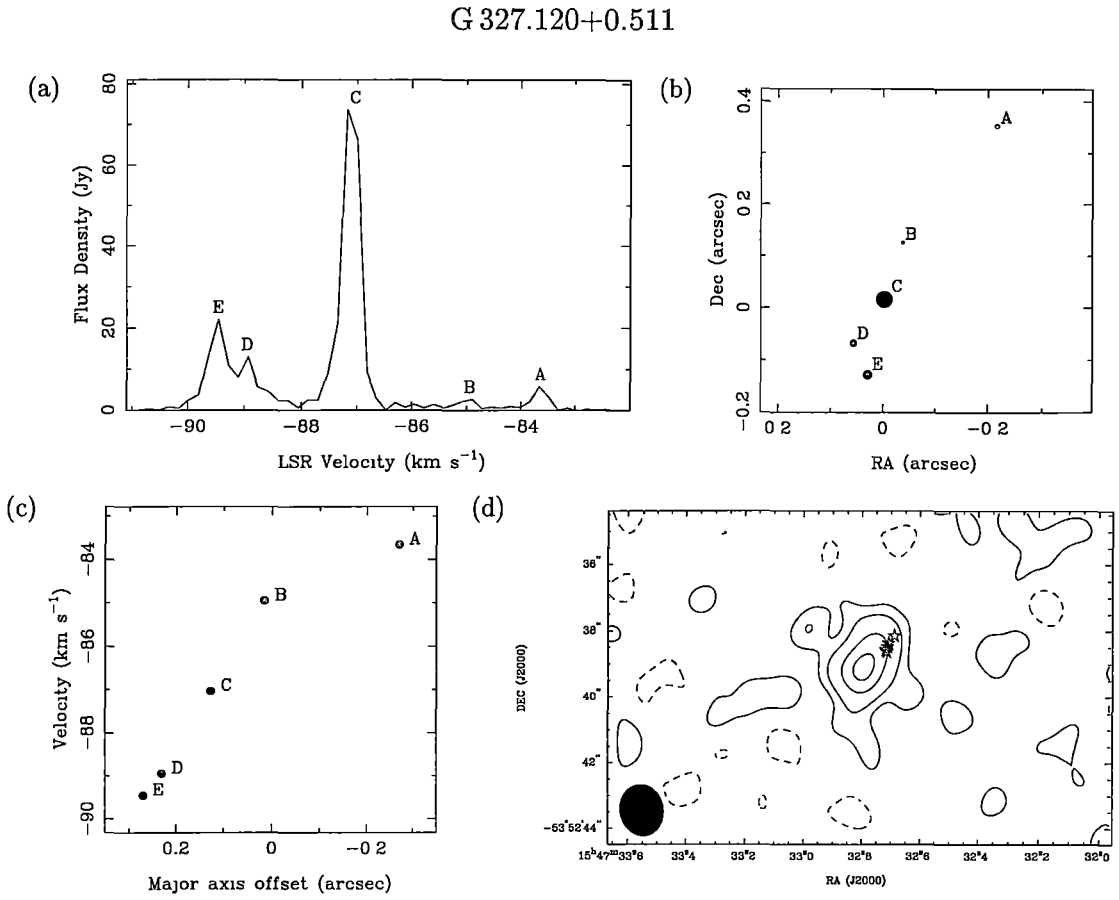

Figure 2.9: (a) Spectrum, (b) map and (c) v-a diagram for G 327.120+0.511. Both the source and v-a diagram are remarkably linear, with an implied central mass of 14.7 $M_{\odot}$ assuming Keplerian rotation. (d) Radio continuum image of G 327.120+0.511 at 8.6 GHz. The contours are at -16, 16, 32, 64 and 90 per cent of the peak flux density (0.5 mJy beam^{-1}). The integrated flux density of the source is 0.8 mJy. The positions of the methanol masers are indicated by stars. The size of the Gaussian restoring beam is 1.31×1.58 arcsec and is shown on the lower left of the plot.

or velocity distribution.

G 327.120+0.511

The spectrum and map of the 6.7-GHz emission, along with the associated 8.6-GHz continuum is show in Fig. 2.9. This is the first high-resolution image of this source. The maser components lie in a line, with a constant velocity gradient (as shown by the v-a diagram). The maser source is associated with an HII region with a peak flux density of 0.39 mJy. This is the weakest continuum source detected in the current observations. The maser line is offset from the peak in the continuum by 1 arcsec. The methanol and continuum flux density of this source makes it difficult to determine whether the source is at the near kinematic distance of 5.5 or at the far distance of 8.7 kpc, though it is more likely to be at the closer distance. If the source is at the near distance, then its size is 3300 AU, while the

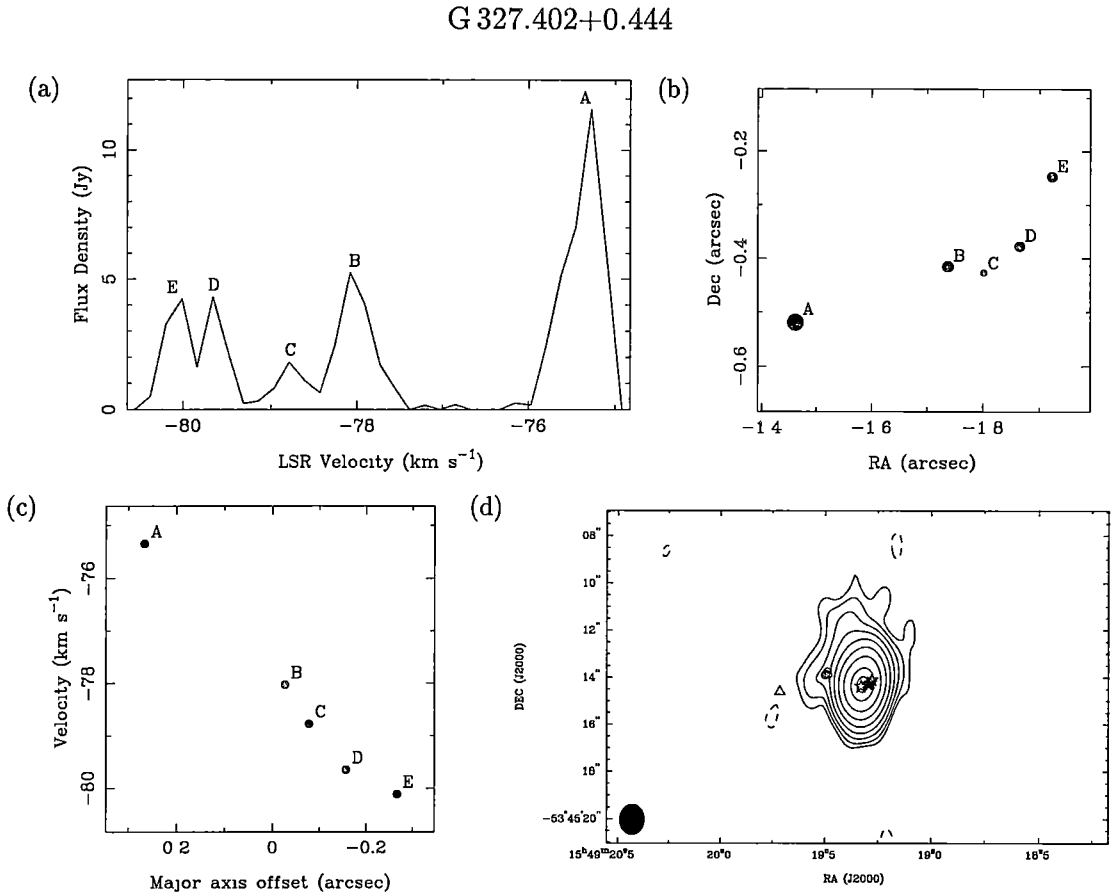

Figure 2.10: (a) Spectrum, (b) map and (c) v-a diagram for G 327.402+0.444. The velocity gradient implies a mass of 1.3 $M_{\odot}$ assuming Keplerian rotation. (d) Radio continuum image of G 327.402+0.445 at 8.6 GHz. The contours are at -0.5, 0.5, 1, 2, 4, 8, 16, 32, 64 and 90 per cent of the peak flux density (59.4 mJy beam^{-1}). The integrated flux density is 101 mJy. The maser positions of G 327.402+0.444 and G 327.402+0.445 are represented by stars and open circles respectively. G 327.402+0.444 is at the centre of this unresolved HII region. The single maser component from G 327.402+0.444E is represented by a triangle is offset by one arcsec east of the HII region. The size of the Gaussian restoring beam is 1.05×1.30 arcsec and is shown on the lower left of the plot.

far kinematic distance gives a size of 5220 AU. An unusual feature of this source is the three-peaked profile which is characteristic of a classical Keplerian disc.

G 327.402+0.445, G 327.402+0.444 & G 327.402+0.444E

The continuum image, the 6.7-GHz spectra and maps are shown in Figs. 2.10 and 2.11. This source has not been imaged before at high resolution. The source, also known as G 327.40+0.44, consists of three clusters separated by 5 arcsec. The maser emission is associated with a partially resolved HII region with an integrated flux density of 101 mJy. The maser source G 327.402+0.444E consists of a single weak (1 Jy) component, and so neither a position nor v-a plot has been produced. Its position relative to the other components is shown on the continuum plot.

Although G 327.402+0.445 is a weak source, it shows a linear structure both

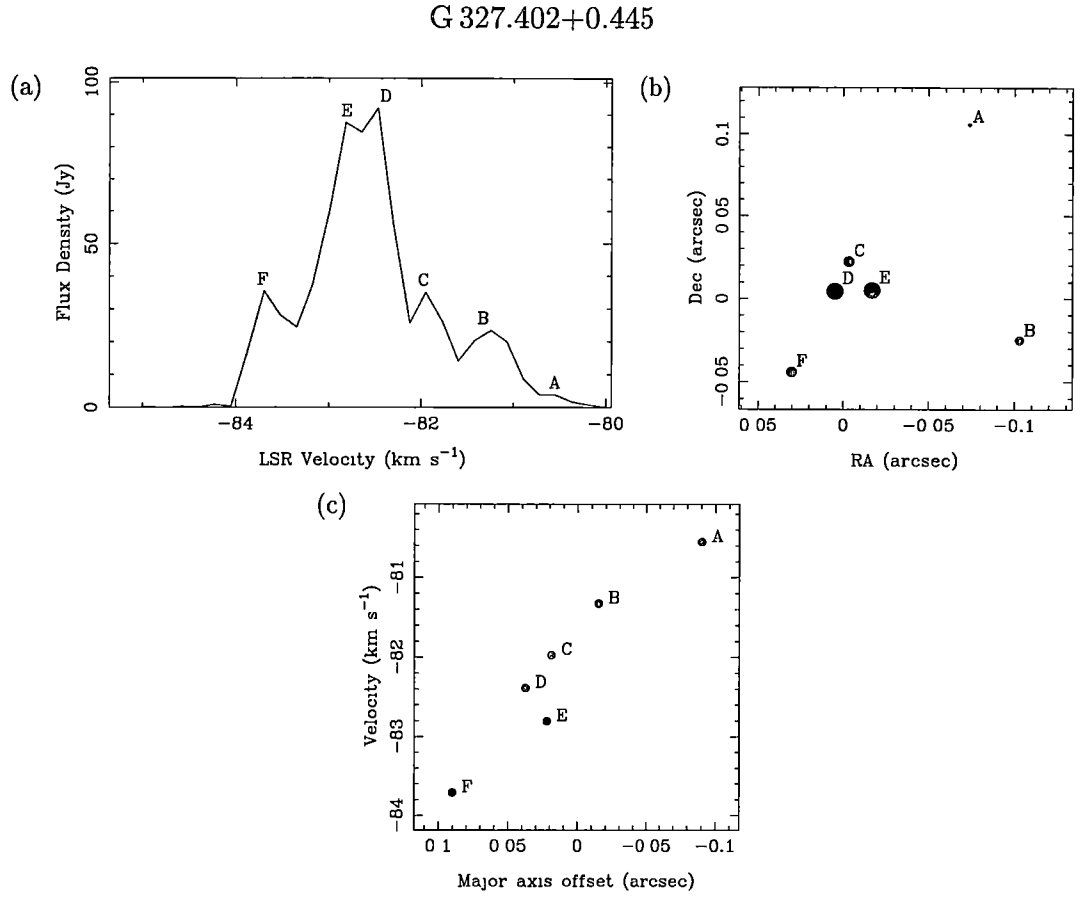

Figure 2.11: (a) Spectrum, (b) map and (c) v-a diagram for G 327.402+0.445. The maser components in this source are also in a line, except for the component 'B'. The velocity gradient implies a mass of 8.9 $M_{\odot}$ assuming Keplerian motion. The maser is at the edge of an UCHII region, shown in Fig. 2.10d.

spatially and in the v-a diagram. The line of maser components goes very nearly though the peak of the UCHII region, although most of the maser components are offset to one side. The near kinematic distance of 4.8 kpc is preferred because the far distance would make the source size very large. The implied source size is 2880 AU.

The maser components of G 327.402+0.444 (excluding 'B') also form a line and show a linear velocity gradient. This source is offset from G 327.402+0.445 by 2 arcsec and is located at the edge of the HII region. The two maser clusters are most likely separated sources. The HII region shows some extension at the location of G 327.402+0.444, which supports this. These two sources are the only instance in the sample of two widely separate maser clusters associated with a single UCHII region. The size of the source is 720 AU (assuming the near distance). If G 327.402+0.444 is associated with a separate star, it is impossible to estimate its spectral type because the larger star is so close by. It is worth noting that although the two lines have a similar position angle, the velocity gradient runs in the opposite direction.

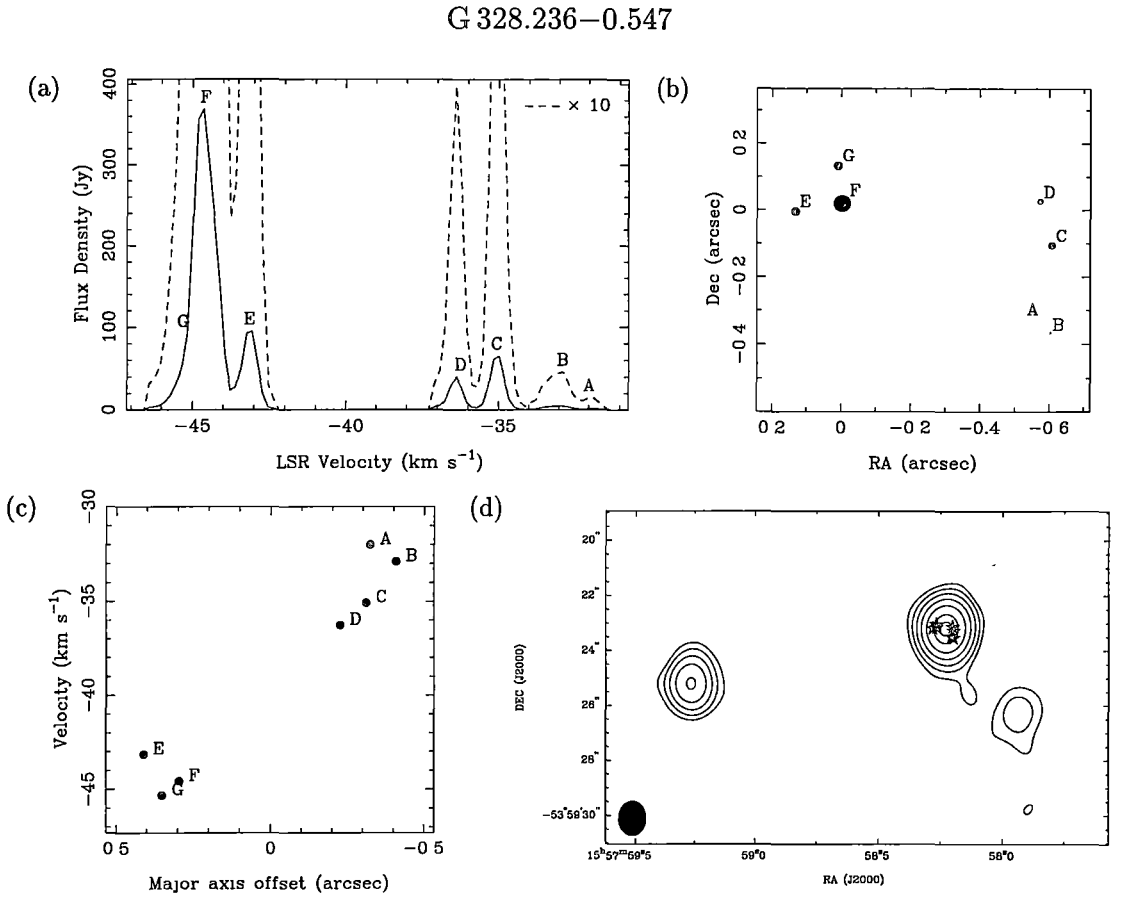

Figure 2.12: (a) Spectrum, (b) map and (c) v-a diagram of G 328.236−0.547. Assuming the two clumps of emission represent the two edges of a circumstellar disc, the velocity separation gives a central mass of $33.8 M_{\odot}$. (c) Radio continuum image of G 328.236−0.547 at 8.6 GHz. The contour levels are at -2, 2, 4, 8, 16, 32, 64 and 90 per cent of the peak flux density (24.3 mJy beam^{-1}). The integrated flux density is 27.7 mJy. The positions of the methanol masers are indicated by stars. The Gaussian restoring beam is 1.02×1.26 arcsec and is shown on the lower left of the plot.

G 328.236−0.547 & G 328.254−0.532

The spectra and images of this pair of sources are shown in Figs. 2.12 and 2.13. These sources, which are separated by 83 arcsec, have been previously imaged by Norris *et al.* (1993). G 328.236−0.547 has a complex spatial morphology, with two clumps on either side of an essentially unresolved HII region which has an integrated flux density of 28 mJy beam^{-1}.

The two maser clusters, on either side of an UCHII region, which comprise G 328.236−0.547 are separated in velocity by almost 10 km s^{-1}. This morphology could be explained by shock fronts, possibly in a bipolar outflow, explaining the large velocity difference between the clusters. Another explanation could be that the two clusters of maser components are on either side of a thick disc. If we assume the near kinematic distance of 3.0 kpc (we can rule out the far distance on the grounds of luminosity), the two clusters are separated by 2400 AU and the central star has a mass of 33.8 $M_{\odot}$ (assuming that the 10 km s^{-1} represents twice

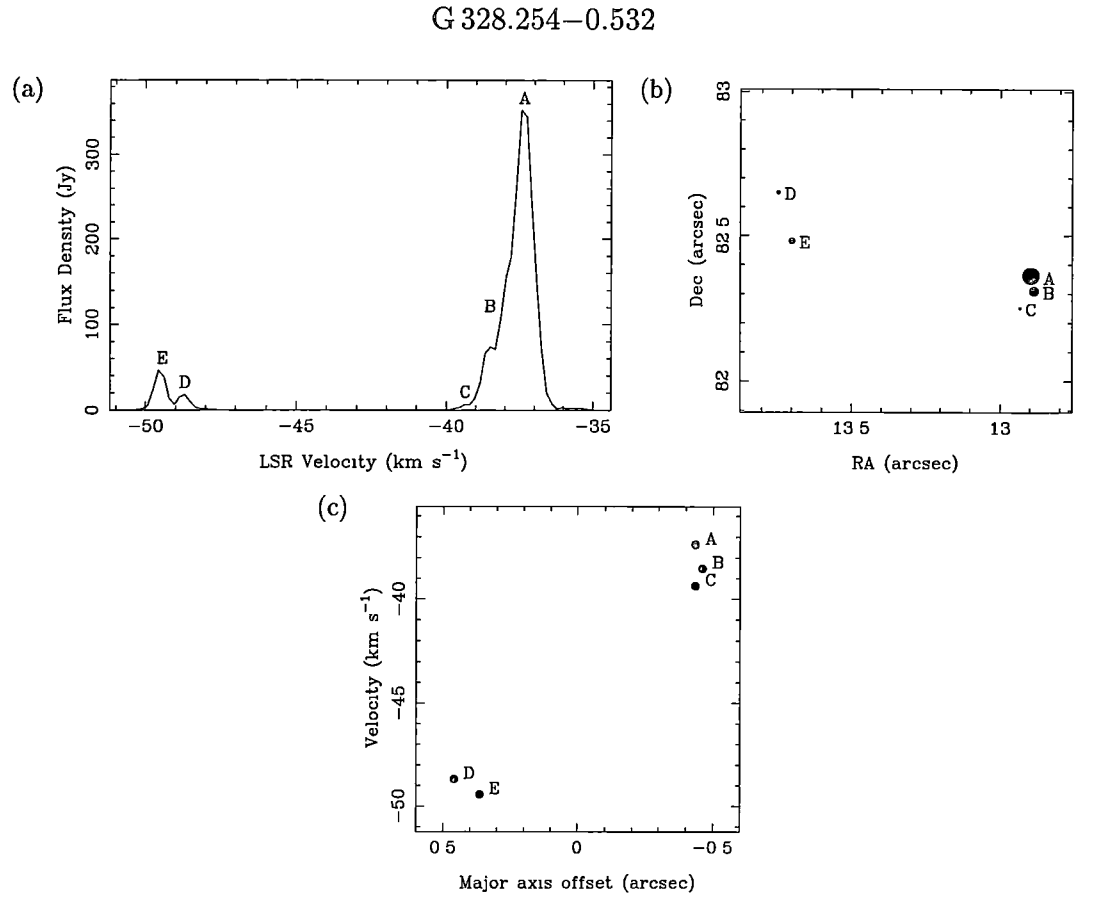

Figure 2.13: (a) Spectrum, (b) map and (c) v-a diagram of G 328.254−0.532.

the rotational velocity of a disc at the radius of the masers). This is discussed more fully in Section 2.6.2. Alternatively, the two clusters may represent two separate sources in a binary system. In this case, the mass derived above would represent the sum of the mass of the two stars.

G 328.254−0.532 has a similar morphology to G 328.236−0.547, but we did not detect any associated continuum emission with a 4-σ limit of 0.6 mJy beam^{-1}. We can also rule out the far kinematic distance. The near distance of 2.6 kpc gives a source size of 2080 AU.

The masses listed in Table 2.1 for both these sources assumes that the emission comes from either side of a rotating disc.

G 331.132−0.244

The 6.7-GHz spectral-line image, along with the source spectrum and continuum image, is shown in Fig. 2.14. This is the first high-resolution image of this source. The source has a roughly linear structure with a velocity gradient, except for the single component 'G'. The maser source is located at the edge of a 7×10-arcsec HII region with an integrated flux density of 199 mJy beam^{-1}. Both Caswell *et al.* (1995c) and Ellingsen *et al.* (1996b) have found this source to be highly

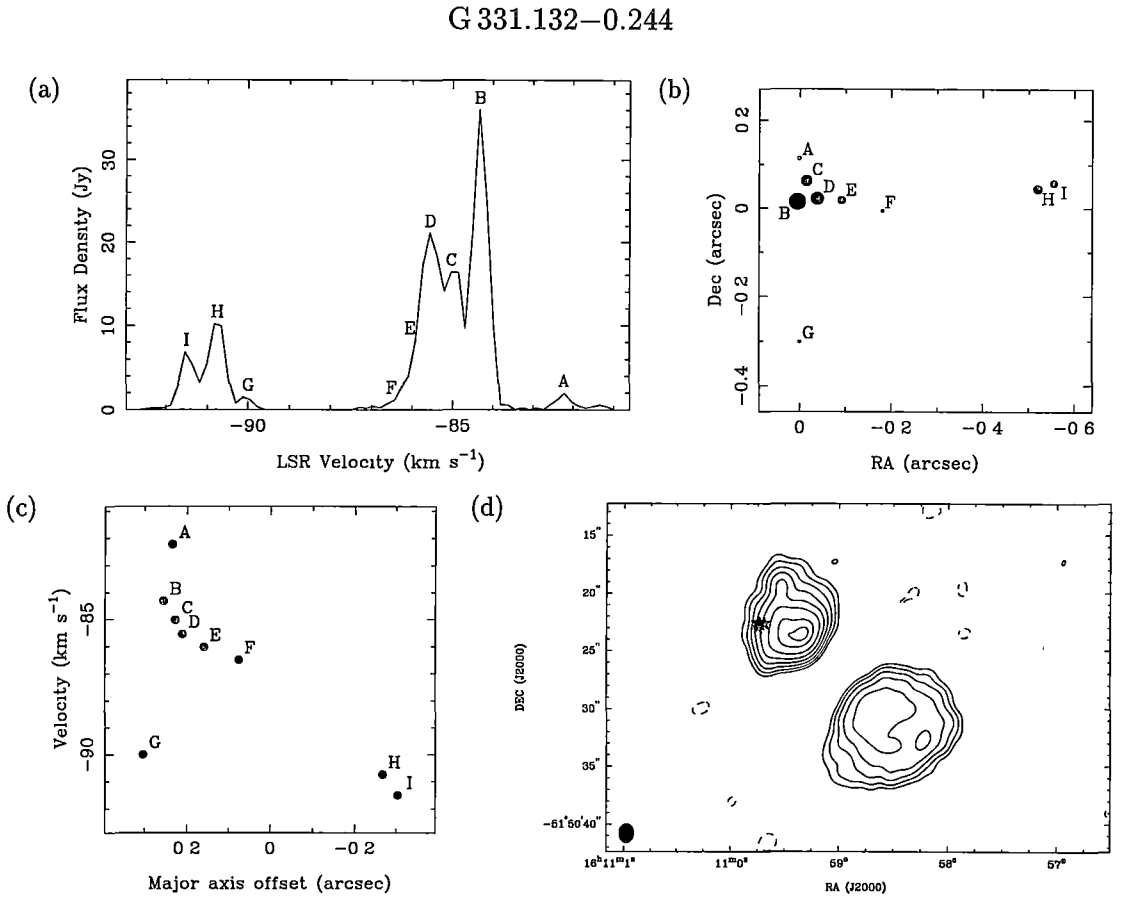

Figure 2.14: (a) Spectrum, (b) map and (c) v-a diagram of G 331.132−0.244. The source has a clear line and velocity gradient, except for the single component 'G'. The implied mass is 21.8 $M_{\odot}$assuming Keplerian rotation. (d) Radio continuum image of G 331.132−0.244 at 8.6 GHz. The contours are at -1, 1, 2, 4, 8, 16, 32, 64 and 90 per cent of the peak flux density (36.5 mJy beam^{-1}). The integrated flux density is 199 mJy. The positions of the methanol maser are indicated by stars. The size of the Gaussian restoring beam is 1.29×1.69 arcsec and is shown on the lower left of the plot.

variable, which is unusual for 6.7-GHz methanol masers (Caswell *et al.*, 1995a). The kinematic distance to this source is ambiguous and may be either 5.2 or 9.7 kpc although, if the source is at the far distance, the associated continuum would be the second most luminous in the sample. Assuming the near distance we obtain an extent of 3100 AU, while the far distance gives 5800 AU. The position of the masers relative to the HII region suggests that there may be more than one star embedded in the UCHII region, which means that the calculated spectral type (O9 assuming the near distance) may not represent the true spectral type of the star associated with the methanol.

G 331.278−0.188

The spectral-line and continuum images for this source are shown in Fig. 2.15. This source has been previously imaged at 6.7 GHz by Norris *et al.* (1993) and is

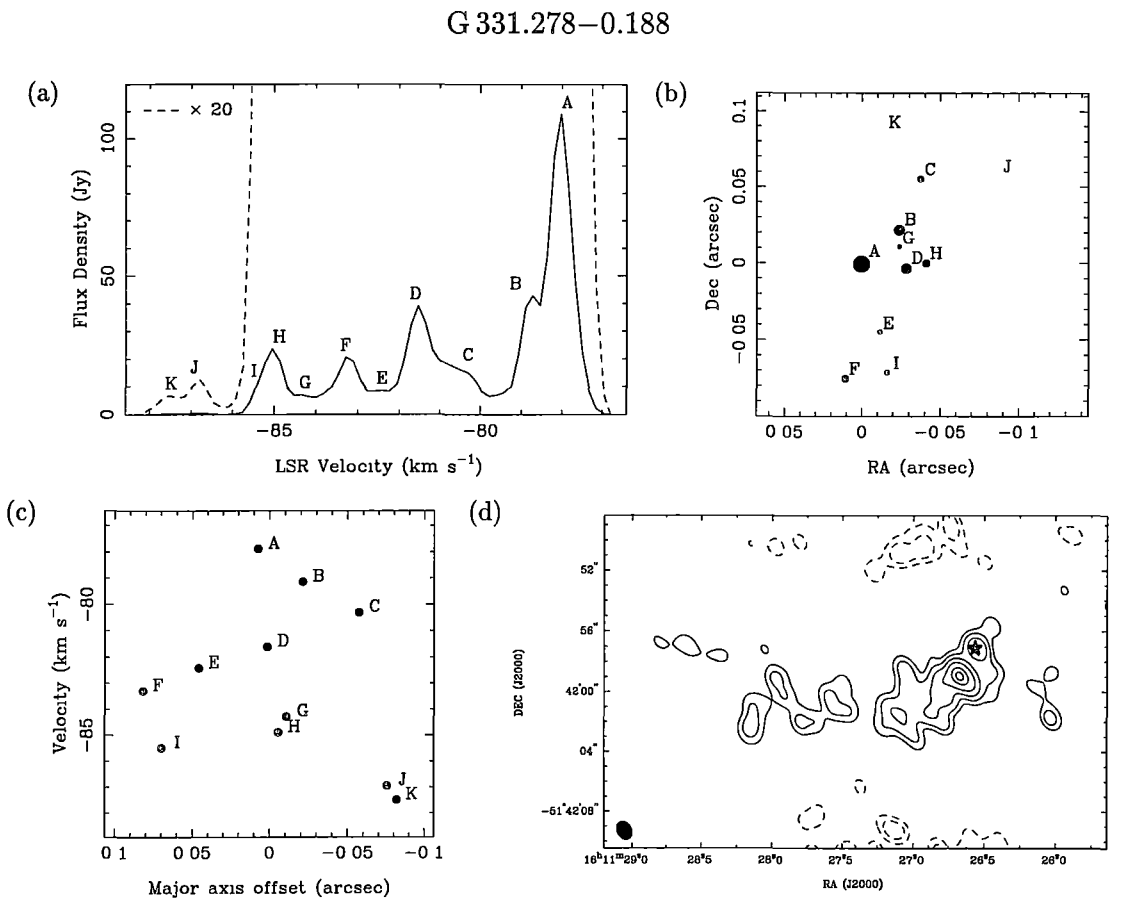

Figure 2.15: (a) Spectrum, (b) map and (c) v-a diagram of G 331.278−0.188. Although the source is slightly elongated, it does not show any velocity gradient. (d) Radio continuum image of G 331.278−0.188 at 8.6 GHz. The contour levels are at -8, -4, 4, 8, 16, 32, 64 and 90 per cent of the peak flux density (3.4 mJy beam^{-1}). The integrated flux density is 4.1 mJy. The extended structure in this source is poorly modeled, due to the limited number of short baselines. The positions of the methanol masers are indicated by stars. The size of the Gaussian restoring beam is 0.98×1.31 arcsec and is shown on the lower left of the plot.

consistent with the current image (within positional errors of 10 - 15 milli-arcsec) although more components have been detected with these data. This source was classified as linear by Norris *et al.*, which is not apparent with these observations (mainly due to the components 'K' and 'J'). The v-a diagram shows that there is no velocity gradient along the source. The maser source is associated with an unresolved HII region with an integrated flux density of 4.1 mJy. The shortest baseline was discarded from the continuum u-v data before imaging, because of the large correlated flux density. This resulted in the shortest baseline equal to 413 m, which corresponds to 17.5 arcsec at 8.6 GHz. The extended emission to the east of the unresolved component is poorly imaged because of the lack of short baselines.

We cannot rule out the far kinematic distance of 10.1 kpc for this source. The near distance of 4.8 kpc gives a source size of 820 AU, while the far distance gives 1700 AU.

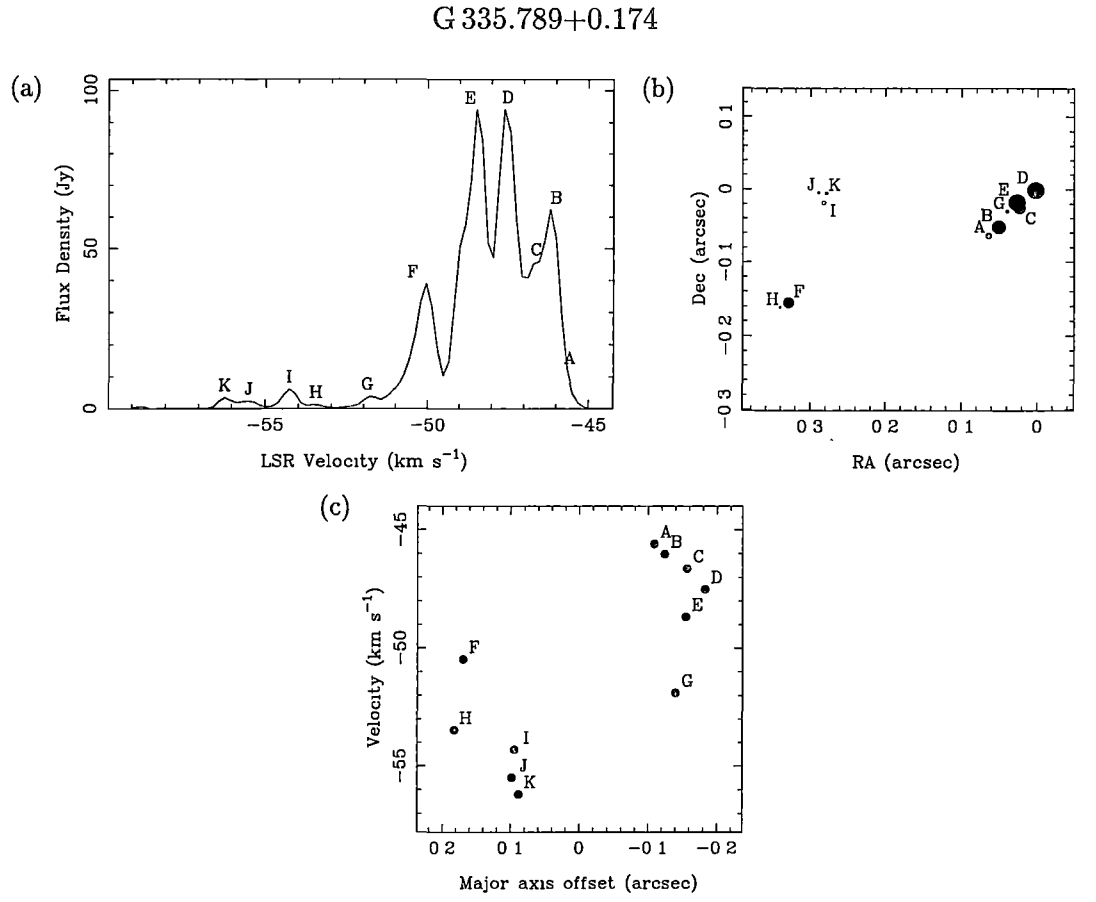

Figure 2.16: (a) Spectrum, (b) map and (c) v-a diagram for G 335.789+0.174

G 335.789+0.174 & G 335.726+0.191

The spectrum and spectral line images for these two are shown in Fig. 2.16 and 2.17. Both these sources have been previously observed using the ATCA by Caswell, Vaile & Forster (1995d) but no component maps have been published.

G 335.789+0.174 has an unusual structure. The stronger maser components 'A' to 'G' in the north-west lie in a straight line. The components 'H' and 'F' are in the direction of this line, but are offset by 0.15 arcsec. The blue-shifted components components 'I' to 'K' form a separate cluster. Ellingsen (1996) imaged this source at 12.2 GHz using VLBI, and found the same structure.

Possibly the three clusters represent separate sources, although this would mean that the size of the source delineated by the stronger components would be much smaller than the other sources in this sample. Possibly the components 'A' to 'G' emanate from the edge of a disc, while the blue-shifted components are in an outflow region (perhaps representing a dense region or shock in the outflow). This source has no associated 8.6-GHz continuum emission, to a 4-σ limit of 0.4 mJy beam^{-1}. If we assume a near kinematic distance of 3.4 kpc, the source size is 1400 AU. We can rule out the far kinematic distance as this would imply an unrealistically high methanol luminosity.

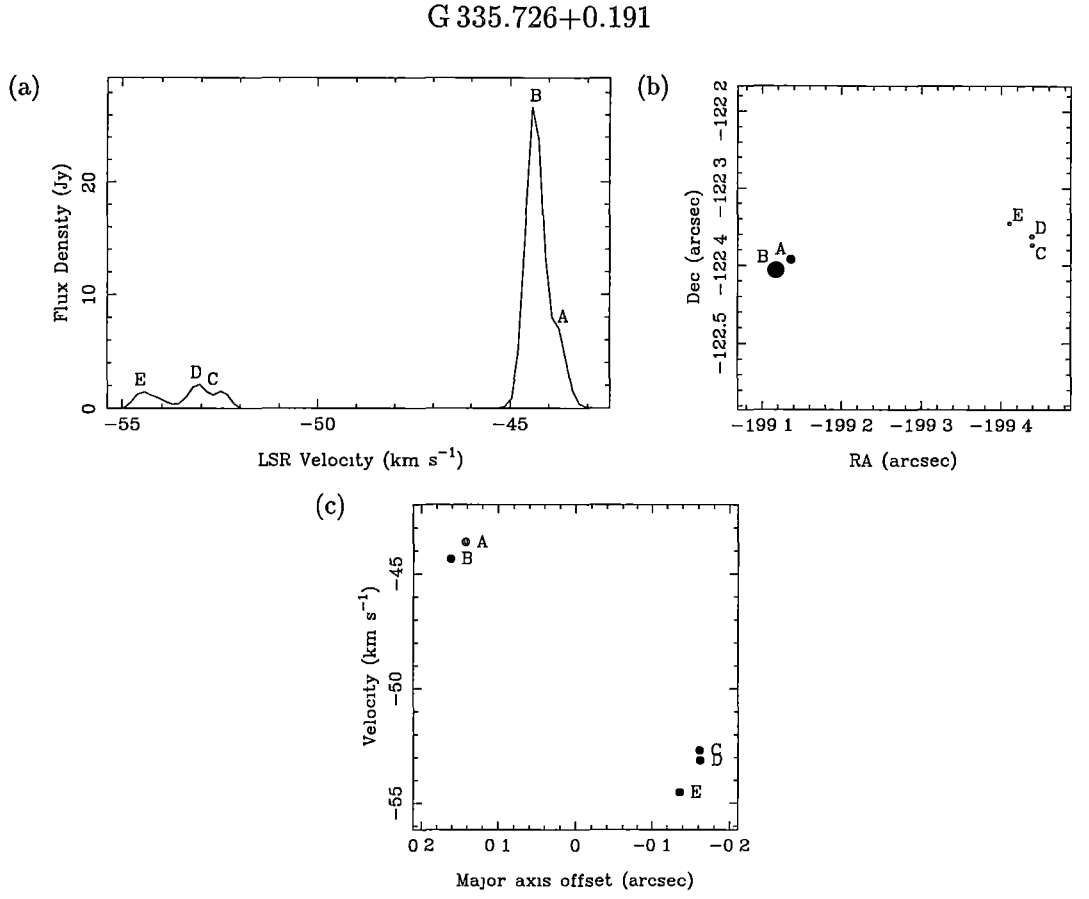

Figure 2.17: (a) Spectrum, (b) map and (c) v-a diagram for G 335.726+0.191

G 335.726+0.191 is offset by 3.9 arcmin and consists of two maser clusters separated by 0.3 arcsec and 10 km s^{-1}, the third in this sample with this morphology. No continuum emission was detected towards this source either, with a 4-σ limit of 0.7 mJy beam^{-1}. We cannot rule out the far kinematic distance of 12.2 kpc nor the near distance of 3.2 kpc. Assuming the near distance, the source size is 1100 AU while the far distance gives 4300 AU. The mass of the central star (15.8 $M_{\odot}$) in Table 2.1 has been calculated assuming that the two maser clusters represent either side of a rotating disc.

G 336.404−0.254, G 336.409−0.257, G 336.410−0.256 & G 336.433−0.262

The spectral-line images and associated continuum are shown in Figs. 2.18 and 2.19. The sources G 336.409−0.257 and G 336.410−0.256 both have only a single maser component, and so neither a position nor v-a diagram has been produced for these sources, although their relative positions can be seen in the continuum image. G 336.410−0.256 is at the centre of an unresolved HII region with an integrated flux density of 1 mJy. G 336.409−0.257 is at the edge of an 8×8-arcsec HII region with an integrated flux density of 30 mJy. G 336.404−0.254 has too few components

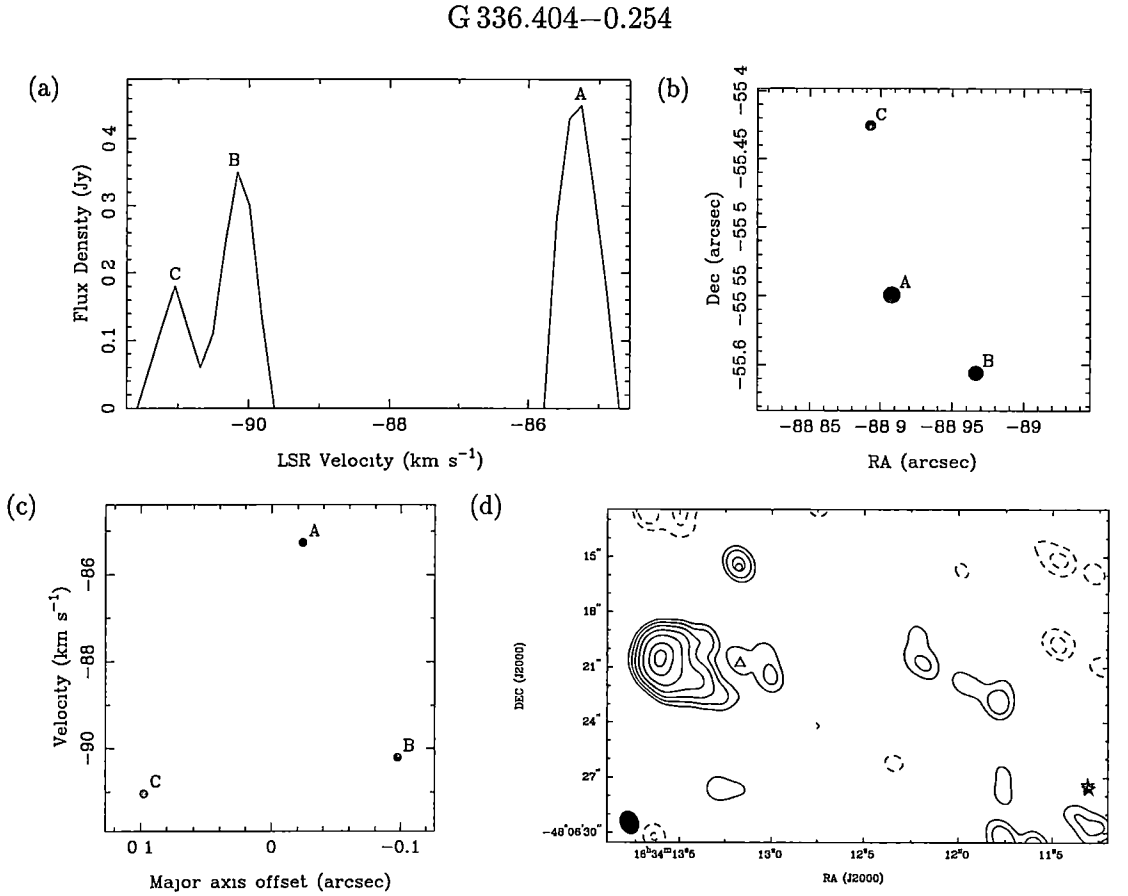

Figure 2.18: (a) Spectrum, (b) map and (c) v-a diagram for G 336.404−0.254. (d) Continuum image of the region containing G 336.404−0.254 (triangle), G 336.409−0.257 (circle) and G336.410-0.256 (stars). The contour levels are at -4, -2, 2, 4, 8, 16, 32, 64 and 90 per cent of peak flux density (9.4 mJy beam^{-1}). G 336.409−0.257 is associated with an UCHII region with a peak flux of 0.3 mJy beam^{-1}. G336.410-0.256 is associated with a 1.0 mJy UCHII region. G 336.404−0.254 is not associated with any detectable continuum emission. The size of the Gaussian restoring beam is 1.02×1.29 arcsec and is shown on the lower left of the plot.

to make any meaningful comment about its structure. It is not associated with any HII emission with a 4-σ flux density limit of of 0.3 mJy beam^{-1}. These three sources correspond to the source G 336.41−0.26 observed by Caswell *et al.* (1995c) using the Parkes 64-m telescope.

G 336.433−0.262 has been previously imaged by Norris *et al.* (1993) with the ATCA. This source has a complex morphology both spatially and in velocity. There is no associated continuum with a flux density limit of 0.3 mJy beam^{-1}. The spectral-line image presented here differs significantly from the Norris *et al.* image, although they note that larger positional errors are expected for this source than for the others because of poor u-v coverage.

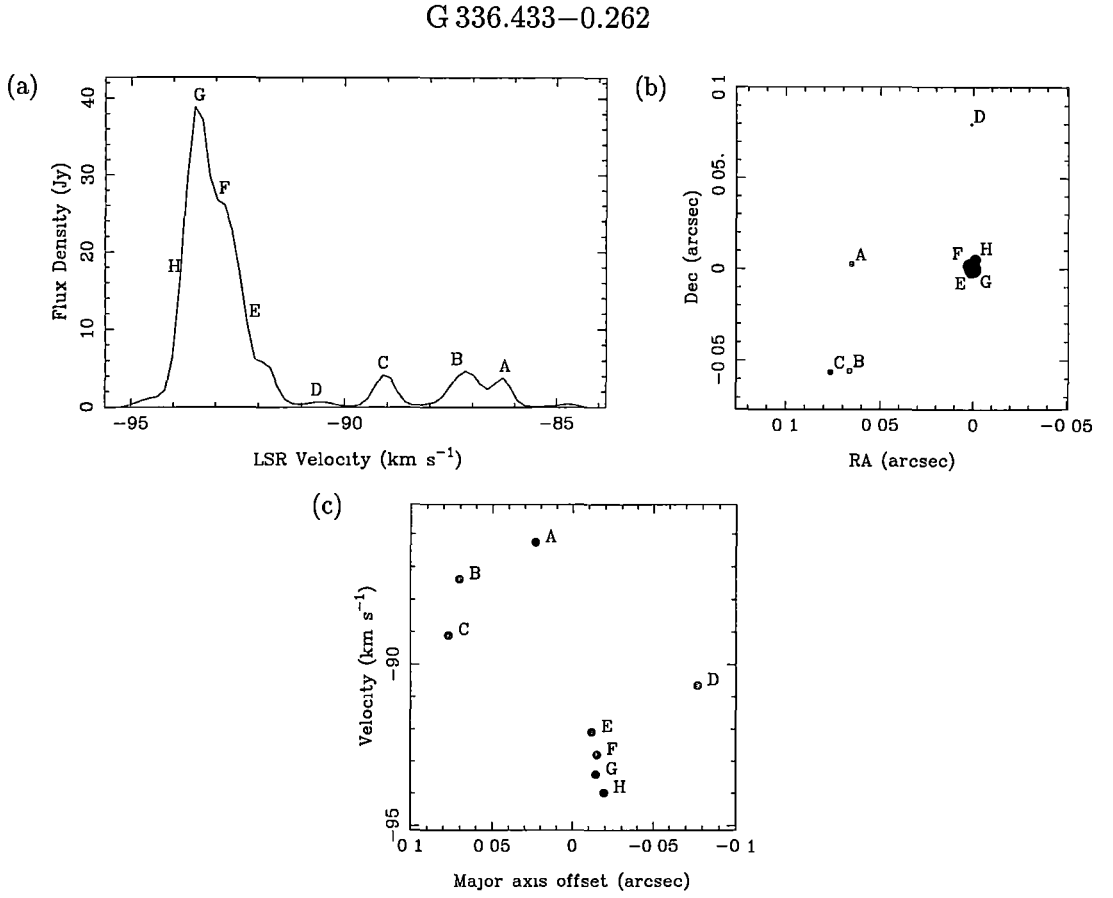

Figure 2.19: (a) Spectrum, (b) map and (c) v-a diagram for G 336.433−0.262

G 337.612−0.060, G 337.632−0.079, G 337.703−0.053 & G 337.705−0.053

The ATCA 6.7-GHz spectrum and images, as well as the continuum images for these four sources, are shown in Figs. 2.20, 2.21 and 2.22. These sources are separated by 5.5 arcmin, with the pointing centre of the observation towards G 337.705−0.053. They have all been previously imaged at 6.7 GHz by Caswell (1997). These observations have significantly improved u-v coverage and continuum sensitivity, although the spectral resolution is not quite as good.

G 337.612−0.060 has two clumps of maser components separated by 0.8 arcsec and no associated continuum above a 4-σ flux density limit of 11.2 mJy. As this source is 5.5 arcmin from the pointing centre (the FWHM of the primary beam is 8.4 and 6.5 arcmin at 6.7 and 8.6 GHz, respectively) the spectral-line flux density and continuum limit are worse than for most other sources.

G 337.632−0.079 is a complex source offset by 3 arcsec from an unresolved HII region with a peak flux density of 11 mJy.

G 337.703−0.053 has only two features and so no position or v-a diagram has been shown. Its position relative to G 337.705−0.053 (offset by 9 arcsec towards the south-west) can be seen in the continuum plot in Fig. 2.22.

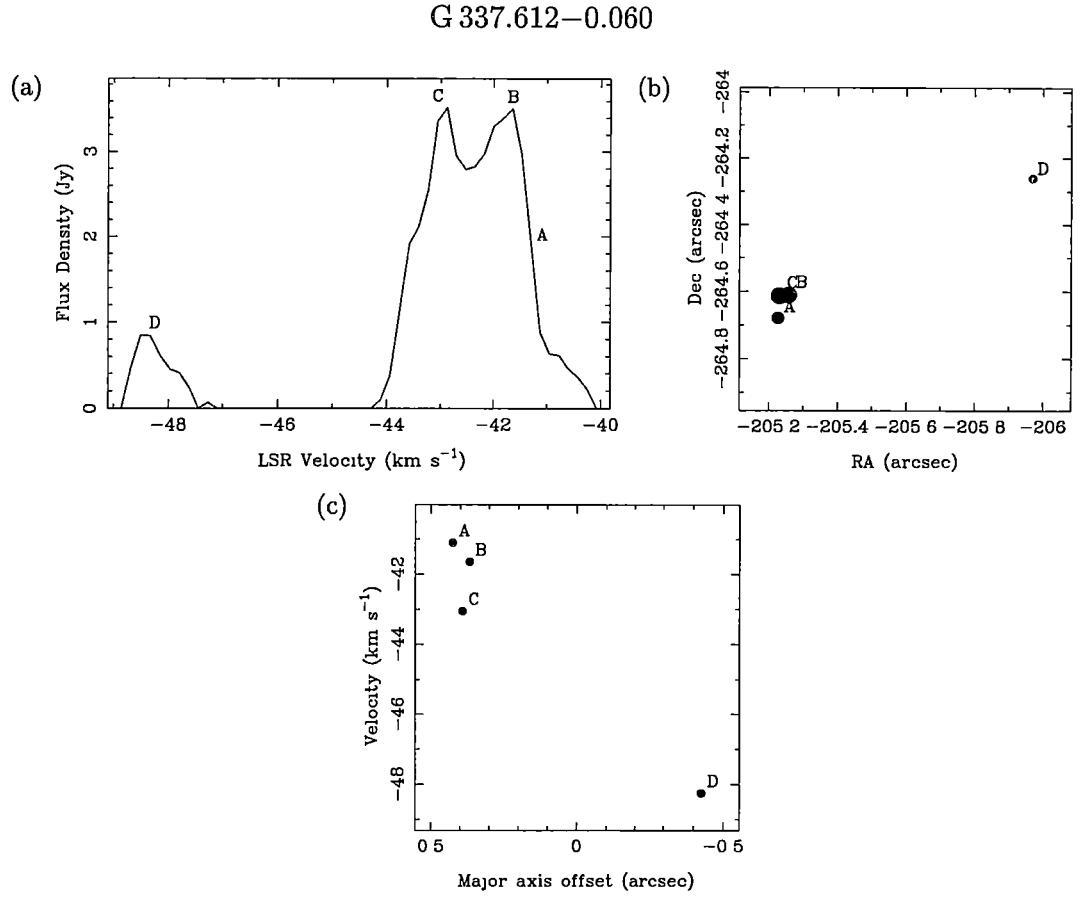

Figure 2.20: (a) Spectrum, (b) map and (c) v-a diagram for G 337.612−0.060

The maser components in G 337.705−0.053 are distributed along a straight line with a single component 'J' offset from the line. Although there is not a monotonic velocity change along the line, there is a definite velocity gradient which is evident in the v-a diagram. The line of masers runs through the centre of an unresolved HII region with an integrated flux density of 192 mJy. Imaging by Caswell (1997) of 6.035-GHz excited OH finds that the excited OH exists in the same region as the methanol (both in velocity and spatially), although there is no correspondence between the individual components.

A near kinematic distance of 3.9 kpc has been assumed for this source. This gives a source size of 55000 AU. The far kinematic distance is unlikely as this would imply an unrealistically large source size and methanol and continuum luminosity. The central star mass listed in Table 2.1 was obtained excluding the component 'J'.

G 338.460−0.245

The spectrum and 6.7-GHz map for this source is shown in Fig. 2.23. It is slightly elongated in the north-south direction but there is no velocity gradient along the source. There is no associated 8.6-GHz continuum with a 4-σ detection limit of

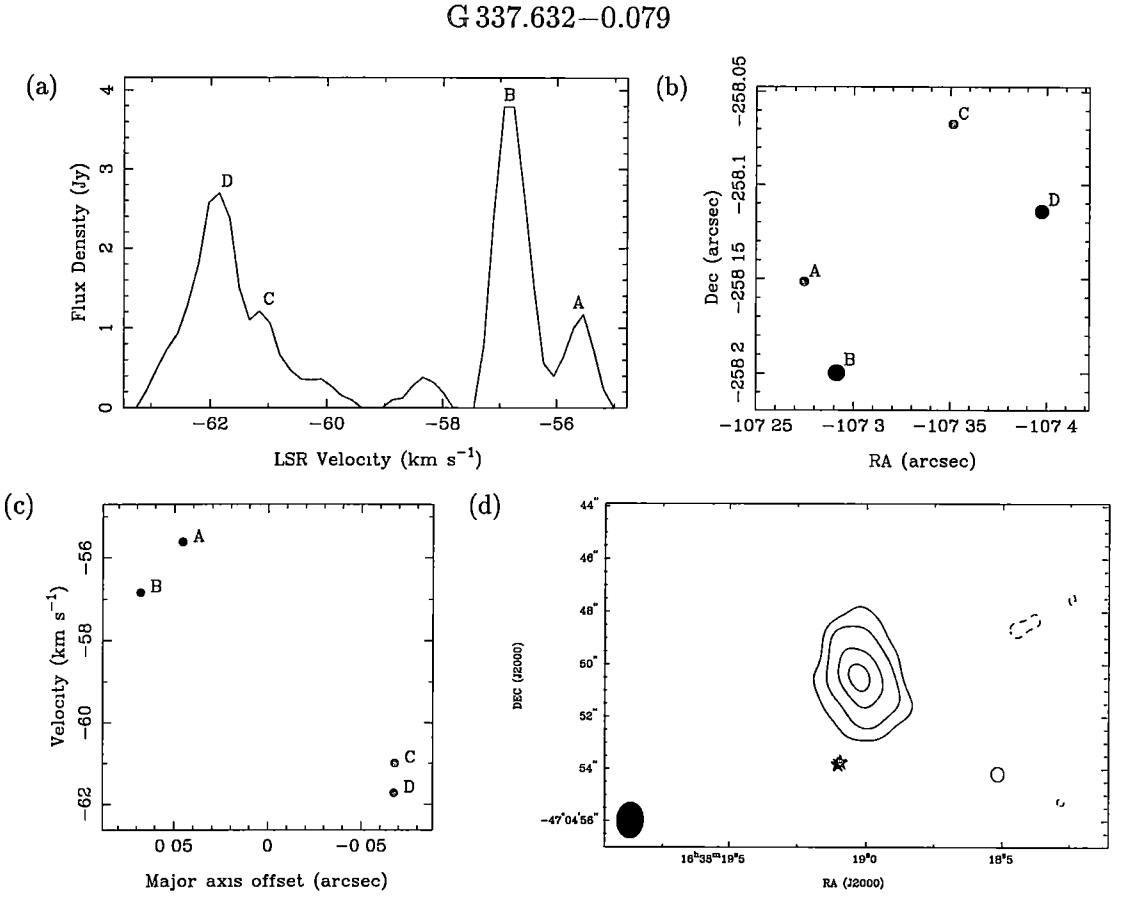

Figure 2.21: (a) Spectrum, (b) map and (c) v-a diagram for G 337.632−0.079. (d) Radio continuum image of G 337.632−0.079 at 8.6 GHz. The contour levels are at -16, 16, 32, 64 and 90 per cent of the peak flux density (17.2 mJy beam^{-1}). The integrated flux density of the UCHII region is 65 mJy. The positions of the methanol masers are indicated by stars and are offset from the continuum peak by 4 arcsec. The size of the Gaussian restoring beam is 1.06×1.39 arcsec and is shown on the lower left.

0.3 mJy beam^{-1}.

If we assume the near kinematic distance of 3.7 kpc, the source has a size of 560 AU.

G 340.785−0.096

The continuum image and the 6.7-GHz spectral-line image for this source are shown in Fig. 2.24. This source has been previously imaged with the ATCA by Norris *et al.* (1993).

The most noticeable feature of this source is its complexity. The source spans a velocity range of -86 to -111 km s^{-1}, which is much larger than the other sources. Although the 19 components are confined to a region smaller than one square arcsec, the velocity range reduces the effect of confusion both spatially and spectrally. VLBI observations are needed to properly study a source as complex as

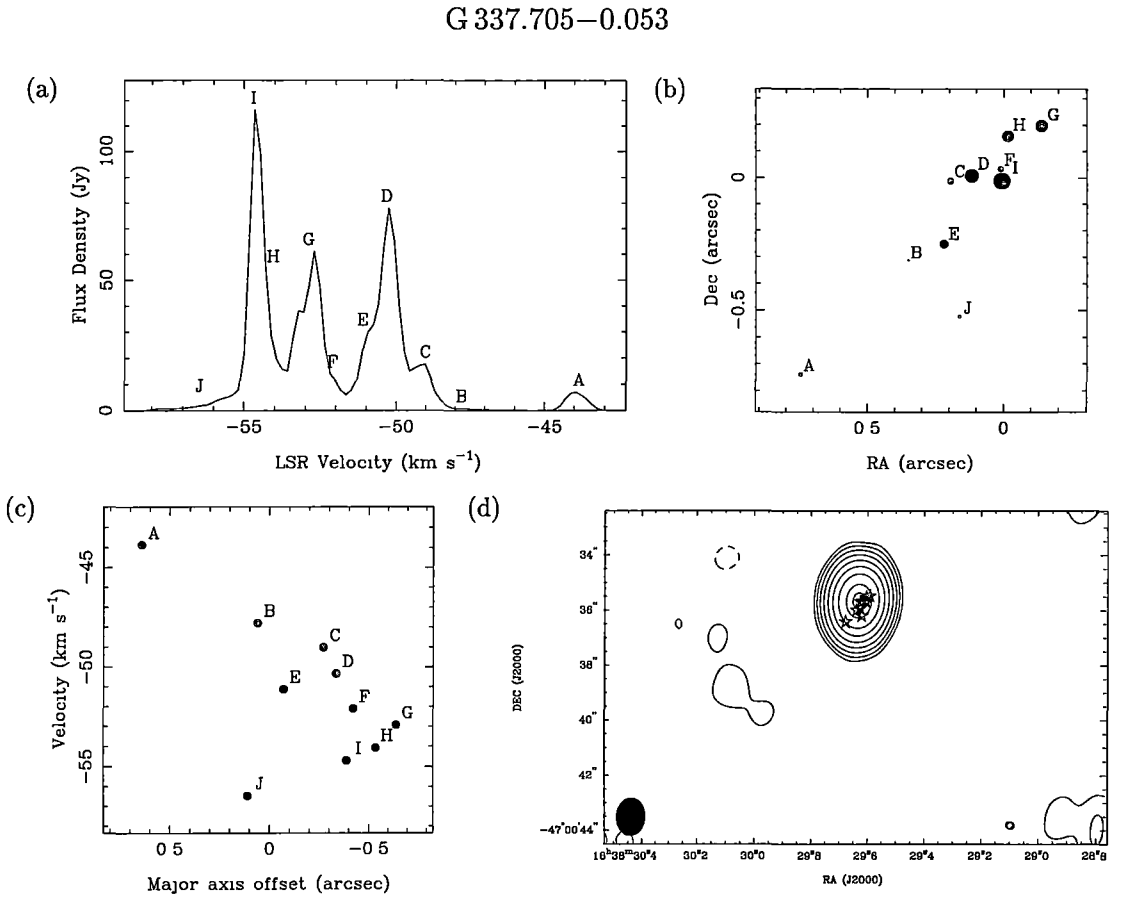

Figure 2.22: (a) Spectrum, (b) map and (c) v-a diagram for G 337.705−0.053. The velocity gradient along the source implies a mass of 72.6 $M_{\odot}$. (d) Radio continuum image of G 337.705−0.053 at 8.6 GHz. The contour levels are at -0.5, 0.5, 1, 2, 4, 8, 16, 32, 64, 90 per cent of the peak flux density (157.5 mJy beam^{-1}). The integrated flux density of the source is 192 mJy. The positions of the methanol masers are indicated by stars, and are aligned with the unresolved HII region. The position of G 337.703−0.054 indicated by triangles, at the lower right. The size of the restoring beam is 1.06×1.39 arcsec and is shown in the lower left of the plot.

this. These positions agree with those of Norris *et al.* with errors of about 50 milliarcsec. The larger errors than those found in the other sources are probably caused by the complexity of this source. The observations of Norris *et al.* did not include the features redshifted below -98 km s^{-1}. Interestingly, the v-a diagram does suggest a trend in velocity along the source. The maser components are associated with an unresolved HII region with a peak flux density of 26 mJy beam^{-1}. We can rule out the far kinematic distance as this would imply a very large linear size for the source. The near distance of 6.2 kpc implies a linear size of 5600 AU.

G 348.550−0.979S & G 348.550−0.979N

The spectral line and continuum images for these sources are shown in Figs. 2.25 and 2.26. This is the first high-resolution image of these sources. G 348.550−0.979S has a linear or curved morphology but the velocity of the components shows no

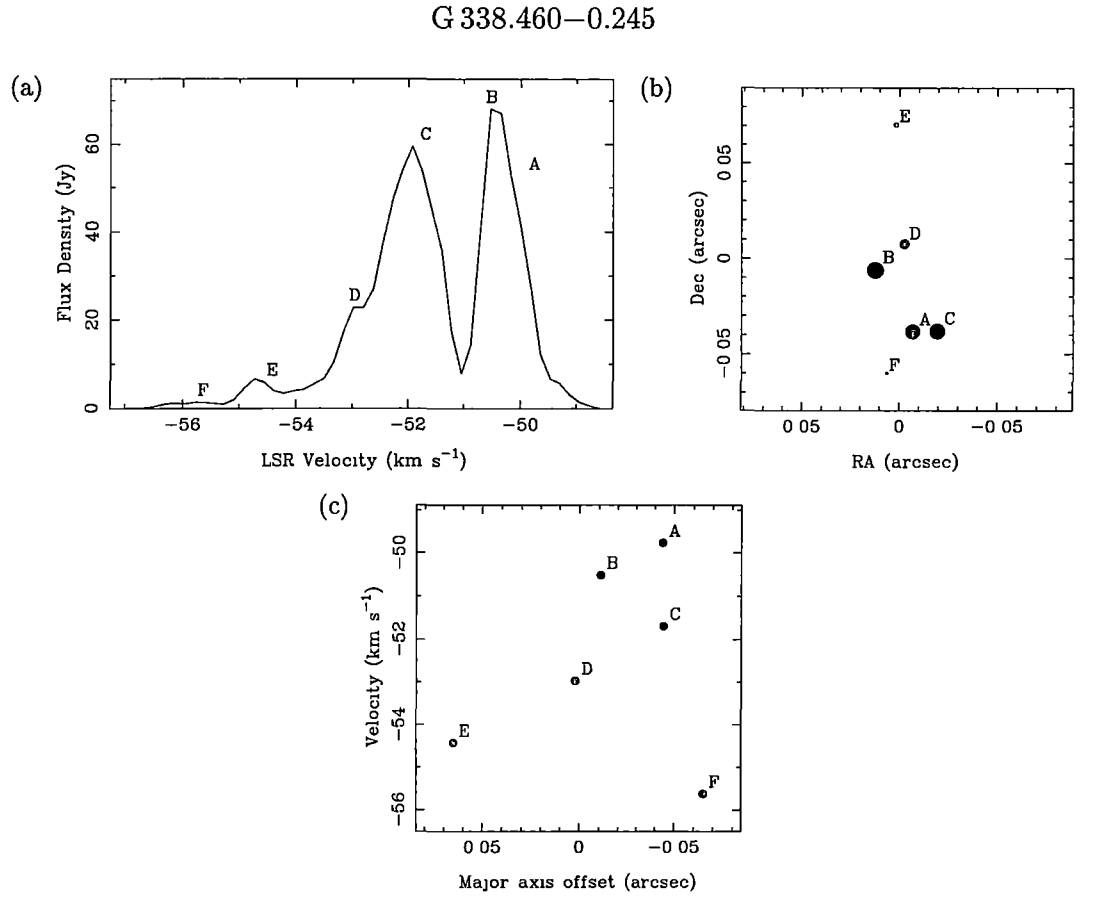

Figure 2.23: (a) Spectrum, (b) map and (c) v-a diagram for G 338.460−0.245

pattern. The maser source is offset by 0.5 arcsec from the peak of a slightly resolved HII region with an integrated flux density of 0.6 mJy. Despite its relatively weak flux density, this source has more spectral components than most of the other sources in the sample. The source is either two separate clusters or a single source with a curved morphology. The far kinematic distance can be rejected for this source as it implies a very large size for the masers, even if this source really is two separate clusters. Because the near kinematic distances of G 348.550−0.979S (1.6 kpc) and G 348.550−0.979N (2.8 kpc) differ by more than we would expect for two sources so close together we have adopted an average value of 2.2 kpc for both. This distance gives the size of the maser source of 2400 AU.

Like many of the linear or curved sources associated with an unresolved or slightly resolved UCHII region, the maser emission is slightly offset from the peak continuum emission. Although this is not entirely consistent with the the edge-on circumstellar disc hypothesis, the alignment of the masers and the continuum is not consistent with a shock front or outflow model.

G 348.550−0.979N has a complex morphology both spatially and in velocity. It is offset from G 348.550−0.979S by 2.5 arcsec and is not associated with any continuum emission with a detection 4-σ limit of 0.5 mJy beam^{-1}. A kinematic distance of 2.2 kpc gives a source size of 440 AU.

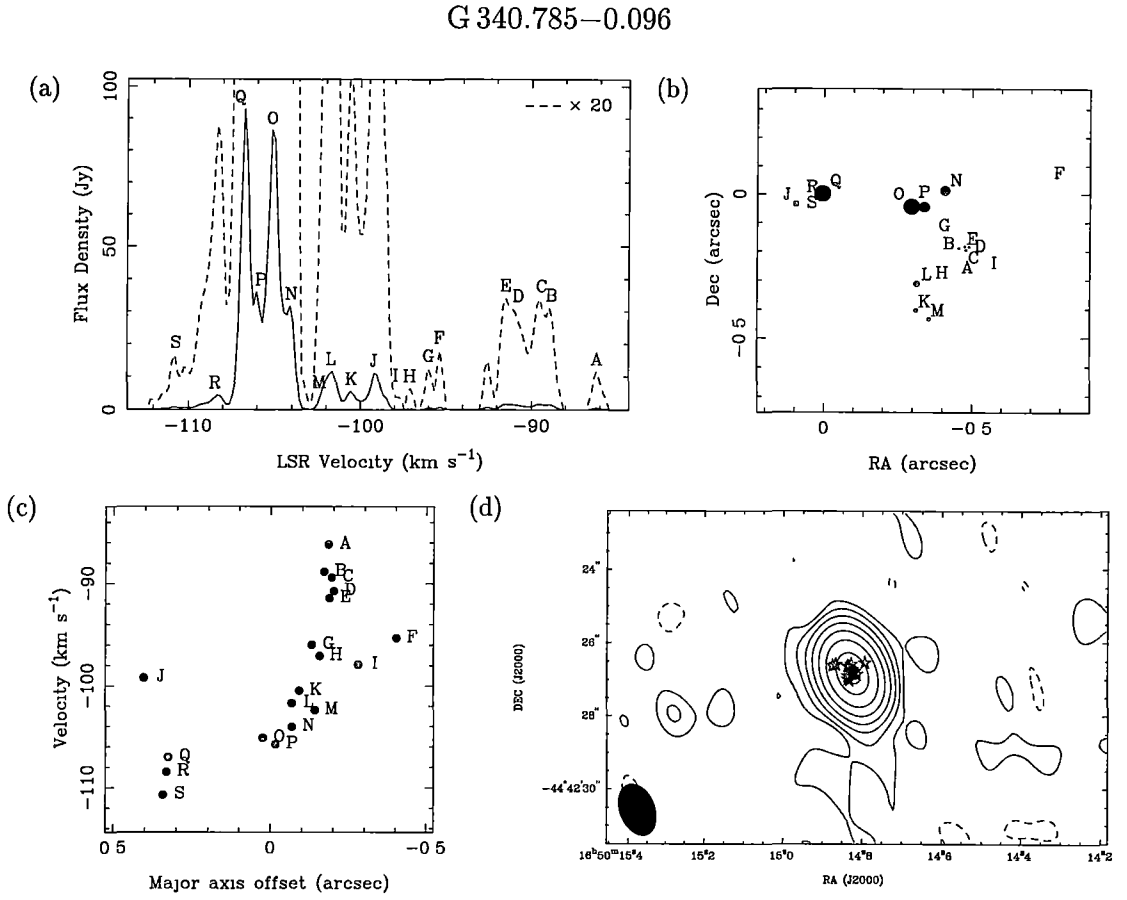

Figure 2.24: (a) Spectrum, (b) map and (c) v-a diagram for G 340.785−0.096. Although this is a very complex source, the v-a diagram does show some evidence of a velocity gradient. (d) Radio continuum image of G 340.785−0.096 at 8.6 GHz. The contour levels are at -1, 1, 2, 4, 8, 16, 32, 64 and 90 per cent of the peak flux density (15.9 mJy beam^{-1}). The integrated flux density is 16.5 mJy. The position of the methanol maser is indicated by stars. The size of the Gaussian restoring beam is 0.99×1.48 arcsec and is shown on the lower left of the plot.

G 353.410−0.360

The continuum image and 6.7-GHz spectrum for this source are shown in Fig. 2.27. This is the first high-resolution image of this source. This source has a linear spatial structure with a velocity gradient. The individual components are spread over only 0.15 arcsec and have a velocity extent of 3 km s^{-1}. The maser source is associated with a 663 mJy HII region, offset from the peak by 1 arcsec. The HII region is slightly extended with a cometary morphology. Although this source is associated with a fairly strong UCHII region, the maser flux density is quite low, has a narrow velocity range and is fairly small. The continuum flux density makes it unlikely that this source is at the far kinematic distance, and so adopting the near distance of 3.9 kpc gives a source size of 624 AU. The velocity gradient across the source gives a mass of only 0.5 $M_{\odot}$ assuming a Keplerian disc model. This value is small because the source is small. If the maser emission accounted for only one third of the actual source size, the calculated star mass would be 27

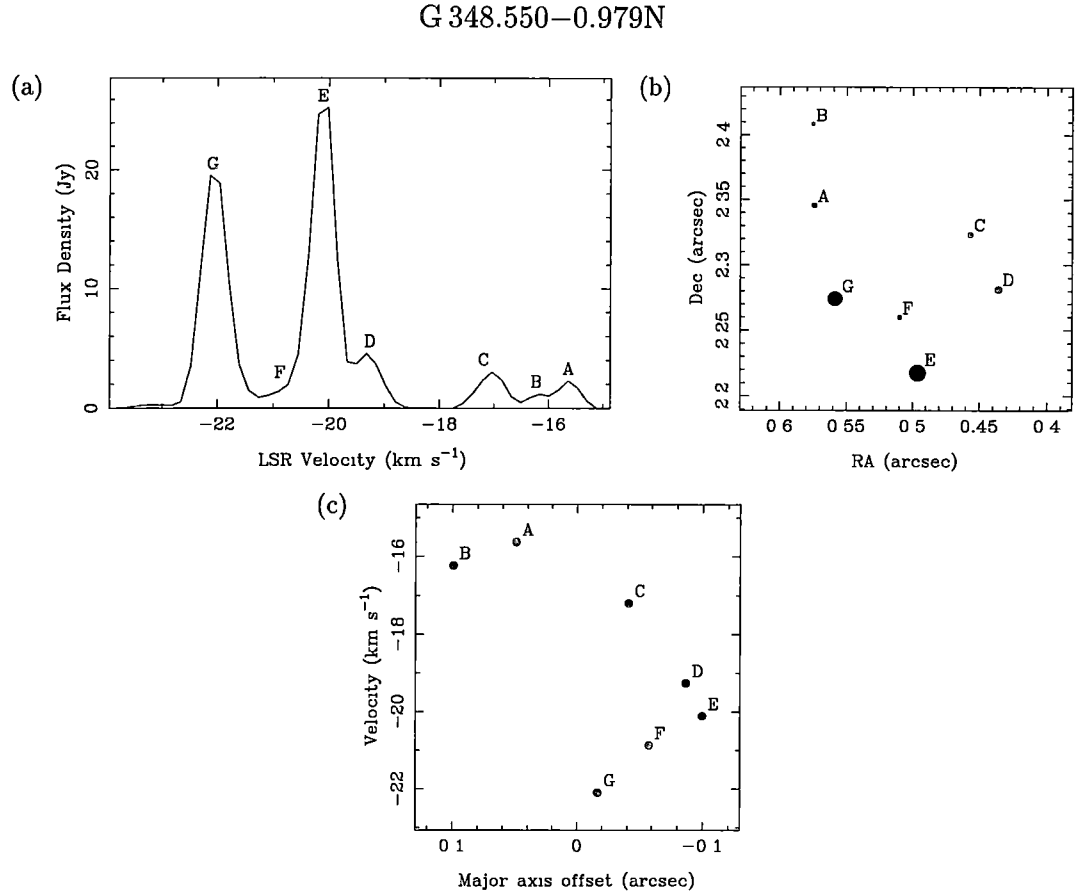

Figure 2.25: (a) Spectrum, (b) map and (c) v-a diagram for G 348.550−0.979N. The maser sources is offset 2 arcsec from an UCHII region, shown in Fig. 2.26d.

times larger.

G 9.621+0.196 & G 9.619+0.193

The continuum and spectral-line maps of these two sources are shown in Fig. 2.28. The 6.7-GHz emission has been previously imaged by Norris *et al.* (1993) and the region has been studied extensively by many people (Kemball *et al.*, 1988; Forster and Caswell, 1989; Hofner *et al.*, 1996; Hofner *et al.*, 1994; Testi *et al.*, 1997a, for example).

The continuum image shows that the source is a complex star-forming region. G 9.621+0.196 has a fairly complex component distribution, though it shows some elongation towards the north-east. This is also seen in the v-a diagram showing some velocity structure. This source is associated with an unresolved UCHII region with an integrated flux density of 6 mJy.

G 9.619+0.193 has a simple structure with only two components, and so a spectrum and component map have not been presented. It is associated with an unresolved HII region with an integrated flux density of 92 mJy.

We have adopted a kinematic distance of 2.0 kpc as suggested by Forster &

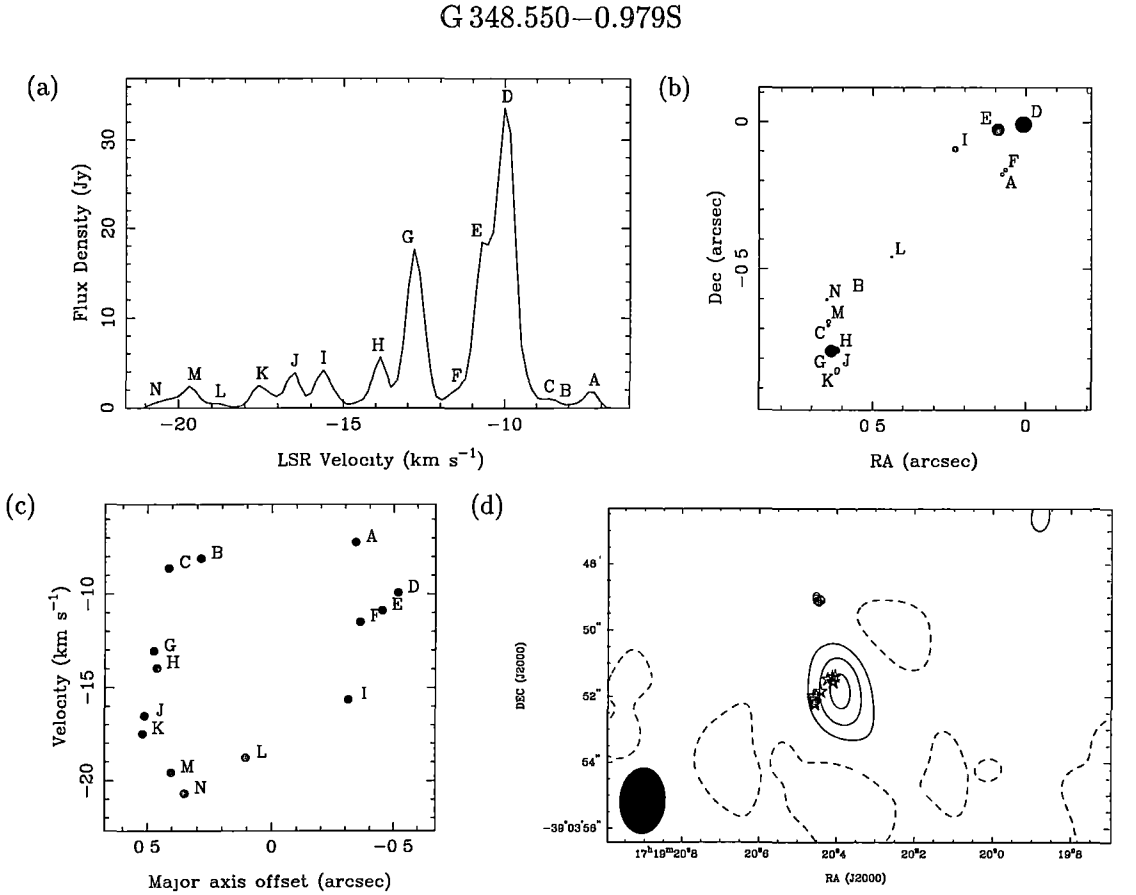

Figure 2.26: (a) Spectrum, (b) map and (c) v-a diagram for G 348.550−0.979S. Although the maser components form a clear line, there is no velocity gradient along the source. (d) Radio continuum image of G 348.550−0.979 at 8.6 GHz. The contours levels are at -32, 32, 64 and 90 per cent of the peak flux density (0.8 mJy beam^{-1}). The integrated flux density is 0.6 mJy. The positions of the methanol masers in G 348.550−0.979S are indicated by stars, while G 348.550−0.979N is indicated by open circles and is offset north by 2 arcsec. The size of the Gaussian restoring beam is 1.40×2.02 arcsec and is shown on the lower left of the plot.

Caswell (1989) from VLA OH observations of the same source. This gives a source size of 700 AU for G9.621+0.196. The mass listed in Table 2.1 depends critically on the single point 'A'.

Ellingsen *et al.* sources

The sources which have been included from Ellingsen *et al.* (1996a) and Ellingsen *et al.* (in preparation) are listed in Table 2.5. The morphology of these sources is briefly summarized.

G 318.949−0.193: This source has a linear morphology with a velocity gradient. It is not associated with any detected continuum emission.

G 328.808+0.633: This source is linear but does not show any velocity gradient. It is associated with a 200-mJy UCHII region with a cometary morphology.

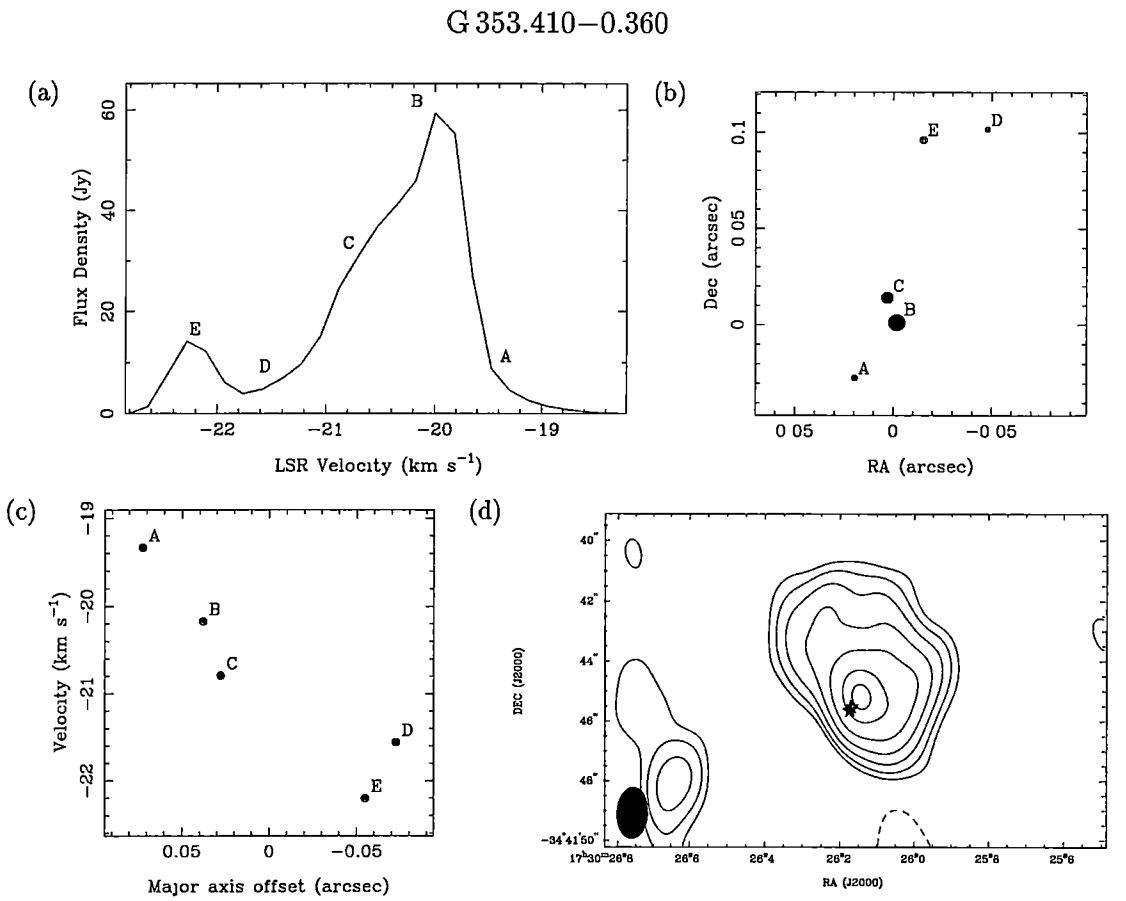

Figure 2.27: (a) Spectrum, (b) map and (c) v-a diagram for G 353.410−0.360. (d) Radio continuum image of G 353.410−0.360 at 8.6 GHz. The contour levels are at -2, 2, 4, 8, 16, 32, 64 and 90 per cent of the peak flux density (215.1 mJy beam^{-1}). The integrated flux density of the source is 663 mJy. The positions of the methanol masers are indicated by stars. The size of the Gaussian restoring beam is 1.08×1.73 arcsec and is shown on the lower left of the plot.

G 328.809+0.633: This source comprises a single maser component separated from G 328.808+0.633 by 2 arcsec. It is associated with an unresolved UCHII region with an integrated flux density of 248 mJy.

G 339.878−1.252: This is a linear source with a velocity gradient. The maser components bisect an unresolved UCHII region with a integrated flux density of 6 mJy.

G 345.003−0.224: This source has a complex morphology and is associated with an unresolved 176 mJy UCHII region.

G 345.003−0.223: This source is offset from G 345.003−0.224 by 3.5 arcsec and has no detected continuum emission. The methanol components have a complex morphology.

G 345.012+1.797: This source forms a line, but shows no velocity gradient. It is not associated with any continuum emission.

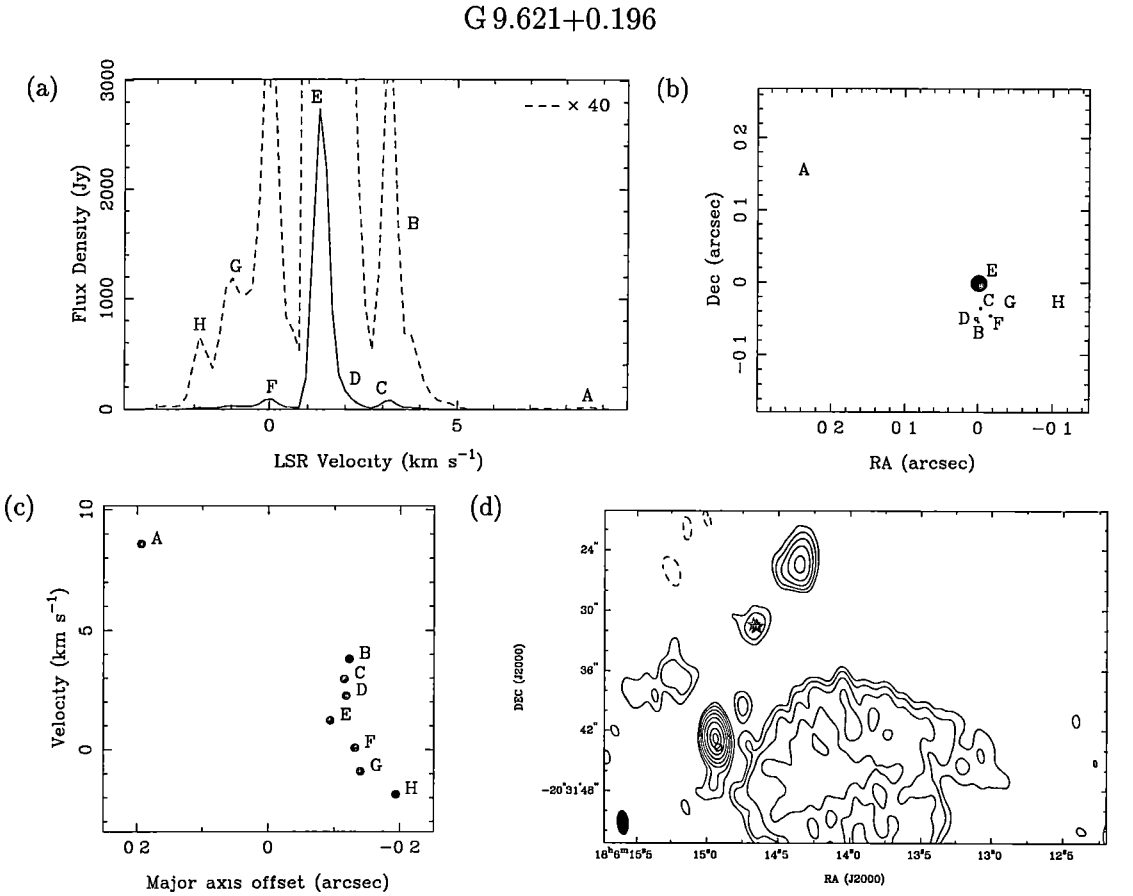

Figure 2.28: (a) Spectrum, (b) map and (c) v-a diagram for G 9.621+0.196. (d) Radio continuum image of the region around G 9.621+0.196. The contours levels are at -1, 1, 2, 4, 8, 16, 32, 64 and 90 per cent of the peak flux density (75.9 mJy beam^{-1}). The positions of the methanol masers in G 9.621+0.196 are indicated by stars, and are associated with an UCHII region with a flux density of 5.7 mJy. G 9.619+0.193 is indicated by open circles and is associated with an UCHII region with a flux density of 91.9 mJy. The size of the Gaussian restoring beam is 1.14×2.41 arcsec and is shown on the lower left of the plot.

G 345.010+1.792: This source is 19 arcsec south of G 345.012+1.797. It has a linear morphology and shows a velocity gradient. The maser components are associated with an unresolved UCHII region with a flux density of 179 mJy. The 12.2-GHz emission in this source has been imaged by Ellingsen *et al.* (1997) using the VLBA.

NGC 6334F: This source has an elongated morphology and shows a velocity gradient. The maser components run along the side of a cometary compact HII region which has an integrated flux density of 536 mJy. The 6.7- and 12.2-GHz masers in this source have been observed using the Australian VLBI network by Ellingsen *et al.* (1996).

NGC 6634F-NW: This source is located 4 arcsec north-west of NGC 6334F. It also has an elongated structure and shows a velocity gradient. No continuum emission has been detected.

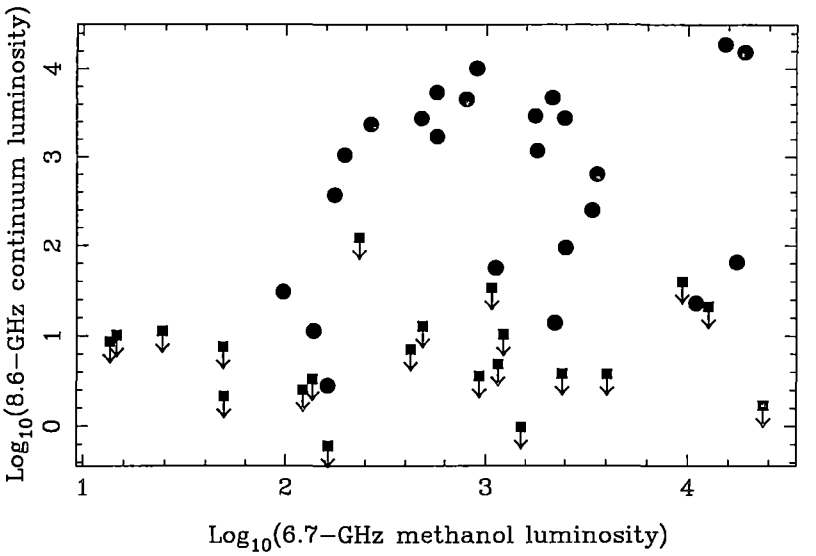

Figure 2.29: Methanol peak luminosity versus continuum luminosity of associated HII region. The luminosity was calculated by multiplying the flux density by the square of the kinematic distance. The squares with arrows represent the 4-σ detection limit for methanol sources without detected continuum emission.

G 351.445+0.660: This source has a complex structure and is not associated with an UCHII region.

G 351.775−0.536: This source has a complex structure. It is associated with an unresolved UCHII region with a integrated flux density of 11 mJy.

2.6 Discussion

2.6.1 Continuum association

Class II methanol masers are generally assumed to be associated with massive star formation and UCHII regions. Roughly half of the sources in this sample are associated with an UCHII with an implied spectral type of the embedded star of between O7.5 to B1. The fact that half the sources are *not* associated with an HII region is quite surprising. Fig. 2.29 shows a scatter plot of the methanol isotropic luminosity versus the 8.6-GHz continuum luminosity. The luminosities have been calculated by multiplying the peak flux density by the square of the assumed kinematic distance. (Integrating across the entire spectral profile, rather than taking the peak flux density, merely changes the luminosity by a constant factor). For masers without associated continuum, the 4-σ HII luminosity limit is indicated by an arrow. There is no apparent correlation of the luminosities for the methanol sources with associated continuum. The maser sources without associated continuum are distributed across the entire range of luminosities.

That there is no correlation between the continuum and methanol flux densities is not surprising as the continuum flux density is mainly caused by ionizing UV photons from the embedded star, while the maser flux density will depend upon

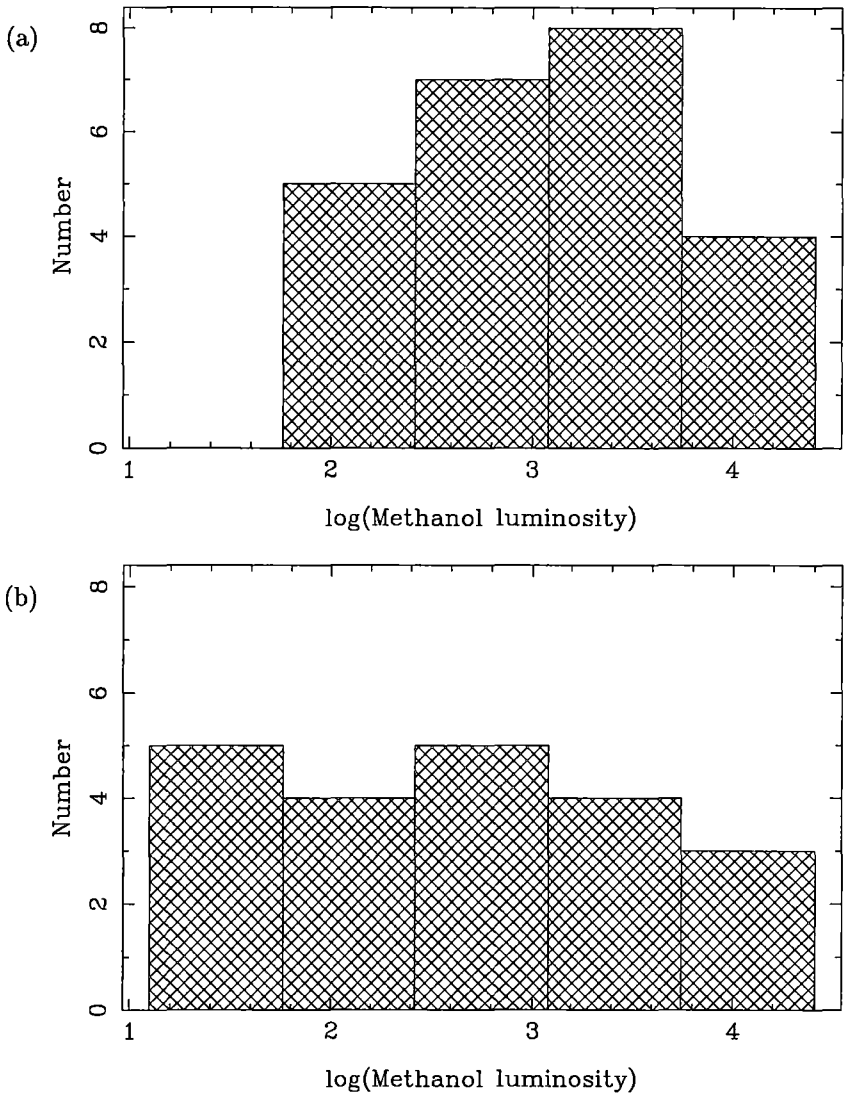

Figure 2.30: Luminosity distribution of the 6.7-GHz methanol sources. (a) Sources with an associated HII region. (b) Sources without any detected continuum emission. There is no statistical difference between the two samples.

the methanol abundance and FIR flux density (assuming that methanol is pumped by FIR radiation). Optical-depth effects, the beaming angle of the methanol and the possibility of multiple ionizing stars, further complicate the picture.

Fig. 2.30 shows the distribution of the methanol luminosity, separating the sample into sources with and without associated methanol. Both populations show a flat distribution, with the only significant difference being that the least luminous masers have no detected continuum. This is also evident in Fig. 2.29 by an absence of points in the top-left of the plot. Applying the Kolmogorov-Smirnov test to the two distributions indicates that there is no statistically significant difference between the two samples.

The continuum distribution of the associated UCHII regions is shown in Fig. 2.31. The distribution is slightly skewed towards higher luminosity. This is

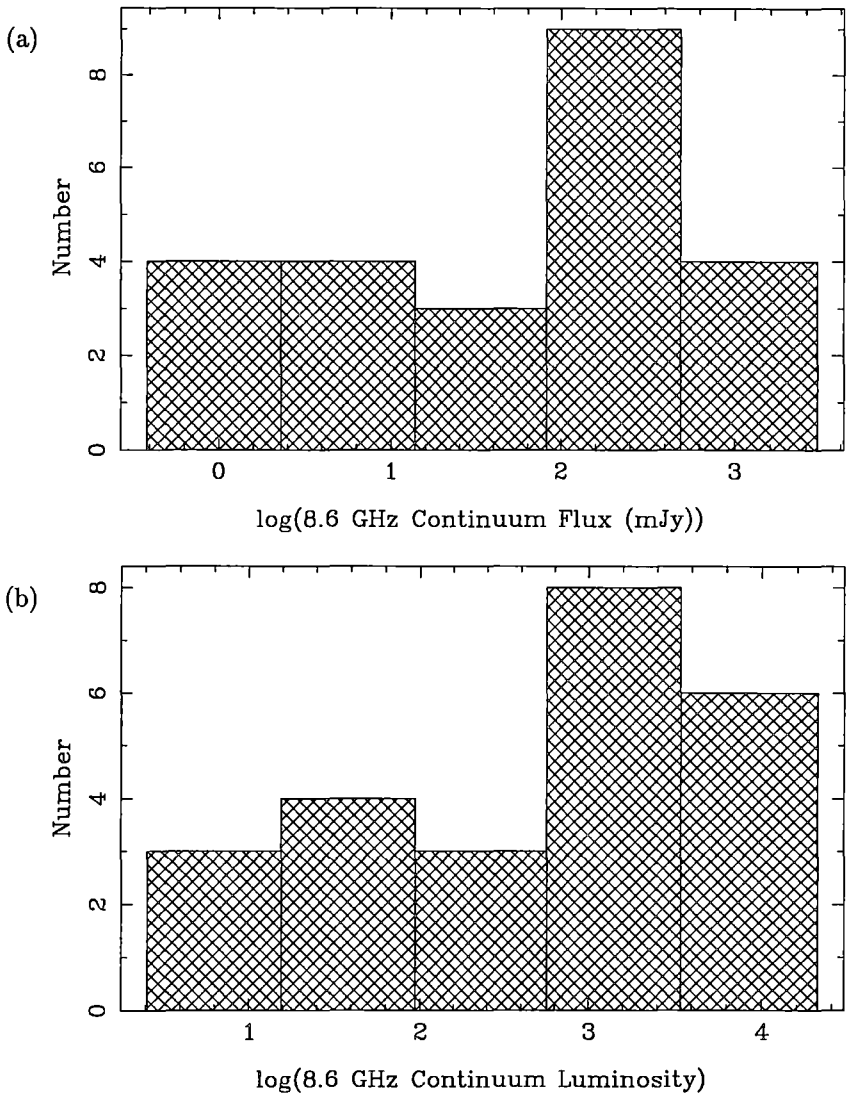

Figure 2.31: Distribution of continuum flux density of UCHII regions associated with 6.7-GHz methanol. (a) Distribution of integrated flux density. (b) Luminosity distribution.

unlikely to be a simple selection effect, as the source selection was based on the methanol flux density which does not show this property (Fig. 2.30). The number of sources with UCHII regions is too small for this to be statistically significant, though. One possible reason for this is that methanol masers are more likely to form around more massive stars, which have a higher ionizing potential. However, the large number of methanol masers without a detected UCHII region suggests this is not the case.

For the maser sources without detected continuum, we cannot rule out HII emission with a flux density below our detection limit, as Fig. 2.29 clearly shows that the observations are sensitivity limited. These observations, however, have a significantly lower detection limit than most previous surveys for UCHII regions.

We propose a few possible explanations for the absence of associated UCHII regions in half the methanol maser sources:

- these sources represent a different class of maser and are not associated with star formation. This is unlikely, as many of these sources are in known star-formations regions and are associated with other maser transitions such as the 1665 MHz OH transition.

- dust around the embedded star is absorbing a large fraction of the UV photons, which will make all the spectral types upper limits. If 90 per cent of the UV photons were absorbed by dust, the observed spectral type would be reduced by roughly one subclass.

- the exciting stars are still embedded in a dense molecular cloud, which is optically thick at 8.6 GHz reducing the flux density of the sources below our detection limits. The spectral index of sources with continuum detected at 6.7 and 8.6 GHz ranges from 0.2 to 2.4 with a median value of 1.1. Optically thick emission would be expected to have a spectral index of 2.0, while optically thin emission would have a spectral index of -0.1 (Gordon, 1988). The equations of Panagia & Walmsley (1978) assume that the HII regions are optically thin, and so will underestimate the spectral index of the embedded star.

- these sources are at the far-kinematic distance. This would increase the spectral-type upper limits by one to two sub-classes. However, as discussed in Section 2.5.1, most (if not all) of the sources in the sample are likely to be at the near-kinematic distance.

- these sources are associated with an earlier stage of the star-formation process, before the embedded star has had a chance to form an HII region. This model has also been suggested by Walsh *et al.* (1997) to explain the small number of UCHII regions found by Ellingsen *et al.* (1996a). The same suggestion has been made to explain the high proportion of H_2O masers without associated HII regions (Codella and Felli, 1995).

  If half of the methanol masers are pre-UCHII then the pre-main-sequence lifetime would equal the time the methanol masers are associated with UCHII regions. The pre-main-sequence lifetime of a protostar is roughly one fifth of the UCHII region lifetime (Molinari *et al.*, 1996) and so the methanol masers would last for only about 20 per cent of the lifetime of the UCHII region (or less as the masers would probably not be present for the entire pre-main-sequence lifetime). There is no evidence that methanol masers are associated only with UCHII regions for a small fraction of their lifetime. Ellingsen *et al.* (1996b) have estimated that there are 3000 UCHII regions in the Galaxy, assuming that all methanol masers are associated with an UCHII region. This number would have to be increased by a factor of 2.5 if half the methanol masers are pre-main-sequence but only existed for 20 per cent of the lifetime of the UCHII region. We think this is highly unlikely.

- these sources are associated with lower mass stars. The upper limits on the spectral types for sources without any detected UCHII is typically B1 or B2

(10-15 $M_{\odot}$), and possibly higher when the effects of dust and optical depth are taken into consideration. Assuming an IMF with a $M^{-1.4}$ dependence for the mass distribution (Sagar *et al.*, 1986), we would expect to find twice as many stars with a spectral type of B5-B0 as those with a spectral type of B0-O5. This is consistent with the number of methanol sources with and without associated UCHII regions.

We consider the most likely reason for the lack of detected UCHII regions is that the embedded stars have lower masses than previously thought. Absorption of UV photons by dust within the UCHII region and optical-depth effects also probably reduce the apparent spectral type of the embedded stars. The masses derived from the velocity gradients of the discs (Section 2.5.2) do not differ significantly between the sources with and without associated continuum (Fig. 2.34), but this may simply reflect the large uncertainties associated with the masses estimated from the velocity gradient.

2.6.2 Source modelling

Many of the sources in this current sample have been imaged several times and with different techniques (PTI, ATCA, VLBI), and so we can be confident that the linearity of the maser sources is not caused by instrumental artifacts. Although some of the sources in the current sample are significantly weaker than sources imaged previously, we are confident that, because of dynamic range limitations for the stronger sources, the positional errors for the weaker sources are not significantly worse than for the stronger sources.

The morphology of the masers varies enormously, making it difficult to devise a single, simple model. This variety probably reflects the different physical conditions such as the mass of the central star and the thickness of the disc. While some of the sources show very little scatter from a straight line and a remarkably linear velocity gradient, other sources show much more scatter or no velocity gradient. As well as the sources with seemingly no structure (the 'complex' sources) there are just as many sources that seem to be elongated, some of which also show a velocity gradient.

Norris *et al.* (1998) have discussed in detail three different models that could be used to explain the linear structure of the methanol masers.

- Jets and collimated outflows: although the lines could represent outflow from a star-formation region, the current data do not support this idea. Narrow, collimated jets are associated with high-velocity components (Rodriguez *et al.*, 1989; Rodriguez *et al.*, 1990, for example), while almost all the sources in this sample have a velocity range of less than 10 km s^{-1}.

- Shock fronts: it has been suggested that OH masers lie in a layer of cool dense gas between the shock and ionization front around a compact HII region (Elitzur, 1992). Given the close association of methanol and OH masers, it is not unreasonable to think that the methanol may also exist in this region. This model does not explain the velocity gradient seen in any of the sources.

A further problem is that many of the sources are not associated with a detected HII region. The relation of the methanol to the UCHII regions for a few of the sources supports this model (e.g. G 309.921+0.479, NGC 6334F).

- Circumstellar disc model: this is the only model that can easily explain the velocity gradient seen along most of the sources.

In the following sections we discuss a few of the main features of the methanol maser sources and their associated UCHII regions.

Linearity and velocity gradient

The large proportion of linear sources in this sample, many with clear velocity gradients, is quite remarkable. The edge-on disc model naturally explains the velocity gradient along the source, while the shock-front and outflow models do not.

To explain the high proportion of edge-on sources that the circumstellar disc model implies, Norris *et al.* (1993; 1998) have suggested two mechanisms. The first is that the column depth of masers lying in the plane of the disc will be much greater than for those perpendicular to the disc. Thus we would expect masers from an edge-on disc to be much stronger. The second mechanism occurs if we assume that the HII region is optically thick at centimetre wavelengths (Hollenbach *et al.*, 1994). The circumstellar disc would be expected to bisect the HII region, so that maser emission perpendicular to the disc would be obscured by the HII region. Norris *et al.* (1998) reject the second model as they saw no evidence for any difference between their 6.7- and 12.2-GHz data, although the 12.2-GHz data should be less affected by this. The current data do not support this second mechanism, as half the sources are not associated with an HII region although, as mentioned in Section 2.6.1, sensitivity may be a problem.

The linear sources with a linear velocity gradient can be explained by assuming that the sources lie in an edge-on, or slightly tilted, disc with the masers all at a constant radius from the central star. The derived masses (assuming Keplerian motion) in Table 2.1 are all reasonable values, although it is impossible to make an accurate guess of the size of the disc, making the derived values a lower limit.

The linear sources which do not show a monotonic velocity progression or velocity gradient can be explained if we assume that the maser sources may emanate from a variety of radii within the disc. We would not expect to see such a simple velocity gradient for these sources. Turbulence within the disc will further distort any velocity structure caused by the bulk motion of the rotating gas. The ratio of the turbulence within the disc to the bulk motion would have to vary significantly among the sources to explain the range of velocity gradients.

Norris *et al.* (1998) predicted that the fraction of linear sources should reduce with lower peak flux densities, as some of these sources would not be edge on. To test this we calculated the 'linearity' of each source by taking the ratio of the average deviation of the maser components from the line of best fit to the length of the source along this line. The 'simple' sources were not considered. The 'double' sources such as G 328.236−0.547 were also eliminated, as they essentially have a

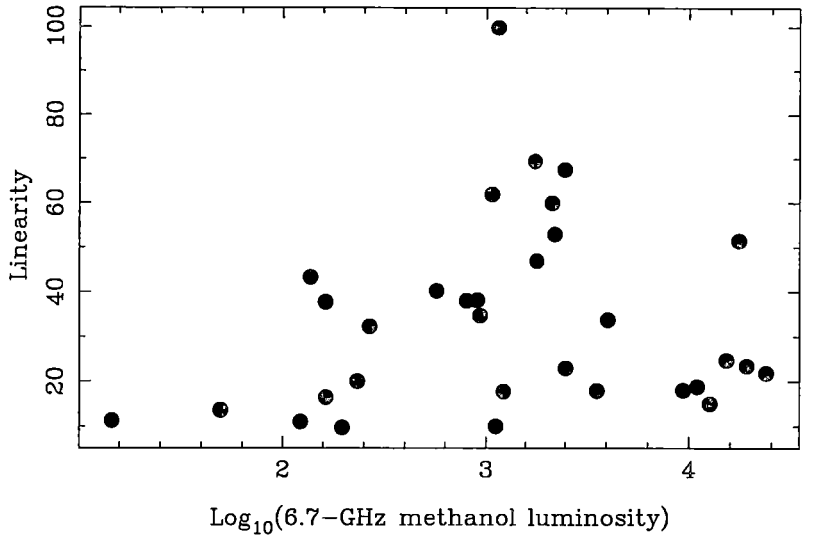

Figure 2.32: Methanol linearity versus methanol luminosity. The 'linearity' of a source is defined as the ratio of twice length of the source to the average deviation of the points from the line of best fit.

two-point morphology which gives an unreasonably high linearity. In Fig. 2.32 we have plotted the linearity of the sources versus the methanol luminosity. In Fig. 2.33 we have plotted the luminosity distribution of the methanol sources listed as linear in Table 2.1 and those that are not. Applying the Kolmogorov-Smirnov test to the two distributions finds no evidence that they are different. Thus, the maser linearity seems unrelated to flux density except for the very weakest sources. This is counter to our preferred model for the predominance of edge-on discs, namely stronger emission from the longer path lengths along the disc. However, the new sources added to the sample in this paper have relatively strong flux densities.

VLBI observations of the water megamaser galaxy NGC 4258 by Miyoshi *et al.* (1995) have clearly identified the source as an edge-on rotation disc. However, the source had previously been identified as an edge-on disc based only on the spectra (Watson and Wallin, 1994), which has a classic three peaked Keplerian profile. The central peak comes from the centre of the disc and is viewed at the rest velocity of the system. The two edge peaks come from the edge of the disc and are doppler shifted to positive and negative velocities, respectively (Ponomarev *et al.*, 1994). A three peaked profile is not generally seen for the linear methanol sources. The most likely explanation of this is that turbulence within the molecular disc obscures the Keplerian signature. This signature is seen in NGC 4258 but not the methanol sources because the ratio of rotational to turbulent velocities is much higher in NGC 4258.

Offset features

Quite a few of the linear sources have a single component that is significantly offset spatially and often in velocity (e.g. component 'G' in G 331.132−0.244).

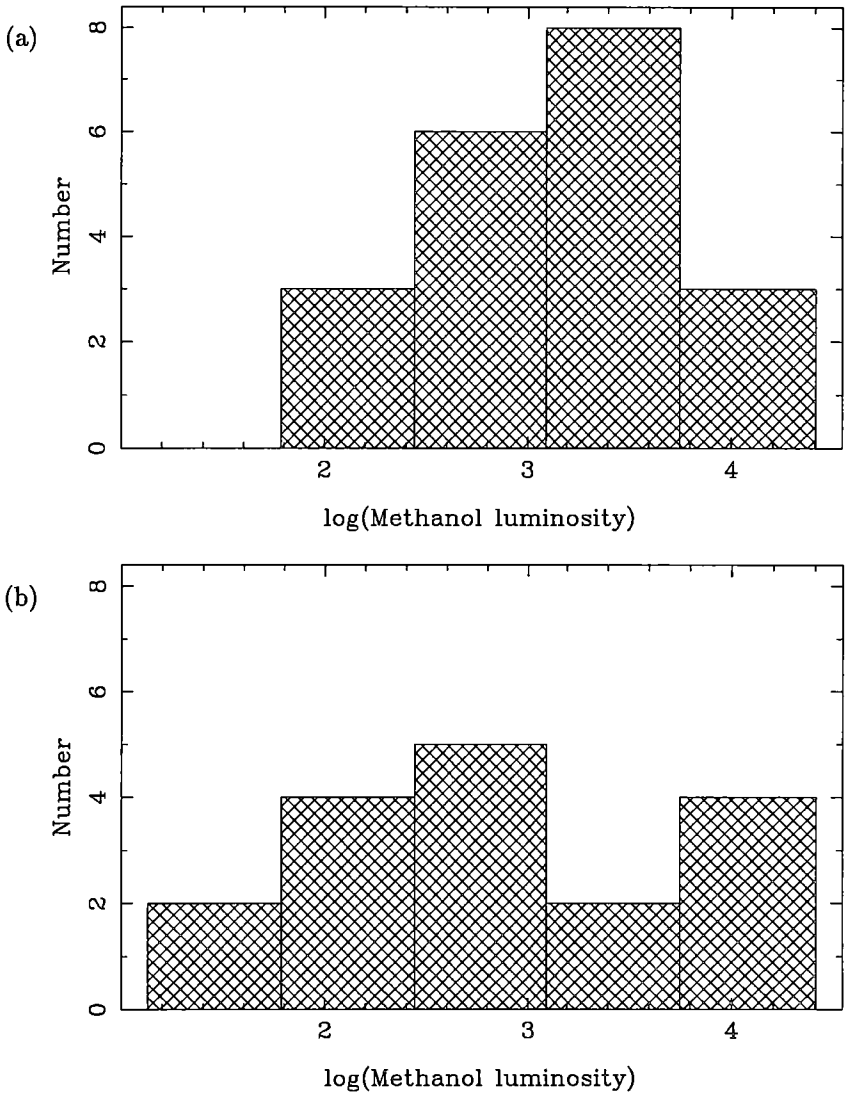

Figure 2.33: Distribution of methanol luminosity for (a) linear and (b) non-linear sources.

All of these components have a relatively weak flux density, but are unlikely to be artifacts. It is possible that these represent a separate source, possibly representing sources in a binary system. However, the most likely explanation is either that these components represent a dense clump in a low velocity outflow region, or that there may be some methanol present with low abundance above the denser circumstellar disc and that the components are denser clumps in this region. Either of these explanations would account for the different velocity and position of the offset component.

Maser position with respect to UCHII region

The position of the methanol sources relative to the UCHII regions neither supports nor rules out any of the models. Some of the sources, such as G 337.705−0.053 and G 339.878−1.252, show a line crossing the centre of an unresolved HII region

which is expected in the edge-on disc model. Others such as G 309.921+0.479, NGC 6334F and G 328.236−0.547, have a morphology which is more consistent with a shock-front model, with the line of masers following the continuum morphology quite closely. Some of the sources are at the edge of an HII region and are roughly perpendicular to it (e.g. G 308.918+0.123, G 331.132−0.244) which could be considered consistent with outflow.

Most of the methanol sources which are associated with HII regions are slightly offset from the peak of the continuum emission. There are a number of possible reasons for this.

- The HII region will, in general, not be symmetric and this could be a projection effect. As most of the UCHII regions are unresolved (or only just resolved) it is not possible to determine their underlying morphology. Relative motion of the star within the parent molecular cloud, or a pressure gradient within the cloud, may also mean that the embedded star is not aligned with the peak continuum emission.

- The peak of the HII region will be at the location of the greatest line-of-sight column depth if the region is optically thin. The UCHII regions are three dimensional, and so if the major axis is at an angle to the line of sight, this position of the peak will shift with respect to the maser position. A similar argument can be applied if the region is optically thick.

- The HII region may contain more than one star. This is almost certainly the case in the more extended sources such as G 308.918+0.123 and G 331.132−0.244.

- If the maser emission occurs in shock fronts within the HII region, we would expect there to be no direct relationship between the maser positions and the continuum emission of the UCHII regions.

Masses of linear sources

Fig. 2.34 shows a plot of the central star mass implied by the flux density of the UCHII region and the mass calculated assuming Keplerian rotation for the linear sources. The mass-spectral-type relationship was taken from Allen (1973). The masses implied by the velocity gradients along the maser sources are significantly less than the mass implied by the UCHII region. This could be because the radius of the disc has been underestimated. If maser emission accounted for only 75 per cent of the size of a disc, the mass of the embedded star would be underestimated by a factor of 2.4, because of the r^3 dependence of the calculated mass on the radius.

Double sources

Three of the sources in the sample have an unusual morphology with two clusters of maser components separated by 0.5 to 1.0 arcsec and 10 km s^{-1}. The individual

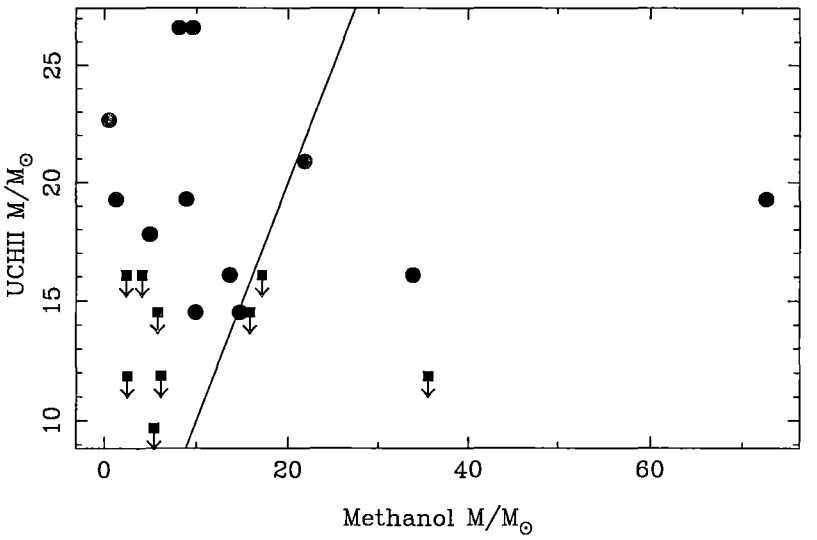

Figure 2.34: Mass of the embedded stars implied by the velocity gradient verses mass implied by the UCHII flux density. The squares with arrows represent sources with no associated UCHII region. The line shows equality.

clusters are elongated roughly perpendicular to the line joining the two clusters and show a velocity gradient. The source G 328.236−0.547 has the two clusters centred around an unresolved UCHII region (Fig. 2.12). The morphology and velocity gradient of these sources is remarkably similar to the SiO maser in Orion-IRc2 (Plambeck *et al.*, 1990). The SiO emission from this source has been modelled as coming from a circumstellar disc tilted by 45° with respect to the line of sight.

It is worth noting that a number of the other sources in the sample also show a gap between two close-by clusters that also could be explained as emission from either side of a disc (e.g. G 327.402+0.445, G 331.132−0.244, G 335.726+0.191, G 335.789+0.174, G 337.612−0.060). Although the archetypal spectral morphology of maser emission from a disc is a triple-peaked profile, it is possible to produce a range of models for which only two or even one peak is seen (Chapman and Cohen, 1985).

2.6.3 Circumstellar disc model

Although the morphology of some of the individual sources could be explained by a number of different models (e.g. G 309.921+0.479 suggests a shock front, if the velocity gradient is ignored), the circumstellar disc model best explains the linear methanol sources.

It is possible that most of the sources in this sample, even the elongated and complex ones, represent edge-on discs. If we assume that thickness and internal turbulence vary significantly between the sources, possibly with stellar mass or evolutionary stage, we can explain most of the observed morphologies. The linear sources have a flat disc, most with relatively little turbulence. The elongated and complex sources have thicker discs and/or higher turbulence. If the disc were

inclined towards the observer, we would expect to see a wide spread of maser components which still showed a velocity gradient. The source G 340.785−0.096 is the only complex source with a structure that cannot be accounted for by this model. However, as it would be difficult to quantify most of the parameters of such a model, it is of little value in understanding the dynamics of the star-forming region. This would also imply that there are many stars with face-on discs which we cannot see, which would increase the number of sources with methanol by a large factor.

A more probable theory is that methanol can mase in a variety of situations. The linear sources represent emission from edge-on discs, while the complex sources arise from different conditions, such as a shock-front. To determine whether there are two or more types of 6.7-GHz masers, a larger sample would be needed selected on rigorous selection criteria.

2.7 Conclusions

We have made simultaneous images of the 6.7-GHz methanol emission and 8.6-GHz continuum emission from 33 Galactic sources. Including 12 sources imaged by Ellingsen *et al.* (1996a) and Ellingsen *et al.* (in preparation) using a similar observing scheme, 17 of the 45 methanol sources have a curved or linear morphology, most showing a velocity gradient along the source. We suggest that the masers are located in an edge-on circumstellar disc around a young massive star. Modelling the velocity gradients gives masses from 1.3 to 73 $M_{\odot}$. Three of the sources have a similar morphology to the SiO maser in Orion-IRc2, which has been successfully modelled as an inclined circumstellar disc.

Twenty-five of the sources are associated with an UCHII region. The sources without an HII region are probably associated with slightly less massive stars than previously assumed.

Most of the methanol sources with an associated HII region are slightly offset from the peak emission. This is not consistent with a circumstellar disc model, although it could be a projection effect. We could not find any distinction between the linear and complex methanol sources nor the sources with and without associated HII emission.

2.8 Acknowledgments

We thank Kate Brooks for assisting with some of the observing and Jim Lovell for useful comments on a draft of this paper. The Australia Telescope is funded by the Commonwealth Government for operation as a National Facility managed by the CSIRO. This research used the SIMBAD data base, operated at CDS, Strasbourg, France.

Chapter 3

Mid-infrared observations of methanol masers

3.1 Introduction

Young massive stars are found embedded in dense molecular clouds, which are heavily obscured at optical wavelengths. As well as ionizing the surrounding gas to form an UCHII region, the embedded star heats the circumstellar dust which then radiates at far-infrared (FIR) wavelengths. It is widely accepted that all the energy from the embedded star is re-radiated in the FIR (Wood and Churchwell, 1989a). For this reason, the FIR is an ideal wavelength for studying OB star-formation. The all-sky survey of the *Infrared Astronomical Satellite* (*IRAS*) made sensitive observations in the wavelength range of 10–100 μm. Thus the *IRAS* Point-Source Catalog (PSC) is an extremely useful tool for selecting young OB stars and studying their FIR properties. The sensitivity of the *IRAS* observations at 60 and 100 μm is sufficient to detect all B3 zero-age main-sequence (ZAMS) stars throughout our Galaxy. At 12 μm, *IRAS* can detect all O9.5 stars (Wood and Churchwell, 1989a).

The IR flux density of most embedded OB stars peaks near 100 μm, indicating dust temperatures of around 25-30K. Although the luminosity varies greatly from one object to another, remarkably the shape of the continuum spectra does not (Chini *et al.*, 1986a; Wood and Churchwell, 1989a). Wood and Churchwell (1989a) used this property to identify embedded massive stars based on their *IRAS* colours. By examining the FIR colours of known UCHII regions (and hence massive stars), they found that by plotting $\log(F_{60}/F_{12})$ versus $\log(F_{25}/F_{12})$, (where F_x is the flux density in the four *IRAS* bands) all the UCHII regions lay in the upper right of the plot, while few other objects in the PSC occupied this region. Specifically they suggest that sources which satisfy the criteria:

$$\begin{aligned} \log(F_{60}/F_{12}) &\geq 1.30 \\ \log(F_{25}/F_{12}) &\geq 0.57, \end{aligned} \tag{3.1}$$

have a high probability of being embedded massive stars. They rejected sources which only had an flux density upper limit in either the 60 or 25 μm bands, but allowed sources with an upper limit in the 12 μm band as this would move the

source further to the upper right of the plot. These criteria (from now on called the WC criteria), have been the basis of a number of successful surveys for H_2O, OH and methanol masers, which are known to identify regions of massive star formation (Braz *et al.*, 1990; Macleod, 1991; Palla *et al.*, 1991; Henning *et al.*, 1992; Schutte *et al.*, 1993). By comparison with optically visible O stars, Wood and Churchwell (1989a) estimated that 15 per cent of an O star's main-sequence lifetime is spent embedded in a molecular cloud.

The FIR continuum flux density spectrum can be modelled well by a cocoon of cool dust around the embedded star with temperature of around 25–30K. Chini *et al.*(1986a) found that the 100-1300 μm portion of the spectrum for embedded O3 – B1 stars is well modelled by a modified Planck curve with a mean temperature of 25K. However, this curve significantly underestimates the flux density short-wards of 100 μm. Chini *et al.*(1986b; 1987) modelled the $1 - 1300$ μm flux density distribution using a two-shell model. The inner shell is hot with a low density and is responsible for emission below 20 μm. The bulk of the emission comes from the outer, cooler, shell which has a high density but large extinction. This model closely fits the observations. However Churchwell *et al.*(1990) have criticized the model for assuming a single size for the dust grains. Churchwell *et al.* developed a similar model, but incorporated a range of grain sizes. They modelled the dust cocoon around a ZAMS O6 star and compared the results to the UCHII region G 5.89−0.39. They found that a large constant-density cocoon with a size of $\sim 10^{18}$ cm is needed to provide enough dust to produce the FIR spectrum. A shell this large would have a mass $\gtrsim$5000 $M_\odot$. A dust-free cavity around the star is required to avoid too high a NIR flux density from hot dust close to the star. The average temperature of the dust cocoon is ~30 K. Both these models predict that the source will be optically thick at wavelengths shorter than ~7 μm.

The WC criteria have been used in many surveys of massive star forming regions. As class II methanol masers are thought to occur in these regions, a number of searches for the 6.7-GHz $5_1 \rightarrow 6_0$ A^+ transition of methanol have been based on the WC criteria (Schutte *et al.*, 1993; van der Walt *et al.*, 1995; van der Walt *et al.*, 1996; Walsh *et al.*, 1997). These surveys have generally included additional constraints such as lower limits on the 60 and 100 μm flux densities. The detection rates range from 3-37 per cent, and so have been very successful at finding new 6.7-GHz methanol masers. Van der Walt *et al.*(1996) found that the detection rate of 6.7-GHz masers decreased for fainter sources selected by the WC criteria. This has been interpreted as meaning that a significant fraction of the fainter WC sources are in fact not embedded ionizing stars, however an alternative explanation could be simply that methanol masers do not always accompany such stars.

Ellingsen *et al.* (1996b) made a blind survey towards 10 deg^2 of the Galactic Plane between the latitudes of 325-335°. As this is a complete survey of the region with a well defined flux density limit it allows an estimation of the true success rate of *IRAS* based searches. In the region surveyed the various modified WC selection criteria would have had a success rate of 22 to 42 per cent. However, Ellingsen *et al.* found that 22 per cent of the detected masers did not have an *IRAS* source within 2 arcminutes. This means the WC based surveys would have only found 37 to 59 per

cent of the 6.7-GHz masers in the region. It is not clear whether these methanol sources without associated *IRAS* sources are associated with UCHII regions or represent another class of object (although there is no evidence to suggest that they are any different from the masers with *IRAS* counterparts).

A major problem with most FIR instruments (including *IRAS*) is the poor spatial resolution. The beam of *IRAS* is 2 arc-minutes at 100 μm and 30 arcsec at 25 and 12 μm. This is much larger than the expected size of a few arcsec for young stellar objects (YSO). As we have already seen in Chapter 2, many of the SFR in which methanol and UCHII regions form are complex with many individual sources. This means there is no way of knowing if the *IRAS* flux density really comes from two or more separate stars. The FIR will be dominated by the most massive star in the region; however there is no guarantee that the largest star in a region will be associated with a particular maser source or UCHII region.

Obviously, to study these objects more carefully, high resolution observations are required. Testi *et al.*(1994; 1997b) have made high-resolution (arcsec) near-infrared (NIR) observations of a number of H_2O and OH maser sources, most of which are also methanol sources. They found a NIR source within 5 arcsec of most of the maser features, many coincident to within 1 arcsec. They suggest the sources are young massive stars in the earliest evolutionary stage. The NIR emission is a combination of: a) the heavily extincted stellar photo-sphere of a massive YSO, b) contributions of free-free and free-bound emission, c) emission from the hot dust surrounding the YSO.

Although the Testi *et al.* results are encouraging, it is through FIR observations that the best understanding of massive YSO will be made. Unfortunately, to make arcsec resolution images in the FIR either interferometry or a large telescope (15 m at 60 μm) is needed. Currently this is not practical at these wavelengths.

To make arcsec resolution IR images of the methanol masers in our sample, we have chosen to image the sources in the mid-infrared (MIR) at 11.5 μm, which is relatively easy to do. Although the flux density of the sources is much less at 11.5 μm than at 60 or 100 μm, the wavelength is long enough that obscuration should not have much effect. Because IR observations penetrate the dust around massive young stars, it may be possible to directly image circumstellar discs. This direct imaging of a disk would provide a direct test of the disc model for linear methanol masers.

3.2 Observations and data reduction

The observations were made over 4 nights on 1996 May 30 and 1997 April 22-25 using the $f/36$ focus of the 3.9-m Anglo-Australian Telescope (AAT) in collaboration with Craig Smith from the Australian Defense Force Academy (ADFA). The detector which was used, NIMPOL, is a MIR imaging polarimeter built at ADFA. The instrument uses an Amber Engineering 128×128 Si:Ga AE159 Focal Plane Array, which is cooled with liquid Helium. On the AAT, the pixel size of the detector is 0.25 arcsec, giving a field of view of 32 arcsec. The detector can be used from 8–18 μm with wavelength selection provided by discrete filters and

a circular variable filter. NIMPOL is described in detail in Smith *et al.*(1997).

The observations were made using a narrow band filter centered on 11.5 μm with $\Delta\lambda$=1.0 μm. The observations were diffraction limited with a FWHM of $\sim$0.7 arcsec which gives a sampling of 2.5 pixels/beam. The sky-chop and beam-switch were 35 arcsec east-west in 1996 and 30 arcsec north-south in 1997. Direct imaging of 27 fields containing maser sources from the sample used in Chapter 2 was performed, a total of 35 maser sources were observed. Due to time constraints, a few of the sources from the sample were not observed. Integration times of 20-60 minutes were used, giving detection levels of 0.1-0.6 Jy arcsec^{-2}. An observation of a close by optical "SNAF" star was made before each observation, to align the pointing of the telescope and so achieve spatial registration.

Data processing and calibration of the imaging and polarimetric observations was done by Craig Smith, using software developed by the ADFA group for reducing data from NIMPOL. Image analysis was performed by myself using the Miriad package (Sault *et al.*, 1995). For the weaker detections the images were smoothed with a 0.75 arcsec FWHM Gaussian, which is equal to the diffraction limit at 11.5 μm.

3.3 Results

Table 3.1 lists the maser sources imaged at 11.5 μm together with the flux density of the detections and the detection limit of the non-detections. Of the 35 maser sources observed, nine had detected emission at 11.5 μm. One MIR source was detected which is not associated with any detected methanol emission. For sources without any detected MIR emission, an 8-σ detection limit is quoted, in Jy arcsec^{-2}. An 8-σ detection limit was chosen as a 4 or 5-σ level was thought to underestimate the true detection limit. Table 3.1 also lists associated *IRAS* PSC sources for all sources in the maser sample (including the sources not observed at 11.5 μm) and a number of derived parameters from the MIR and *IRAS* flux densities.

Figures 3.1 to 3.10 show the CCD images of the detections. Included on these images are the positions of the maser sources and the positions of the NIR sources found by Testi *et al.*(1997b). For sources with an associated UCHII region as well, a separate plot overlaying the MIR and the radio-continuum is included. The radio images have been taken from Chapter 2 and from Ellingsen *et al.*(1996a; 1998).

The sources G 309.921+0.479 and G 308.918+0.123 were observed on three separate nights, which allows us to estimate the positional accuracy of the observations. The measured position of G 308.918+0.123 changed by 3.4 arcsec and G 309.921+0.479 by 1.24 arcsec. These relatively large errors are probably due to telescope tracking errors and misalignment between the optical tracking telescope and the MIR camera. All the MIR detections are within 4 arcsec of a methanol source or UCHII region, so we have assumed that the sources are associated and the offset is instrumental. Given the complex nature of the regions studied, it is possible that some of the associations are chance alignments. Using the density

of MIR sources found in these observations (ten MIR sources in 27 30×30-arcsec fields) and assuming a random distribution of MIR sources, the chance of a MIR source within 5 arcsec of a methanol source is 3 per cent. Thus, of the 10 IR detections there is a 1 in 4 chance that one of them is a chance detection and and insignificant chance that they are all chance associations.

Astrometry was not viable because there are too few sources detectable at 11.5 μm. Because of these relatively large positional errors, it it impossible to conclusively say whether the methanol is closely associated with the IR source (as would be expected if the methanol emanated from a circumstellar disc) or offset (which would be expected if the methanol was in outflow regions or shock-fronts).

During the 1996 observations, the chopping secondary was slightly misaligned. This results in a slight extension of the sources in the east-west direction.

3.3.1 Individual sources

In the following section the methanol sources found to have a 11.5 μm association are briefly described.

G 305.199+0.206

The MIR image of this source is shown in Fig. 3.1. This source is not associated with any detected methanol emission but is associated with a compact HII region with a flux density of 195 mJy. The MIR and UCHII source are offset from the methanol maser G 305.202+0.207 by 15 arcsec. This is the only MIR source detected in these observations which is not associated with a methanol source.

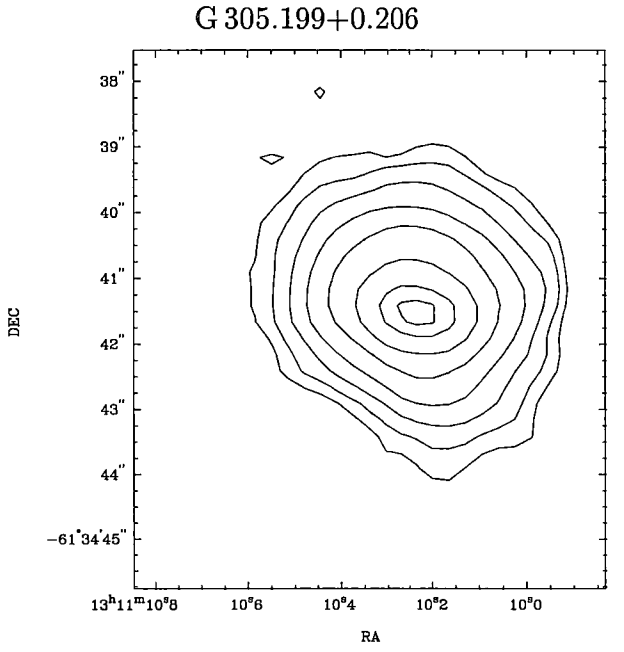

Figure 3.1: The 11.5 μm emission of G 305.199+0.206. This source does not show any methanol emission and is associated with a compact HII region with an integrated flux density of 195 Jy.

Table 3.1: Sources observed at 11.5 μm using the AAT and associated *IRAS* sources.

Source	Epoch[a]	Flux Density (Jy)[b]	UCHII Flux Density (mJy)	*IRAS* Assoc-n[c]	*IRAS* Sep-n (Arcsec)	*IRAS* Flux Density 12 μm (Jy)	25 μm (Jy)	60 μm (Jy)	100 μm (Jy)	Luminosity MIR[d] ($L_\odot \times 10^4$)	*IRAS*[e]	Spectral Type[f] MIR	*IRAS*	UCHII
G 305.199+0.206	96	49.40												
G 305.202+0.207	96	<0.14	<0.88							<0.04		<B3		<B1
G 305.208+0.206	96	<0.14	<0.55							<0.07		<B3		<B1
G 308.918+0.123	97	265.90	167.1	13395−6153	17.4	250.7	602	2701	3566	140.1	25.7	>O4	O6	O9.5
G 309.921+0.479	97	58.80	676.2	13471−6120	3.5	76.3	668	3930	<4473	30.1	29.7	O6	O6	O7.5
G 316.640−0.087	97	<1.19	<0.36	14404−5942	10.1	<4.0	24	538	918	<0.03	0.2	<B3	B2	<B3
G 318.949−0.193	96	<0.25	<0.66							<0.02		<B3		<B2
G 323.740−0.263	97	<0.83	<0.16	15278−5620	29.8	23.6	167	1960	3259	<0.14	5.6	<B3	O8.5	<B2
G 323.741−0.263	97	2.15	<0.16							0.5		B1		<B2
G 327.120+0.511	97		0.5	15437−5343	3.3	6.0	75	988	1425		7.3		O7.5	B1
G 327.402+0.445	97	2.27	101.3							0.8		B0.5		O9.5
G 327.402+0.444	97	<0.66	101.3							<0.27		<B2		O9.5
G 327.402+0.444E	97	<0.66	<0.51							<0.22		<B2		<B1
G 328.236−0.547	97	<0.25	27.7							<0.03		<B3		B0.5
G 328.254−0.532			<0.56	15541−5349	2.2	<12.0	<111	3033	6415		5.4		O8.5	<B2
G 328.809+0.633	96	6.38	302.8							0.9		B0.5		O9.5
G 331.132−0.244	97	<0.53	198.6	16071−5142	26.7	4.5	53	742	2903	<0.21	7.3	<B2	O8	O9
G 331.278−0.188	96	0.84	4.1	16076−5134	9.9	36.0	237	2823	5930	0.3	18.5	B2	O6.5	B0.5
G 335.726+0.191	97	<0.58	<0.69							<0.09		<B3		<B1
G 335.789+0.174	97	<0.57	<0.42							<0.10		<B3		<B2
G 336.433−0.262	97	<0.52	<0.33							<0.24		<B2		<B1
G 337.612−0.060			<11.24	16344−4658	11.8	7.1	47	1130	<4034		4.2		O9.5	<B0.5
G 337.703−0.054	96	<0.25	<0.65	16348−4654	6.7	7.4	45	843	<4034	<0.04	3.9	<B3	O9.5	<B1
G 337.705−0.053	96	<0.25	191.9	16348−4654	7.9	7.4	45	843	<4034	<0.05	5.2	<B3	O8.5	O9.5

continued on next page

continued from previous page

Source	Epoch[a]	Flux Density (Jy)[b]	UCHII Flux Density (mJy)	*IRAS* Assoc-n[c]	*IRAS* Sep-n (Arcsec)	*IRAS* Flux Density 12 μm (Jy)	25 μm (Jy)	60 μm (Jy)	100 μm (Jy)	Luminosity MIR[d] ($L_\odot \times 10^4$)	*IRAS*[e]	Spectral Type[f] MIR	*IRAS*	UCHII
G 338.460−0.245	97	<0.40	<0.26							<0.08		<B3		<B2
G 339.878−1.252			6.4	16484−4603	12.3	<9.9	192	3444	5347		8.5		O7.5	B0.5
G 340.785−0.096	97	<0.52	16.5							<0.30		<B2		B0
G 345.003−0.224	97	<0.39	215.9	17016−4124	16.2	3.1	241	3669	7028	<0.04	7.5	<B3	O7.5	B0
G 345.003−0.223	97	<0.39	<0.22	17016−4124	12.4	3.1	241	3669	7028	<0.04	6.0	<B3	O8	<B2
G 345.010+1.792	97	11.50	264.2	16533−4009	8.4	26.4	<471	7136	13290	0.9	8.2	B0.5	O7.5	B0
G 345.504+0.349	96	20.40	<0.06	17008−4040	26.4	68.4	539	2713	<18230	1.6	6.6	B0.5	O8	<B3
G 348.550−0.979S	97	<0.64	<0.52							<0.05		<B3		<B2
G 348.550−0.979N	97	<0.64	0.6							<0.05		<B3		B2
NGC 6334F	97	52.30	2675.0	17175−3544	16.8	103.5	1400	11360	<22050	5.5	18.7	O8.5	O6.5	O7.5
NGC 6634F−2	97	<0.44	<6.33							<0.04		<B3		<B0.5
G 351.445+0.660	97	<0.52	<2.64							<0.04		<B3		<B1
G 351.775−0.536	97	<0.90	11.6	17233−3606	23.2	4.5	229	8787	20400	<0.07	11.4	<B3	O7	B0.5
G 353.410−0.360	96	<0.26	662.8							<0.06		<B3		O8.5
G 9.621+0.196	96	<0.27	5.7	18032−2032	22.6	38.6	292	4106	7844	<0.02	4.4	<B3	O9	B1
G 9.619+0.193	96	<0.27	91.9	18032−2032	20.1	38.6	292	4106	7844	<0.02	4.4	<B3	O9	B0

Notes:

(a) During the 1996 observations, the chopping secondary was slightly misaligned. This results in a slight extension of the source in the east-west direction.

(b) For detections the integrated flux density of the source is quoted. For non-detections, the 8-σ detection limit is quoted, in Jy arcsec^{-2}. Sources with a blank in this column were not observed with the AAT, but do have an *IRAS* counterpart within 30 arcsec.

(c) *IRAS* sources separated by more than 30 arcsec are assumed not to be associated.

(d) The MIR luminosity is extrapolated from the detected 11.5 μm flux density, or upper limit (see section 3.4.4).

(e) The *IRAS* luminosity was calculated by adding the *IRAS* flux densities and assuming 40 per cent of the luminosity is outside the *IRAS* bands.

(f) The Spectral types were calculated using the values tabulated in Panagia (1973).

G 308.918+0.123

The MIR image of this source is shown in Fig. 3.2 together with the associated UCHII region for comparison. The MIR source is strong with a flux density of 266 Jy and is a point source. The apparent halo around the object is a result of the point spread function. The source is offset by 17.4 arcsec from the *IRAS* source 13395-6153, which has a 12 μm flux density of 251 Jy. Although this separation is outside the *IRAS* error ellipse, the two are most likely the same source as they have similar flux densities. The associated UCHII region with this source is complex, with a peak offset by 4.5 arcsec from the MIR and maser sources. This source has been observed three separate times and the measured positions cluster around the the maser position. It is thought unlikely that the IR source is at the same position as the peak of the HII region.

Assuming the IR source is associated with the methanol source implies that there must be at least two embedded stars in the region. One of the stars, without any associated methanol, is responsible for most of the detected radio-continuum, but has small MIR flux density. The other star, with a strong MIR flux density, has little (or no) radio-continuum emission. Since the more massive star would be expected to have both the brighter IR emission and a brighter HII region, these possibilities are apparently in conflict, and can only be reconciled by contriving more complex models, for example an evolutionary difference between the two embedded stars.

G 309.921+0.479

The MIR image of this source and the associated UCHII region is shown in Fig. 3.3. The offset between the methanol position and the MIR source is 1 arcsec, which is less than the expected errors and the two can safely be assumed to be associated. The *IRAS* source 13471-6120 is offset from the maser position by only 3.5 arcsec and the *IRAS* 12 μm flux density of 76 Jy is comparable to the measured 59 Jy 11.5 μm flux density.

The IR image shows a weak second feature offset by one arcsec to the south-west. This is not present in the UCHII region, which may be an effect of the lower spatial resolution. VLBI observations at 6.7 and 12.2 GHz suggest that the curved maser source may in fact be two separate sources (Section 4.5.1). The separation of the two maser clusters is similar to the separation of the IR sources.

G 323.741−0.263 & G 323.740−0.263

The MIR image of this source is shown in Fig. 3.4. There is no detected UCHII region associated with either of the two methanol maser sources, which are separated by 3 arcsec. The MIR source is offset by 1 arcsec from G 323.741−0.263 and the two are probably associated. The stronger methanol source, G 323.740−0.263 is 4 arcsec offset from the MIR source. Given the large positional errors, it is possible that the MIR actually is associated with G 323.740−0.263. Fig. 3.4 shows what may be a weak detection of a second source to the north-west of the main emission. The separation of the two IR sources is roughly the same as the two

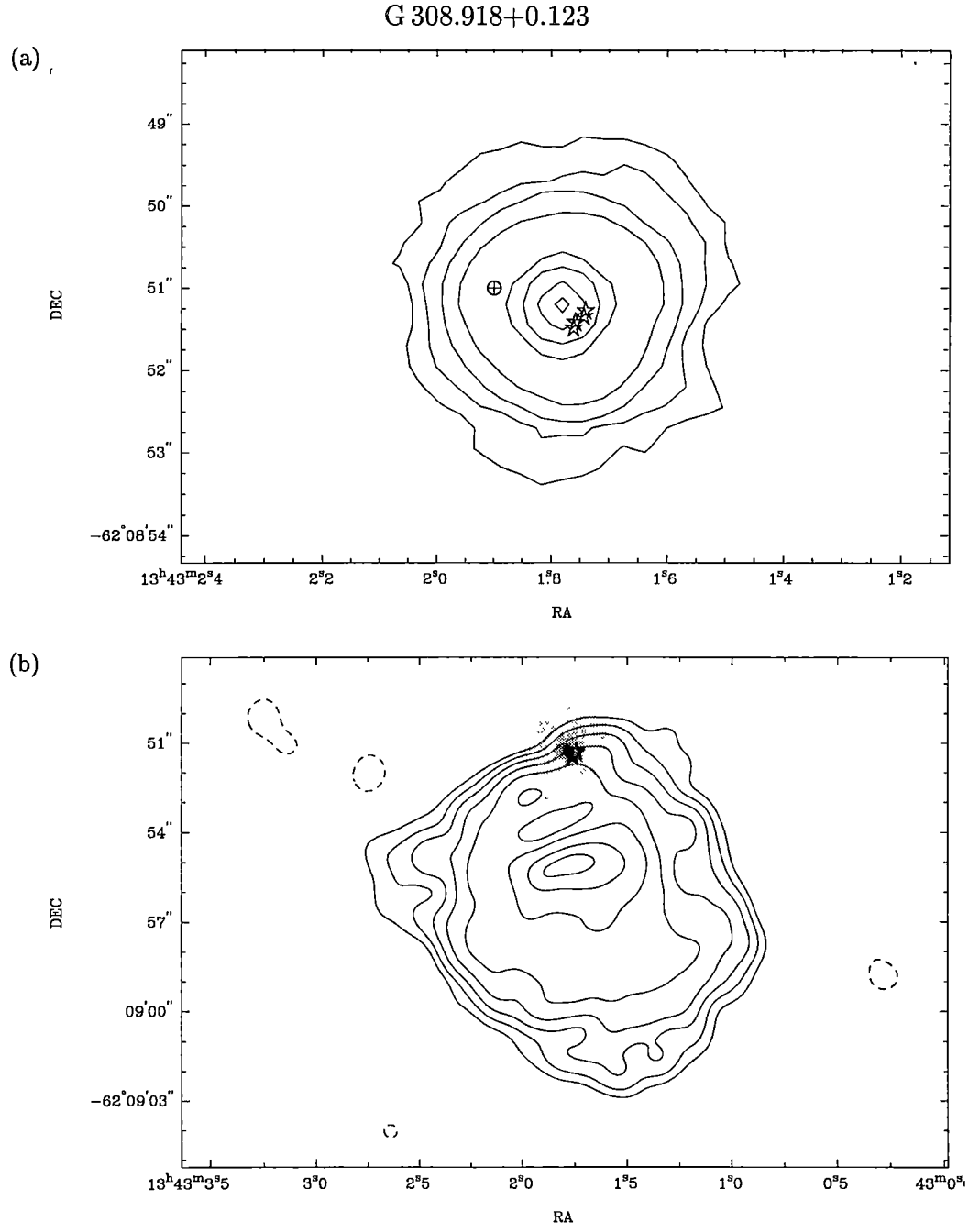

Figure 3.2: (a) The 11.5 μm source associated with the methanol maser G 308.918+0.123. The individual maser components are represented by stars. The crossed circle represents the position of the IR source from Braz & Epchtein (1983). The contour levels are at 1, 2, 4, 8, 16, 32, 64 and 90 percent of the peak flux density. The integrated flux density of the source is 266 Jy. (b) The 11.5 μm (grey-scale) and UCHII region (contours) associated with the methanol maser G 308.918+0.123. The contour levels are at -1, 1, 2, 4, 8, 16, 32, 64 and 90 percent of the peak flux density. The maser components are represented as stars. The MIR source is almost certainly a separate source to the UCHII region.

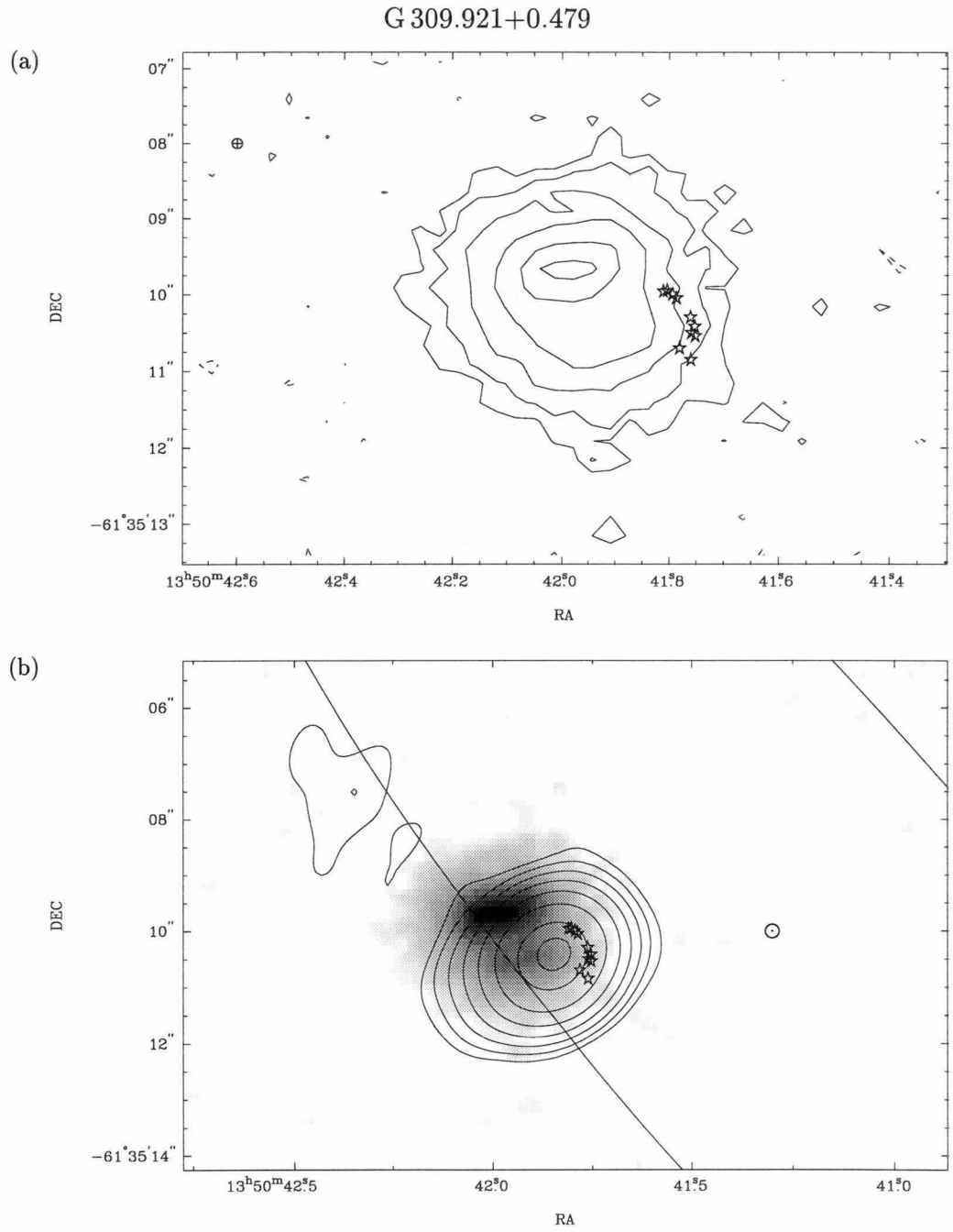

Figure 3.3: (a) The 11.5 μm source associated with the methanol maser G 309.921+0.479. The individual maser components are represented by stars. The crossed circle represents the position of the IR source from Braz & Epchtein (1983). The contour levels are at -1, 1, 2, 4, 8, 16, 32, 64 and 90 percent of the peak flux density. The integrated flux density of the source is 266 Jy. (b) The 11.5 μm (grey-scale) and UCHII region (contours) associated with the methanol maser G 309.921+0.479. The contour levels are at -1, 1, 2, 4, 8, 16, 32, 64 and 90 percent of the peak flux density. The maser components are represented as stars. The position of the *IRAS* PSC source 13471-6120 is indicated by a circle. The partially visible ellipse is the *IRAS* error ellipse.

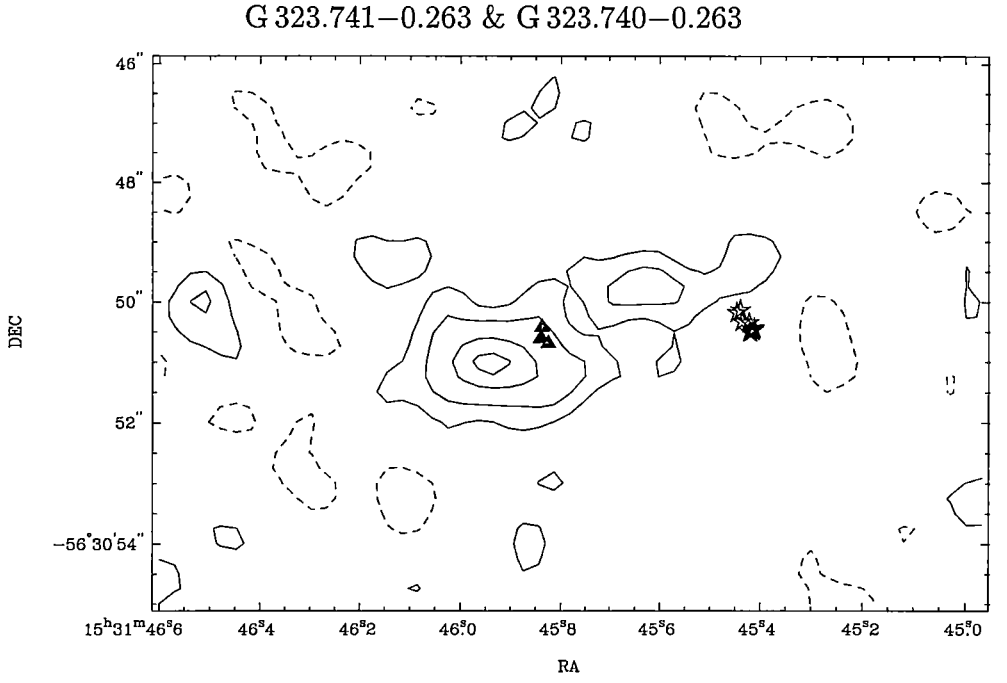

Figure 3.4: The 11.5 μm emission associated with the methanol maser sources G 323.741−0.263 and G 323.740−0.263. The stars mark the position of the maser components in G 323.740−0.263, while the triangles mark G 323.741−0.263. The MIR is probably associated with G 323.741−0.263, however the errors in the positional alignment are large enough for it to be possible that G 323.740−0.263 is associated with the MIR. The contour levels are at -16, 16, 32, 64 and 90 percent of the peak flux density. The integrated flux density of the source is 2.1 Jy.

maser sources. However, it is not clear that the second MIR sources is real or not. The sources are offset by 30 arcsec from the *IRAS* source 15278-5620.

G 327.402+0.445 & G 327.402+0.444 & G 327.402+0.444e

The MIR image of the region around these sources is shown in Fig. 3.5. G 327.402+0.445 is 2 arcsec east from the peak of a 2.3 Jy MIR source, and the two are probably associated. However, G 327.402+0.444 is 4 arcsec offset from the MIR source, which is within the positional errors of the observations. G 327.402+0.445 is aligned with a barely resolved 100 mJy UCHII region and it seems reasonable to assume that the UCHII region and the MIR source are aligned. Both the UCHII region and the MIR source show some extension towards the north-east. There is no *IRAS* PSC entry within 30 arcsec of these maser sources.

G 328.809+0.633

The MIR image of this source is shown in Fig. 3.6, together with the associated UCHII region. The MIR source has a flux density of 6.4 Jy and is aligned with the methanol source. The radio continuum observations show an unresolved UCHII region separated by 2.5 arcsec from a cometary HII region. This morphology shows that there are two OB stars in this region, and the single maser component to the

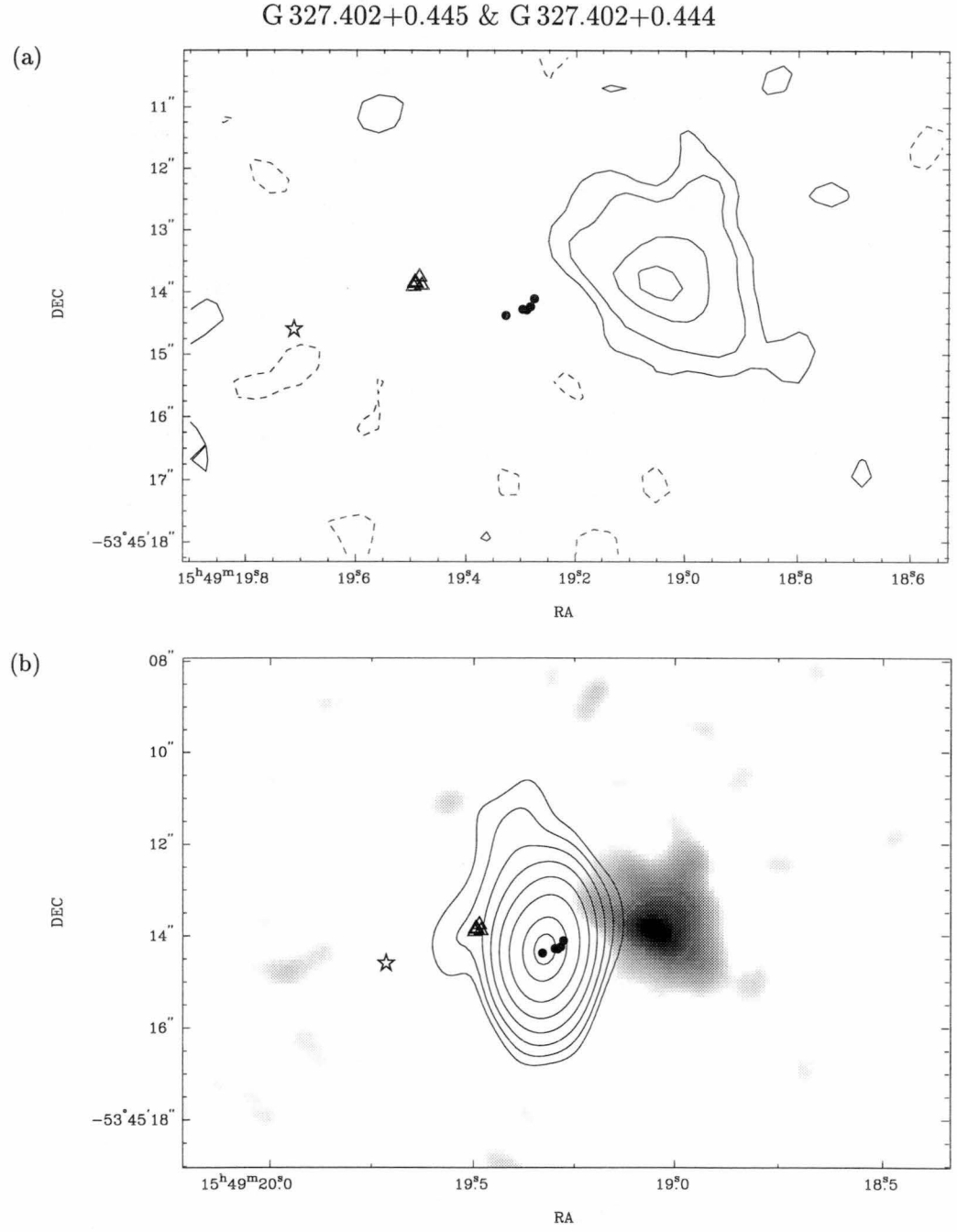

Figure 3.5: (a) The 11.5 μm emission associated with the methanol maser sources G 327.402+0.445 & G 327.402+0.444 & G 327.402+0.444e. The star marks the position of G 327.402+0.444e, while triangles mark G 327.402+0.444 and the filled circles mark G 327.402+0.445. The contour levels are at -16, 16, 32, 64 and 90 percent of the peak flux density. The integrated flux density is 2.3 Jy. (b) The 11.5 μm (grey-scale) and UCHII region (contours) associated with the methanol masers G 327.402+0.445 & G 327.402+0.444 & G 327.402+0.444e. The contour levels are at -1, 1, 2, 4, 8, 16, 32, 64 and 90 percent of the peak flux density. The maser components are represented by the same symbols as in (a).

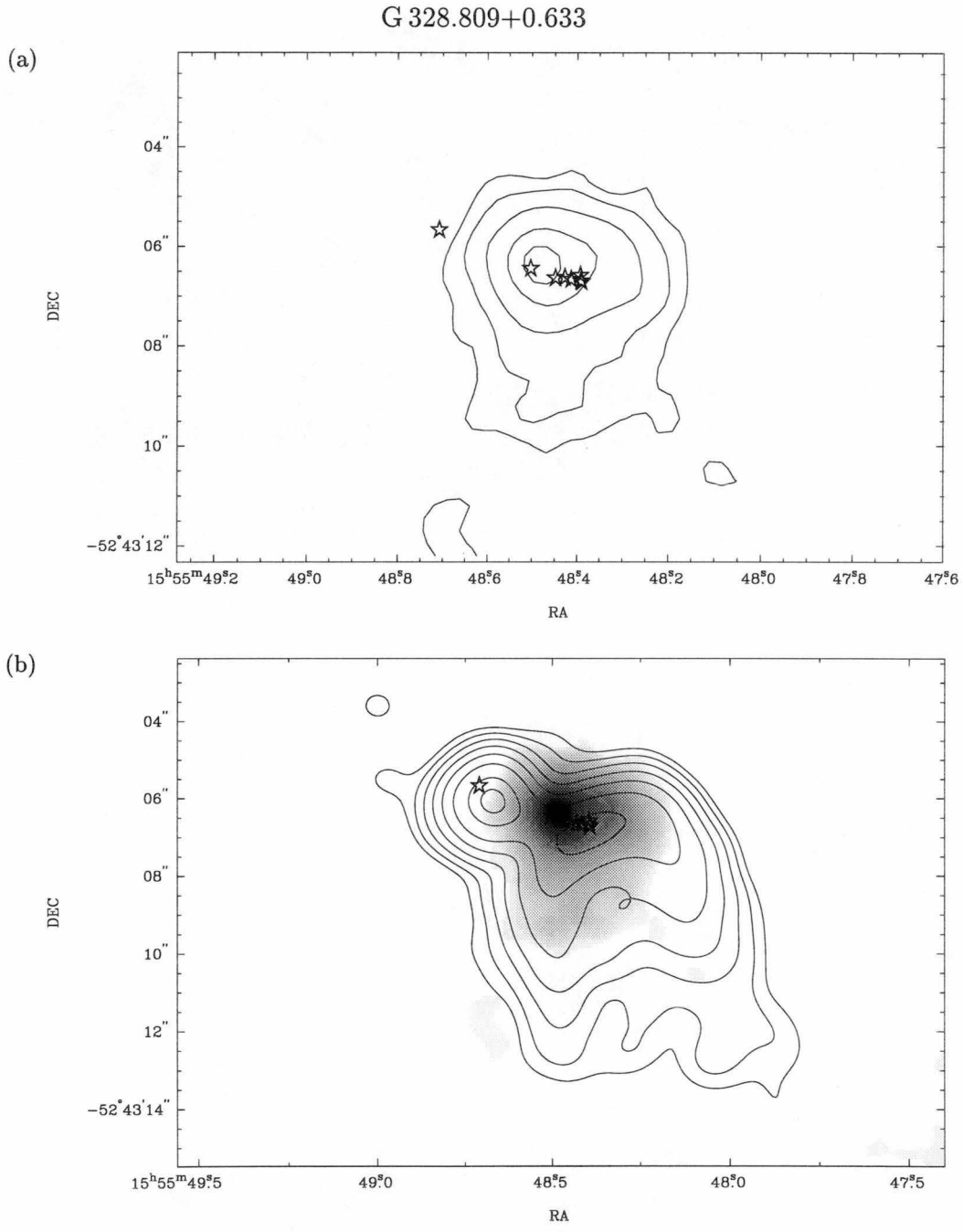

Figure 3.6: (a) The 11.5 μm emission associated with the methanol maser G 328.809+0.633. The position of the maser components are marked by stars. The contour levels are at 8, 16, 32, 64 and 90 percent of the peak flux density. The integrated flux density is 6.4 Jy. (b) The 11.5 μm (grey-scale) and UCHII region (contours) associated with the methanol maser G 328.809+0.633. The contour levels are at -1, 1, 2, 4, 8, 16, 32, 64 and 90 percent of the peak flux density. The maser components are represented by stars.

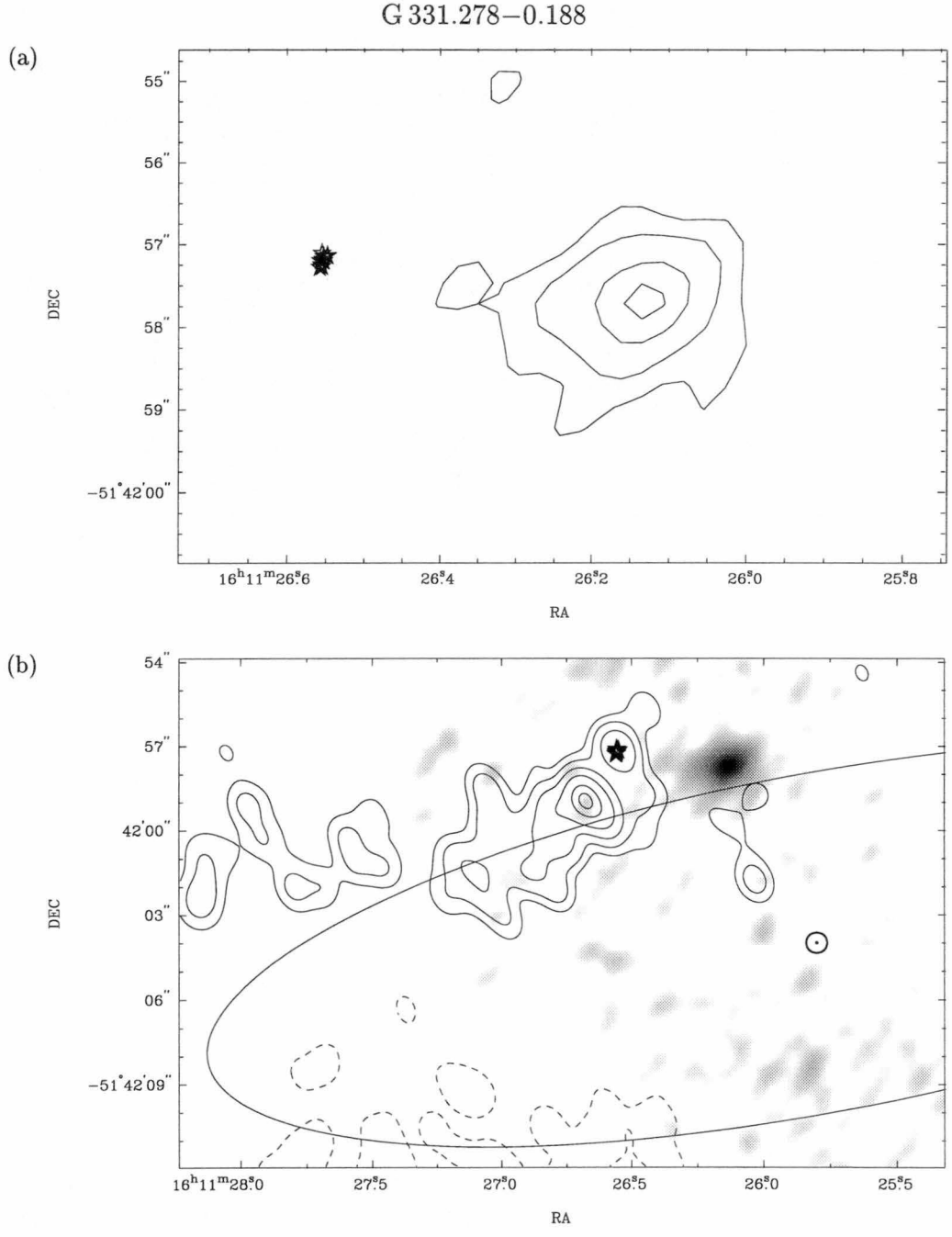

Figure 3.7: (a) The 11.5 μm source associated with the methanol maser G 331.278−0.188. The individual maser components are represented by stars. The contour levels are at 16, 32, 64 and 90 percent of the peak flux density. The integrated flux of the source is 0.8 Jy. (b) The 11.5 μm (grey-scale) and UCHII region (contours) associated with the methanol maser G 331.278−0.188. The contour levels are at -4, 4, 8, 16, 32, 64 and 90 percent of the peak flux density. The maser components are represented as stars. The position of the *IRAS* PSC source 16076-5134 is shown by a circle. The ellipse is the *IRAS* error ellipse.

UNIVERSITY OF TAS LIBRARY

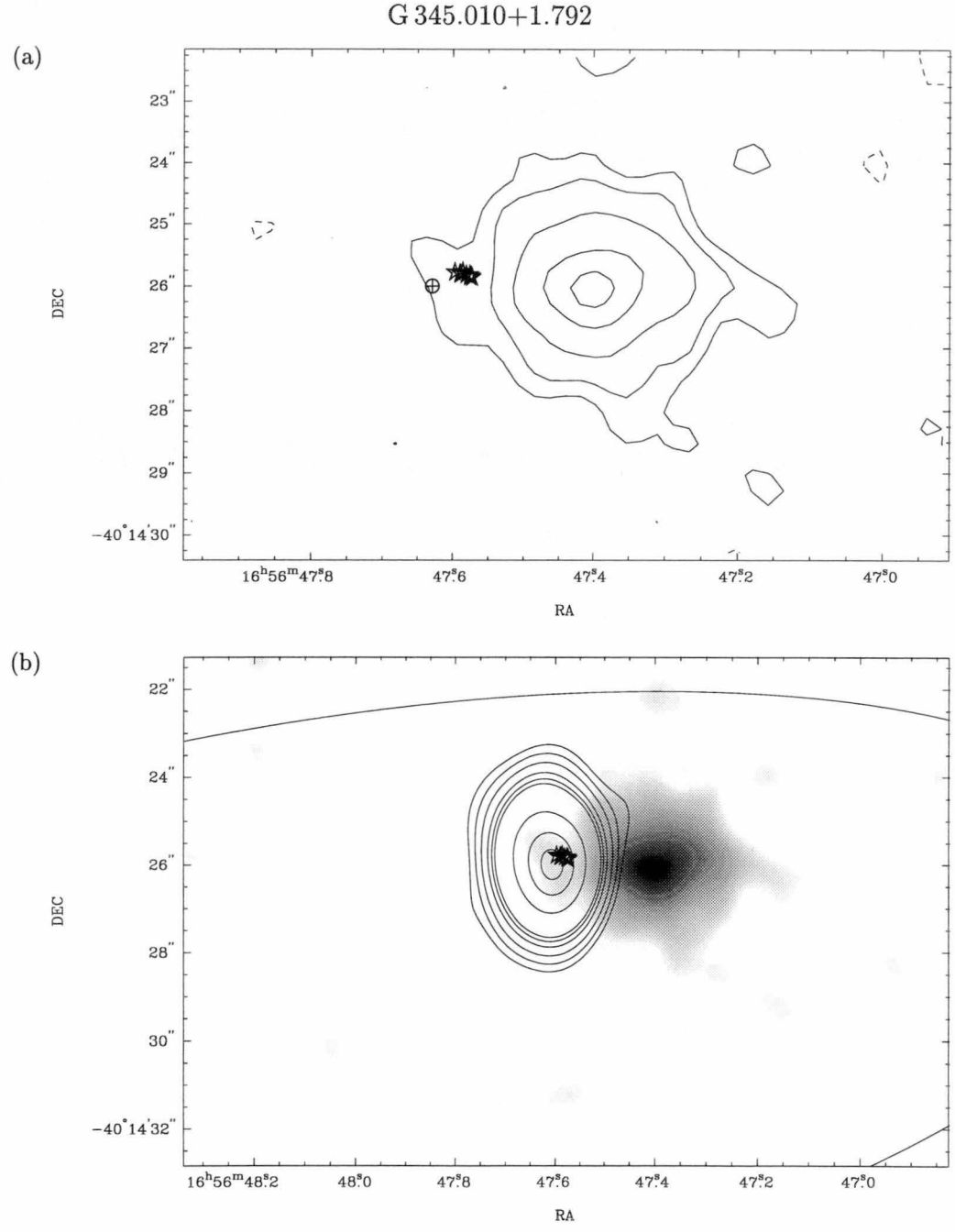

Figure 3.8: (a) The 11.5 μm source associated with the methanol maser G 345.010+1.792. The individual maser components are represented by stars. The contour levels are at -8, 8, 8, 16, 32, 64 and 90 percent of the peak flux density. The integrated flux density of the source is 11.5 Jy. The cross circle shows the position of the NIR source imaged by Testi *et al.* (1997a). (b) The 11.5 μm (grey-scale) and UCHII region (contours) associated with the methanol maser G 345.010+1.792. The contour levels are at -0.5, 0.5, 1, 1, 2, 4, 8, 16, 32, 64 and 90 percent of the peak flux density. The maser components are represented by stars. The partially visible ellipse is the error ellipse of the *IRAS* PSC source 16533-4009.

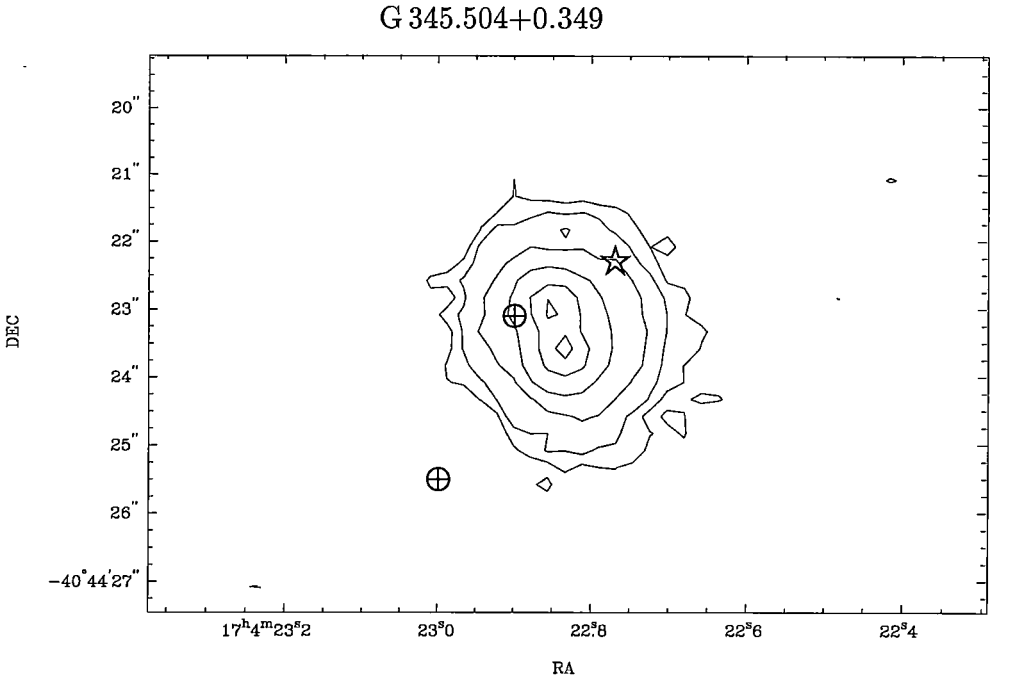

Figure 3.9: The 11.5 μm source associated with the methanol maser G 345.504+0.349. The position of the peak methanol emission is marked by a star (Caswell, 1997). The contour levels are at -4, 4, 8, 16, 32, 64 and 90 percent of the peak flux density. The integrated flux density of the source is 20 Jy. The crossed circles mark the position of the NIR sources imaged by Testi *et al.* (1997a)

east of the others is probably a separate source. Given the small separation of the UCHII regions, it is impossible to know which of the two the MIR source is associated with. For the discussion I have assumed the MIR source is associated with the main methanol emission (Section 3.4). The slight east-west elongation of the source is most likely a result of the misalignment of the chopping secondary. There is no *IRAS* PSC source within 30 arcsec of this source.

G 331.278−0.188

The MIR image of this source is shown in Fig. 3.7, together with the HII emission in the region. The methanol source is offset 4 arcsec east of the MIR source, which has a flux density of 0.84 Jy. From the UCHII images, it is clear that this region is complex, with a number of separate HII regions. It is unclear whether the MIR source is associated with the methanol source, or the HII region 2 arcsec to the south-east. I have assumed the methanol source is associated, as it is closer the observed MIR position. The apparent east-west elongation is a result of the misalignment of the chopping secondary. The position of the *IRAS* source 16076-5134 is 10 arcsec offset from the maser position.

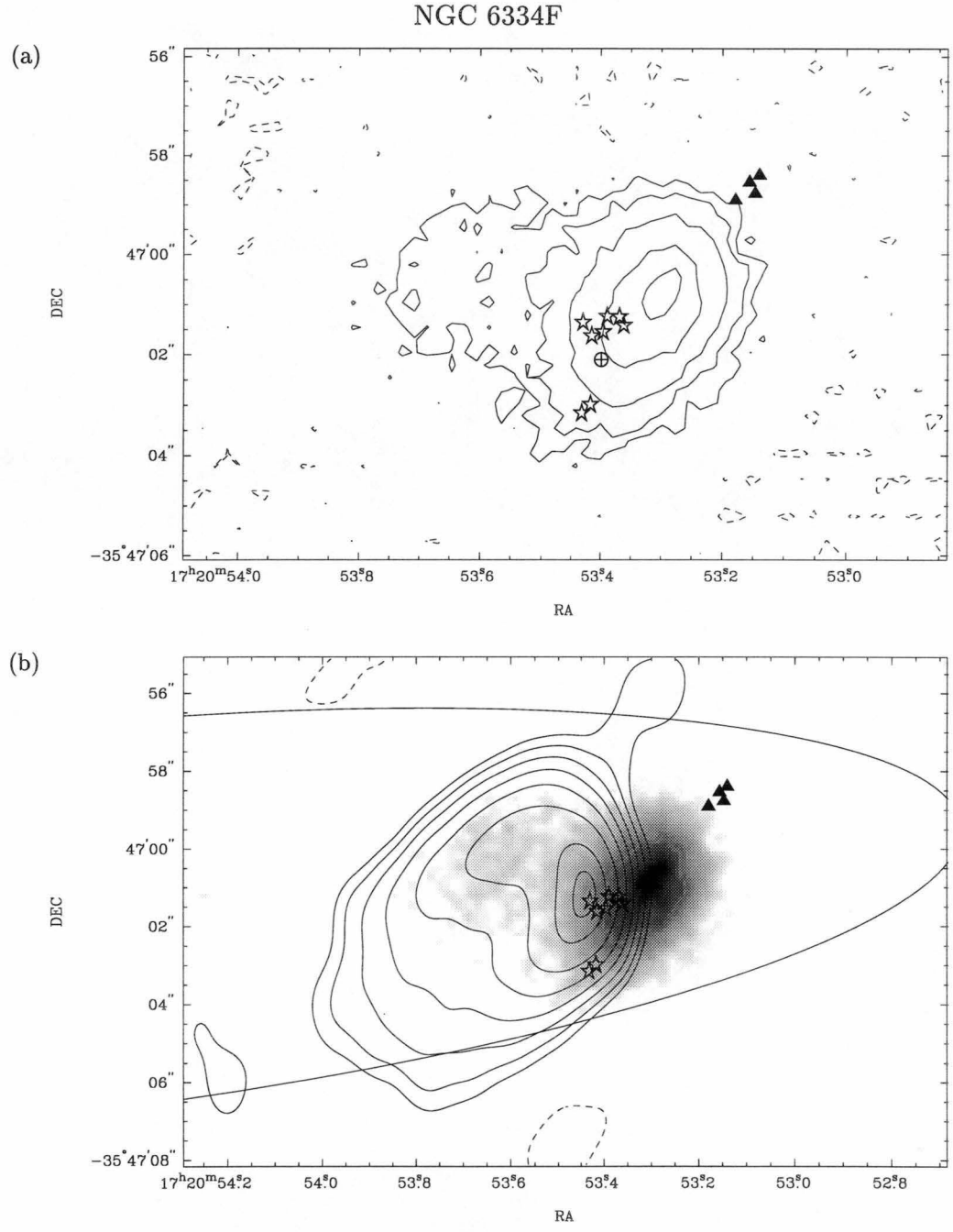

Figure 3.10: (a) The 11.5 μm source associated with the methanol masers in the source NGC 6334F. The individual maser components are represented by stars and triangles. The contour levels are at 1, 2, 4, 8, 16, 32, 64 and 90 percent of the peak flux density. The integrated flux density of the source is 52 Jy. The crossed circle marks the position of the NIR source imaged by Testi *et al.*(1997a). (b) The 11.5 μm (grey-scale) and UCHII region (contours) associated with the methanol masers in NGC 6334F. The contour levels are at -1, 1, 2, 4, 8, 16, 32, 64 and 90 percent of the peak flux density. The maser components are represented by stars and triangles. The ellipse represents error ellipse of the *IRAS* source 17175-3544.

G 345.010+1.792

The MIR image of this source is shown in Fig. 3.8, together with the associated UCHII region. The methanol and UCHII region are offset from the MIR by 2 arcsec, and are assumed to be associated. The MIR source shows a slight extension in the direction of the line of maser components. The maser source is located 8 arcsec from the *IRAS* PSC source 16533-4009.

G 345.504+0.349

The MIR image of this source is shown in Fig. 3.9. There is no detected UCHII region associated with the maser. The single maser position shown in Fig. 3.9 has been taken from Caswell *et al.*(1995d). The MIR source has an unusual double peaked morphology. The *IRAS* PSC source 17008-4040 is located 26 arcsec from the maser source.

NGC 6334-F

The MIR image of this source is shown in Fig. 3.10. This source has by far the brightest IR and UCHII region of all the methanol masers in the sample. Both the UCHII region and the MIR source are quite extended, with a similar morphology. The position of the *IRAS* source 17175-3544 is offset from the maser positions by 17 arcsec. The measured 11.5 μm flux density (846 Jy) is much larger than the *IRAS* flux density of 103 Jy.

3.4 Discussion

3.4.1 Morphology of the MIR sources

One of the aims of these observations was to directly image the disc that may be associated with methanol masers. There is no evidence that any discs have been seen. The extent of the methanol lines is comparable to, or smaller than, the size of the MIR sources detected, so it is possible that the observations do not have enough resolution to image discs even if they are present. This indicates that either the observations do not have enough resolution to resolve the disc or that the observations are sensitive to circumstellar dust around the embedded stars. In either case, the circumstellar disc model of methanol masers cannot be confirmed nor refuted with these observations.

All of the MIR detections are essentially point sources, although a few show some low level extension. For the three sources which show this extension most clearly (G 327.402+0.445, G 328.809+0.633 and NGC 6334-F), it is in the same direction as the extension in the low level UCHII emission. This suggests that the dust is in the same region as the ionized gas of the UCHII region.

Of the nine methanol masers with an associated MIR source, seven also have an associated UCHII region. This is a much higher proportion than the 50 per cent of methanol sources which have an UCHII region association found in Chapter 2. Given the small sample size, the probability of this occurring by chance is 16 per

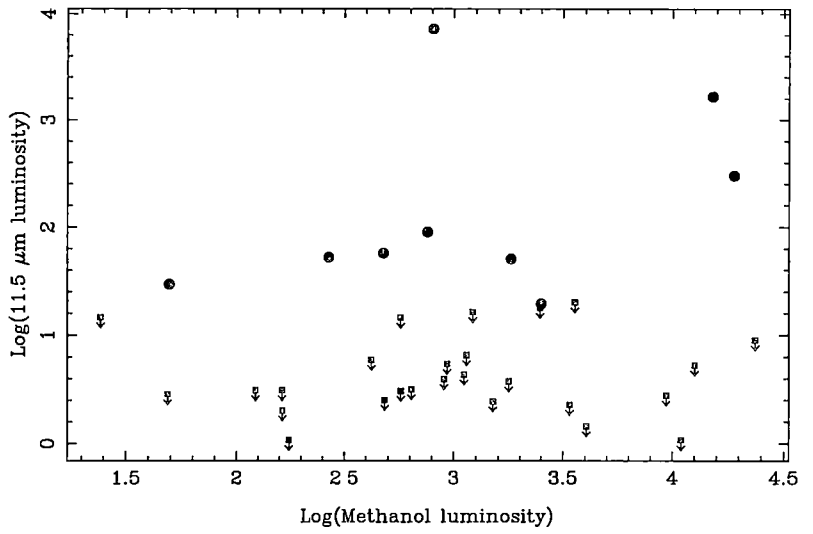

Figure 3.11: Luminosity of methanol versus luminosity of the associated 11.5 μm IR source. The luminosity has been calculated as the flux density times the square of the kinematic distance. The filled circles represent methanol sources with an associated MIR source, while the squares with arrows represent the upper limits of sources with no detected 11.5 μm emission.

cent so the result is not statistically significant. As most of the methanol sources with a MIR associated are also associated with a UCHII region, few, if any, can be pre-main-sequence stars. The simplest explanation for this is that the masers with detected MIR emission represent high-mass embedded stars which are more likely to have an associated UCHII region. A larger sample size is needed to distinguish whether or not most methanol masers with a MIR associations are also associated with an UCHII region.

Because of the large positional errors associated with the IR observations, a meaningful comparison of the position of the methanol masers with respect to the IR emission is not possible.

Class II methanol masers are generally thought to be pumped by IR photons (Sobolev *et al.*, 1997b) from thermal dust at 175 K. Because of the small variability of Class II methanol masers, they are assumed to be saturated. The methanol flux density should then depend on the flux density of the pumping photons. Fig. 3.11 shows a plot of the "luminosity" of the 11.5 μm emission versus the "luminosity" of the methanol. (The luminosity has been calculated simply as the measured flux density times the square of the kinematic distance, in kpc). There is no correlation between the MIR and methanol luminosities. The methanol sources with a MIR association extend over the entire range of luminosities. Similarly sources without an associated MIR source include both the least and most luminous sources. This suggests either that the methanol is not pumped by the 11 μm photons or that the pumping process is limited by some other factor, such as the methanol abundance. This does not rule out methanol being pumped by longer wavelength IR photons.

In Fig. 3.12 the luminosity of the 11.5 μm sources is plotted against the UCHII region luminosity. As both these values depend on the spectral type of the embedded star, a correlation would be expected. If only the sources with detected UCHII

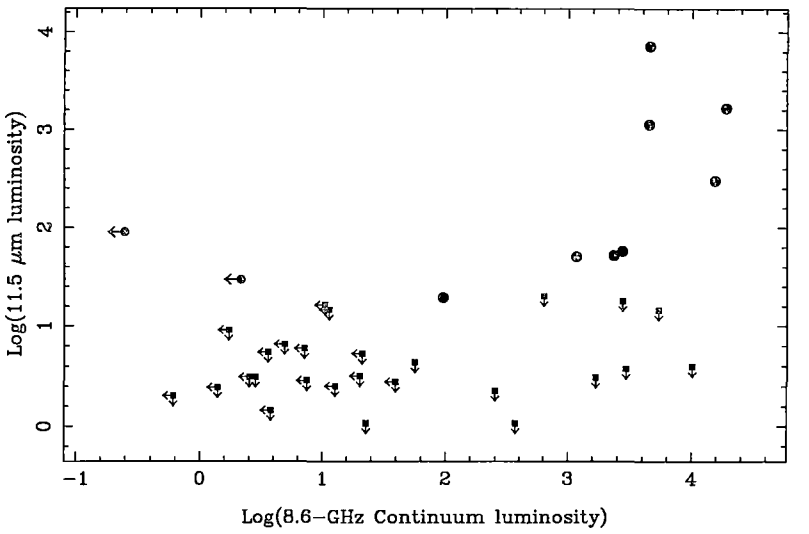

Figure 3.12: Luminosity of UCHII regions associated with methanol masers versus the luminosity of the 11.5 μm IR source. The filled circles represent sources with detected MIR detected emission, while the squares represent sources without any detected emission. The arrows indicate upper limits for both the MIR and UCHII flux density.

and 11.5 μm emission are considered, a weak correlation is seen, but it is not statistically significant. However, there are two sources with relatively strong 11.5 μm luminosities but no detected UCHII region and many bright UCHII regions with no detected MIR sources.

3.4.2 *IRAS* associations

For all the sources in the sample, described in Chapter 2, the *IRAS* PSC catalogue has been searched for entries within 30 arcsec of the maser position. These "associations" are listed in Table 3.1. The 30 arcsec criterion is much smaller than typically used when studying *IRAS* associations of maser and UCHII sources. Many previous comparisons of methanol and *IRAS* sources have used single-dish positions for the masers, which have positional accuracies of the order of an arcminute (Schutte *et al.*, 1993; van der Walt *et al.*, 1995; van der Walt *et al.*, 1996). However the the size of the *IRAS* error ellipse is usually smaller than 30 arcsec. Ellingsen *et al.*(1996b) have shown that there is about a 7 per cent probability of a chance association of an *IRAS* source within 1 arcminute of another object in the Galactic Plane, and 1 per cent chance of a chance association with an *IRAS* source which satisfied the WC criteria. However, these values assume that the *IRAS* sources are randomly scattered within $\pm 0.5^\circ$ of the Galactic Plane, which is not the case. As the associations with UCHII regions have shown, many or all methanol masers are found in regions of massive star formation. As many stars are thought to form in a cluster, simple calculations of association probability fail and the probability of chance associations will increase. A separation of 30 arcsec was chosen arbitrarily as a compromise between the expected errors in the *IRAS* positions and excluding chance associations.

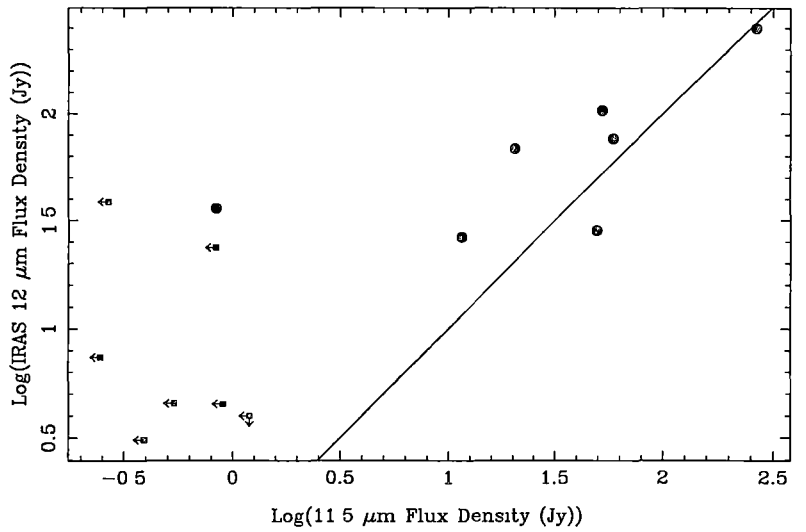

Figure 3.13: *IRAS* 12 μm flux density versus observed 11.5 μm flux density. The straight line indicates equality. Sources with an upper limit for the 11.5 μm observations are indicated by a left pointing arrow, while *IRAS* upper limits are indicated by an arrow pointing downwards.

Of the 48 methanol maser sources in the sample, 21 are within 30 arcsec of an *IRAS* source. Three of these associations have two separate methanol sources within 30 arcsec of the same *IRAS* source. In these cases, if one of the maser sources was found to be associated with a MIR source, it was assumed to be associated also with the *IRAS* source, and the other to have no association.

Fig. 3.13 shows a plot of the *IRAS* 12 μm flux density versus the measured 11.5 μm flux density. For sources with a MIR flux density of greater than about 10 to 30 Jy, the flux densities are roughly the same. For the weaker sources there are many *IRAS* sources with no detected 11.5 μm emission and many 11.2 μm sources with no *IRAS* association. There are are number of reasons why the *IRAS* flux densities may be so different from the current observations.

- The *IRAS* bandwidths are wide with the 12 μm band extending from 8.5 to 15 μm. The flux density changes considerably across the band. However, the colour corrections (which have not been applied) would affect the flux density by less than 10 per cent (Churchwell *et al.*, 1990).

- The *IRAS* beam is quite large and would be sensitive to extended low-surface-brightness emission. For example, a 30×30 arcsec region with a surface brightness of only 20 mJy arcsec^{-2} would have an *IRAS* flux density of 18 Jy. The current observations would not detect this emission. However, this would require a very large region of heated dust, and so is improbable.

- The *IRAS* observations may be contaminated by a number of low luminosity stars. The flux density of these stars would have to be $\lesssim$ 0.5 Jy, otherwise they would be detectable in the 11.5 μm observations. Thus to get *IRAS* flux densities of the order of 10 Jy, twenty of these sources would be required within the *IRAS* beam.

- The *IRAS* beam at 12 μm is 0.75×4.5 arcmin. For an isolated source a position can be measured which is significantly more accurate than the size of the beam. However, in regions with many sources in a small area the observations will become confused and the positions and fluxes will have large errors. This is thought to be the most likely explanation.

The most important implication of this is that *IRAS* sources with flux densities less than about 10 to 30 Jy suffer from source confusion. Because of the larger *IRAS* beam in the 60 and 100 μm *IRAS* bands, source confusion will certainly be worse. However, if the confusion is due to sources with a different spectral index to the dust cocoon around a young massive star, the confusion may be less. For example, at 12 μm there may be many sources detectable (e.g. lower mass stars) while at longer wavelengths the emission may be dominated by a single massive star which have much larger flux densities at 100 μm than at 12 μm. Without high spatial resolution images at these longer wavelengths, it is impossible to know what effect source confusion at these wavelengths will have.

These observations show that source confusion is definitely a problem, and cast some doubt on many of the comparisons of methanol masers (and other molecular emission) to their *IRAS* counterparts. Similarly, calculating the luminosity of an *IRAS* source (and hence the spectral type) will lead to an overestimation. The two sources with detected MIR emission, but no associated *IRAS* source, are most likely a consequence of this confusion.

This brings into question the value of detailed studies of the *IRAS* sources "associated" with methanol masers, or any other specific sources. Generally these studies have assumed *IRAS* sources within 1 to 3 arcminutes of a maser source are associated. Such large difference means there is a large chance of mistaken associations, in addition to the effects of confusion. Clearly the *IRAS* PSC is a powerful way of identifying star-formation regions. However assuming individual *IRAS* sources represent a single embedded star associated with any particular maser source is fraught with uncertainty.

3.4.3 Wood and Churchwell diagram

Following Wood and Churchwell (1989a), sources with an *IRAS* counterpart within 30 arcsec have been plotted in a colour-colour diagram in Fig. 3.14. Most of the *IRAS* associations do lie within the WC criteria region, however the single *IRAS* source (G 308.918+0.123) which lies outside the region is an UCHII region. For this source, confusion is unlikely to be a problem as the *IRAS* 12 μm flux density is the same as the 11.5 μm flux density. This shows that some portion of UCHII regions lie outside the bounds defined by Wood and Churchwell.

There does not seem to be any relationship between the position of the sources on the WC diagram and whether or not 11.5 μm emission was detected. However, there are not really enough sources in this sample for this to be significant. The sources without a detected UCHII region seem to cluster around a narrow range on the $\log_{10}(F_{25}/F_{12})$ axis. Sources in this position of the WC diagram have a flatter spectrum and are therefore hotter than sources towards the upper-right. The Kolmogorov-Smirnov test found no statistical difference between the the F_{25}/F_{12}

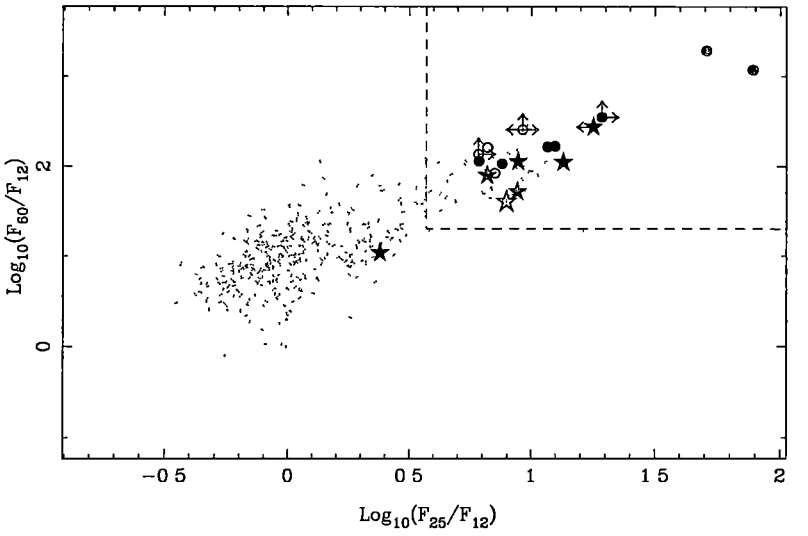

Figure 3.14: Colour-colour diagram of methanol sources with a *IRAS* source within 30 arcsec. The stars represent sources with detected 11.5 μm emission and the circles those without. The solid symbols have an associated UCHII region and the hollow symbols do not. The arrows indicate limits in the *IRAS* catalogue. The small dots are the colours of all the *IRAS* sources in the Galactic Plane between latitudes 320-350° and longitude ±0.75°.

values for the two two distributions. This is probably because of the small number of sources, which makes it difficult to draw any firm conclusions. As has been demonstrated in Section 3.4.2, the *IRAS* flux densities are affected by confusion and some of the assumed associations may not be real.

If this is assumed to be a real effect, there are a number of possible causes.

- If the absence of UCHII emission indicates an earlier phase of the embedded star, this would imply that pre-main-sequence sources tend to be hotter than more evolved sources, which seems unlikely.
- If the absence of a detected UCHII indicates the star is less massive, this would suggest smaller stars are hotter, which is also unlikely. However, less massive stars with weak (or no) UCHII regions may have a greater proportion of dust closer to the star, which will be hotter.
- This could be an optical depth effect. More massive stars will be embedded in a large amount of dust, so the optical depth will be larger. This will reduce the flux density at 12 μm more than at 25 μm, giving a larger spectral index. This assumes that the sources without an associated UCHII region are lower mass.
- Sources without an UCHII region may have a lower *IRAS* luminosity (if they are lower mass stars). These would be more likely to be subject to confusion with brighter stars, which are hotter.

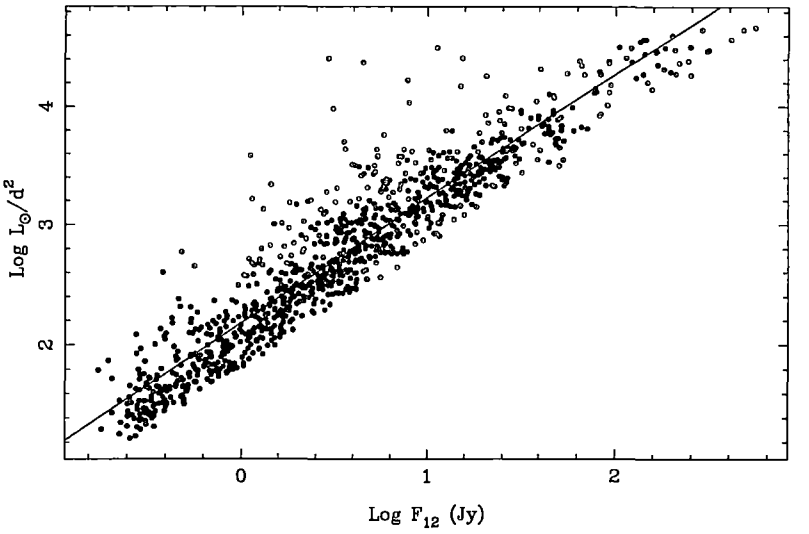

Figure 3.15: The 12 μm flux of *IRAS* sources satisfying the Wood and Churchwell criteria versus the single-star luminosity, divided by the square of the distance to the source. Sources with any upper limits were eliminated. The straight line is the least-squares line of best fit.

3.4.4 Source luminosities

If the *IRAS* flux densities are assumed to come from a single embedded star, then they can be used to estimate the luminosity of the star (assuming all the luminosity of the star is emitted at IR wavelengths). A portion of the emission will be long-wards of 100 μm and outside the *IRAS* bands. Walsh *et al.* (1997) used the spectra from Chini *et al.* (1986a) which extends to 1300 μm for a handful of sources and estimated that 40 per cent of the luminosity from an embedded star is outside the *IRAS* bands. This factor has been used to estimate the luminosity of all sources (Table 3.1). Due to source confusion in the large *IRAS* beam, these values will almost certainly be overestimates, and in some cases the luminosity of a star not associated with the methanol.

Ideally, an estimate of the luminosity could be made from the 11.5 μm flux density measurements which do not suffer from confusion. As the bulk of the emission from embedded stars is at a wavelength longer than 11.5 μm, a direct estimation of the luminosity is not possible. The shape of the spectrum of embedded stars does not change much from one source to another (Chini *et al.*, 1986a; Wood and Churchwell, 1989a), so in principle it should be possible to produce a template spectrum which can be scaled to fit the 11.5 μm flux density. This was attempted, using all *IRAS* PSC sources which satisfy the WC criteria, excluding sources with any upper limits. To test this template spectrum, the 12 μm flux density of the WC sources were used to estimate the *IRAS* single-star luminosity and these values compared to the luminosity calculated using all the *IRAS* bands. The extrapolated luminosities significantly underestimated the "true" luminosity.

Fig. 3.15 shows a plot of the *IRAS* 12 μm flux density versus the single-star "luminosity" divided by the square of the distance to the source. As there is a strong correlation between the two, the parameters of line of best fit have been used

to estimate the star luminosity from the 11.5 μm flux density. The scatter around the line of best fit amounts to an order of magnitude difference in luminosity, so the values estimated using this technique can only be used as a rough estimate of the true luminosity of the embedded star. The relationship between the spectral type of a star and its luminosity is exponential, so the derived spectral type is less affected by these errors. The 11.5 μm upper limits were also used to estimate an upper limit of the spectral type of the stars.

Seven of the of the 11.5 μm detections have an *IRAS* counterpart within 30 arcsec. For 4 of these sources, the *IRAS* single-star luminosity and the extrapolated 11.5 μm luminosity give the same (or almost the same) spectral type for the embedded star. This indicates that the extrapolation process gives a reasonable estimation of the spectral type, if the *IRAS* counterparts of these sources are (relatively) free of confusion. For the source G 308.918+0.123, the extrapolated luminosity is much larger than the *IRAS* luminosity. This source is one of the strongest IR sources in the sample and seems to have a flatter spectrum than the average. Only in one case (G 331.278−0.188) is the *IRAS* single-star luminosity much larger than the extrapolated luminosity, which is surprising given the expected source confusion.

The extrapolated luminosity of sources without any detected 11.5 μm emission gives a spectral type less than B3. These limits cannot be accurate as roughly half of the sources have an associated UCHII region, some of which are quite luminous. This suggests that methanol masers must be associated with sources with a significant range of properties, which may have an evolutionary or morphological origin.

3.4.5 MIR associations of methanol masers

It is somewhat surprising that no 11.5 μm source was detected towards most of the methanol sources in the sample. This raises the question as to what is the difference between the maser sources with and without an associated MIR source, and why so few methanol sources have detectable MIR emission? Assuming that all of the stars luminosity is emitted at IR wavelengths, the observations should have detected any embedded stars in the sample with a spectral type B3 or brighter, so it is not because of sensitivity. I suggest a number of possible differences between the sources with and without a detected MIR source.

- Evolution: The presence of MIR emission may represent a different evolutionary stage of the sources. That eight of the ten MIR sources are also associated with an UCHII region indicates that these sources are not pre-main sequence. However, most of the maser sources with an associated UCHII region do not have any detected MIR emission. If evolution is the only difference between these sources, the UCHII regions associated with the older class of objects should be larger. There seems to be no difference in the morphology of the sources with and without an associated MIR source, so evolution is not likely to be a significant effect.

- Mass: the presence of detectable MIR emission may simply be a direct reflection of the mass of the embedded star. If this is the case, the sources with brighter IR emission should also have brighter UCHII regions. Fig. 3.12 shows that there is a weak correlation between the MIR and UCHII luminosities. Many of the bright UCHII regions are not associated with MIR sources, which contradicts this. However, as mentioned in section 2.6.1, the UCHII flux density depends on a variety of factors, such as the absorption of UV photons by dust.

- Optical Depth: if the regions around the embedded stars were optically thick at 11.5 μm then the observed luminosity of the sources at this wavelength would depend critically on the extinction, which may vary with source size and evolution. Optical depth is generally not thought to be a problem at wavelengths longer than approximately 7 μm (Chini *et al.*, 1986b; Churchwell *et al.*, 1990).

- Source Structure: the presence of 11.5 μm emission may indicate a quantity of dust closer to the embedded star which is warmer. This could be an evolutionary effect, or indicate a difference in the geometry of the source. Hillenbrand *et al.*(1992) suggest that the IR excess from Herbig Ae/Be stars implied the presence of a circumstellar accretion disc. However, there is no real evidence that the linear sources from a maser sample are preferentially associated with MIR emission.

3.4.6 Spectral class calculations

Fig. 3.16 plots the relative spectral class of the embedded stars as calculated from the *IRAS*, 11.5 μm and UCHII flux densities. Upper limits are indicated by arrows. The *IRAS* and 11.5 μm spectral types have been calculated assuming all the luminosity of the star is emitted at IR wavelengths.

The most striking feature of these plots is the lack of correlation. This is most likely a result of the many assumptions that go into these calculations (such as the effect of dust on the UCHII region, confusion for *IRAS* sources and the extrapolation used for the 11.5 μm observation).

However, there are a few notable features of these plots. On the *IRAS* versus 11.5 μm plot, the spectral type of all the stars with no MIR limit is remarkably constant (O8 to O6). This is probably due to confusion towards lower spectral type stars which are less luminous. The *IRAS* versus UCHII region plot supports the earlier claim (Section 2.6.1) that the spectral type derived from the UCHII regions are an under-estimate, while the *IRAS* spectral types are overestimates with an average difference of 2 to 3 spectral sub-classes. The derived spectral type from the UCHII and 11.5 μm flux density is similar, there are however a large number of UCHII regions with no detected 11.5 μm emission. This would indicate that there must be a range of properties of the regions around the young stars. What these differences are is impossible to say at present, but factors such as evolution, mass and specific environmental factors (e.g. the density of dust or the surrounding molecular cloud) may all play a role.

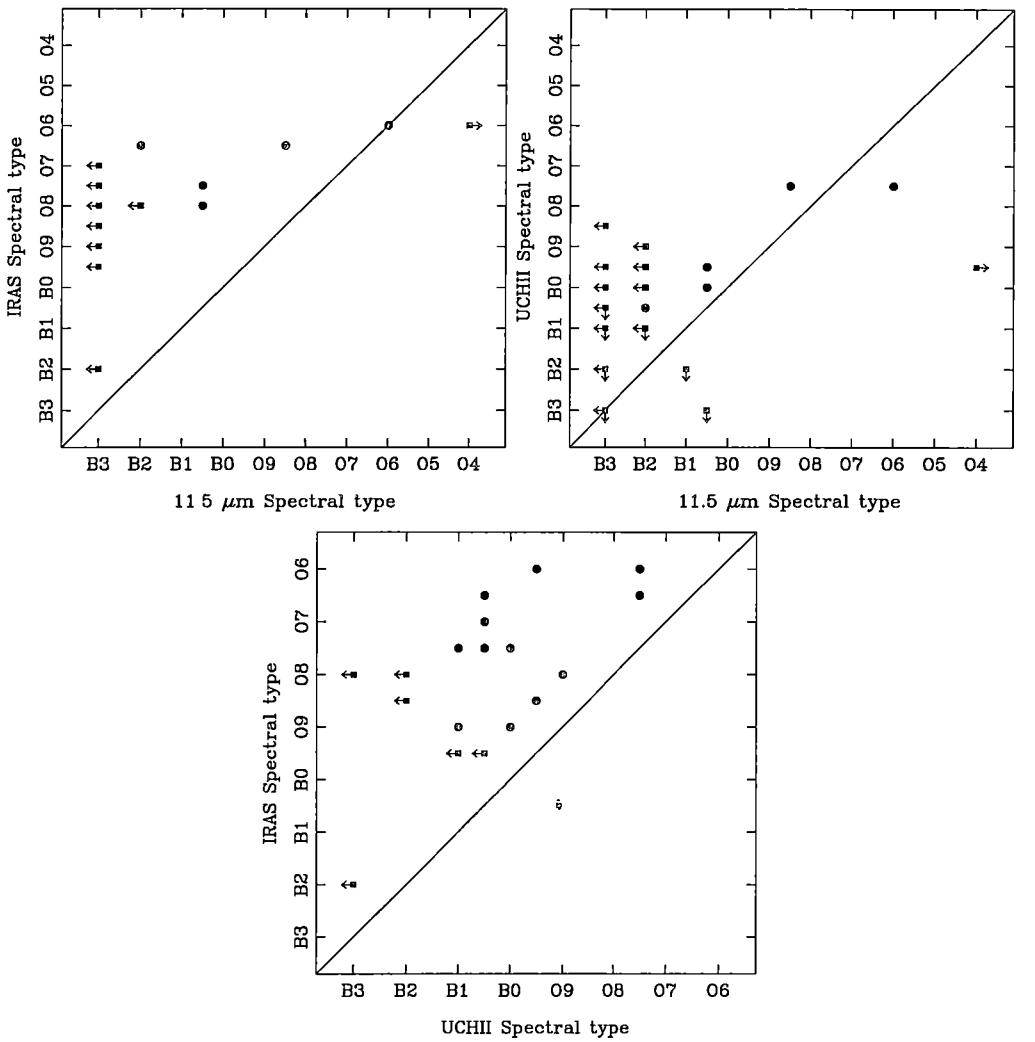

Figure 3.16: The spectral type of the embedded star associated with methanol maser sources. The spectral type has been calculated based on the *IRAS*, UCHII and 11.5 μm flux densities. Upper limits are indicated by arrows.

3.5 Conclusion

Mid-infrared observations at 11.5 μm were made of 35 methanol maser sources in 27 fields. Nine of the masers were found to be associated with a MIR sources, and one MIR source was detected associated with a compact HII region but not associated with any methanol emission. No correlation was found between the luminosity of the methanol sources and the MIR luminosity. A correlation would be expected if MIR photons were responsible for pumping the methanol masers.

None of the MIR detections had a disc structure. Because of large positional errors associated with the 11.5 μm observations, a detailed comparison of the methanol position relative to the MIR source was not possible.

Comparing *IRAS* PSC sources within 30 arcsec of the maser sources and the detected MIR sources demonstrates that the *IRAS* observations suffer from confusion at 12 μm, particularly for sources with a flux density of less than about 20 Jy.

This confusion is likely to be worse at longer wavelengths. This clearly brings into question the value of detailed comparisons of the *IRAS* sources "associated" with maser sources.

The large number of methanol masers without an associated MIR (or *IRAS*) source is surprising, as the observations should be sensitive to embedded stars later than B3. Possible reasons for this include evolution, mass of the embedded star and differences in the environment around the stars.

Comparing the spectral class of the embedded star derived from the 11.5 μm, *IRAS* and UCHII region flux densities shows that these techniques all have large errors associated with them, many spectral sub-classes in some instances.

Chapter 4

Proper-motion of methanol masers

4.1 Introduction

The ATCA observations of the $5_1 \rightarrow 6_0$ A^+ 6.7-GHz transition of methanol (Chapter 2) have shown that it is likely that many of these sources represent edge-on circumstellar discs around young massive stars. Unfortunately, due to the large variety of morphologies seen among the sources, these observations can neither confirm nor refute this model conclusively.

Assuming that the masers do delineate an edge-on Keplerian disc, the maser spots would be expected to exhibit proper-motion. Whatever the detailed kinematics, the 6 km s^{-1} velocity spread typical of the masers would suggest a proper-motion the order of 0.3 milli-arcsec yr^{-1} for a source at a distance of 2 kpc (assuming the line-of-site velocity spread is similar to the transverse velocities). Measuring this with the ATCA is not practical as the relative positions of the individual components can only be determined to, at best, 20 milli-arcsec and it would take in the order of 60 years to detect proper motion, which is probably longer than the lifetime of the components (and a PhD student). Thus in order to measure the proper-motion of some of the maser sources, VLBI observations are needed. Proper-motion observations allow the transverse component of the velocity (perpendicular to the observer) to be measured. The observed Doppler velocity gives the line-of-sight velocity, so the two allow the full three-dimensional velocity of the maser components to be measured. If Keplerian (or some other rotational) motion is detected, this will provide unequivocal evidence that the masers lie in a disc. Even if Keplerian motion is not detected, proper-motion observations will immensely improve our understanding of these interesting objects.

Although VLBI is similar in concept to connected element interferometry, there are a number of important differences. The most obvious difference (for ad-hoc arrays such as the Australian Long Baseline Array (LBA)) is the wide variety of antennas. Each antenna (generally) has different collecting area, receivers, filters etc. This makes the calibration more difficult and less reliable than for a homogeneous array such as the ATCA. As the individual antennas cannot be connected in real time, each antenna has a separate time standard and LO system which must

be corrected for in the calibration. Atmospheric variations are also unrelated, meaning absolute phase measurements cannot be made, unless a phase reference source is observed (which generally is not done). Despite these difficulties, the large separations of the antennas (for even an array of modest size such as the LBA) give resolutions that are not achievable with other observing techniques (at any wavelength).

To date there have been very few published milli-arcsec resolution observations of the 6.7- or 12.2-GHz transitions of methanol. Norris *et al.* (1988) and McCutcheon *et al.* (1988) used the single baseline Parkes-Tidbinbilla interferometer (PTI) to observe the 12.2-GHz $2_0 \rightarrow 3_{-1}$ E transition of Methanol. At 12.2-GHz the fringe spacing of the PTI is ~20 milli-arcsec. The observations of McCutcheon *et al.* consisted of short (<20 minute) scans of eight sources. The correlated amplitude towards all but one of the sources (G 309.921+0.479) were significantly reduced, which they attribute to beating between separate components at the same velocity. Norris *et al.* observed seven sources, typically for about 6 hours, and made the first milli-arcsec images of the 12.2-GHz methanol transition. These were the first observations to see the linear source morphology.

Menten *et al.*(1988; 1992) have made VLBI observations of the 12.2- and 6.7-GHz methanol transitions in W3(OH). The 12.2-GHz observations also showed a reduction in the correlated amplitude (of about 50% compared to the total power spectrum) with a minimum fringe spacing of 6 milli-arcsec. They estimate the component spot size to be less than 2 milli-arcsec and they also attribute the amplitude reduction to blending of spatially separate features. For the 6.7-GHz observations, the measured intrinsic spot size was around 1.4 milli-arcsec (or 3 AU). By comparing the 6.7- and 12.2-GHz maps they found that the positions (and velocities) of the strongest features agreed to within a milli-arcsec.

Ellingsen (1996) used the LBA to image the 6.7- and 12.2-GHz methanol transitions from NGC 6334F and the 12.2-GHz emission from G 335.789+0.174. Comparing the 6.7- and 12.2-GHz observations, Ellingsen found that 5 out of 9 12.2-GHz maser components were coincident to within ~5 milli-arcsec (and in velocity) which is comparable to the relative positional accuracy of the observations. This is in agreement with the earlier observations of W3(OH) by Menten *et al.* and provides a strong constraint for any pumping mechanism for Class II methanol masers. Ellingsen also performed a "spot size" experiment at 6.7- and 12.2-GHz including all the Australian antennas and Hartebeesthoek in South Africa. No fringes were detected to Hartebeesthoek at either frequency, which implies a spot size greater than 0.1 milli-arcsec. These results suggest that the maser spots have a core-halo structure with a halo size of 0.5-1.0 milli-arcsec (10-40 AU) and core size <0.5 milli-arcsec (<10 AU). The only other milli-arcsec resolution observations of the two strong Class II transitions of methanol are the 12.2-GHz observations by Norris *et al.* (1998) of G 309.921+0.479.

Proper-motion studies of of OH and H_2O masers have shown the great power of multi-epoch VLBI observations of masers. Proper-motion observations of H_2O masers towards star-forming regions (Genzel *et al.*, 1981b; Genzel *et al.*, 1981a; Reid and Moran, 1988; Gwinn *et al.*, 1992) and evolved stars (Marvel, 1996)

Table 4.1: The methanol maser sources in the VLBI proper-motion sample.

Source Name	RA (J2000)	Dec. (J2000)	Peak Flux (Jy)	LSR Vel. (km s^{-1})	Dist. (kpc)	Diam. (AU)	Mass ($M_\odot$)
G 309.921+0.479	13:50:41.79	−61:35:10.1	540	−59.6	5.3	4310	7.9
G 318.949−0.193	15:00:55.33	−58:58:42.0	700	−34.7	2.4	2460	11.8
G 323.740−0.263	15:31:45.42	−56:30:50.5	2167	−51.2	3.3	1300	6.1
G 331.278−0.188	16:11:26.57	−51:41:57.1	109	−77.9	4.8	790	1.0
G 337.705−0.053	16:38:29.61	−47:00:35.7	116	−54.7	3.9	5460	72.6
G 339.878−1.252	16:52:04.66	−46:08:34.2	1700	−38.7	3.2	4310	18.0
G 345.010+1.792	16:56:47.58	−40:14:25.9	410	−18.0	2.1	736	5.8
NGC 6334F	17:20:53.37	−35:47:01.3	3300	−10.4	2.4	5450	6.5
NGC 6634F−NW	17:20:53.18	−35:46:59.3	1500	−11.2	2.5	2073	3.7

has done much to elucidate the dynamics of these objects. Comparing the measured line-of-sight velocities with the observed proper-motions allows a geometric estimation of the distance to the source to be made. The star forming region Sagittarius B2 is close to the Galactic centre, allowing Reid *et al.* (1988) to obtain an estimate of the distance to the Galactic centre of 7 ±1.5 kpc. Proper-motion observations of the H_2O megamaser galaxy, NGC 4258, have conclusively shown that the disc surrounding the Galaxy (which can be well modelled with a single VLBI observation) must be warped (Herrnstein *et al.*, 1996; Herrnstein *et al.*, 1997). The proper-motions also allow a distance estimate to be made for the galaxy (7.3 Mpc), which is a purely geometrical estimation (Herrnstein, 1997). This will help calibrate other distance yardsticks, such as Cepheid variables. Proper-motion observations of OH maser spots in W3(OH) (Bloemhof *et al.*, 1992) have shown that the maser spots are in expansion from the UCHII region, ruling out earlier suggestions that they were in a collapsing circumstellar envelope (Reid *et al.*, 1980).

4.2 Source selection

Eight sources were chosen for this experiment, and are listed in Table 4.1. The sources had all been previously imaged at 6.7-GHz using the ATCA and shown to have a linear morphology with a velocity gradient. Preference was given to sources with multiple components and which had strong emission at both 6.7- and 12.2-GHz. Observations of both transitions is important for the following reasons.

- Twice as many maser spots in each source are observed, which will reduce errors in any derived parameters (by approximately $\sqrt{2}$). It also provides a check against spurious results, since the two frequencies ought not be subject to the same systematic errors.
- It will allow us to study further the close association between the two transitions, which will be crucial in improving pumping models.

Many of the H_2O maser proper-motion experiments were hampered by limited secular coverage. The problem is that the H_2O masers are variable, individual

features change brightness by a factor of ten over a few months (Gwinn *et al.*, 1992), and it is necessary to have several measurements of a maser spot spread uniformly over an extended time interval to ensure that the same maser spot is being observed at all epochs. When observing the H_2O masers towards Sagittarius B2, Gwinn *et al.* (1988) found that although around 50 maser spots could be detected at each epoch, only half could be tracked from one epoch to the next.

Temporal variations are not a problem for the majority of Class II methanol sources as they are slowly varying, and are "quasi-periodic" with individual components persisting for many years, despite multiple flares (Caswell *et al.*, 1995a; Macleod and Gaylard, 1996). A sampling interval of one year has been chosen which should adequately cope with the variability of the masers. A sample size of eight was chosen as a compromise between the advantage of a large sample size which increases the chance of detecting unambiguous proper-motion, and the availability of telescope time.

4.3 Observations

The four main LBA antennas (Parkes, Mopra, Culgoora and Hobart) have been used for this experiment. The basic properties of these antenna have been summarized in Table 4.2. None of the Tidbinbilla DSN antennas were used, as they are no longer capable of making 12.2-GHz observations (and have never been equipped with 6.7-GHz receivers). Hartebeesthoek was not used, as the observations of Ellingsen (1996) found no fringes on those baselines. Both left and right circular polarisations were recorded using the S2 VLBI system with a 4-MHz bandwidth. Correlation of the data was performed using the LBA S2 correlator at the ATNF headquarters in Sydney. For the 6.7-GHz data, the correlator was configured to produce 2048 complex cross-correlation channels and the same number of auto-correlation channels. This gives a spectral resolution of 0.17 km s^{-1} after Hanning smoothing. The 12.2-GHz data were correlated using 1024 channels, which gives a spectral resolution of 0.19 km s^{-1}. This is well matched to the 0.5 km s^{-1} width of the individual maser components (Ellingsen *et al.*, 1996b).

For each observing session (12-16 hours), 20 minute observations of four sources were interleaved (giving a cycle time of 1h 20m). Thus to observe all eight sources at both frequencies requires four such sessions each year. Regular (about once every four hours) observations of the extra-galactic sources 1921-293 and 1144-379 were made so that the observatory clock rates and delay offsets could be calibrated.

Four epochs of the experiment have so far been performed over the periods 1994 October 26-29, 1995 July 1-3, 1996 August 11-16, 1997 September 27-30. The 1997 observations have not yet been correlated and are not included as part of this thesis. A brief summary of the first three experiments follows.

October 1994

The day before these observations were scheduled to occur, the main bearing on the Parkes antenna failed, so consequently Parkes could not participate. As well

Table 4.2: The diameter and system equivalent flux density at 6.7- and 12.2-GHz of the four LBA antennas which participated in the VLBI observations.

Antenna	Diameter (m)	SEFD 6.7-GHz (Jy)	SEFD 12.2-GHz (Jy)
Parkes	64	150	300
Hobart	26	800	1000
Mopra	22	1000	1700
Single ATCA	22	1300	3000
Phased ATCA	5×22	400	-

as significantly reducing the u-v coverage of the experiment, this also reduced the sensitivity of the experiment, because Parkes is by far the most sensitive antenna in the array. This is particularly important at 12.2-GHz as both Mopra and the single ATCA antenna have only room temperature receivers. The receivers on the ATCA antenna are linearly polarised, so they need to be converted to circular polarisation using a "hybrid". This was not done perfectly, so that the cross-polarisation was about 20 per cent. This resulted in a slight amplitude reduction on all cross-correlations to this antenna.

July 1995

The second epoch of this experiment was observed after less than one year, because of the failure of Parkes in the first experiment. No data were recorded from the ATCA due to a recording failure, again reducing the observations to a three baseline experiment. However, the sensitivity and position of Parkes makes these data more useful and reliable than those of the first epoch. Due to time pressures on Parkes, only three sessions of observing were allocated. All eight sources were observed at 6.7-GHz, but only four at 12.2-GHz.

August 1996

All four antennas worked successfully for this experiment. At 6.7-GHz five of the ATCA antennas were used in a phased array , significantly improving the sensitivity of this VLBI element. Only one of the ATCA antenna is equipped with a 12.2-GHz receiver, so a phased array could not be used at this frequency.

4.4 Data reduction

After correlation, the data were calibrated and imaged using the *AIPS* and Difmap packages. The antenna based delay and fringe rates were initially calculated using the *AIPS* task FRING on the continuum calibrators PKS 1921-293 and PKS 1144-379. These values were extrapolated and applied to the spectral line sources. PKS 1921-293 was also used to determine the antenna-based bandpass shape. Normally the autocorrelations are used to do this for spectral line VLBI, but this does not permit any phase corrections to be made. As the phase varied by about 10-20

degrees across the bandpass, a full complex bandpass correction was performed using the cross-correlations.

Amplitude calibration was performed using the auto-correlations by comparing the auto-correlation spectra at each antenna with a template spectrum to obtain the relative gain with time (*AIPS* task ACFIT). This allows amplitude corrections to be made on a relatively short time scale (4 minutes) and, in principle, corrects for antenna pointing errors as well. Because the system temperature measurements for the antennas were either unreliable or impossible to obtain, absolute amplitude calibration was made by comparing the spectrum peak flux density with previous single-dish observations. This is adequate, as the sources are not very variable.

Next, the task FRING was used again on a single strong spectral channel of each of the program sources to improve the fringe rate calculation. The delay value cannot be calculated from the maser sources (as the individual components are essentially mono-chromatic), so the delay value derived from the continuum calibrator was used.

The phases were calibrated using phase self-calibration (assuming a point source model) on the same channel used for FRING and applying the corrections to all the channels. A six second integration time was used. Often, phase-referencing is used rather than self-calibration for calibrating the phases. This assumes that the reference feature is unresolved and subtracts the phase of the reference feature from the rest of the channels. It was decided to use self-calibration for two reasons:

- self-calibration more easily allows the data to be averaged before the corrections are applied. Phase-referencing is applied to the individual samples (2 seconds) and so increases the thermal noise in each channel (except the reference channel). As the smallest phase variations were over a time scale of 20 seconds or more, six second averaging reduces the thermal noise in the calibration.

- phase-referencing is applied to each baseline while self-calibration is antenna-based using a least squares technique. This makes self-calibration more robust especially as the reference features were typically slightly resolved.

The Difmap program was then used to image the reference feature and improve the phase self-calibration. For a few of the sources, a second weak component was found close to the main emission. Where possible, amplitude self-calibration was also performed, with a careful check that the amplitude corrections were sensible. Once the calibration was thought to be satisfactory, a few separate channels were imaged to check for artifacts that erroneous self-calibration may have caused.

The data were finally averaged into Stokes I and imaged in *AIPS* using the IMAGR task. A low resolution spectral line cube was first made (without any of the long baselines to Hobart) to identify where the emission from each channel came from. A high resolution image was then made for each channel separately, with tight "clean-boxes" around identified emission. The high resolution images were made small (256×256 with a pixel size of 1 milli-arcsec) to conserve computing resources so it is possible that some emission would have been missed if it was not identified in the low resolution images. The positions of the maser components

were measured by fitting two-dimensional Gaussian profiles to the images using the task JMFIT. As the emission from individual components typically spanned a number of channels, the measured positions were grouped and averaged (weighted by the signal to noise ratio for each image). Channels with poor SNR, or for which two close components were confused, were discarded.

Because of the scale of this project (in effect, 44 separate VLBI observations), not all the correlated data have been processed yet.

A subsample of the data has been processed, to check that the experiment is viable with respect to the relative positional accuracy obtained. The 6.7-GHz data has been processed for the sources G 318.949−0.193, G 339.878−1.252, G 345.010+1.792 and NGC 6334F from the August 1996 observations, as well as the 6.7- and 12.2-GHz observations for G 309.921+0.479 from the October 1994 observations. The sources G 345.010+1.792 and G 339.878−1.252 have been imaged at multiple epochs.

4.5 Results

The VLBI imaging results of the sources are presented below, together with the spectra of the source and the v-a diagram. The spectra correspond to the integrated flux density of the 2-D Gaussian fitted to the image data when the positions of the components were measuring.

4.5.1 G 309.921+0.479

The ATCA image of G 309.921+0.479 shows a curved source with a linear velocity gradient (Chapter 2. The VLBI image of this source is shown in Fig. 4.1, and a close-up of the northern components is shown in Fig. 4.2. It has been imaged at both 6.7- and 12.2-GHz using the October 1994 data, while the rest of the sources in this section have been imaged at 6.7-GHz only, using the August 1996 data. Because the ATNF S2 correlator was still under development when the data were correlated, the LCP and RCP polarisations had to be correlated separately at 6.7-GHz. The 6.7-GHz data used for Fig. 4.1 uses only the RCP. (The was data was the first correlated, and the LCP and RCP were correlated separately due to limited correlator capacity. However there are no tasks in *AIPS* to combine two polarisations. The data has since been re-correlated). The 12.2-GHz data uses an average of LCP and RCP. The data from this epoch has since been re-correlated, which will allow the two polarisations to be combined more easily.

This source has been interpreted by Norris *et al.* (1993; 1998) as a single source with a curved morphology. However, the current data suggest that it may be comprised of two separate sources. In particular:

- the maser components form two distinct groups, which separately are linear.
- the 12.2-GHz emission is only present in the northern group.

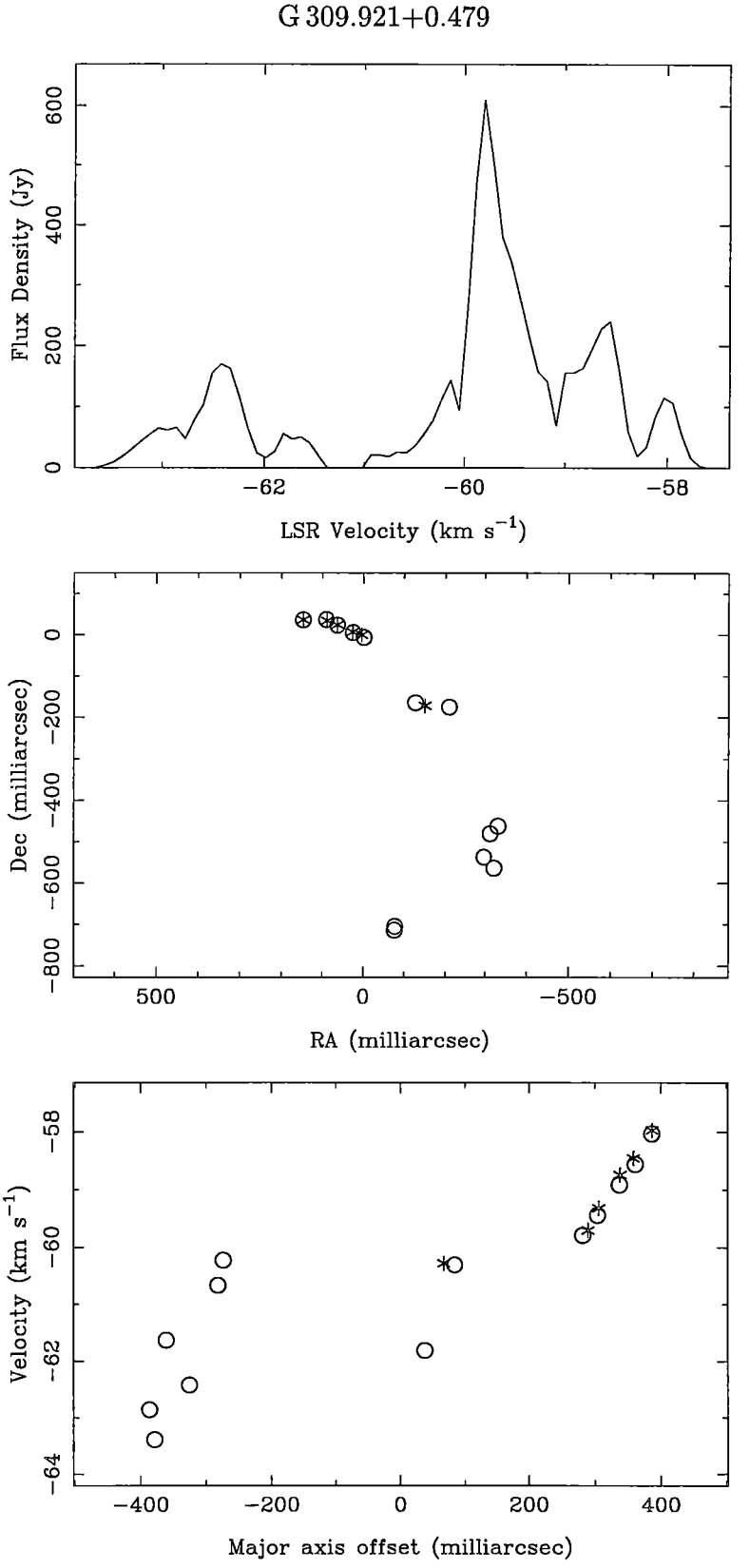

Figure 4.1: From top to bottom: spectrum, map and v-a diagram for G 309.921+0.479. The open circles represent the positions of the 6.7-GHz components, while the stars represent the 12.2-GHz components.

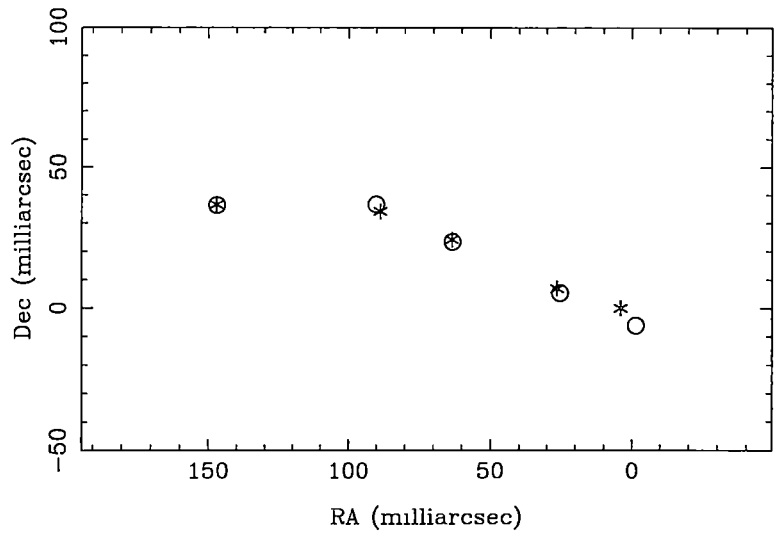

Figure 4.2: The northern section of the G 309.921+0.479 in more detail. Symbols are the same as in Fig. 4.1.

- the velocity profile across the source and the v-a diagram have slightly different velocity gradients. The v-a diagram for the two separate groups is shown in Fig 4.3.

If the two clusters do represent two separate maser sources, then the presence of the 12.2-GHz emission in one of the sources, but not the other, may indicate different conditions in the masing regions around the two stars. If proper-motions are detected towards this source, they would be quite different depending on whether there are one or two sources present.

Four of the 12.2-GHz components are coincident with a 6.7-GHz component spatially and in velocity (Fig. 4.2). The average offset between the components is 1.45 milli-arcsec and the maximum offset is 2.9 milli-arcsec. This is comparable to the expected accuracy of the observations.

Comparison with the ATCA observations

Fig. 4.4 shows a detailed comparison of the VLBI and ATCA observations (Chapter 2). The component comparison is given in Table 4.3. The overall morphology and velocity profile of the source is the same for the two observations. The ATCA positions of the components 'B', C', 'D', 'I' and 'J' all align closely with the VLBI positions, with a mean offset of 10 milli-arcsec and a maximum offset of 17 milli-arcsec. No VLBI component was found in the positions of the ATCA component 'A', probably because its flux density is only 1 Jy. The ATCA component 'F' is a blend of two separate components with similar flux densities, and it is roughly at the centroid of the two. The positions of the components 'E', 'G' and 'H' have offsets between 55 and and 155 milli-arcsec. The offsets are towards other components with a similar velocity, and so are probably due to slight blending.

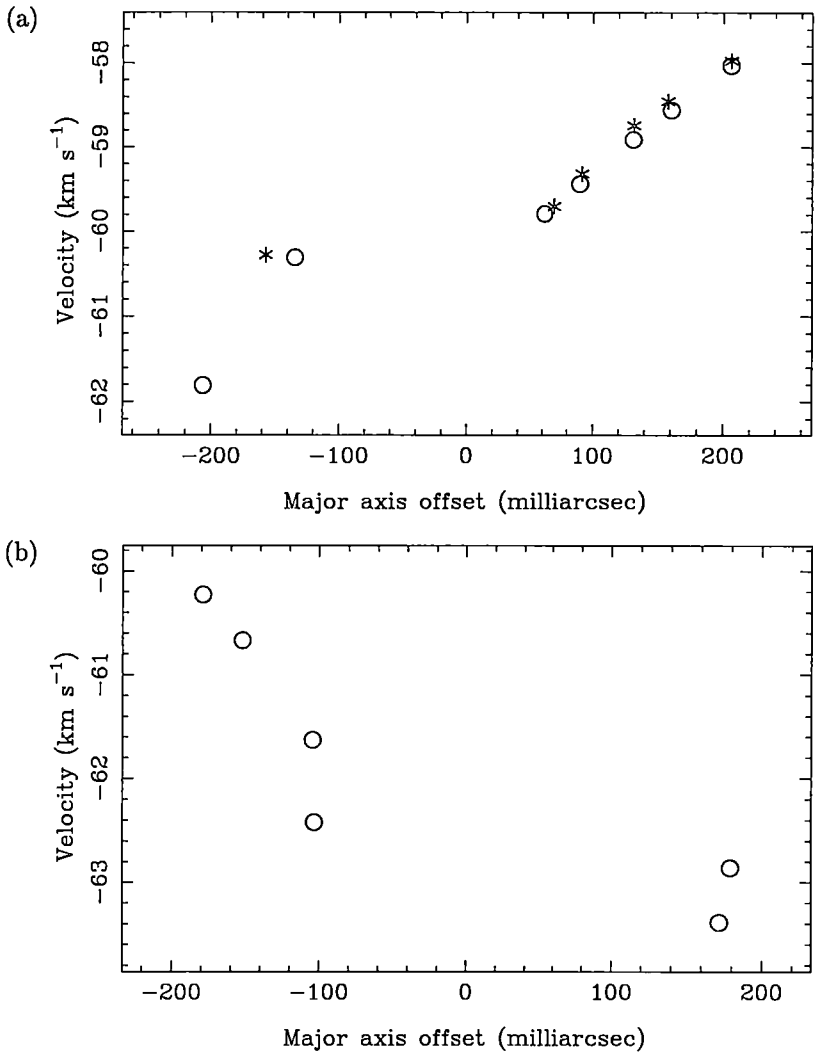

Figure 4.3: v-a diagrams of the northern and southern sections of G 309.921+0.479, calculated separately. Symbols are the same as in Fig. 4.1.

Table 4.3: Detailed comparison of ATCA and VLBI positions for G 309.921+0.479.

Component	Flux Density (Jy)	Velocity (km s^{-1})	Positional Offset (milli-arcsec)
A	1.3	−54.20	-
B	88.5	−57.78	8.4
C	188.4	−58.47	9.4
D	289.4	−59.26	10.5
E	540.2	−59.61	82.0
F	264.5	−60.23	167.6
			193.3
G	69.8	−60.76	85.1
H	69.1	−61.62	153.8
I	153.7	−62.33	16.6
J	62.8	−63.18	3.4

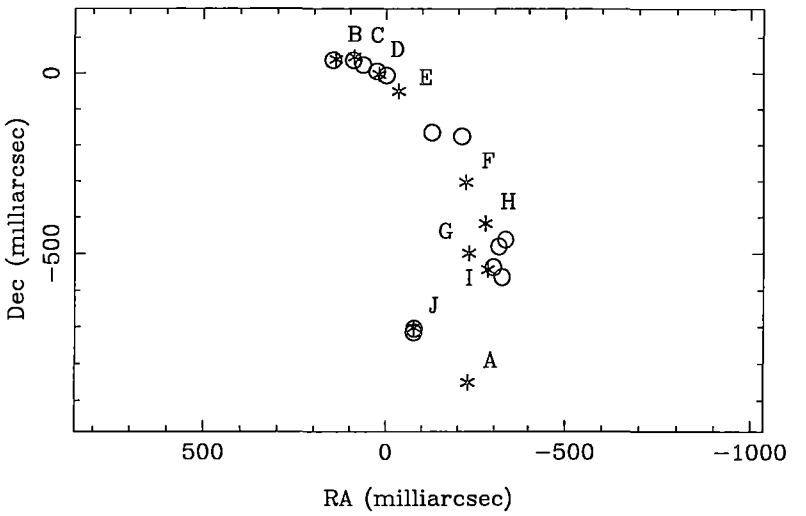

Figure 4.4: Comparison of VLBI positions (open circles) and ATCA positions (stars) for G 309.921+0.479.

4.5.2 G 318.949−0.193

The ATCA image of G 318.949−0.193 is linear with a velocity gradient (Norris *et al.*, 1993). The source has an unusual spectral morphology, with a single strong component with a peak flux density of 700 Jy, while the flux density of other components is less than 100 Jy. The current VLBI image is shown in Fig. 4.5. The source has a curved morphology. The v-a diagram shows the source has a velocity trend along the curve, though the individual components have a large amount of scatter from a straight line. It is worth noting that all the stronger components are in the central region of the curve which is quite straight. The curved nature of this source can be explained if we assume an inclined disc with a relatively high internal turbulence to explain the large scatter in the v-a diagram.

Comparison with the ATCA observations

Fig. 4.6 shows a detailed comparison of the VLBI and ATCA observations (Norris *et al.*, 1993). The component comparison is given in Table 4.4. A number of the components ('C', 'D' and 'G') have very similar positions (with offsets less than 10 milli-arcsec). The components 'A' and 'B' have quite large offsets (>200 milli-arcsec) because they are a blend of two separate features. The components 'E' and 'F' are each slightly blended with the other and have offsets of around 90 milli-arcsec. For this source the average offset in the ATCA positions is quite large, although the overall morphology of the source is the same. The VLBI observations have detected many more, mainly weak, components. These extra components reveal the curved morphology, while the ATCA observations show only a linear source.

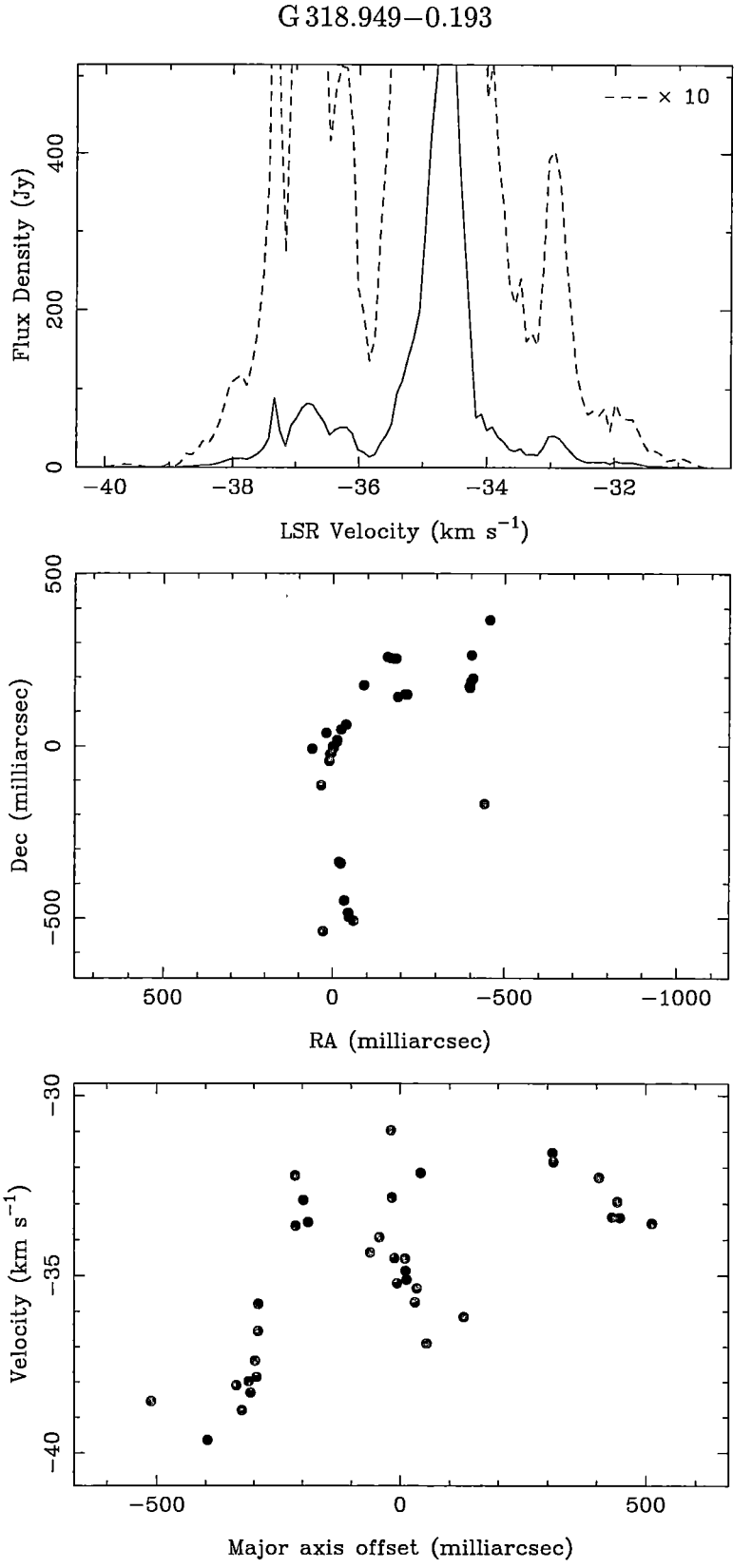

Figure 4.5: From top to bottom: spectrum, map and v-a diagram for G 318.949−0.193.

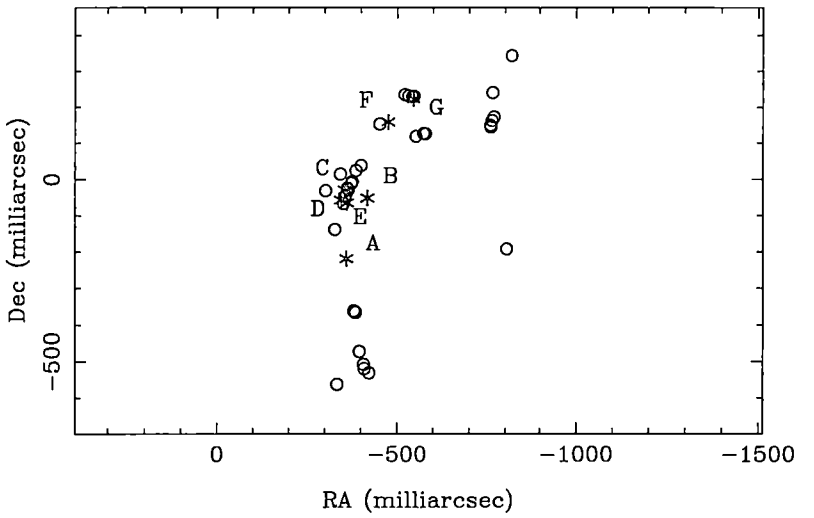

Figure 4.6: Comparison of VLBI positions (open circles) and ATCA positions (stars) for G 318.949−0.193.

Table 4.4: Detailed comparison of ATCA and VLBI positions for G 318.949−0.193.

Component	Flux Density (Jy)	Velocity (km s^{-1})	Positional Offset (milli-arcsec)
A	11.4	−32.90	234.5
	15.1		304.4
	3.6		388.9
B	5.8	−33.50	207.4
	2.4		517.5
	2.3		236.4
C	112.7	−34.70	31.1
	303.6		9.5
	223.3		9.6
D	71.0	−35.40	14.4
E	35.8	−36.20	81.2
F	57.7	−36.70	92.0
G	20.0	−37.30	8.0

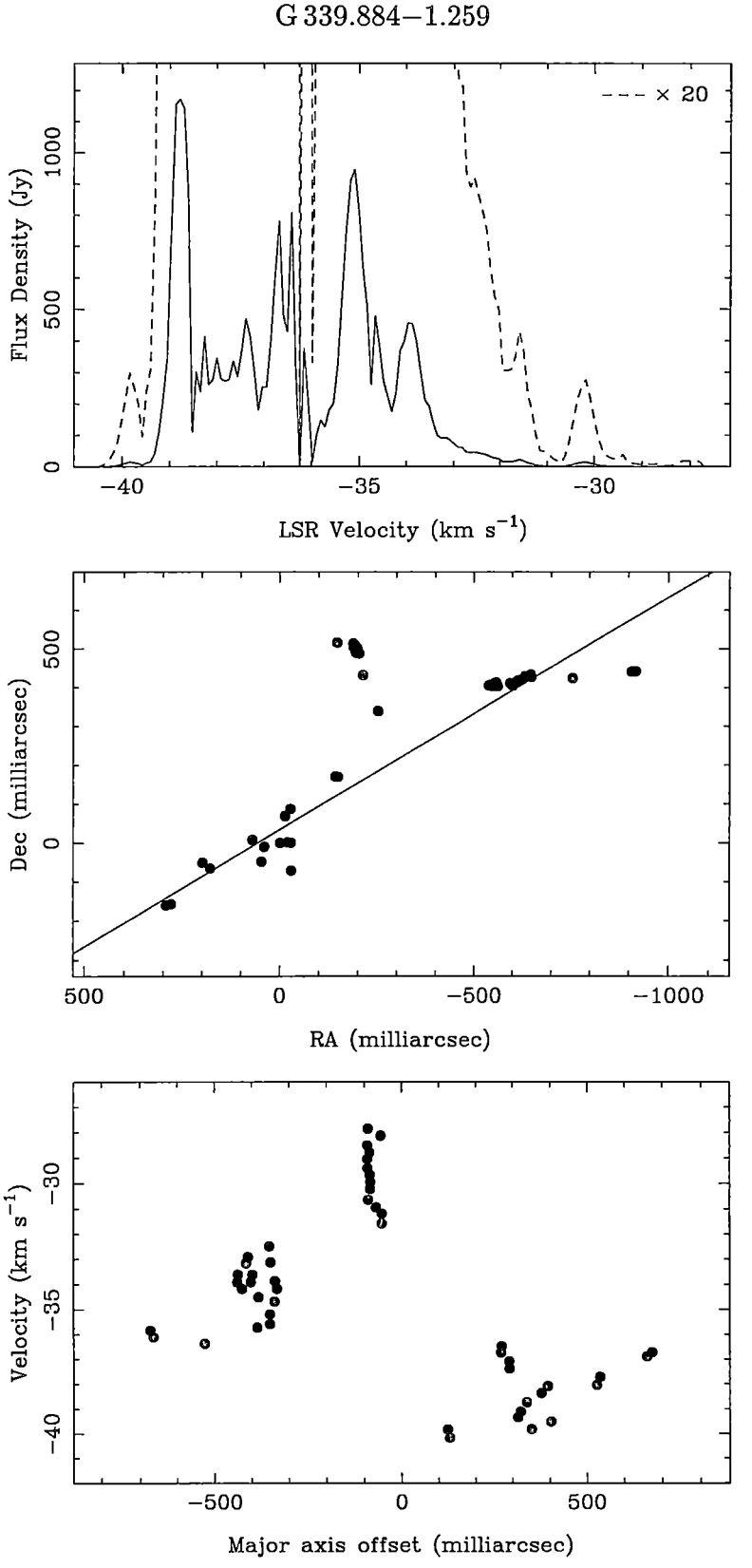

Figure 4.7: From top to bottom: spectrum, map and v-a diagram for G 339.884−1.259.

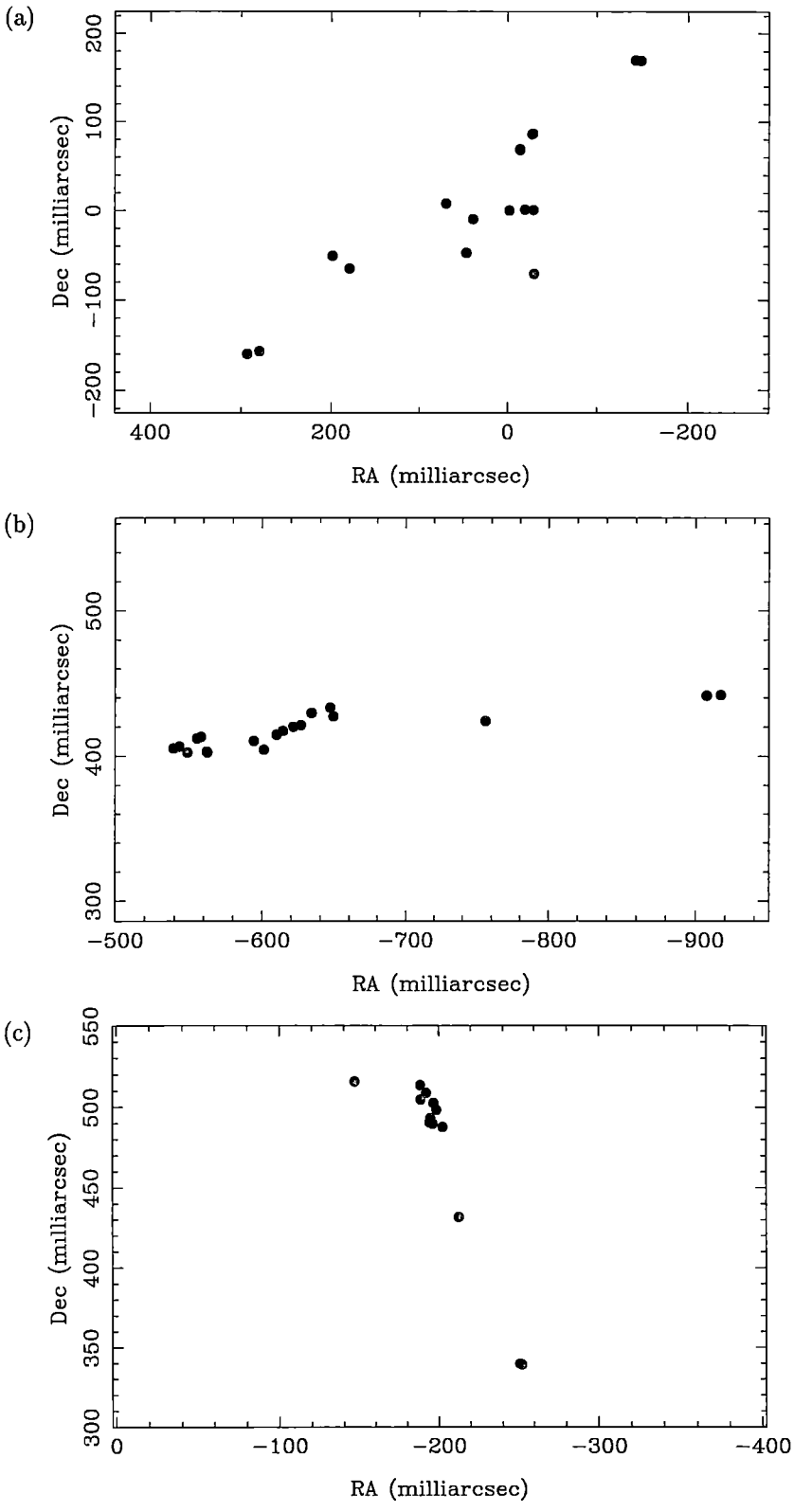

Figure 4.8: Close-up of the (a) eastern, (b) western and (c) northern clusters of G 339.884−1.259.

4.5.3 G 339.884−1.259

ATCA observations of this source (Norris *et al.*, 1993; Ellingsen *et al.*, 1996a) show a linear source (with linear velocity gradient) aligned with the centre of a largely unresolved UCHII region having a peak flux density of 5.6 mJy. The VLBI images of the 6.7-GHz methanol transition are shown in Fig. 4.7, together with the v-a diagram and spectrum. Fig. 4.8 shows the three clusters in more detail. The spectrum has been obtained from the integrated flux obtained when the two-dimensional Gaussian fits were made to the individual components.

The morphology of the source is quite complex. The source is comprised of three main regions. The east and west clusters form a line, though the v-a diagram shows that there is not a velocity gradient along the line. The two clusters are separated in velocity by 4 km s^{-1} and can be divided into separate quadrants of the v-a diagram which, as explained in Section 4.7.1, would be expected if the maser components emanated from a range of radii within a disc.

The northern cluster of masers is slightly surprising. These are blue shifted by about 4 km s^{-1} from the other components and are perpendicular to the line formed by the other two clusters. This cluster was not detected by Norris *et al.* (1993), presumably because they did not image the full velocity range. This blue-shifted emission is seen in Parkes single dish observations (Caswell *et al.*, 1995c). If we interpret the other two clusters as delineating an edge-on disc, then a natural interpretation is that the blue shifted components represent an outflow region. A detailed view of this region (Fig. 4.8) show that the maser components are tightly confined to a line with a well defined velocity gradient (though the v-a diagram is is not perfectly linear). Alternatively, the blue shifted components could represent a disc, while the components detected by Norris *et al.* represent outflow. If either of these scenarios are correct, this poses serious problems for the circumstellar disc model, as it discounts our main reasons for dismissing outflow models as an explanation of linear sources a we would expect a collimated outflow to have a wide velocity range, while low velocity outflow would be extended (as we have already discussed in Section 2.6.2).

A simpler model is that the three clusters are two separate sources, that happen to be aligned by chance. The ATCA observations (Chapter 2) have demonstrated that these regions of star-formation are quite complex with many separate sources. It is then not surprising to see two separate sources aligned so closely. If any proper-motion is detected towards this source, the true dynamics of the source will become clearer.

Comparison to the ATCA observations

Fig. 4.9 shows a comparison of the ATCA observations of G339.884-1.259 (Norris *et al.*, 1993) and the current VLBI observations. The most striking differences between the two observations are the number of extra components found using VLBI. The missing blue shifted components from the ATCA observations are unlikely to be due to any fundamental weakness of the ATCA observations, as the full velocity range was probably not imaged by Norris *et al.*A detailed comparison of the the ATCA components and the corresponding VLBI components (based on

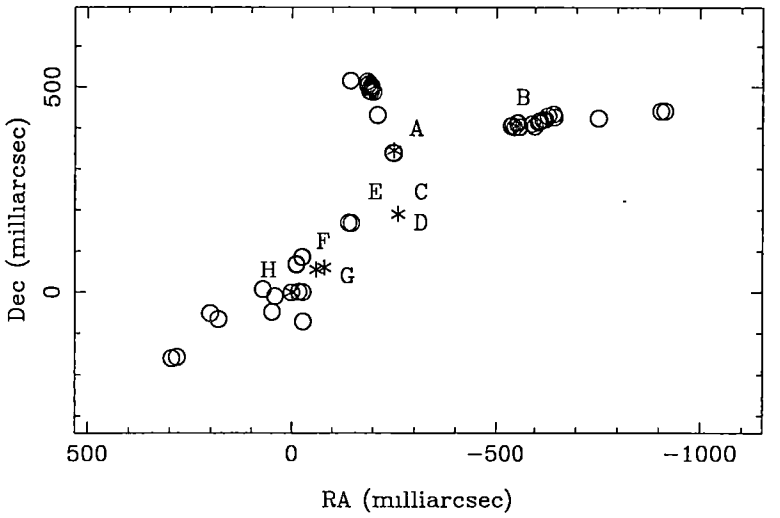

Figure 4.9: Comparison of VLBI positions (open circles) and ATCA positions (stars) for G 339.884−1.259.

Table 4.5: Detailed comparison of ATCA and VLBI positions for G 339.884−1.259.

Component	Flux Density (Jy)	Velocity (km s^{-1})	Positional Offset (milli-arcsec)
A	15.2	−31.60	6.6
B	37.4	−32.60	9.4
C	114.4	−34.10	454.3
	64.3		350.4
D	161.7	−34.70	356.0
E	660.7	−35.20	367.3
F	81.7	−36.70	416.0
	306.6		46.0
G	376.6	−37.40	68.9
H	777.5	−38.70	1.2

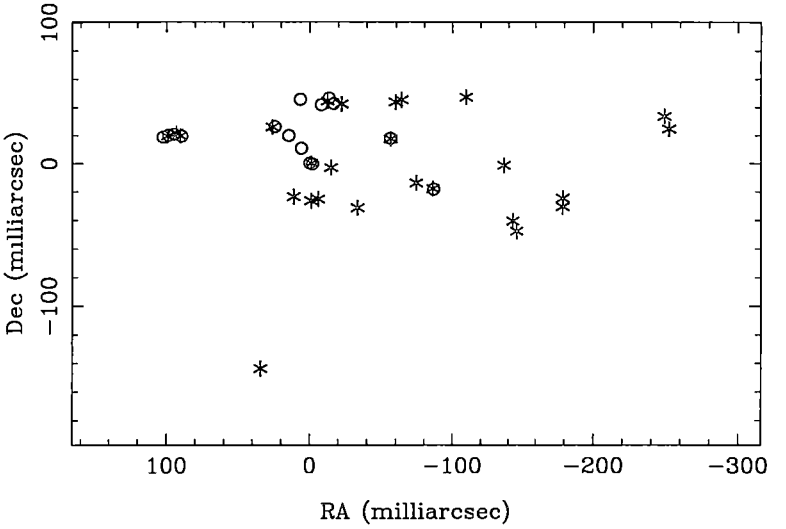

Figure 4.10: Positions of the 6.7-GHz (stars) and 12.2 GHz (open circles) maser components in G 345.010+1.792.

the velocity) is shown in Table 4.5. The (ATCA) components 'A', 'B', 'F', 'G' and 'H' are all close to the corresponding VLBI components with an average offset of 30 milli-arcsec. The components C-E all have a positional offset of around 350 milli-arcsec. It is difficult to explain why these three components all have such large offsets, as there is no evidence in the VLBI image of a second component at the same velocity but at a different position. It is exceedingly unlikely that a variable second component exists, as it would have to have a flux density of around 500 Jy, and the VLBI detection limit is of the order of a few Jy.

4.5.4 G 345.010+1.792

ATCA observations of G 345.010+1.792 show a slightly thickened line with a linear velocity gradient (Norris *et al.*, 1993). The line of masers is associated with the centre of an UCHII region with a peak flux density of 180 mJy beam^{-1}. Fig. 4.11 shows the VLBI image of this source, along with the spectrum and v-a diagram. The morphology of the source is best described as elongated (rather than linear), however, the v-a diagram shows a tight correlation of velocity with major axis offset. This may indicate that the source is inclined with-respect to the line of sight. The weak offset feature to the south is not present in the October 1994 nor in the July 1995 observations. This could either be due to a change in the flux density of the component, or because the earlier observations had less sensitivity. The source has been observed by Ellingsen *et al.*(1997) at 12.2-GHz using the VLBA. A comparison of the 6.7-GHz and 12.2-GHz VLBI is shown in Fig. 4.10. Eight of the maser components have coincident emission at 6.7- and 12.2-GHz. The average offset between the two transitions is 1.1 milli-arcsec and the maximum offset is 2.1 milli-arcsec.

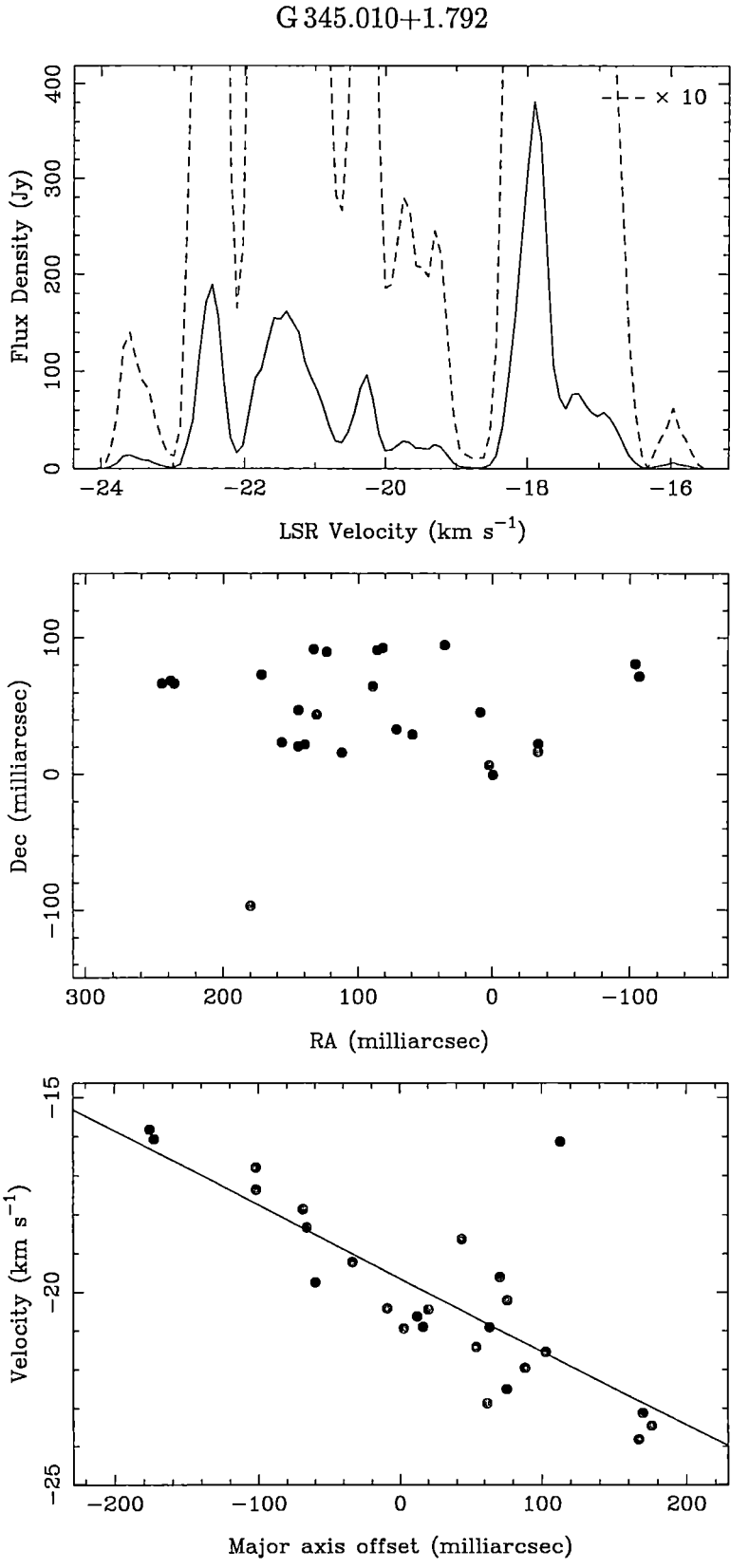

Figure 4.11: From top to bottom: spectrum, map and v-a diagram for G 345.010+1.792.

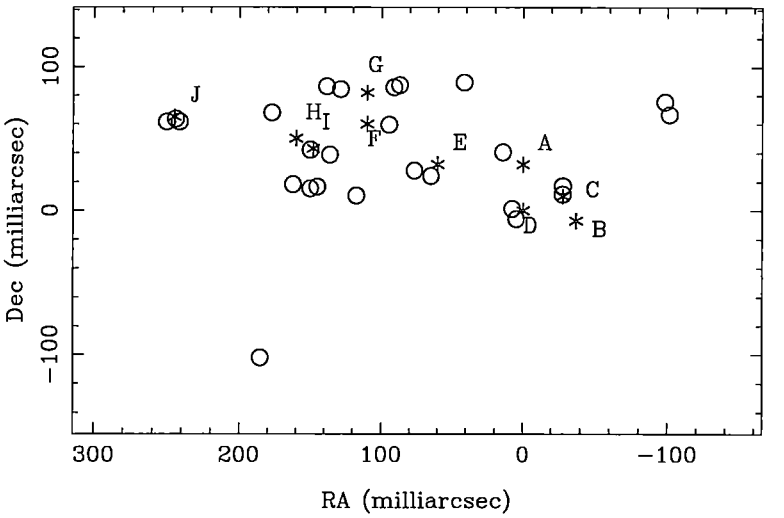

Figure 4.12: Comparison of VLBI positions (open circles) and ATCA positions (stars) for G 345.010+1.792.

Table 4.6: Detailed comparison of ATCA and VLBI positions for G 345.010+1.792.

Component	Flux Density (Jy)	Velocity (km s^{-1})	Positional Offset (milli-arcsec)
A	2.5	−16.00	107.5
	0.4		228.7
B	35.6	−16.80	25.9
C	62.9	−17.40	1.3
D	295.8	−17.90	7.6
E	12.9	−19.70	86.5
	7.2		46.4
F	49.3	−20.30	59.9
	43.1		15.3
G	47.3	−21.10	28.9
	16.7		63.5
H	106.2	−21.80	24.9
I	183.2	−22.40	2.2
J	4.2	−23.70	5.0

Comparison with the ATCA observations

Fig. 4.12 compares the ATCA observations of this source (Norris *et al.*, 1993) with the current VLBI observations. A detailed comparison of the points is shown in Table 4.6. The components B, C, D and I are all associated with a single VLBI component and have an average offset of only 10 milli-arcsec. The other components have two (or more) individual components at the same velocity, and the ATCA positions are at a position roughly midway between the points. Even so, the positional offsets of many of these blended components is less than 50 milli-arcsec.

4.5.5 NGC 6334F

The NGC 6334F source is a well studied region of massive star formation. The 6.7- and 12.2-GHz methanol masers in the source have been imaged using VLBI by Ellingsen (1996). The source comprises three clusters of masers, the central and southern cluster associated with the edge of a cometary compact HII region with a integrated flux density of 2.7 Jy. The north-west component is not associated with any detectable continuum emission. The current VLBI image of the the source is shown in Fig 4.13, with close-ups of the three clusters shown in Figs. 4.14 and 4.15. Ellingsen (1996) found that five of the nine detected 12.2-GHz components were coincident (to within 4 milli-arcsec) with a 6.7-GHz component.

Comparison with the ATCA observations

Fig. 4.16 shows a comparison of the VLBI data with the ATCA data. A detailed component comparison is shown in Table 4.7. The overall morphology of the source is generally the same in the observations; however a detailed component by component comparison shows that there are quite large positional differences. The ATCA components 'D', 'F', 'G', 'H' and 'J' have positional offsets of 71 milli-arcseconds or less (the mean offset is 43 milli-arcsec) though the offsets for the rest of the components range as high as 300 milli-arcsec. The large positional offsets in the ATCA positions are probably due to the complexity of the source. The size of the source (4 arcsec) is larger than the ATCA synthesised beam, but the three clusters overlap in velocity and so blending is probably quite significant, particularly between the central and southern clusters.

4.6 Oh, When the masers come marching in!

As discussed in Section 4.3, the positions of the components shown in Fig. 4.1 - 4.13, are derived from the average of individual consecutive channels. In principle, we would expect the emission to be coming from the same region in the molecular cloud and so averaging the individual channels will improve the accuracy of the measured positions by (roughly) the square root of the number of channels averaged. Figs. 4.17 and 4.18 is a magnified plot of some of the individual components for the sources G 345.010+1.792 and NGC 6334F before the channels are averaged.

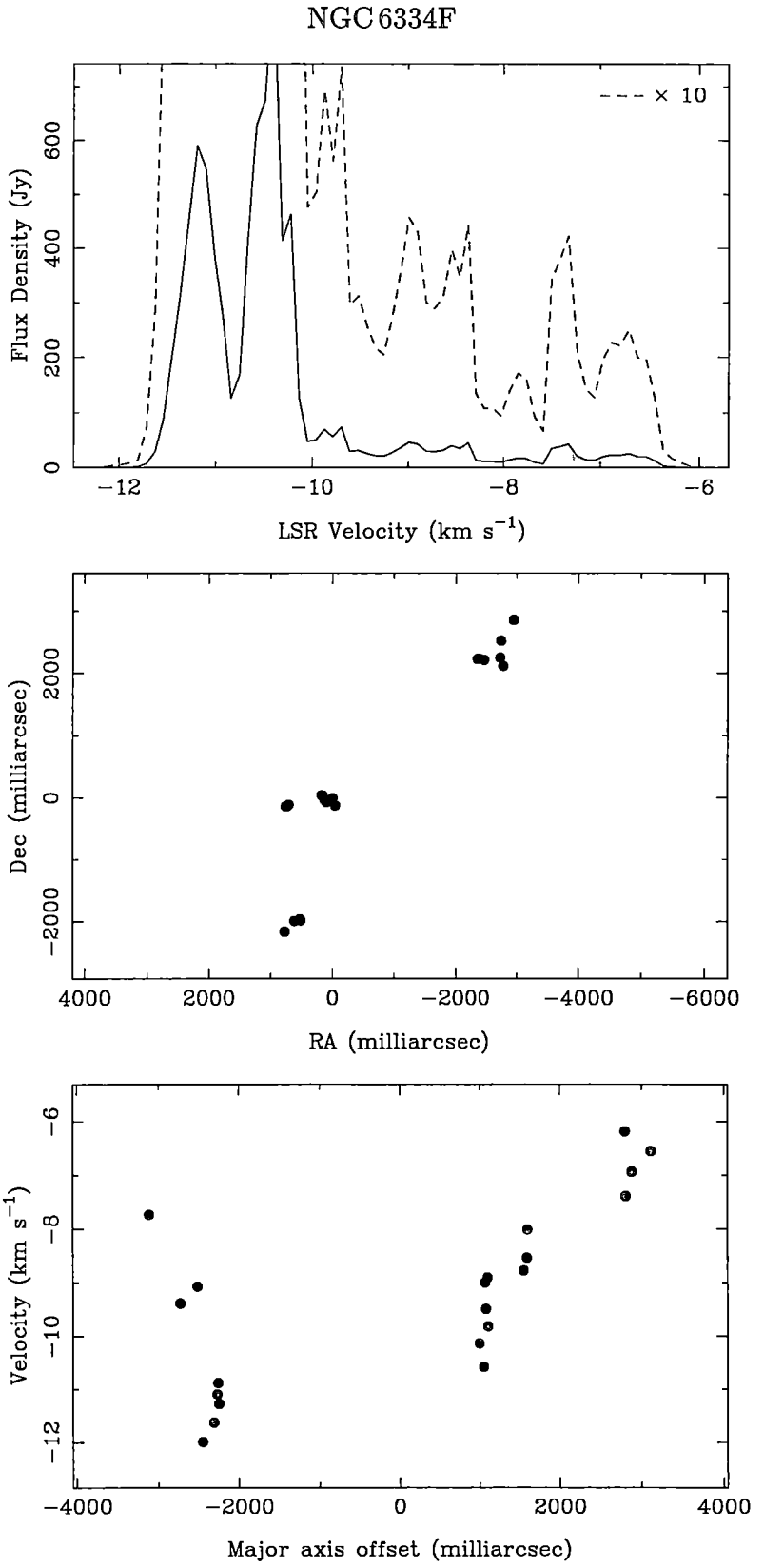

Figure 4.13: From top to bottom: spectrum, map and v-a diagram for NGC 6334F.

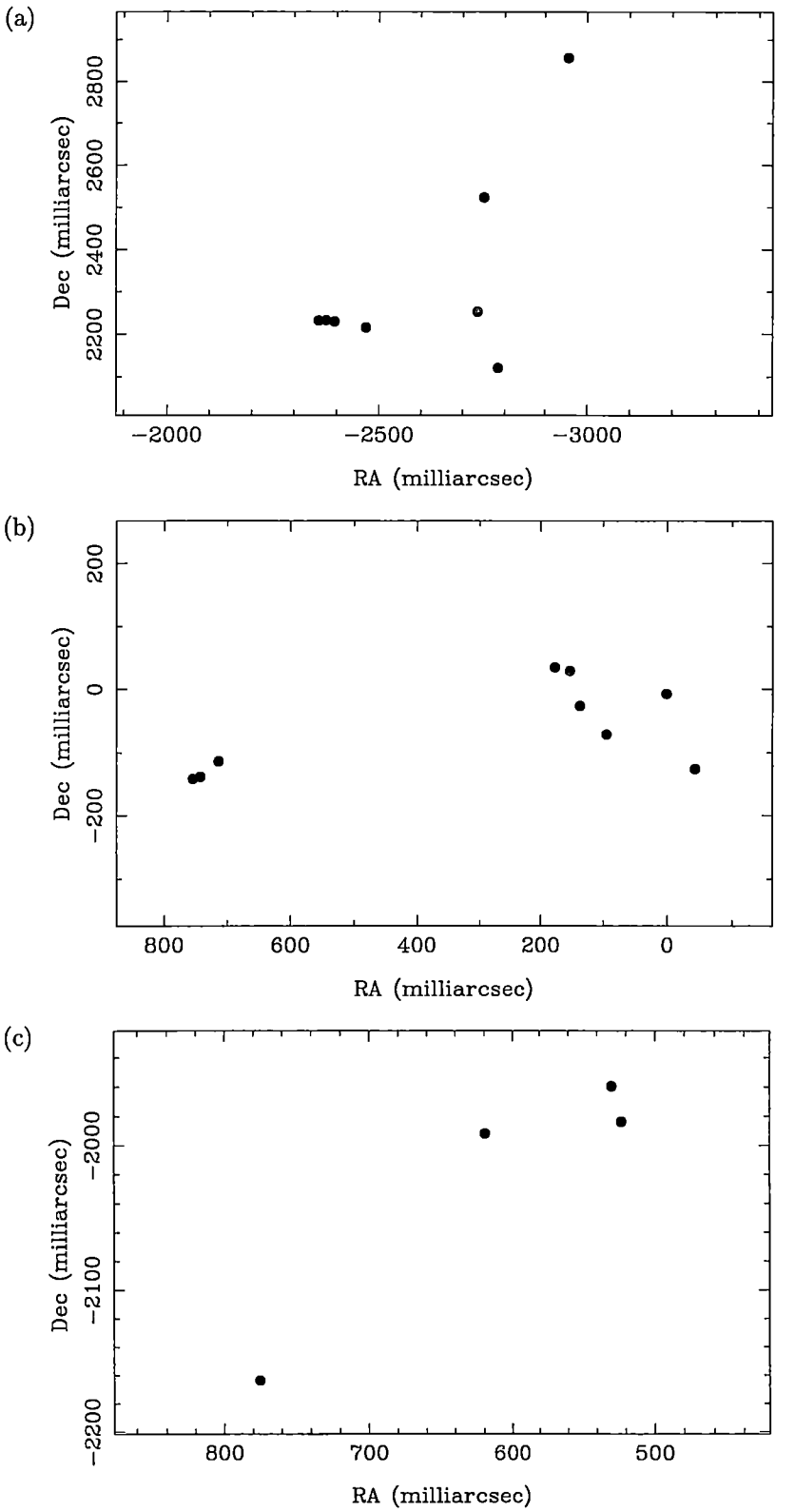

Figure 4.14: Close up of the (a) north-west, (b) central and (c) southern clusters in NGC 6334F.

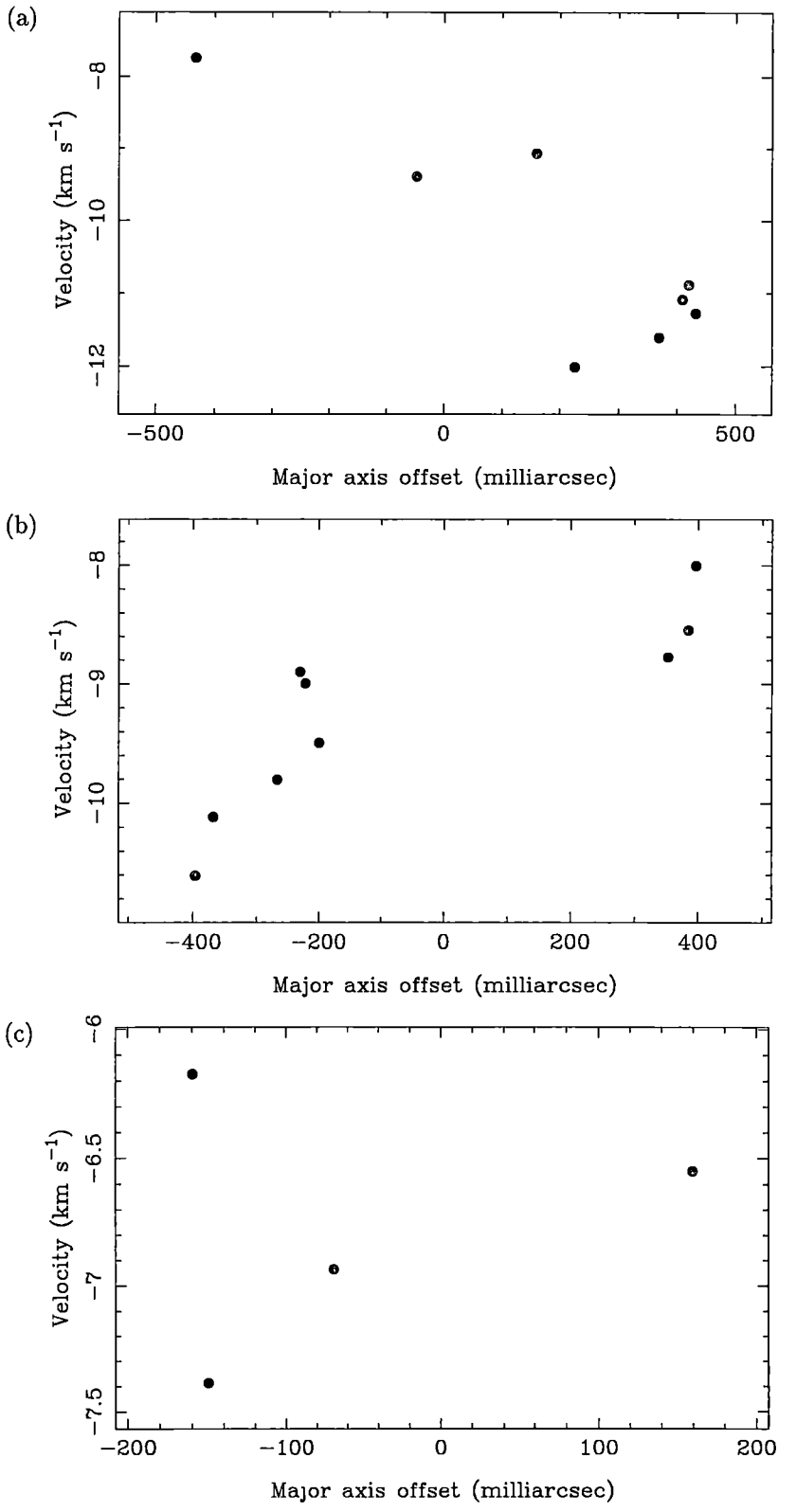

Figure 4.15: v-a diagrams for the (a) north-west, (b) central and (c) southern clusters in NGC 6334F, calculated as separate sources

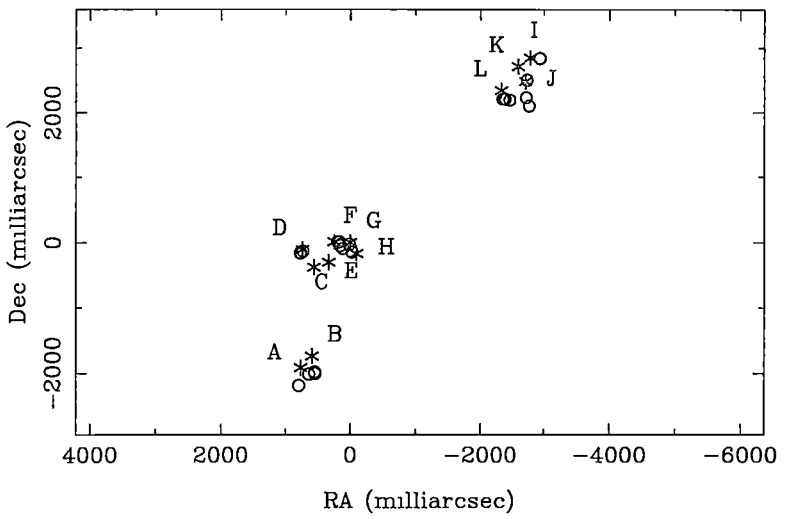

Figure 4.16: Comparison of VLBI positions (open circles) and ATCA positions (stars) for NGC 6334F.

Table 4.7: Detailed comparison of ATCA and VLBI positions for NGC 6334F.

Component	Flux Density (Jy)	Velocity (km s^{-1})	Positional Offset (milli-arcsec)
A	2.5	−16.00	107.5
	0.4		228.7
B	35.6	−16.80	25.9
C	62.9	−17.40	1.3
D	295.8	−17.90	7.6
E	12.9	−19.70	86.5
	7.2		46.4
F	49.3	−20.30	59.9
	43.1		15.3
G	47.3	−21.10	28.9
	16.7		63.5
H	106.2	−21.80	24.9
I	183.2	−22.40	2.2
J	4.2	−23.70	5.0

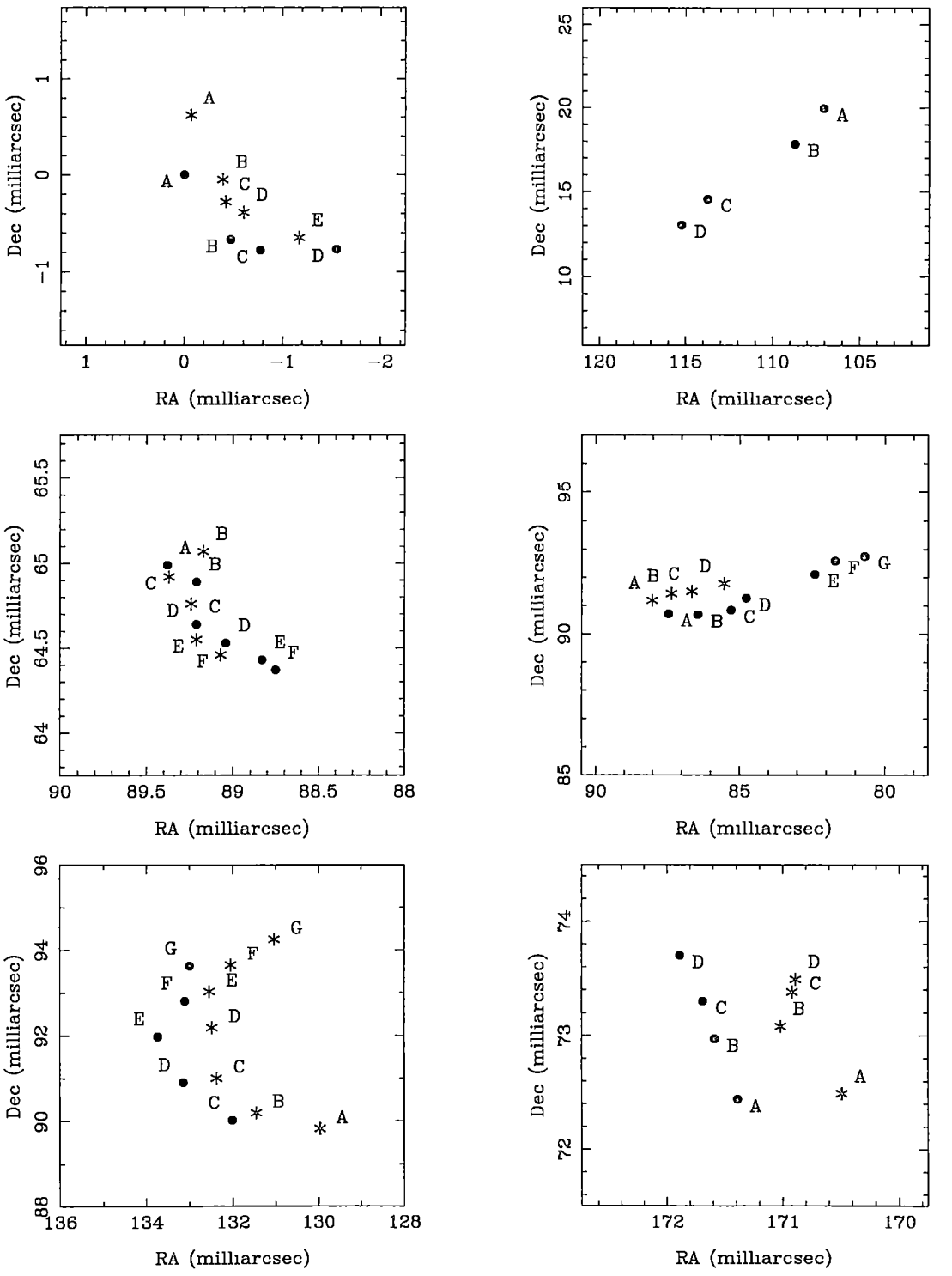

Figure 4.17: A selection of individual components in the source G 345.010+1.792, with the individual channel positions shown. The symbols represent the position of individual channels, stars from the July 1995 epoch and solid circles from the August 1996 epoch. The relative velocity of the channels is indicated by the characters which increase with velocity. The two epochs have not been aligned. The shift in position probably represents a velocity gradient in the masing molecular cloud.

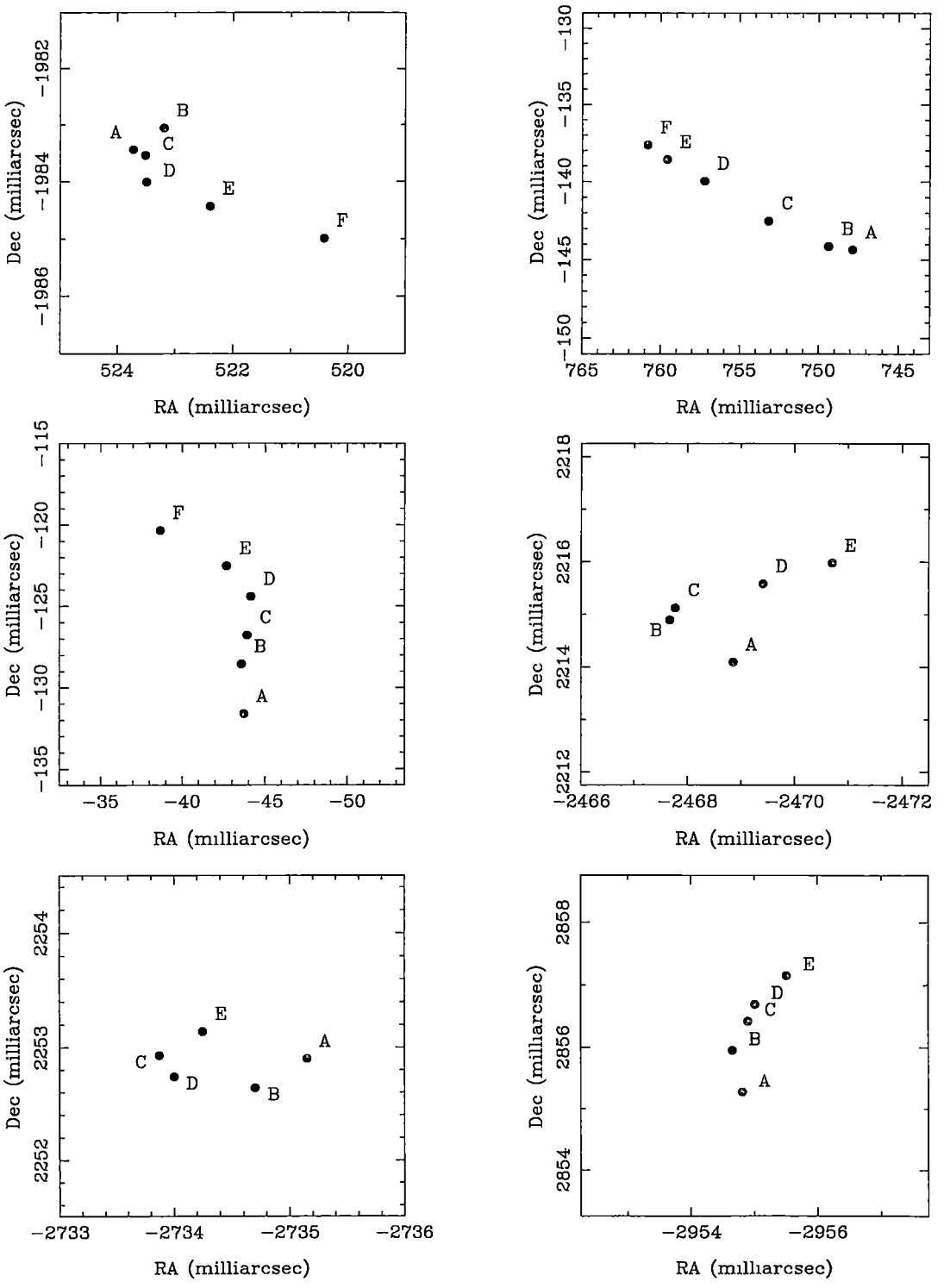

Figure 4.18: Same as Fig. 4.17 for the source NGC 6334F.

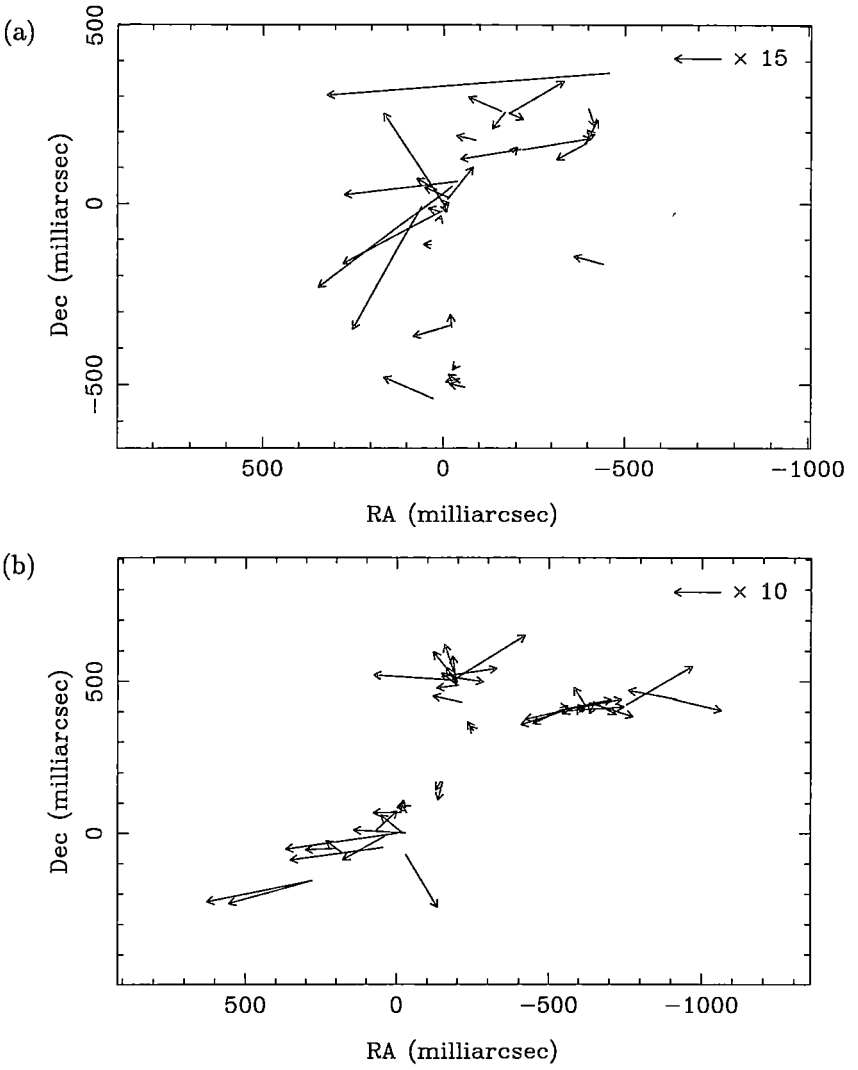

Figure 4.19: (a) "March" vectors for the source G 318.949−0.193. The magnitude of the march vector represents the size of the shift across the component, divided by the velocity width of the component in km s^{-1}(so the units of the vector are milli-arcsec per km s^{-1}). The size of vectors have been multiplied by 15 for clarity. (b) Same as (a) but for the source G 339.884−1.259. The vectors have been multiplied by 10.

This "marching" is seen by eye when comparing the the individual channel images, and so is unlikely to be due to erroneous Gaussian fitting. Almost every component shows this effect, although a few show the expected more-or-less random positions with about one milli-arcsec scatter. Figs. 4.19 and 4.20 shows a vector diagram of the magnitude and direction of the channel shift for each component of the four 6.7-GHz sources from the August 1996 observations.

An obvious cause of this would be some sort of phase calibration error, which scales with frequency (i.e. a delay error or problem with the bandpass correction). The largest shifts are of the order of 15 milli-arcsec across 7 frequency channels. This corresponds to a phase error of roughly 490 degrees, or 70 degrees per channel. Most of the components have more modest shifts of about 2 milli-arcsec over 5

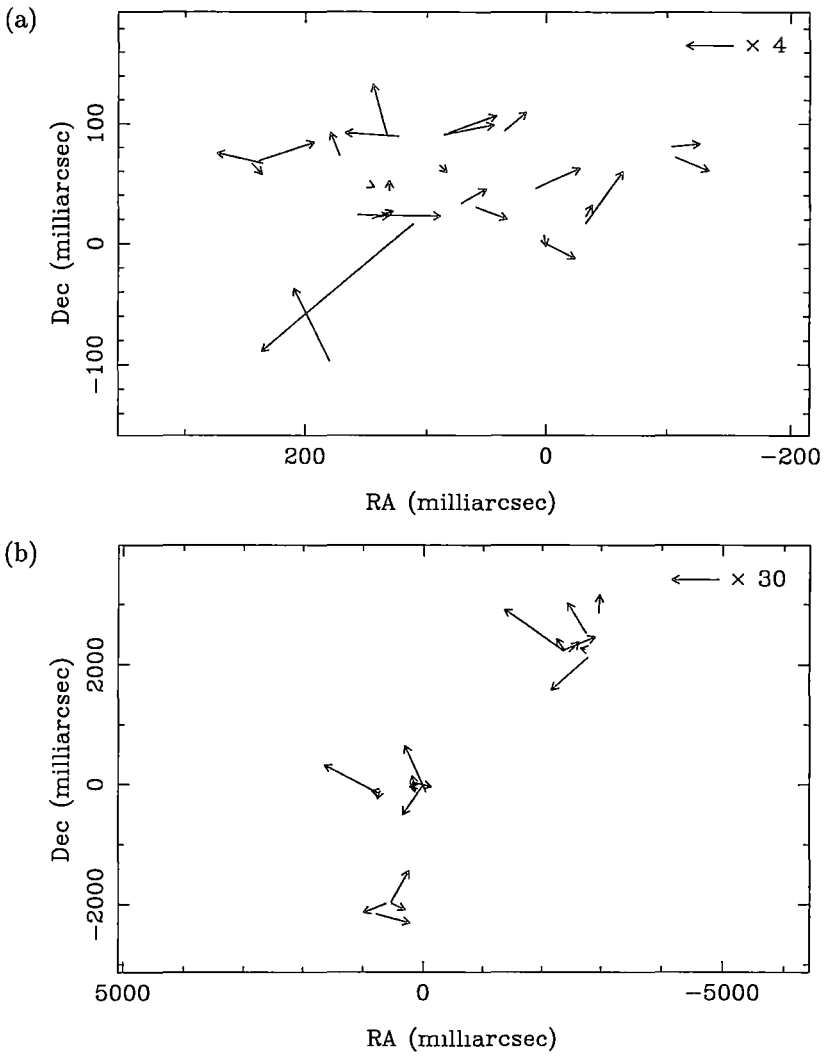

Figure 4.20: Same as Fig. 4.19 for the sources (a) G 345.010+1.792 and (b) NGC 6334F. The vectors have been multiplied by 4 and 30 respectively.

channels. This still corresponds to a phase shift of 72 degrees or 14 degrees per channel. If the calibration had not properly corrected the delay, then a frequency dependent phase error would be expected. Delay errors of 100 and 20 microseconds (respectively) would be needed to explain the phase errors calculated above. The delay *corrections* derived from the observed continuum sources were of the order of 50 nanoseconds or less, so the residual delay errors should be significantly less than this.

The marching channels is unlikely to be due to a simple calibration error for the following reasons.

- The implied delay and phase errors are unreasonably large.
- As Figs. 4.19 and 4.20 show, the magnitude and direction of the shifts varies from one component to the next. This virtually rules out errors introduced by self-calibration as the errors would be same for all channels.

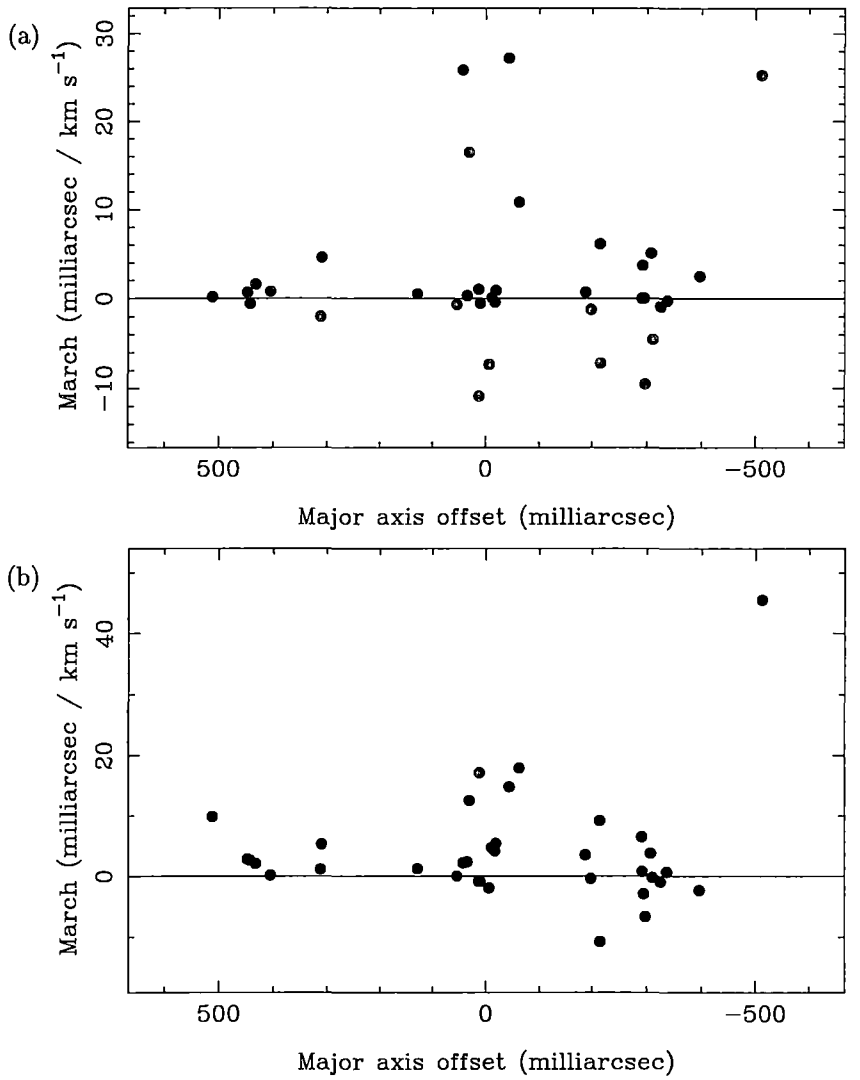

Figure 4.21: (a) Component of the "march" vector parallel to the line of best fit to the maser components for the source G 318.949−0.193. (b) Same as (a) but the perpendicular component to the line of best fit. The left and central clusters are biased in a positive manner, indicating a systematic component to the position shift.

- As Fig. 4.17 shows, the component channel shifts are very similar for separate observations. It is exceedingly unlikely that calibration or instrumental errors would be the same from one year to the next.
- A similar effect has been seen by other observers for VLBA observations of the 12.2-GHz transition of methanol and H_2O masers. (Ellingsen 1997 & Marvel 1997, private communication).

If the marching effect is a calibration error or a deficiency in the data processing (either a software bug in the correlator or *AIPS* or an "operator error") the chance of detecting proper-motion in the order of 0.3 milli-arcsec yr^{-1} is unlikely. However, I consider these to be unlikely causes because of the reasons stated above. The effect is probably caused by a velocity gradient within the molecular gas which

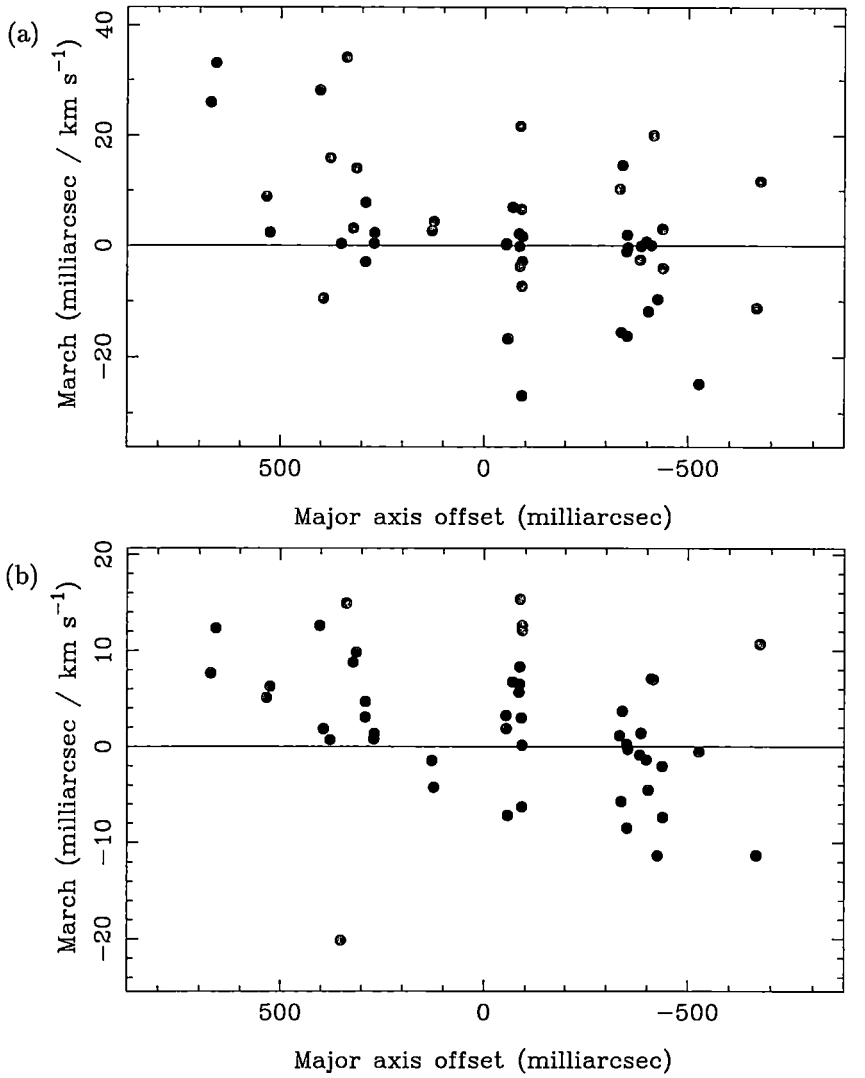

Figure 4.22: Same as Fig. 4.21 for the source G 339.878−1.252. (a) A positive systematic component is present in the parallel component of the left cluster. (b) A positive systematic component is present in the left and central cluster. This can also be seen in Fig. 4.19a.

is masing. Detailed modelling of this is beyond the scope of this thesis. If the maser sources are edge-on Keplerian discs, velocity gradients would be expected within the gas. This is due to the centripetal acceleration and $r^{-1/2}$ dependence on the rotational velocity.

An important consideration is whether the size of the shift could be explained due to accelerations within a rotating disc. A simplistic approach to this is to compare the velocity extent of the individual channels of each component to the shift in position. A typical shift is 5 milli-arcsec over 6 velocity channels (0.5 km s^{-1}). This corresponds to 0.1 km s^{-1} over 1 milli-arcsec. This analysis is too simplistic, however, as it it ignores two important facts:

- the size of the individual maser components is of the order of 10 milli-arcsec and the positions plotted in Figs. 4.1 to 4.13 are position of the peak of the

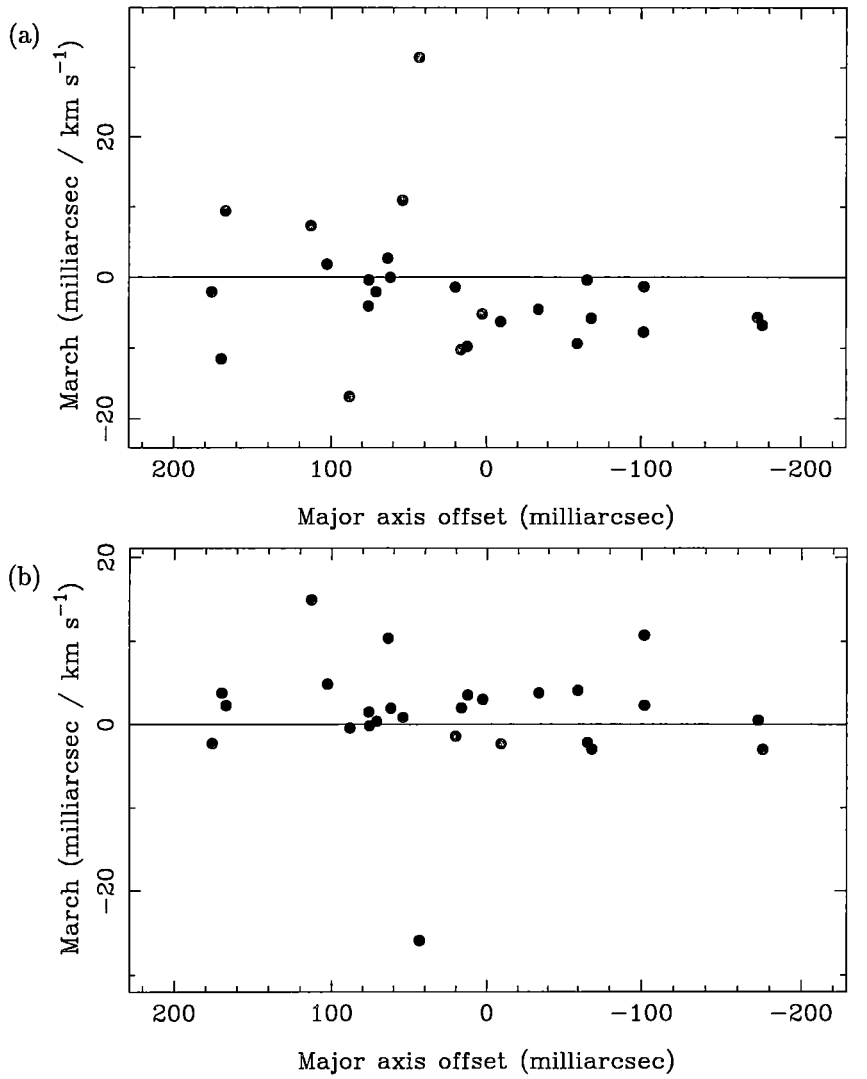

Figure 4.23: Same as Fig. 4.21 for the source G 345.010+1.792. A systematic component is seen both parallel and perpendicular to the line of best fit.

best fit Gaussian.

- any particular point in the masing region will emit at a (narrow) range of frequencies.

If a column of masing gas has a velocity gradient through it, the observed emission at a specific frequency (i.e. spectral channel) will come from the full spatial extent of the masing region, although the specific observed velocity may not equal the *average* velocity of each point within the masing region. The implication of this is that the measured component position at a specific velocity is not necessarily the point in the masing gas which has that average line-of-sight velocity. This is best demonstrated with a simple model of the situation.

For simplicity, I have used a one-dimensional model in order to estimate the expected positional shifts for a masing region with a velocity gradient through

it. The observed flux density will depend on both the position on the sky and the frequency. For a specific position on the sky, emission is assumed to have a Gaussian velocity profile, centred on an average velocity v_0, i.e:

$$e^{-(\frac{v-v_0}{\sigma_v})^2} \tag{4.1}$$

where v is the velocity and σ_v is the width of the velocity profile. The positional dependence of the emission is also assumed to have a Gaussian shape with the form:

$$e^{-(\frac{x}{\sigma_x})^2} \tag{4.2}$$

where x is is the position in the one-dimensional space. If v_0 is assumed to change linearly with position, then

$$v_0 = xv_x \tag{4.3}$$

where v_x is the gradient of the change. Putting all these components together give the following model for the emission:

$$F(x,v) = Ae^{-(\frac{x}{\sigma_x})^2}e^{-(\frac{v-xv_x}{\sigma_v})^2}dxdv \tag{4.4}$$

where A is a constant. For a fixed $v\,dv$ interval, this is a product of two Gaussians in x, which is also a Gaussian. As this is a symmetrical function, the position that would be measured will equal the position with the peak emission. This can easily be calculated and is:

$$x_{pos} = v\left(\frac{{\sigma_x}^2 v_x}{{\sigma_v}^2 + {\sigma_x}^2 {v_x}^2}\right) \tag{4.5}$$

Thus the fitted position varies linearly with the observed velocity. If we assume the FWHM of the velocity profile is 0.5 km s^{-1} and the spatial FWHM is 12 milli-arcsec, then a positional shift of 0.1 km s^{-1} per milli-arcsec yields a velocity gradient of 0.015 km s^{-1} per milli-arcsec. This is very similar to the velocity gradient which would be expected from a Keplerian disc. Of course, this does not prove either that the observed shifts are due to a velocity gradient or that the velocity gradient is due to a rotating disc. It does show, however, that the size of the observed shifts are *consistent* with them being due to a rotating disc.

As the velocity gradient along the disc is constant, the observed shifts should all be of a similar magnitude and in the same direction (assuming the emission all comes from a constant radius). This is not seen, which indicates that other effects, such as turbulence, are more important. However systematic offsets *are* seen in the directions of the march vectors. This is best demonstrated in Figs. 4.21 to 4.23, which plot the magnitude of the march vector parallel to, and perpendicular to, the line of best fit of the maser components as a function of the semi-major axis offset. For the sources G 318.949−0.193 (Fig. 4.21), the parallel component of the march vectors shows no systematic direction (the values are clustered around zero), but the perpendicular components are clearly offset in a positive sense. The source G 339.884−1.259, shows systematic effects in the march vector plot. The two clusters of components in the south-east and north both have the march

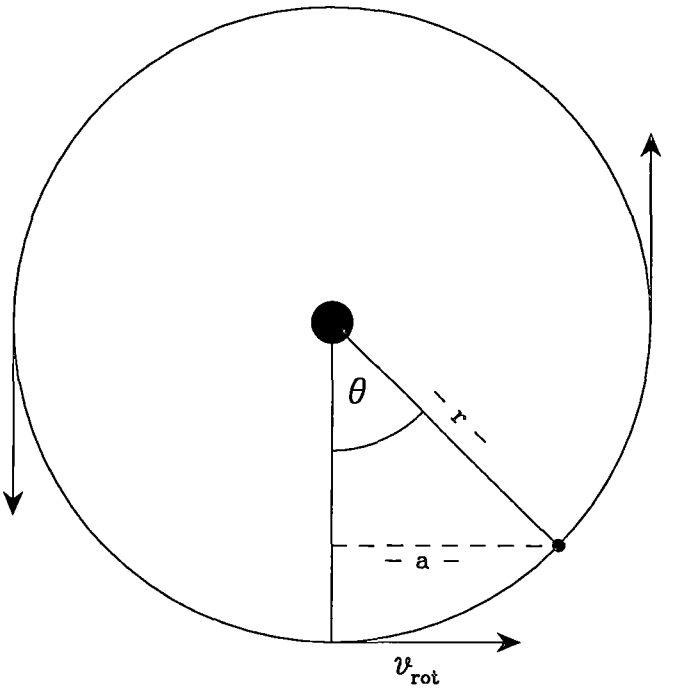

Figure 4.24: Geometry of the proper motion equations. The disc is view from above and the observer is at the bottom of the page.

vectors aligned in one direction, while the western cluster shows no systematic alignment. This can also be seen in Fig. 4.22. Finally, G 345.010+1.792 shows a tendency for the march vectors to point towards the north-west.

This systematic marching indicates that there is a kinematic cause for velocity gradients, although there is a quite large non-systematic component as well. If a theoretical model for the marching can be produced, this may significantly improve our understanding of the dynamics of methanol maser sources. As well as having a kinematic cause, the marching may represent large scale turbulence through the masing molecular clouds.

The effect of the marching points on the proper motion is discussed in Section 4.9.3.

4.7 Proper-motion modelling

In the following section some simple models of rotating Keplerian discs and the expected proper-motion of these discs are developed.

4.7.1 The basic equations

The geometry used for this model is shown in Fig. 4.24. The Keplerian rotation velocity, v_{rot}, of a point source at a distance, r, from a central mass, M is given

by:

$$v_{rot} = \left[\frac{GM}{r}\right]^{1/2} \tag{4.6}$$

where G is the gravitational constant. The line-of-sight velocity depends on the position of the feature within the disc, θ, and the inclination angle, i:

$$v_{los} = v_{rot}\sin(\theta)\cos(i), \tag{4.7}$$

while the tangential (along the plane of the disc) velocity is:

$$v_{tangential} = v_{rot}\cos(\theta). \tag{4.8}$$

If the disc is inclined with respect to the observer, there will also be a velocity perpendicular to the disc:

$$v_{perpendicular} = v_{rot}\sin(\theta)\sin(i). \tag{4.9}$$

The observed position of a component on the sky is the displacement along the semi-major axis, a, which equals $r\sin(\theta)$. Inserting this into Equation 4.7 gives:

$$v_{los} = v_{rot}\frac{a}{r}\cos(i), \tag{4.10}$$

Thus if the maser emission comes from a constant radius (or a narrow range of radii) around the central star, the observed line-of-sight velocity will vary linearly with a. Combing Equations 4.6 and 4.10 gives the equation used in Section 2.5.2 to calculate the mass of the central star from the measured slope in the v-a diagram:

$$\frac{dv}{da} = \left[\frac{GM}{r^3}\right]^{1/2}\cos(i). \tag{4.11}$$

Any observed proper-motions will be proportional to the tangential velocity (Equation 4.8) over a sufficiently small time interval. Given the observed rotational velocities (5 km s^{-1}) and the size of the discs (radii $\sim$2000 AU) the tangential velocities will not change by more than 1 or 2 percent over 10 years. This means that the components can be assumed to have negligible acceleration. It would also be difficult to detect any velocity shifts in the single dish spectrum of the source.

The most important property of Equation 4.8 is that the tangential velocity (i.e. the observable proper-motion) is maximum in the centre of the disc (equal to v_{rot}) and minimum at the edge of the disc (zero at the very edge).

The implications of these equations are best understood using a few simple diagrams. The expected proper-motion and v-a diagram has been calculated for a range of radii around a central mass of 20 $M_{\odot}$, with the disc aligned edge-on. Fig. 4.25 shows the geometry of the model used, viewed from above the disc.

Fig. 4.26 shows the position in the v-a diagram for emission coming from the four radii. The positions of individual maser components from within the disc will only lie in opposite quadrants. If the central position of the star and the systemic velocity were known this would be a powerful test of the disc model for methanol

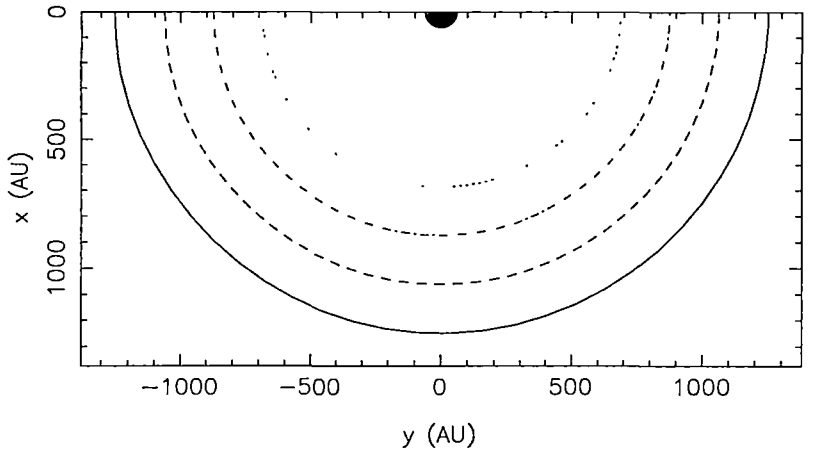

Figure 4.25: Geometry of the disc used in Figs. 4.26 to 4.28. The disc is viewed from above and the observer is at the bottom of the page. The mass of the central star has been set to 20 $M_{\odot}$.

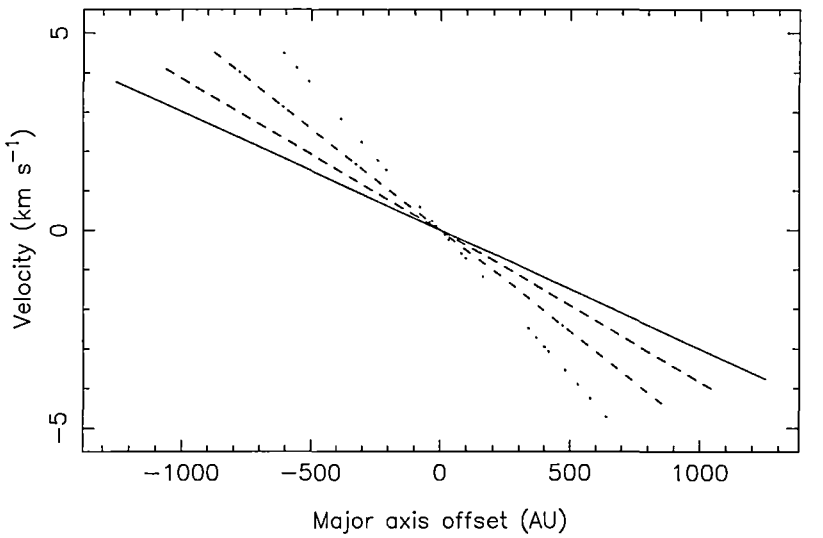

Figure 4.26: v-a diagram which would be observed given the geometry in Fig. 4.25.

masers. However, these values are not known. It should be possible to divide the observed components in the v-a digram into two quadrants, but this is not nearly so powerful a test. Norris *et al.* (1998) found that they could divide the v-a plot in this way for all the linear sources observed by them using the ATCA and the PTI (Norris *et al.*, 1993; Norris *et al.*, 1988). It is worth pointing out, that although a reasonably large range of radii has been used for this modelling, the components in the v-a diagram are confined to a relatively small region of the diagram. This means that in sources which show a line in the v-a diagram with a modest amount of scatter, the components may still come from a significant range of radii.

Fig. 4.27 shows the expected proper-motion in the plane of the disc as a function of the distance along the semi-major axis. There are two important features of this plot. Firstly, for a given radius, the proper-motion will be small at the edge

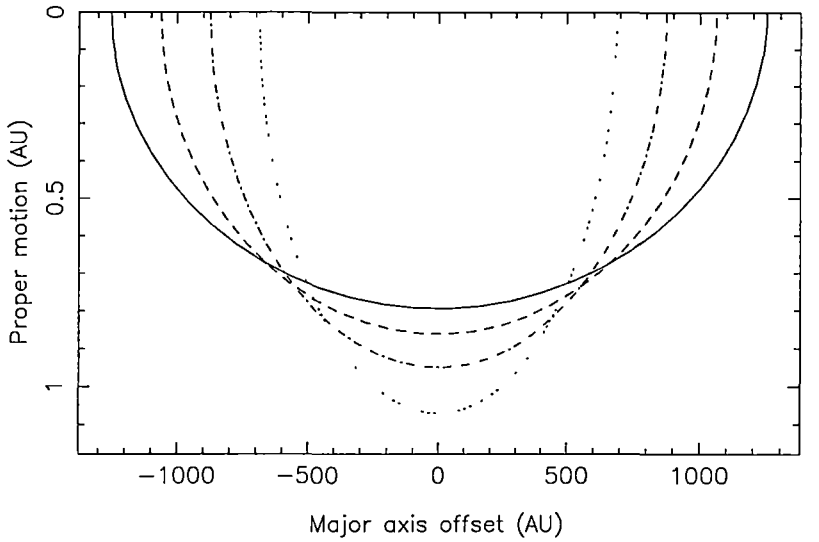

Figure 4.27: Proper-motion (parallel to the disc) versus semi-major axis (p-a diagram) which would be seen in 1 yr assuming the geometry in Fig. 4.25. The largest proper motions are seen in the central part of the disc, particularly for the inner radii.

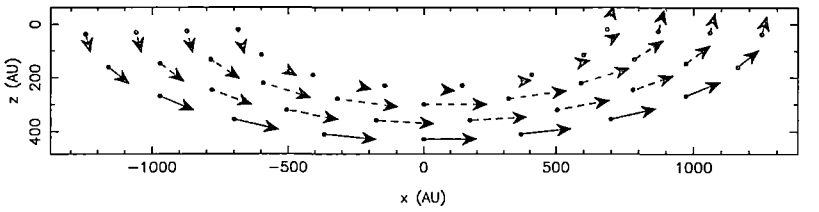

Figure 4.28: The proper-motion which would be seen assuming the geometry in Fig. 4.25, with a disc inclination of 20°. The size of the vectors has been multiplied by 250. Note that the units of the axes are in AU.

of the disc and maximum in the central region with the magnitude of the proper-motion defined by an ellipse. The largest proper-motions come from the inner radii. The proper-motions which would be seen on the sky are also also shown in Fig. 4.28. In this diagram, the disc has been assumed to have an inclination of 20° to allow the radial dependence of proper-motion to be seen.

The effect of inclination

If an observed disc is inclined with-respect to the observer, Eqn. 4.7 shows that observed line-of-sight velocity will decrease as the cosine of the inclination angle. For modest inclination angles the reduction will be quite small (a 7 per cent reduction for i=20°). This will reduce the value of dv/da measured from the v-a diagram, which in turn will reduce the estimated mass of the central star (Eqn. 4.11). The estimated mass depends on the square of the velocity gradient, and so will be under-estimated if the inclination angle is significant. The measured radius of the source is not affected by the inclination angle. The tangential velocities and proper-motions are also not affected by the inclination angle. Obviously for an

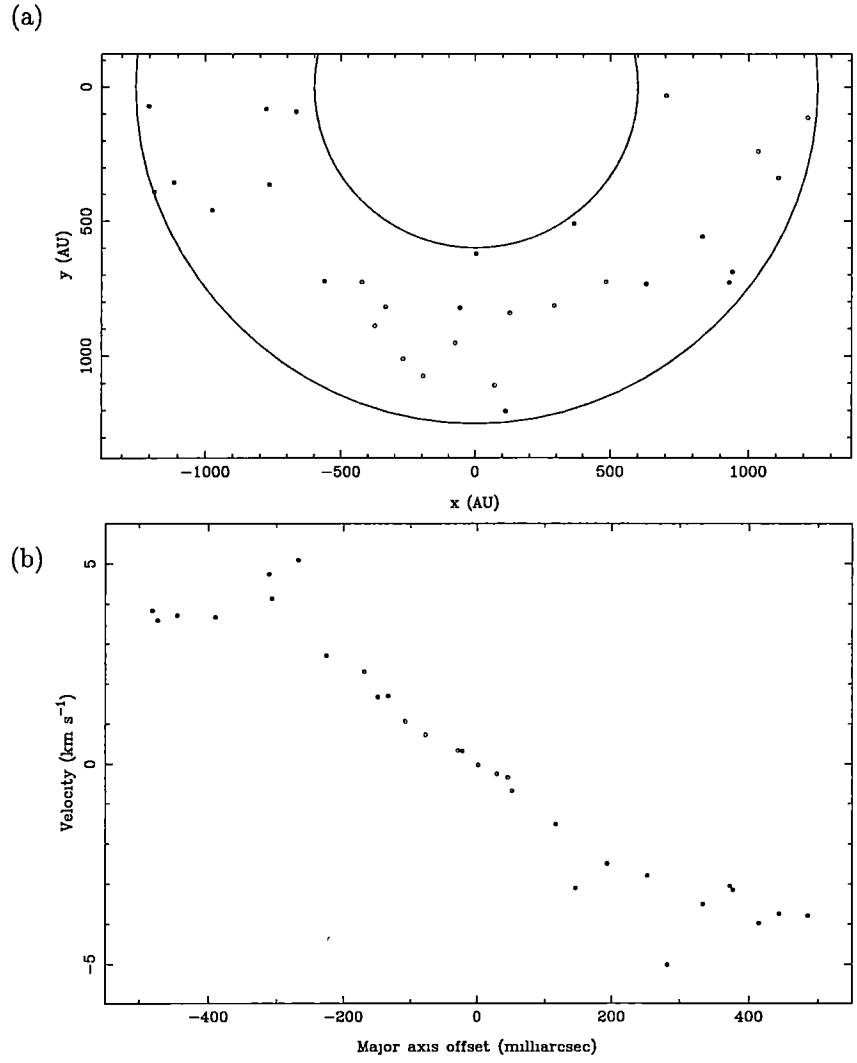

Figure 4.29: (a) Model of the simulated disc, seen from above. The observer is at the bottom of the page. The mass of the central star is 20 $M_{\odot}$. (b) The v-a diagram which would be observed using the model shown in (a).

inclined disc, a proper-motion perpendicular to the disc should also be present, however it will be significantly less than the tangential proper-motion (with a $\sin(i)$ dependence), and so difficult to detect.

4.7.2 Proper-motion simulations

To estimate the proper-motions which we would expect to see in the sources selected for this experiment, I have used the equations developed in Section 4.7.1 and created simulated data. The parameters used for this model have been chosen as representive of values for the sources in the VLBI sample. A central mass of 20 $M_{\odot}$ has been used, and maser emission has been assumed to come from radii between 600 and 1250 AU. Thirty maser components were chosen at random within these radius limits in the front half of the disc. Measurement errors for

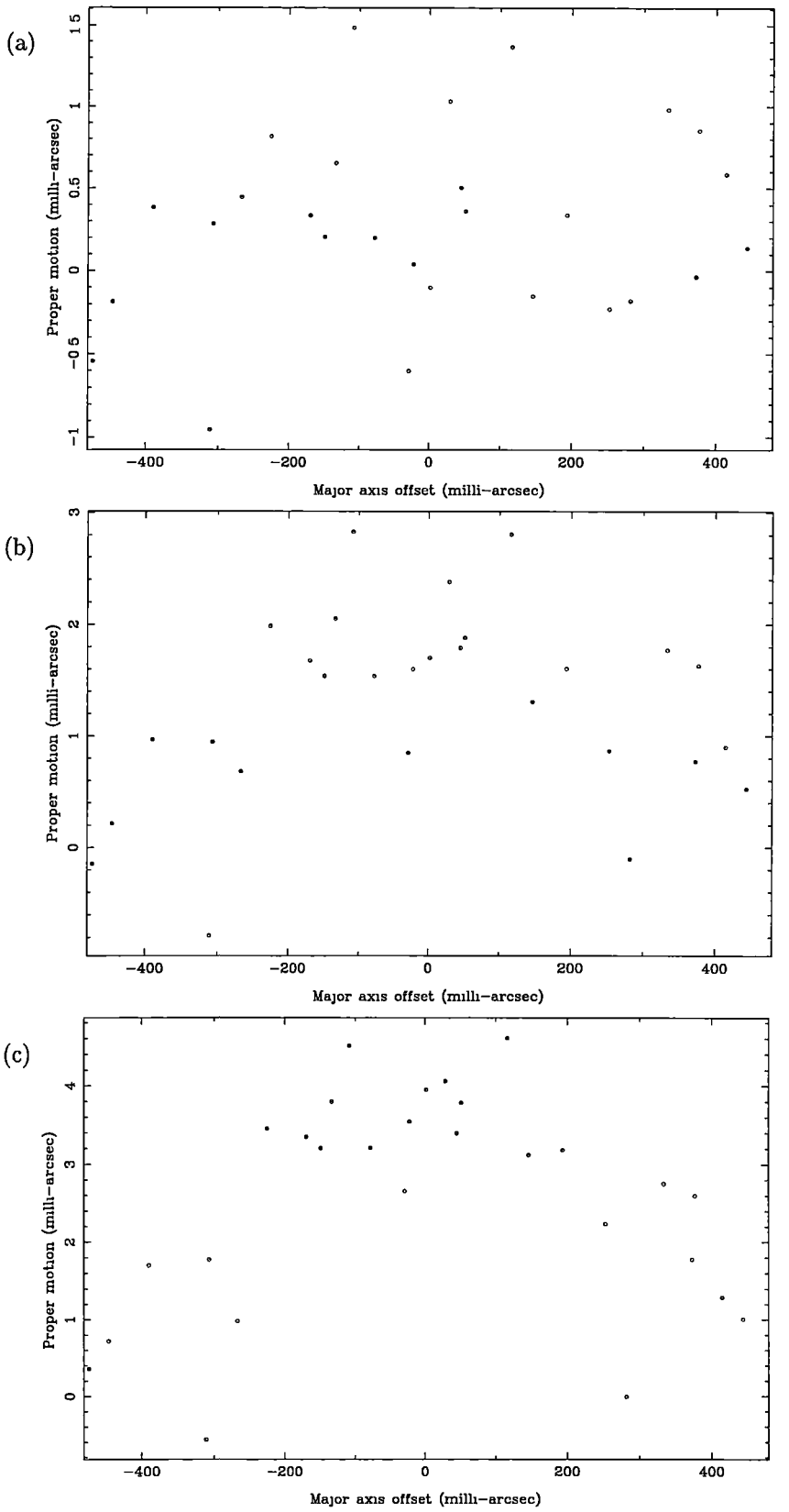

Figure 4.30: The p-a (proper-motion versus major-axis offset) diagram which would be seen after (a) 1, (b) 5 and (c) 10 yrs, using the model geometry in Fig. 4.29. A positional error of 0.5 milli-arcsec has been assumed.

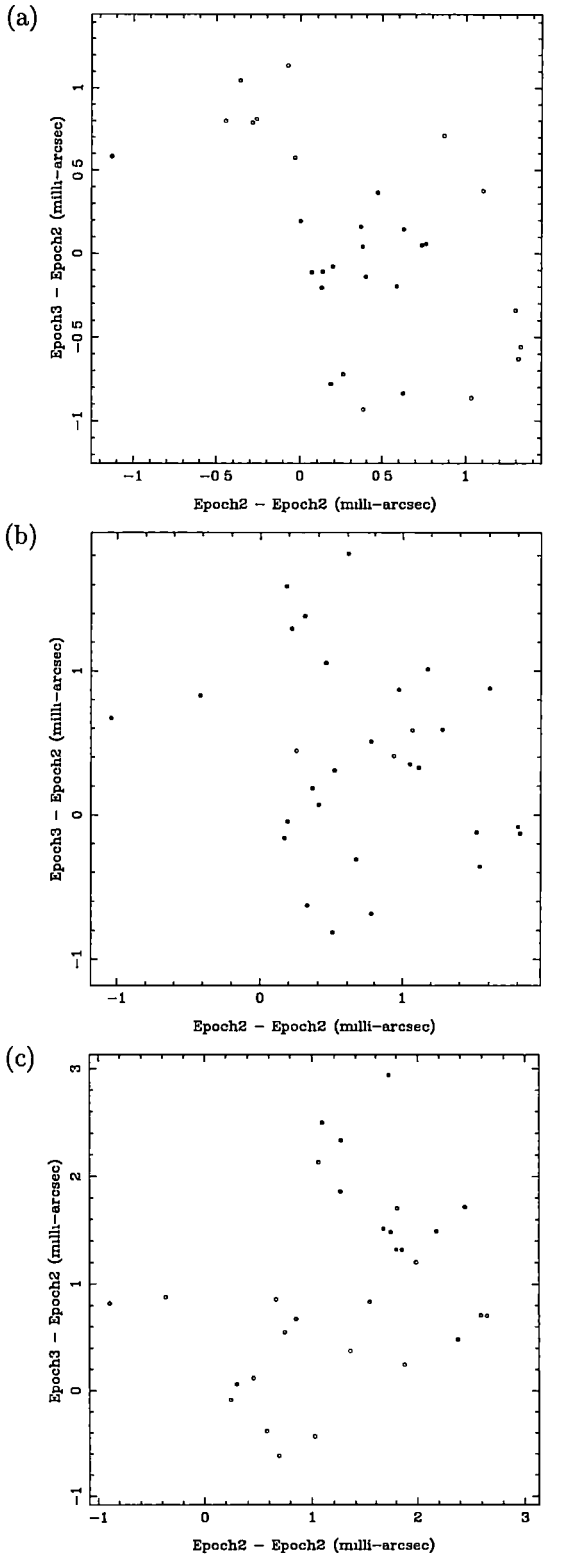

Figure 4.31: Proper motion between the first and second epoch versus proper-motion between the second and third epoch. With no measurement errors, this should lie on a line with a slope equal to 1.0. (a) 1 yr between epochs, (b) 2.5 yrs between epochs and (c) 5 yrs between epochs (giving 2, 5, 10 yrs total time-span respectively.

each epoch were assumed to be Gaussian with a 0.5 milli-arcsec standard deviation (comparable to the errors derived from the real data). The distance to the source was set to 2.5 kpc. Fig. 4.29 shows the geometry of the model seen from above and the corresponding v-a diagram.

Fig. 4.30 shows the "observed" proper-motion in the direction of the disc as a function of the major axis offset. This is shown for three time-ranges of 1, 5 and 10 years. No proper-motion is detectable on a one year timescale. The variation of proper-motion is seen on the five and ten year timescales; however a detection after five years would be marginal.

An alternative method for detecting proper-motion, which does not assume anything about the underlying cause of the proper motion, is to plot the proper-motion observed between two epochs versus the proper-motion of the next two epochs. If acceleration is negligible then these two values should be equal, and be scattered on a line with slope of 1. Fig. 4.7.2 shows this plot for the simulated data, for three epochs spaced over 2, 5 and 10 years. Even with a full 10 years durations, no correlation can be seen in this plot.

Both of the two plots described above are robust with respect to positional alignment between the epochs. If there is an alignment error between any of the epochs, this will only affect the position of the origin of the plot, not the relative point to point positions. This is because any alignment errors will add a constant to all positions measured at one epoch, which will shift all the points in the same direction (by the same amount) on the plots.

4.8 Proper-motion results

The 6.7-GHz data for the source G 345.010+1.792 has been fully processed for all three correlated epochs, and the data for G 339.878−1.252 has been processed for the August 1996 and July 1995 epochs. The two sources G 309.921+0.479 and NGC 6334F have both previously been observed using VLBI by Norris *et al.* (1998) and Ellingsen (1996), respectively.

For these four sources a vector plot of the observed "proper-motion" is shown in Figs. 4.32 to 4.39 along with a proper-motion versus major-axis offset (p-a) diagram. In order to produce these plots, individual components which were within 5 milli-arcsec and 0.5 km s^{-1} between epochs were assumed to represent the same point. As the sources show little variability, there is little difficultly identifying components between epochs. Because the absolute position offset between images at the different epochs is uncertain, the offset between the pairs points was minimized using a least-squares method (which simply involved subtracting the average offset of the components in Right Ascension and Declination).

4.8.1 G 309.921+0.479

The source G 309.921+0.479 has been previously imaged at 12.2-GHz by Norris *et al.*(1998) in 1990. This gives a separation of 4.5 years to the October 1994 observations presented in this thesis. The proper-motion vector plot and p-a

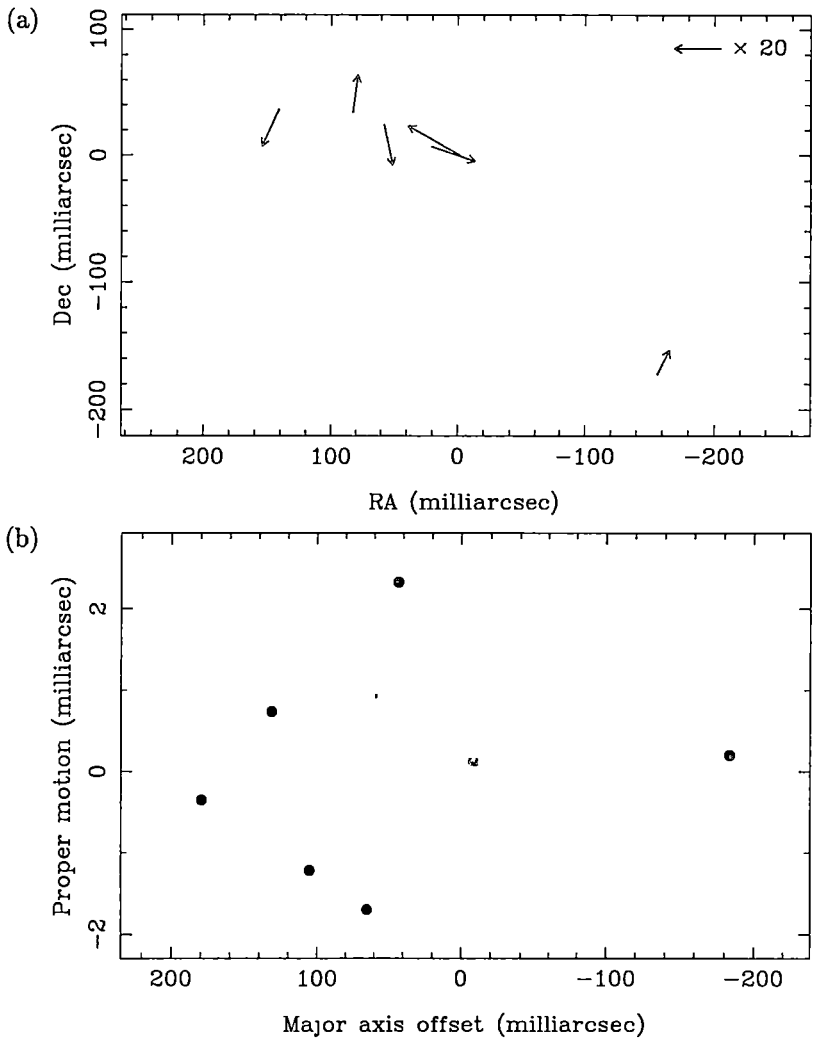

Figure 4.32: (a) Proper-motion vector diagram for G 309.921+0.479. (b) p-a diagram for G 309.921+0.479.

diagram are shown in Fig. 4.32. No systematic offsets are seen across the sources. The average offset between the components is 1.6 milli-arcsec and the standard deviation is 1.7 milli-arcsec. The largest offset of the components is 2.3 milli-arcsec, so a limit of 0.5 milli-arcsec yr^{-1} can be placed on the *relative* proper-motion. This is larger than the expected proper-motion, assuming an central star of mass 10 $M_{\odot}$, as implied by the velocity gradient along the source.

4.8.2 G 339.878−1.252

Fig. 4.33 shows the proper-motion vector plot and p-a diagram for the source G 339.878−1.252. Neither plot shows any systematic variations between the two epochs, which are separated by 13 months. If two sets of observations are aligned, the average offset between the points is 1.2 mas, and the standard deviation of the offsets is 1.5 milli-arcsec (these values are after removing two pairs with the offset greater than 5.5 milli-arcsec or 3.7 σ). As these errors are a combination of the

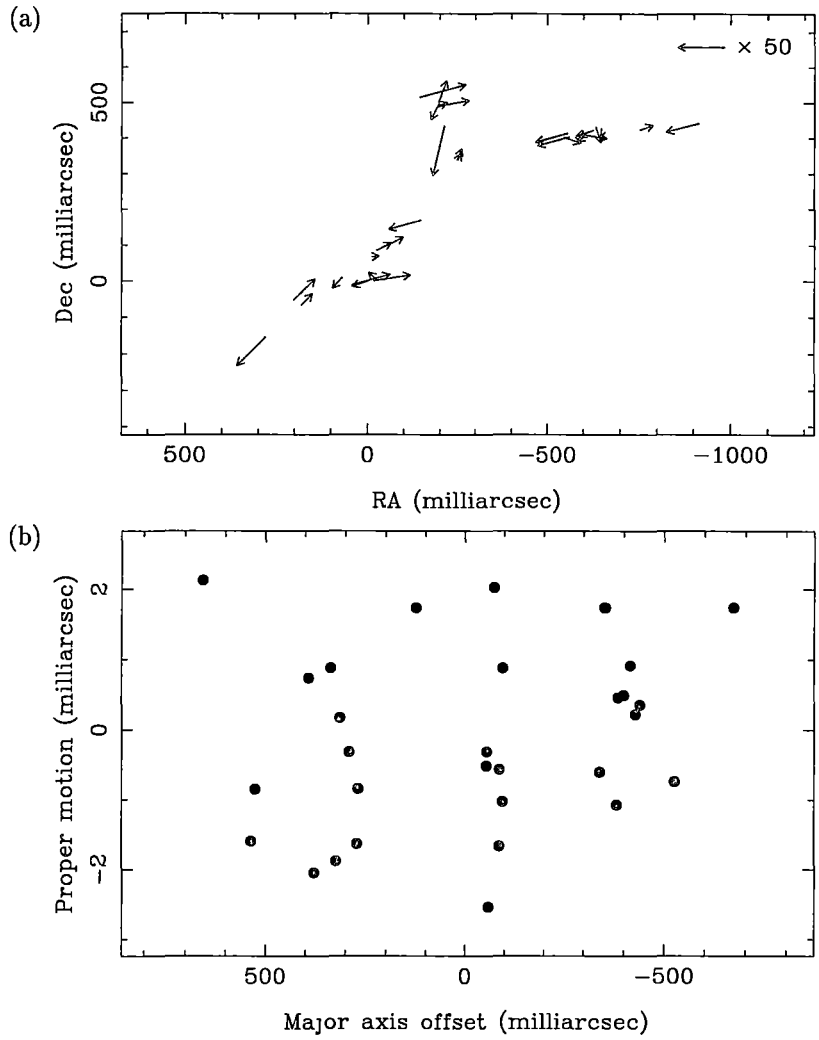

Figure 4.33: Proper-motion and p-a diagram for G 339.878−1.252.

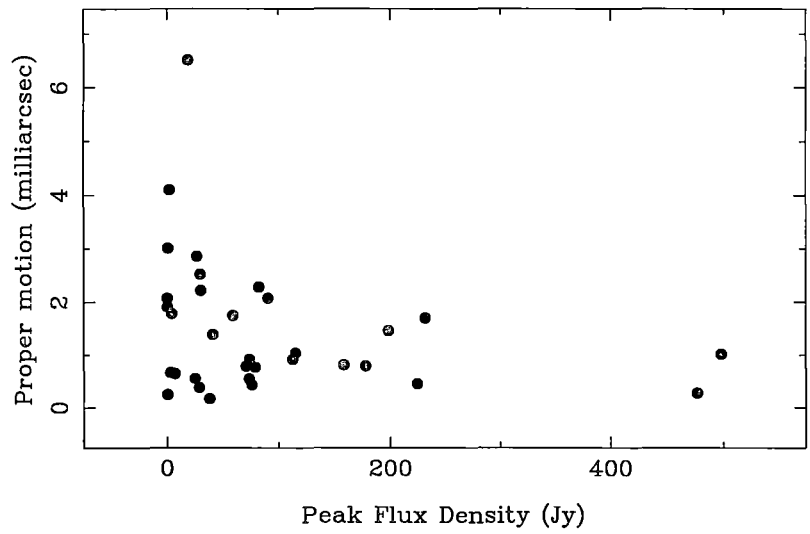

Figure 4.34: Observed proper-motion versus flux density for G 339.878−1.252.

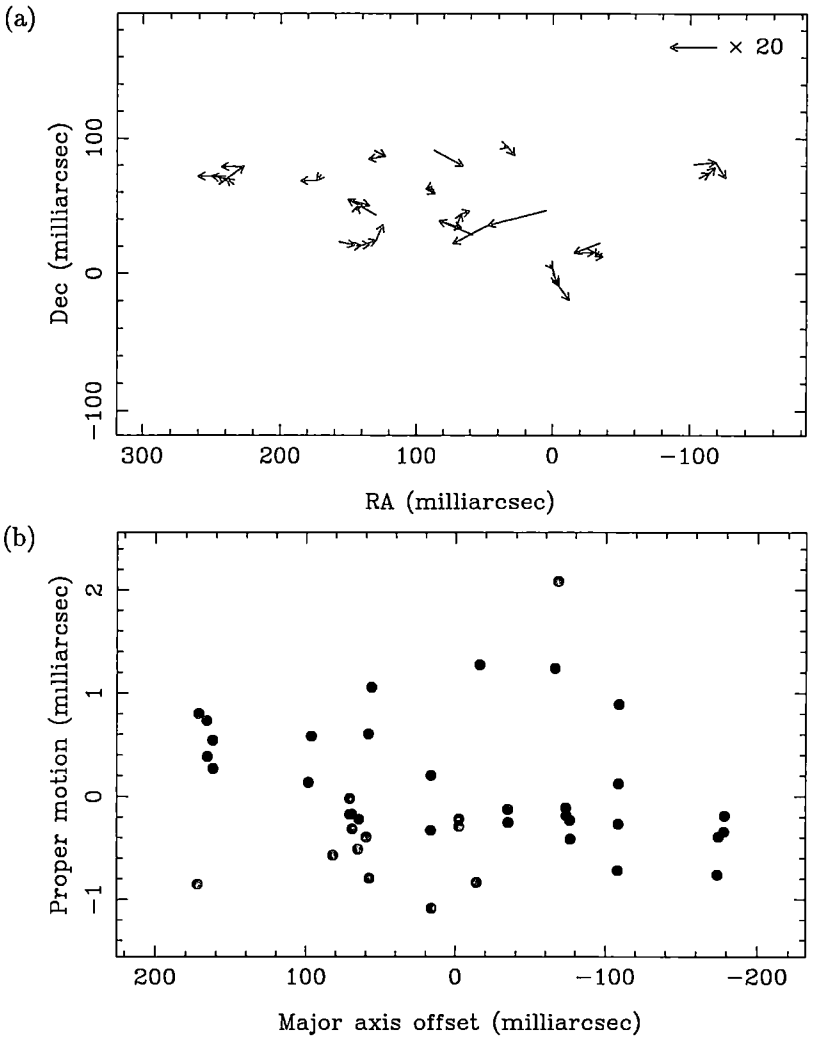

Figure 4.35: Proper-motion and p-a diagram for G 345.010+1.792.

errors from the individual epochs, they are $\sqrt{2}$ larger than the individual errors. This means the standard deviation of the positional accuracy is approximately 1.1 milli-arcsec for the individual epochs. Fig. 4.34 is a plot of the positional offset of the maser components between the two epochs versus the peak flux density of the component. The diagram shows that the observed positional difference between the two epochs has a strong flux dependence. Half of the components have positions within 1 milli-arcsec and most are within 2 milli-arcsec.

4.8.3 G 345.010+1.792

Fig. 4.35 shows the proper-motion vector plot and p-a diagram for the source G 345.010+1.792. All three epochs have been processed for this source (i.e. October 1994, July 1995 and August 1996) which are separated by 9 and 13 months. Fig. 4.36 shows the p-a diagram between the October 1994 and August 1996 epochs. There are no systematic offsets present in any of these plots. As three epochs have been observed for this source, the proper-motion of the first two

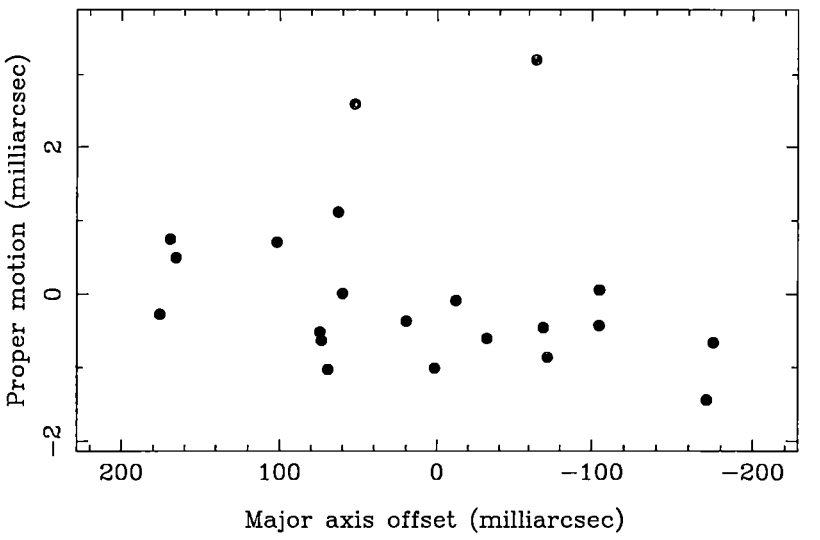

Figure 4.36: p-a diagram for G 345.010+1.792 between October 1994 and August 1996

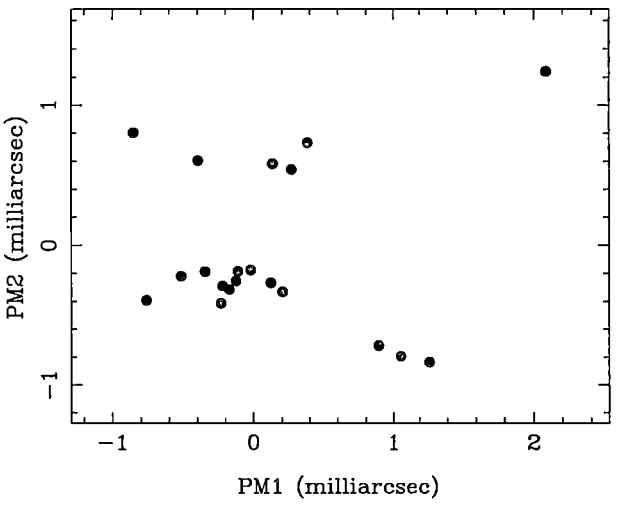

Figure 4.37: Proper-motion between October 1994 and July 1995 epochs versus the proper-motion between July 1995 and August 1996 for G 345.010+1.792.

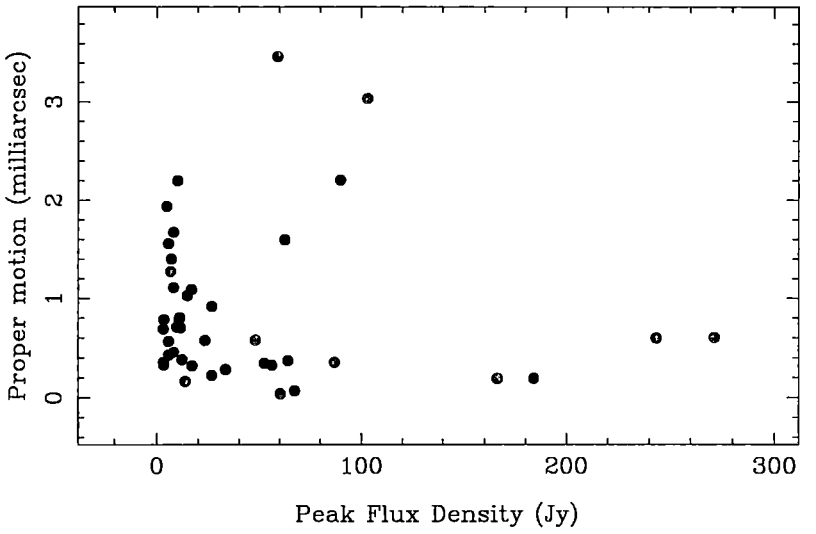

Figure 4.38: Observed proper-motion versus versus flux density for G 345.010+1.792.

epochs can be plotted as a function of the next two (Section 4.7.2) and the components should lie on a line with slope of 1.4 (the ratio of 9 to 13 months). Such a plot (Fig. 4.37) does show a weak anti-correlation, though a Spearman Rank-Order Correlation test does not find the correlation significant. The same plot between different pairs of the three epochs (e.g. epoch 3 - epoch 1 versus epoch 3 - epoch 2) does not show any correlation. The simulated data showed that it would be unlikely to see any correlation on this plot within the time range.

After aligning the points, the average offset between the first two epochs is 0.74 milli-arcsec with a standard deviation of 0.91 milli-arcsec. The average deviation between the second and third epochs is 0.58 milli-arcsec with a standard deviation of 0.72 milliarcsec. These values do not include two points with an offset greater that 3.0 milli-arcsec (4.2-σ). This gives a single epoch standard deviation of about 0.5 milli-arcsec. The larger scatter between the first two epochs is probably a function of the quality of the observations, with the third epoch the being the only experiment with four antennas. Fig. 4.38 shows a plot of the scatter among the components versus the peak flux density of the maser components. The scatter in the potions shows a strong dependence on the flux density of the component, which is to be be expected.

The limit on proper-motion is about 1.1 milli-arcsec yr^{-1}. The implied mass of the central star (from the v-a diagram) and the size of the source give a maximum proper-motion of about 1.0-1.5 milli-arcsec. However, as the experiment can only detect relative proper-motion this value is consistent with the limit on proper-motion measured.

4.8.4 NGC 6334F

The source NGC 6334F has previously been imaged at 6.7-GHz by Ellingsen (1996) using MkII VLBI in May 1992. This gives a 4.25 yr time-range till the August 1996 observations. Fig. 4.39 shows the proper-motion vector and p-a diagrams. The

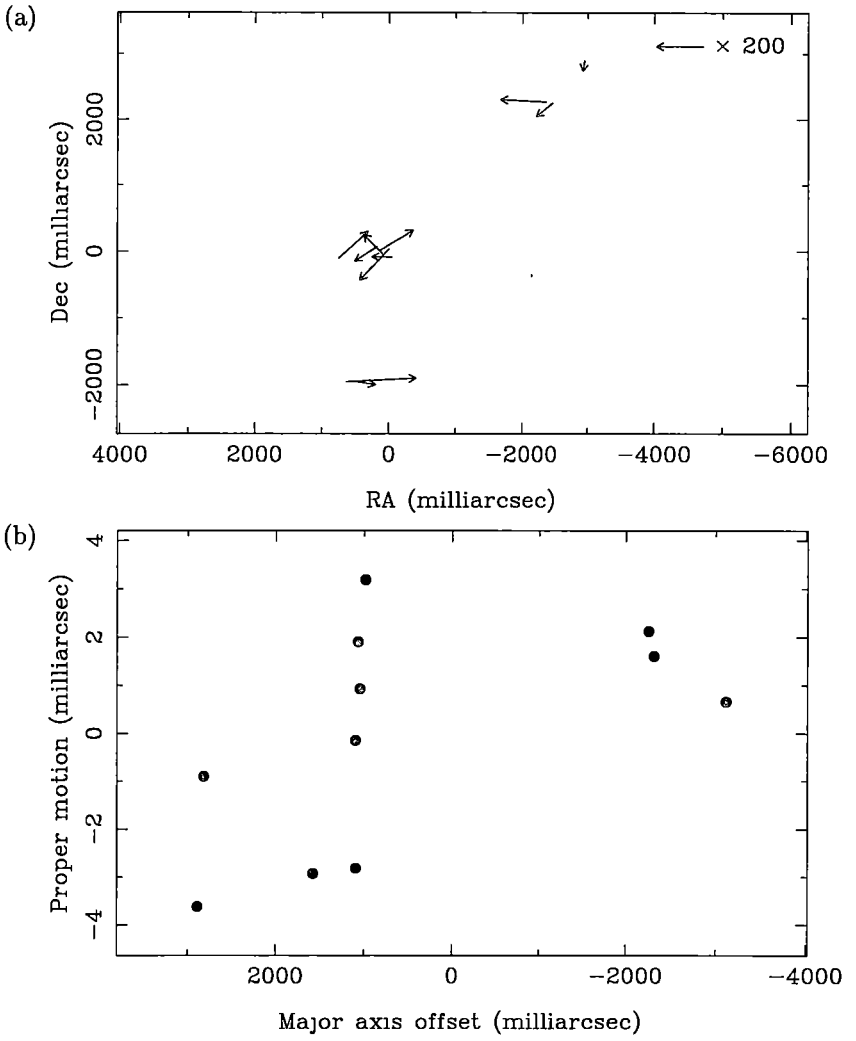

Figure 4.39: Proper-motion and p-a diagram for NGC 6334F.

average offset between the components is 2.5 milli-arcsec with a standard deviation of 2.7 milli-arcsec. The errors in the 1992 observations are expected to be larger than than the current S2 observations because of the limited spectral resolution and less sensitive receivers available in 1992. The largest offset is 5 milli-arcsec, giving a proper motion limit of 1.2 milliarcsec yr^{-1}.

4.9 Discussion

4.9.1 Coincidence of 6.7- and 12.2-GHz components

The present observations have doubled the number of methanol maser sources which have been imaged using VLBI at both 6.7- and 12.2-GHz. All sources which have been imaged at both transitions (W3(OH), NGC 6334F, G 309.921+0.479 and G 345.010+1.792) have a significant number of components which are coincident in both space and velocity. This provides a stringent constraint on any

pumping scheme for methanol, as it must be capable of producing strong maser emission in both transitions. Many 6.7- and 12.2-GHz components do not have any detected emission at the other transition. This may simply be because the "missing" emission is too weak to detect. However, given the brightness of many of the components (>100 Jy) and the sensitivity of the current observations (~1 Jy) this does not seem likely. Any pumping scheme for methanol must be capable of producing both strong 6.7- and 12.2-GHz emission as well as strong emission at one of the transitions and weak, or no emission in the other.

4.9.2 Comparison with ATCA observations

A detailed comparison of the ATCA and VLBI data show that the ATCA observations determine the overall morphology of the maser sources very well. The position of many of the ATCA components is accurate to a few tens of milli-arcsec, though a significant fraction of the observed components are a blend of spatially separate emission, which can be up to hundreds of milli-arcsec apart. Although the basic shape and velocity profile obtained with the ATCA is consistent with the VLBI observations the ATCA data tend to show straighter lines with a more uniform velocity gradient. This is partly because the lower resolution observations of the ATCA are averaging the full emission of the source, which will tend to eliminate effects of turbulence within the masing molecular cloud. In this respect the ATCA observations give a better *overall* picture of the methanol emission from the source.

4.9.3 Viability of the proper-motion experiment

As the modelling in Section 4.7.2 has shown, the expected proper-motions (if the masers are in Keplerian discs) is quite small, and a significant period is needed in order to see the relative proper-motions across the disc.

The main limitations on the accuracy of the observations are:

- the u-v coverage. With only four antennas (and sometimes only three) which have a north-south separation the u-v coverage is limited. There is also a significant un-sampled region in the u-v plane corresponding to intermediate baselines, as the baselines to Hobart are significantly longer than between the other three antennas (see Fig. 4.40). The most significant problem with the limited u-v coverage is the large side-lobes which make reliable cleaning of an image difficult if there are multiple components present at the same velocity (which is common). A small number of antennas also makes self-calibration less robust. The implied rms of 0.5 milli-arcsec is derived by comparing a 3 baseline experiment with a 6 baseline experiment. Thus a better rms should be achievable when comparing two 6 baseline experiments. When the Ceduna antenna (in South Australia) becomes available at 6.7-GHz the u-v coverage in the east-west direction will be significantly improved, which should dramatically enhance the quality of the VLBI data.

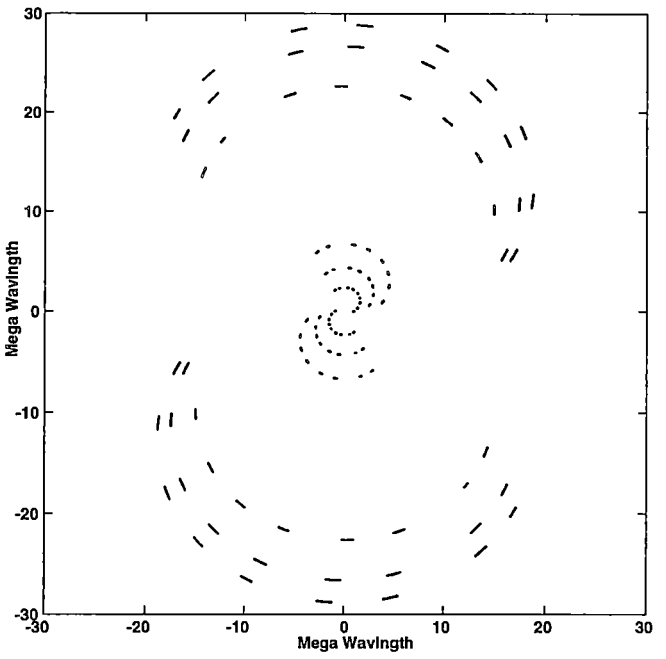

Figure 4.40: A typical u-v coverage for a 4 antenna experiment.

- the components are resolved. As the ATCA observations have shown, the positions of unresolved components can be measured to a fraction of the size of the synthesised beam. Although the components are partially resolved, the u-v data could be well modelled with 2-dimensional Gaussians, so fitting a Gaussian to the image data should still yield a meaningful position. The positional accuracy of the individual components will vary, depending on how resolved a component is, and its flux density.

- the individual components show a significant shift in position with respect to velocity (Section 4.6). The final position of the component is a flux density weighted average of the individual channels. As the position shift is the same from one epoch to the next, the measured proper motion is still meaningful, unless the relative flux density from the separate channels varies, which will give an apparent change in position. Note that calculating of the proper-motion channel by channel and then averaging the proper-motion vectors is no different than averaging the channel positions at each epoch then calculating the proper-motion.

The errors in the positions of the components of the two sources which have been imaged at multiple epochs, G 339.878−1.252 and G 345.010+1.792, have a standard deviation of 1.1 and 0.5 milli-arcsec respectively. The G 345.010+1.792 components tended to be less resolved than those in G 339.878−1.252, which is probably the reason for the smaller errors. As these offsets are based on comparison of a three baseline and a six baseline experiment, the achievable accuracy will

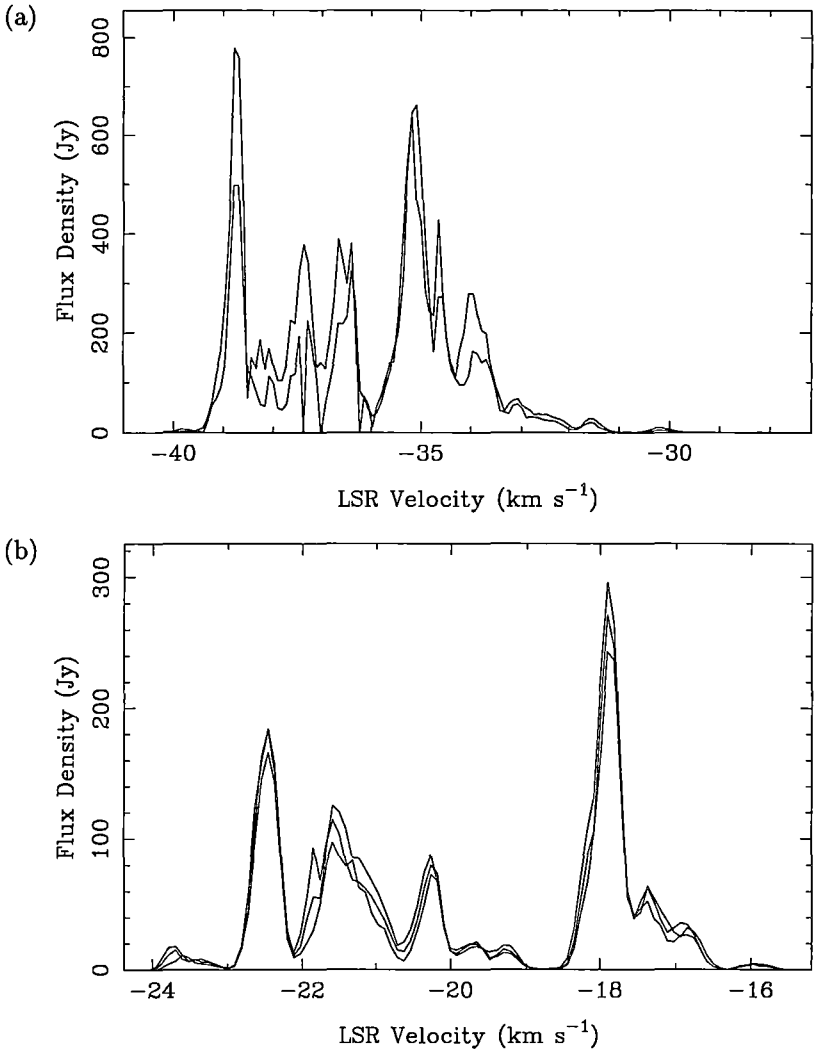

Figure 4.41: Flux density variations for (a) G 339.878−1.252 and (b) G 345.010+1.792.

probably be better than this in the future

Proper motion experiments on H_2O masers are severely hampered by temporal changes in the maser flux density. Fig. 4.41 shows the spectrum of the sources G 339.878−1.252 and G 345.010+1.792 at the epochs currently processed. The spectrum has varied slightly, but not enough to cause any problems identifying components from one epoch to the next. As mentioned before, Caswell *et al.* (1995a) find that the methanol maser flux density variations occur in a quasi-periodic fashion and individual components persist for many years.

Assuming proper-motions are detected, it may be debatable whether or not the cause has an underlying kinematic origin (such as a rotating circumstellar disc) or is some non-kinematic effect such as a traveling excitation wave through the molecular cloud or chance realignments of coherency paths. Bloemhof *et al.*(1996) found that the shape and orientation of maser spots in W3(OH) persisted between two epochs spaced by eight years, despite proper-motions larger than the spot size. This would be expected if the maser shapes are largely inherited from the

underlying maser-emitting gas clouds and rules out non-kinematic effects.

When this proper-motion project commenced, it was anticipated that the time scale of the project would the of the order of 5 years. However the simulations have shown that it will be difficult to detect proper-motions over this timescale and a period of the order of ten years will be needed. Given the large amount of telescope time this would require, and the huge quantity of data produced, it seems more realistic to increase the time between epochs to two years. Variations of the flux densities is small enough that a two year sampling period should be adequate. Alternatively, if the quality of the observations can be improved, the time required would also decrease.

4.10 Conclusion

Milli-arcsec resolution VLBI images have been made of the 6.7-GHz emission of 5 methanol sources, as the first stage in a proper-motion experiment. The VLBI images confirm that theses sources have a linear morphology with a velocity gradient, and rule out the possibility that instrumental effects are the cause of the linear sources.

Comparing the ATCA and VLBI data, the accuracy of the ATCA data is very good and gives the overall shape of the source well. The ATCA positions are accurate to a few tens of milli-arcsec for many of the components, though blending of multiple components in the ATCA images does occur in a significant number of components.

For many, but not all, of the components the 6.7- and 12.2-GHz emission is coincident to within two milli-arcsec in all four sources which have been imaged at frequencies using VLBI. This places a strong constraint on any pumping scheme which must be capable of producing both strong 6.7- and 12.2-GHz emission as well as strong emission in one of the transitions but not the other.

The positions of individual channels which comprise the maser components show an ordered shift with velocity. This has been shown to be consistent with a velocity gradient across the masing molecular cloud. Calibration errors have been excluded. The marching shows a systematic directional behavior in several of the sources, indicating that the cause may have a kinematic origin.

For the sources which have been imaged at multiple epochs in the current experiment, or previously imaged using VLBI, no proper-motion has been detected. The time-scale of these observations is too short for this to place any meaningful constraints on the disc model of methanol masers.

Simulations of maser components in a Keplerian disc show that it will be difficult to detect proper-motion within a five year period given the quality of current observations. As it will take closer to 10 years to detect proper-motion, the time period between observations should be increased to 2 years. Variations in the flux density of the sources should not cause any problems.

Chapter 5

A comprehensive search for extragalactic 6.7-GHz methanol masers

C.J. Phillips,[1] R.P. Norris,[2] S.P. Ellingsen[1] and D.P. Rayner[1]

[1] Department of Physics, University of Tasmania, GPO Box 252-21, Hobart, TAS 7001, Australia

[2] CSIRO Australia Telescope National Facility, PO Box 76, Epping, NSW 2121, Australia

5.1 Abstract

We have used the Australia Telescope Compact Array (ATCA) to search for 6.7-GHz methanol maser emission towards 87 galaxies. We chose the target sources using several criteria, including far-IR luminosities and the presence of known OH megamasers. In addition, we searched for methanol masers in the nearby starburst galaxy NGC 253, making a full spectral-line synthesis image. No emission was detected in any of the galaxies, with detection limits ranging from 25 to 75 mJy. This is surprising, given the close association of OH and methanol masers in Galactic star formation regions, and significantly constrains models of OH megamaser emission. This absence of maser emission may be a result of low methanol abundances in molecular clouds in starburst galaxies.

5.2 Introduction

Extragalactic maser emission was first discovered in NGC 253 in the 1665- and 1667-MHz transitions of OH (Whiteoak and Gardner, 1974) with a luminosity about 100 times greater than typical Galactic OH masers. In 1982 an OH 'megamaser', a maser a million times more luminous than the most luminous Galactic OH masers, was discovered in Arp220 (IC 4553) (Baan *et al.*, 1982). Since then

more than 50 extragalactic OH sources (often collectively called megamasers, although some of them extend to lower luminosities) have been discovered (Baan, 1993). These OH sources are characterized by broad emission lines (up to several 100 km s^{-1}) and stronger emission at 1667 MHz than at 1665 MHz. This is in contrast to Galactic OH masers in star-forming regions which have a typical velocity range of 10 km s^{-1} and emission stronger at 1665 MHz than at 1667 MHz.

The standard model of OH megamasers (typified by Arp220) is that low-gain amplification occurs in a molecular disc around the nucleus of the galaxy (Norris, 1984). The gas is pumped by far-infrared radiation (Baan, 1989) and amplifies the nuclear continuum emission.

The number of known extragalactic H_2O masers is smaller than the number of OH masers, and can be divided into two types. The first extragalactic H_2O maser was discovered in M33 (Churchwell *et al.*, 1977). This has a luminosity similar to the brightest Galactic maser, W49. Over a dozen H_2O masers of a similar luminosity have been discovered in other galaxies, including NGC 253. In 1979 a new class of H_2O masers was discovered in NGC 4945 (Dos Santos and Lépine, 1979). The intrinsic brightness of NGC 4945 is about 100 times greater than W49. 15 similarly bright masers have since been discovered, and the strongest, TXFS2226-184, is 5000 times more luminous than W49, and seven orders of magnitude stronger than typical Galactic H_2O masers (Koekemoer *et al.*, 1995). These H_2O megamasers occur within a few pc of the galactic nucleus (Claussen and Lo, 1986; Greenhill *et al.*, 1990). In the Claussen & Lo model the maser emission occurs in a dense disc of gas and dust close to the nucleus of the galaxy. The masers are believed to be collisionally pumped as a result of the gas being heated by X-rays (Neufeld *et al.*, 1994; Neufeld and Maloney, 1995).

OH and H_2O megamasers are extremely powerful astrophysical tools. For example, VLBI observations of the H_2O megamasers in NGC 4258 have arguably given the strongest evidence yet for the existence of massive black holes in active galaxies. The masers in this galaxy clearly show a Keplerian rotation, indicating a central mass of 3.5×10^7 $M_\odot$ in a region with a radius less than 0.13 pc (Miyoshi *et al.*, 1995; Greenhill *et al.*, 1995). Similar results are being found in NGC 1068 and the Circinus galaxy (Greenhill *et al.*, 1996; Greenhill *et al.*, 1997).

Strong methanol emission in the 12.2-GHz ($2_0 - 3_{-1}$ E) and 6.7-GHz ($5_1 - 6_0A^+$) transitions is often found in regions of star-formation (Batrla *et al.*, 1987; Menten, 1991a). VLBI observations show that the 12.2- and 6.7-GHz masers are often spatially coincident (Menten *et al.*, 1992; Ellingsen, 1996). These methanol transitions are also closely associated with OH, often coincident to within less than 1 arcsec (Caswell *et al.*, 1995d).

Interferometric imaging of these sources has shown that they are often located in lines or arcs, with a simple velocity gradient along the line (Norris *et al.*, 1993; Norris *et al.*, 1998; Phillips *et al.*, 1996). Norris et al. (1998) interpret these sources as edge-on circumstellar discs around young massive stars.

Although ~400 Galactic 6.7-GHz methanol masers have been found (Ellingsen *et al.*, 1996b, and references therein), only three extragalactic methanol masers are known, all in the Large Magellanic Clouds (Sinclair *et al.*, 1992; Ellingsen *et al.*, 1994a; Beasley *et al.*, 1996). These masers are unremarkable and their

intrinsic brightness is similar to Galactic methanol masers. Only one published search for 6.7-GHz methanol megamasers has been made, in which 10 known OH and H_2O megamaser galaxies were searched for 6.7-GHz emission, but none was found (Ellingsen *et al.*, 1994b). Given the close association of methanol and OH in Galactic masers, this is surprising.

We present here a survey of 87 galaxies for 6.7-GHz megamaser emission, covering a variety of different types of galaxies. We have also done full spectral-line imaging on the edge-on starburst galaxy, NGC 253, to detect either megamaser emission or else strong maser emission associated with star-formation regions.

5.3 Observations

5.3.1 NGC 253

The observations were made with the Australia Telescope Compact Array during an 11-h period on 1994 July 28 with the array in the 6A configuration, which gives 15 baselines ranging in length from 337 to 5939 m. A bandwidth of 8 MHz was used with the correlator configured to give 1024 spectral channels in each of two orthogonal linear polarizations. The typical system temperature of the antennae at 6.7-GHz is 120 K.

Two pointing centres were required to accommodate the large velocity spread across the galaxy ($\sim$450 km s^{-1}) and its large angular size (20 arcmin compared with a primary beam FWHM of 8.4 arcmin). The positions used were (00:47:38.98, -25:16:13.2) and (00:47:27.39, -25:18:19.1) J2000, with central frequencies 6664 and 6660 MHz, respectively. The two pointing centres were each observed 11 times for 25 min over 11 h, interspersed with observations of the secondary calibrator 0023-263.

The data were calibrated and imaged using the Astronomical Image Processing System (AIPS). 1934-638 was used as the primary flux calibrator, with an assumed flux density of 3.93 Jy at 6.6 GHz. After the initial calibration, the spectral channels were averaged and a continuum image made. The centre of the galaxy was clearly detected in both images with a flux density of 220 mJy. These continuum images were then phase self-calibrated (improving the signal-to-noise ratio from 130 to 300) and the improved phase calibration applied to the non-averaged spectral-line data. Because the spectral resolution of 0.35 km s^{-1} is comparable to a typical FWHM of 0.5 km s^{-1} for Galactic masers (Ellingsen *et al.*, 1996b), the data were not Hanning smoothed. Two 825-channel spectral cubes (with a velocity span of 290 km s^{-1}) were made for each of the pointing centres. Each frequency channel of the cube covered 256$\times$256 arcsec^2 with an angular resolution of 2.9$\times$1.3 arcsec^2. Together the two cubes covered approximately the inner third of the galaxy.

5.3.2 Megamaser survey

Since methanol is likely to be abundant only in molecule-rich galaxies, which are typically *IRAS* sources, the source selection for this survey included only southern

IRAS galaxies, with known redshifts, known 60 μm flux density, and declination $< +20°$(except Arp 220). No sources with z > 0.15 were considered. Preference was given to sources that satisfied one or more of the following criteria:

(i) known OH megamaser galaxy;

(ii) known H_2O megamaser galaxy;

(iii) 60-μm flux (S60) > 10 Jy;

(iv) S60 (Jy) $\times$ z > 0.3;

(v) $\log(L_{\rm FIR}/{\rm L}_\odot) > 12$.

The observations were made between 1996 May 28 and 1996 June 3 using the ATCA, with the array in the 750D configuration, with 10 baselines ranging in length from 30.6 to 719.4 m. A bandwidth of 16 MHz was used with the correlator configured to give 512 channels for two orthogonal linear polarizations.

87 sources were observed from the sample discussed above. Table 5.1 lists the observed sources and their selection criteria. Each source was observed for 1 h, with an observation of a secondary calibrator made before and after each source. Sources were observed as close to transit as possible to simplify data processing (as discussed below), although this meant some of the observed sources did not satisfy any of the selection criteria specified above (because of the uneven distribution of the sources on the sky).

There are several advantages in using an interferometer instead of a single dish for spectral-line detection experiments.

(i) Single-dish observations are often made in 'position-switch' mode, spending half the observing time at a reference position and creating a "quotient spectrum". This is not required for an interferometer, enabling the same sensitivity to be achieved in one quarter of the time.

(ii) Interferometers are also less susceptible to variations in the bandpass, enabling longer integrations.

The disadvantages are that neither a scalar nor a vector average of interferometer data produces the same response as a single dish.

(i) A scalar average spectrum of the data (averaging the individual power spectra from each baseline and each integration period) produces a lower sensitivity to weak spectral features because of noise bias (Thompson *et al.*, 1986), which appears as a positive baseline offset in the spectrum, but under which weak spectral features are submerged.

(ii) A vector average of the data (adding the real and imaginary parts separately, after phase rotation to a suitable phase centre position) overcomes problem (i), but the spectrum is restricted to an area the size of the synthesised beam of the interferometer, centred at the averaging phase-centre.

For many of the sources in the sample, the position of the centre of the galaxy was not sufficiently well known to guarantee that the maser would lie at the phase centre of the synthesised beam. Making spectral cubes of all sources observed was not practical and so, instead, we overcame this problem by making all observations close to transit, so that the synthesised beam was approximately 15 arcsec $\times$ 2 arcmin, elongated in a north-south direction. We then plotted a series of spectra each with a different phase centre. By making a series of seven plots with the phase centre shifted by 10 arcsec from east to west across the observed position, we are sensitive to emission from sources within $\pm$30 arcsec of the nominal galaxy position.

For normal interferometric observations the antenna-based gains and delays need to be determined before each observing session, by observing both a primary and secondary flux calibrator at each observing frequency. To maximize the efficiency of the search, we chose not to do a full amplitude calibration, but instead estimated gains based on the assumed secondary calibrator flux density, with additional calibration observations planned in the event of a detection. Since only rough delay calibration was used, we expect a 10-20 per cent error caused by decorrelation during the observation. The amplitude calibration should be better than about 30 per cent for most sources, though some may be only within a factor of 2.

Basic calibration of the data was done using the AIPS software. A series of seven spectra, shifted in position as described above, was plotted for each source. To facilitate the detection of both narrow and broad emission, plots were produced with no smoothing, Hanning smoothing, and boxcar smoothing over 5 and 10 channels. The spectral resolution of the four smoothing schemes was 1.5, 3.0, 7.4 and 14.9 km s^{-1} respectively.

5.4 Results

5.4.1 NGC 253

The rms noise was typically 23 mJy in each 0.35 km s^{-1} channel of the two image cubes. The peaks in each cube were found (the largest $\sim$ 130 mJy) and carefully checked for real emission in the image cube and u-v data. We did not detect any methanol emission. Plots of the spatial distribution of the peaks in the cube were consistent with noise, and there was no correlation with the position of the galaxy. The noise profile was nearly Gaussian but with slightly broader wings. Assuming a 5σ detection threshold implies no 6.7-GHz methanol stronger than 107 mJy. Assuming a distance of 3.4 Mpc to NGC 253 (Huchtmeier, 1972), the most luminous Galactic 6.7-GHz methanol maser, G 340.78$-$0.10 (Norris *et al.*, 1993), would have a flux density of 2.6 mJy in NGC 253. Thus our observations were not sensitive enough to detect Galactic-strength methanol masers in NGC 253, but would have detected masers 35 times stronger. The OH masers in NGC 253 are about 100 times stronger than those in our Galaxy, and so a corresponding experiment at OH wavelengths would have detected the masers at the 14σ level.

Table 5.1: The selected sample of galaxies

IRAS Name	Alias	Position (J2000) RA	Dec	OH Peak (mJy)	H_2O Flux (mJy)	z	*IRAS* 60μm Jy	Sel.[a] Crit.	RMS[b] Noise (mJy)	References[c]
00198−7926		00:21:54	−79:10:08			0.0724	3.2	o	14.3	
00335−2732		00:36:01	−27:15:34	<20		0.0691	4.4	z	9.1	52,53
00450−2533	NGC 253	00:47.33	−25:17.18	120	5000	0.001	759.0	hszw	16.6	1,3,13,15,16,27,29 33,38,46,52,56,59
01418+1651	III Zw 35	01.44:31	+17·06:09	240		0.0273	11.9	hsz	19.0	20,24,29,30,38,42,45 46,50,53,58,63
01458−2828		01:48:09	−28.14:02			0.1352	0.8	o	19.7	
02401−0013[d]	NGC 1068	02:42:41	−00·00:48	5	670	0 0038	186 0	o	30.0	10,15,18,56,59,60,61,62
02512+1446	Z 440-30	02:54:02	+14:58:15			0.031	7.7	o	21.0	
03317−3618	NGC 1365	03:33:36	−36:08:23	50	<210	0.0055	78 2	hsz	22.8	40,59,61
03359+1523		03:38:47	+15:32:54			0.035	5.8	o	18.5	
03540−4230[d]	NGC 1487	03:55·45	−42:22.07			0.0026	3 3	o	8.0	56
04189−5503	NGC 1566	04:20.00	−54·56:18	<32	<340	0 005	12.7	s	25.2	40,56,61
04191−1855	ESO 550-25	04:21:20	−18:48:39			0.0308	5.8	o	25.3	
05059−3734	NGC 1808	05·07:42	−37:30:46	<32	<300	0.0033	97.1	sz	34.2	40,52,59,61
05100−2425		05:12:09	−24:21:54	18		0.0338	4.1	h	13.6	46,52
05189−2524		05:21:01	−25:21:45	30		0.0415	13.9	hsz	14 6	24,40,52
05238−4602	ESO 253-3	05:25:18	−46:00:18			0.0407	2 8	o	1.9	
06035−7102		06:02:54	−71:03:12	<30		0.0796	5 0	lz	11.4	52
06076−2139		06:09.45	−21:40:22	<15		0.0374	6.3	o	10 8	52
06102−2949	ESO 425-13	06:12:12	−29:50·31	<40		0 0611	4.4	o	14.5	52
06206−6315		06:21:01	−63·17·23	<20		0 0917	4.0	lz	9.3	52
06219−4330		06.23:25	−43:31:45	<25		0.063	4.7	o	8.1	52
06259−4708	ESO 255-7	06:27:22	−47:10:37	<25		0.038	9.4	z	8.7	52
08014+0515	Mrk 1210	08:04:06	+05:06:50		160	0.013	1.8	w	22.7	54,61
08071+0509		08:09:48	+05:01:03	y[e]		0.0543	4.8	h	9.3	43
08520−6850		08:52:32	−69:01:54	<20		0.0463	5 8	o	23.8	52
09004−2031	ESO 64-11	09:02:46	−20:43:30	<15		0.0085	8 7	o	96 2	24,52
09149−6206	QSO0914-621	09:16:09	−62:19:29			0.0573	2 5	o	15.6	
10039−3338	ESO 374-32	10:06:07	−33:53:22	240		0.0337	9.1	hz	18 0	34,46,47,52,56,58,63
10173+0828		10:20:00	+08:13:34	100		0.0485	6.1	h	21.9	30,38,46
10221−2317	ESO 500-34	10:24:31	−23:33:12	<70		0.013	11.3	s	27.0	40
10257−4338	NGC 3256	10:27:52	−43:54:09	<30		0.0096	94.6	sz	78 8	40,52
11095−0238		11:12:03	−02:54:18			0.106	3 2	lz	12.7	
11143−7556		11:16:04	−76:12:53	<20		0.0054	47.7	s	48 4	40,52
11365−3727	NGC 3783	11:36:33	−37:27:42		<250	0.0107	3.4	o	23.6	61
11506−3851	ESO 320-30	11:53:12	−39:07:49	90	<850	0.010	34 2	hsz	22.2	17,29,38,40,46,52,53,56,61
11581−2033	ISZ 096	12:00:43	−20:50:07			0.0621	1.7	o	11.9	
12112+0305		12:13:46	+02:48:41	45		0.073	8 4	hlz	12.9	32,38,42,46,49,51,53
12232+1256	NGC 4388	12:25:47	+12:39:41	<20	<60	0.0085	10 9	s	25 7	16,51,61
12243−0036	NGC 4418	12:26:57	−00.52:50	7	<125	0.007	43.9	hsz	29.3	24,29,31,36,38,40,46 53,56,58,61
12294+1441	NGC 4501	12.31:59	+14:25·10		<160	0.0077	14.2	s	27.6	15,61
13001−2339	ESO507-70	13:02:52	−23.55.17	<18		0.0209	14.1	s	26.3	40,52
13025−4911	NGC 4945	13:05:26	−49:28·16		6200	0.0020	388.1	wsz	160.7	1,2,4,9,29,46,52,59,61
13225−4245	Centaurus A	13:25:28	−43:01·09	120	<580	0.0018	171.0	hsz	645.5	29,57,61
13335−2612		13:36:22	−26:27:30			0.1248	1.4	o	15 5	
13451+1232		13:47:33	+12:17:24	1.7		0.122	2.0	h	45 1	48
14092−6506	Circinus	14:13:10	−65:20:22		16000	0.0013	248.7	wsz	56.3	6,9,19,29,56,59,61,64
14147−2248		14:17:36	−23.02:02	<25		0.0794	2 4	o	11.2	52
14348−1447	GNH 35	14·37:38	−15:00:24			0.0824	6 8	lz	16.6	
14376−0004	NGC 5713	14·40:11	−00.17:20	<12		0.007	19.8	s	41.1	16,51
14378−3651		14:40:58	−37:04·25	<20		0 0682	6.5	lz	11.7	52
15107+0724	Zw 049.057	15:13·13	+07:13:35	13		0 012	21.6	hs	19.3	21,26,35,38,46,53
15247−0945		15:27·26	−09.55.57	y[e]		0.0400	4.7	h	13 2	44,46
15268−7757	ESO 22-10	15:33:36	−78:07:28	<25		0.0087	4.2	o	16.5	52
15322+1521	NGC 5953	15:34:32	+15:11:42		<90	0.0066	10.4	s	20.0	61
15327+2340	Arp220	15:34:57	+23:30:12	300	<200	0.0182	104.0	hsz	28.0	5,7,8,11,12,15,16,23 24,25,28,29,38,39,46 53,55,56,58
16164−0746		16:19:12	−07:54.03	<25		0 021	10.2	s	25.4	40

Table 5.1: *continued...*

IRAS Name	Alias	Position (J2000) RA	Dec	OH Peak (mJy)	H_2O Flux	z	*IRAS* 60μm Jy	Sel.[a] Crit.	RMS[b] Noise (mJy)	References[c]
16330−6820	ESO 69-6	16:38:13	−68.26:43	<35		0.0456	7.2	z	121.4	52
16399−0937		16:42:40	−09:43:14	25		0.0267	8.5	h	16.8	22,46
16504+0229	NGC 6240	16:52:59	+02.23.59	<20	<90	0.0245	23.5	sz	13.4	24,29,40,61
17208−0014		17:23:21	−00:17·00	125		0.0428	34 1	hlsz	10.6	14,24,28,38,40,41,42 46,53,58
17260−7622		17:33:14	−76:24:48	<20		0.0181	4.2	o	18 1	52
17422−6437	IC 4662	17:47:06	−64:38:25	<12		0.0011	8.3	o	22.1	52
18093−5744	ESO 140-10	18:13:40	−57:43:38	<25		0.017	15.2	s	20.9	52
18293−3413		18:32.40	−34:11:26	<18		0.018	35.3	sz	41.2	40,52
18325−5926	Fair 49	18:36:59	−59:24:09	<32	<575	0.0192	3.2	o	20 7	4061
18401−6225	ESO 140-43	18:44:47	−62:21:57	<35	<290	0.0136	2.0	o	18.1	40,61
18421−5049	ESO 230-10	18:46:02	−50.46:30	<20		0.0177	5.1	o	15.9	52
18508−7815	QSO1850-782	18:58:33	−78·11·49			0.1618	1.1	o	11.3	
19115−2124	ESO 593-8	19:14:32	−21:19:04	<20		0.0495	6.2	z	17.6	52
19254−7245	Superantennae	19.31:21	−72·39·22	<40		0.0615	5 2	z	3.6	52
19297−0406		19:32:21	−04·00:06			0.0856	7.2	lz	14.1	
19393−5846	NGC 6810	19:43:34	−58:39.21	<25		0.006	18.1	s	20.2	40
20087−0308		20:11:23	−02:59:54			0.1033	4.6	lz	15.6	
20100−4156		20:13:30	−41:47:35	200	<3500	0.129	5.2	hlz	4.8	37,46,49,52,58,61,63
20414−1651		20:44:17	−16·40:14			0 0871	4 7	lz	11.5	
20491+1846	Z 448-16	20:51:26	+18.58:08	y[e]		0.0283	2.8	h	9.4	43
20550+1656	II Zw 96	20:57:24	+17.07.40	40		0 0362	13.1	hsz	9.2	21,24,38,46,53
20551−4250	ESO 286-19	20:58:27	−42·39·06	<30		0.0428	12.7	sz	11.6	40,52
21130−4446		21.34:15	−44:32.43	<20		0.0925	3.2	l	12.2	52
21219−1757	QSO2121-179	21:24:42	−17:44:46			0.113	1.1	o	8 7	
21330−3846	ESO 343- 13	21:36:11	−38:32:37	<35		0.0191	6.8	o	12.5	52
21453−3511	NGC 7130	21:48:19	−34:57:09	<20	<450	0.0161	16.7	s	24.7	40,52,61
22287−1917	ESO 602-25	22:31:25	−19:01:60	<25		0.025	5.8	o	15.7	51
22467−4906	ESO 239-2	22:49:40	−48:50:59	<20		0.0423	6.6	o	15.4	52
22491−1808		22:51:49	−17:52:24	15		0.0777	5.5	hz	10.5	51,46,49
23007+0836	NGC 7469	23:03:16	+08:52:26	<8	<60	0.0162	27.0	sz	15.6	24,40,59,61
23128−5919	ESO 148-2	23:15:47	−59:03:17	<22		0 0447	11.1	sz	17.8	40,52
23156−4238	NGC 7582	23:18:23	−42·22:11	<32	<265	0.0053	48.0	s	35.4	40,52,61
23230−6926		23:26·04	−69:10:16	<20		0.1062	3.7	lz	13.5	52

Notes:

(a): The selection parameters satisfied by this source (see Section 2 2). s=S60>10; z=S60×z>0 3; l=logLIR>12; h=known OH megamaser; w=known H_2O megamaser; o=other *IRAS* galaxy.
(b): The quoted rms is after boxcar smoothing of five channels. The data were also inspected visually with no smoothing, Hanning smoothing and box-car smoothing of five and ten channels.
(c): 1=(Whiteoak and Gardner, 1974); 2=(Whiteoak and Gardner, 1975); 3=(Lépine and Marques Dos Santos, 1977); 4=(Dos Santos and Lépine, 1979); 5=(Baan *et al.*, 1982); 6=(Gardner and Whiteoak, 1982); 7=(Baan and Haschick, 1984), 8=(Norris, 1984); 9=(Moorwood and Glass, 1984); 10=(Claussen *et al.*, 1984); 11=(Norris *et al* , 1985); 12=(Norris, 1985); 13=(Turner, 1985); 14=(Bottinelli *et al.*, 1985); 15=(Henkel *et al.*, 1986); 16=(Unger *et al.*, 1986); 17=(Norris *et al.*, 1986); 18=(Claussen and Lo, 1986), 19=(Whiteoak and Gardner, 1986); 20=(Chapman *et al.*, 1986); 21=(Bottinelli *et al.*, 1986); 22=(Staveley-Smith *et al.*, 1986); 23=(Baan *et al.*, 1987b), 24=(Staveley-Smith *et al.*, 1987); 25=(Baan and Haschick, 1987); 26=(Baan *et al.*, 1987a); 27=(Ho *et al.*, 1987); 28=(Henkel *et al.*, 1987); 29=(Norris *et al.*, 1987); 30=(Mirabel and Sanders, 1987); 31=(Bottinelli *et al.*, 1987); 32=(Mirabel *et al.*, 1988); 33=(Nakai and Kasuga, 1988), 34=(Kazes *et al.*, 1988); 35=(Martin *et al.*, 1988a); 36=(Martin *et al.*, 1988b); 37=(Staveley-Smith *et al.*, 1989); 38=(Baan, 1989); 39=(Diamond *et al.*, 1989); 40=(Norris *et al.*, 1989); 41=(Mirabel *et al.*, 1989); 42=(Baan *et al.*, 1989); 43=(Bottinelli *et al.*, 1989); 44=(Kazes *et al.*, 1989); 45=(Chapman *et al.*, 1990); 46=(Haschick *et al.*, 1990); 47=(Kazes *et al.*, 1990); 48=(Dickey *et al.*, 1990); 49=(Kazes and Baan, 1991); 50=(Montgomery and Cohen, 1992); 51=(Baan *et al.*, 1992); 52=(Staveley-Smith *et al.*, 1992), 54=(Braatz *et al.*, 1994); 55=(Lonsdale *et al* , 1994); 56=(Ellingsen *et al.*, 1994b); 57=(van Langevelde *et al.*, 1995); 58=(Randell *et al.*, 1995), 59=(Nakai *et al.*, 1995), 60=(Gallimore *et al.*, 1996); 61=(Braatz *et al.*, 1996); 62=(Greenhill *et al.*, 1996); 63=(Killeen *et al.*, 1996); 64=(Greenhill *et al.*, 1997);
(d): These sources were not part of the current survey, but were observed by Ellingsen et al. (1994b) and included for completeness.
(e): These sources have been detected, but only the isotropic luminosity has been published.

5.4.2 Megamaser survey

All spectra for each source (phase-shifted and smoothed) were inspected visually for possible peaks in the data. A summary of the results is shown in Table 5.1. None of the 87 observed sources contained detectable 6.7-GHz emission. Assuming a detection threshold of 5σ this gives a flux-density limit of 15 to 25 mJy for most sources, which is sufficient to detect almost all known OH and H_2O megamasers. The peak flux density of known OH and H_2O megamasers associated with these sources (as well as peak flux density limits) is also given in Table 5.1.

5.5 Discussion

The 6.7-GHz $5_1 - 6_0$ A^+ transition of methanol is the second strongest masing transition observed in Galactic sources and is extremely common, which implies that it is relatively easy to produce the conditions needed for the molecule to produce maser emission. These masers are believed to exist in regions of star formation only and are closely related to OH masers. Most OH masers sources also show methanol emission, and vice-versa. Caswell et al. (1995d) have shown that the OH and methanol emission is generally coincident to within 1 arcsec. This is interpreted as meaning that the OH and methanol masers require similar physical conditions. 23 known OH megamaser sources were included in the sample (see Table 5.1). Given the close association of Galactic OH and methanol masers it is surprising that methanol emission is not seen in any of these sources.

5.5.1 NGC 253

In NGC253, the OH maser emission has a flux density of 0.1 Jy. If the Galactic methanol/OH maser intensity ratio ($\sim$10) were to apply in NGC253, then we would expect to observe a 1-Jy methanol maser, which is ruled out by our observations.

Even if the methanol maser emission does not scale with the OH emission, the high star formation rate in NGC253 might lead us to expect NGC253 to contain stronger methanol masers associated with star formation than those in our own Galaxy. Our limit of 107 mJy rules out Galactic-type masers 35 times stronger than those in our own Galaxy.

5.5.2 Megamaser survey

Our sample of megamaser candidates encompasses most of the types of galaxies in which methanol megamasers might reasonably be expected to be found. Thus our failure to detect any suggests that 6.7-GHz methanol megamasers do not exist. This result has immediate implications for models of OH megamasers.

One such model suggests that OH megamasers represent a large collection of Galactic-type masers (Baan *et al.*, 1982). As methanol is typically ten times stronger than OH in Galactic sources (Caswell *et al.*, 1995c) methanol should be

observable with our sensitivity in some, if not all, OH megamaser galaxies. Thus these observations rule out this model of OH megamasers.

We also note that our result rules out another (unpublished) model for megamasers in which a massive black hole at the galactic nucleus gravitationally lenses normal masers in star-formation regions on the far side of the galaxy. Since Galactic OH masers are usually accompanied by much stronger methanol masers, this model predicts that we should detect methanol megamasers in a substantial fraction of the OH megamaser galaxies.

This result has implications for the "standard" model of megamaser emission (Norris, 1984), in which low-gain maser amplification of a background source occurs in molecular clouds within the galactic disc. Within a megamaser galaxy, the maser path need not be confined to any one molecular cloud, but instead may encompass many different regions with widely varying conditions. Only those regions which have the right abundance, pump conditions, and velocity will contribute to the intensity of the maser. However, this process is not critically dependent on any one condition (e.g. the precise value of optical depth to the pump), because the maser path will generally sample a wide range of conditions.

An OH megamaser galaxy has, by virtue of its OH emission, already demonstrated that it has a high column density of molecular material, aligned at a suitable velocity against a suitable input source to the maser amplifier, so that all the conditions for methanol megamaser emission are already satisfied provided that (a) the methanol abundance is sufficiently high, and (b) that somewhere along the line of sight, there exist suitable pumping conditions to invert the methanol population.

We now consider possible reasons for the absence of methanol megamasers.

(i) The methanol abundance may be too low in these galaxies to support masing on the scale needed for megamaser emission. However, Henkel et al. (1987) detected methanol at millimetre wavelengths towards NGC 253 and IC 342, with abundances similar to those in our own Galaxy. This rules out a low methanol abundance as the reason for the lack of methanol megamasers.

(ii) Methanol may not form on large scales. If the methanol abundance was not sufficiently high in the molecular clouds which constitute the maser amplifiers, we would not expect to see megamaser emission. Galactic methanol masers are seen only in star formation regions and the molecules are generally thought to form on the surface of dust grains, and are released upon the destruction of the grain (Herbst, 1991). If there were processes operating within molecular clouds that depleted the abundance of methanol, then methanol abundances sufficient for maser action might be confined to star formation regions and not exist on the large scales needed to produce megamasers.

(iii) Appropriate pumping conditions may not exist for methanol masers to operate on a sufficiently large scale. We consider this less likely because (a) both OH megamasers and (Galactic) methanol masers are believed to be pumped by IR radiation, (b) the widespread nature of methanol masers in

star formation regions suggests that it is relatively easy to pump methanol and (c) as noted above, it is unlikely that the appropriate conditions do not occur anywhere along the masing path. However, we note that the methanol pumping mechanism is not yet fully understood, and it is possible that it requires special conditions, such as very high densities.

In this section, we have not considered implications of this result for H_2O megamasers, as the pump mechanisms for OH and methanol (probably IR) is significantly different from that of H_2O megamasers (collisionally pumped by X-ray-heated gas).

5.6 Conclusions

A survey of 87 *IRAS* galaxies for 6.7-GHz methanol masers detected no emission towards any of the galaxies. Our detection limits are sufficiently low to detect most known OH and H_2O megamasers. Our sample encompasses most of the types of galaxies in which we might expect to find methanol megamasers, and the sample size is large enough that we can reasonably conclude that methanol megamasers do not exist. This result has two significant implications:

(i) the absence of methanol megamasers rules out models for OH megamasers involving large numbers of HII regions similar to those in our Galaxy.

(ii) it suggests that OH megamasers are located in large molecular clouds in which the abundance of methanol is much lower than that of OH.

5.7 Acknowledgments

The Australia Telescope is funded by the Commonwealth Government for operation as a National Facility managed by the CSIRO. This research used the SIMBAD data base, operated at CDS, Strasbourg, France and the NASA/IPAC Extragalactic Database (NED) which is operated by the Jet Propulsion Laboratory, California Institute of Technology.

Chapter 6

Conclusions

For this thesis I have taken a large sample (45) of Class II methanol masers and imaged the 6.7-GHz maser transition using the ATCA. Simultaneous observations of the 8.6-GHz continuum have been made to image any UCHII regions associated with the masers and the AAT has also been used at 11.5 μm to image thermal dust in the region. This constitutes the largest sample of methanol masers which have been studied at high resolution and in detail. A VLBI proper motion experiment has commenced on a subsample of the methanol sources.

The aim of this thesis was to critically evaluate the circumstellar disc model, and obtain strong evidence for either supporting or refuting the model. The ATCA and VLBI observations have confirmed that the linear sources and velocity gradients are real and found more sources with this morphology. Unfortunately, there is no strong support of the disc model, nor is there evidence which would contradict the model. The morphology of the environment of the masers has been shown to be very complex with a wide range of properties.

The observations have found a variety of interesting and important phenomena.

- Seventeen of the 45 methanol sources have a linear or curved morphology, most showing a velocity gradient along the source. These sources are interpreted as edge-on circumstellar discs around young massive stars. Three of the sources have a morphology similar to the SiO maser in Orion-IRc2, which has been successfully modelled as an inclined circumstellar disc.

- Assuming a simple geometry for masing within a circumstellar disc, perfectly edge-on discs would be expected to be brighter than inclined discs and face-on discs weaker again, because of reduced path lengths. There is no preference for the linear sources to be brighter than the complex sources. However, the brightness of the maser components will be a function of many variables, such as beaming, molecular abundance and densities, temperature etc.

- Twenty-five of the maser sources are associated with an UCHII region. It is generally assumed that all methanol masers are associated with stars massive enough to produce an UCHII region. The sources without an associated UCHII region most likely represent lower mass stars. Absorption of UV

photons by dust within the UCHII region and optical depth effects will also reduce the observed flux density of the UCHII region. It is unlikely that methanol sources without an UCHII region are pre-main-sequence stars, as has previously been suggested.

- Most of the methanol sources associated with an UCHII region are slightly offset from the peak of the UCHII region. This is not consistent with a circumstellar disc model, but may be a projection effect. Few of the methanol sources are located at the edge of an HII region, which would be expected in a shock-front model.

- Nine out of 35 of the maser sources are associated with detectable 11.5 μm continuum emission. No correlation was found between the MIR flux density and the flux density of the maser sources.

- None of the MIR sources had a morphology consistent with a disc.

- The large number of methanol maser sources without an associated MIR source is somewhat surprising as the observations should be sensitive to embedded stars later than B3. This gives additional support to the conclusion that many methanol sources are associated with less massive stars.

- The flux density of the methanol masers shows no correlation to the MIR flux density. Many bright methanol masers have no detectable 11.5 μm emission. This may cause problems for models which pump methanol with MIR wavelength photons.

- Methanol masers are commonly assumed to be associated with *IRAS* PSC sources which have nominal positions 1 to 2 arcmin from the position of the maser. The MIR observations have shown that at 12 μm the *IRAS* observations suffer from source confusion below about 30 Jy, and assuming individual *IRAS* sources represent a single embedded star associated with any particular maser source is fraught with uncertainty.

- Comparing the derived spectral type from the UCHII flux density, MIR flux density, and *IRAS* associations shows that all these techniques have large uncertainties associated with them.

VLBI observations at 6.7 and 12.2 GHz have been made of 8 methanol maser sources which have a linear morphology. Simulations show that it will take close to 10 yrs to detect proper-motion, unless the positional errors can be reduced.

- The VLBI observations have verified that the sources have a linear structure which was suggested by ATCA observations. The positions obtained with the ATCA are accurate to a few tens of milli-arcsec in many instances, though blending of two spectral components at the same velocity can be a problem.

- Comparing the position of the 6.7- and 12.2-GHz maser components in the sources G 309.921+0.479 and G 345.010+1.792 shows that a number of the components are coincident within 2 milli-arcsec, as previously found in W3(OH) and NGC 6334F. This places strong constraints on any pumping models for Class II methanol.

- Individual components show a significant positional shift with velocity across the component. The most likely cause of this shift is a velocity gradient within the masing molecular gas. There is some evidence for systematic shifts among the components, indicating a kinematic origin.

A survey of 87 *IRAS* galaxies for 6.7-GHz methanol masers detected no emission towards any of the galaxies. The sensitivity of the observations was sufficient to detect most known OH and H_2O megamasers. The sample encompasses most types of galaxies in which methanol "megamasers" would be expected to exist, so they can reasonably be concluded not to exist. The non-detection is somewhat surprising given the widespread nature of 6.7-GHz methanol masers within our own Galaxy. This finding rules out models for OH megamasers involving large numbers of HII regions similar to those in our Galaxy, as Galactic OH and methanol masers are almost always found associated with the same HII region. This also suggests that OH megamasers are located in large molecular clouds in which the abundance of methanol is lower than OH, or the density of the gas is too low for methanol to mase efficiently.

Further work

In order to get a better understanding of the environment and dynamics of the circumstellar environment of young massive stars, further high resolution observations are needed of a range of molecular species and at a range of wavelengths.

- Methanol and OH masers are closely associated, but in few sources have both species been imaged at high resolution, and with sufficient sensitivity, to compare the distribution of the individual components of the two. I have started a project using the ATCA to do this for all methanol maser sources in the thesis sample with OH flux densities greater than 5 Jy. However, the spatial and spectral resolution of the ATCA is quite poor at 1.6 GHz, so VLBI observations will be required to do this properly.

- High resolution observations of H_2O masers associated with the methanol should also be made.

High resolution observations of methanol, H_2O and OH will give a clearer picture of the masing environment of massive stars and will help resolve questions such as whether methanol and OH are associated with shocked gas in some or even all of the sources. Similar observations of other molecules such as NH_3 may also help determine at what stage in the evolution of the stars the masers appear.

It would be highly desirable to directly image the disc which the methanol masers are thought to delineate. This would be difficult to do at high resolution

at FIR wavelengths, but may be possible using millimetre and sub-millimetre interferometry. Continuum observations could be used to image the thermal dust, and spectral observations to image thermal molecular lines. Molecular lines would have the advantage of also giving the velocity profile across the disc. The molecular line chosen should be a tracer of very high densities, which would be expected within a disc. Towards this end, the millimetre receiver on the Mopra telescope has been used to identify molecular lines which are associated with methanol and are compact (relative to the large Mopra beam).

Unfortunately, there are at present no millimetre interferometers in the Southern Hemisphere and W3(OH) is the only northern methanol source for which high resolution observations have been published. A sample of northern methanol masers is needed to study with millimetre interferometry, before the ATCA is fitted with appropriate receivers. Some EVN antennas are fitted with 6.7-GHz receivers, although the lack of a connected element interferometer will cause problems because of relatively poor single dish positions.

Clearly additional epochs of the proper-motion experiment must be obtained, and the size of the positional errors reduced. Detecting proper-motion (Keplerian or otherwise) will be one of the most powerful ways of elucidating the dynamics of these interesting objects.

Appendix A

ATCA UCHII regions

I the following pages, I have included images of the continuum sources which were serendipitously observed in the ATCA observations which constituted Chapter 2, and are not associated with any detected methanol emission.

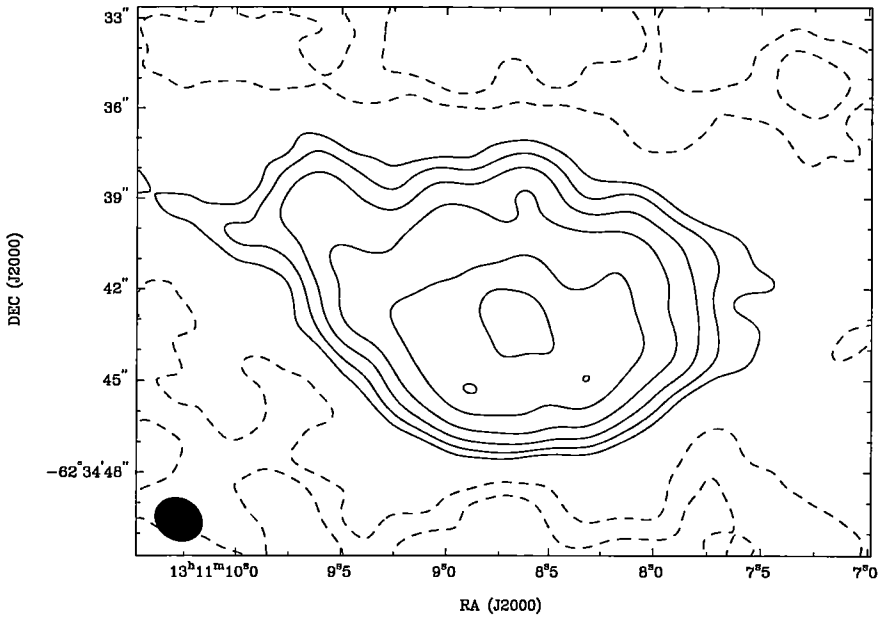

Figure A.1: Radio continuum image of G 305.199+0.206 at 8.6 GHz. The contours are at -8, -4, 4, 8, 16, 32, 64 and 90 per cent of the peak flux density (10.3 mJy beam^{-1}). The integrated flux density of the source 195 mJy. The size of the Gaussian restoring beam is 1.65×1.38 arcsec and is shown on the lower left of the plot.

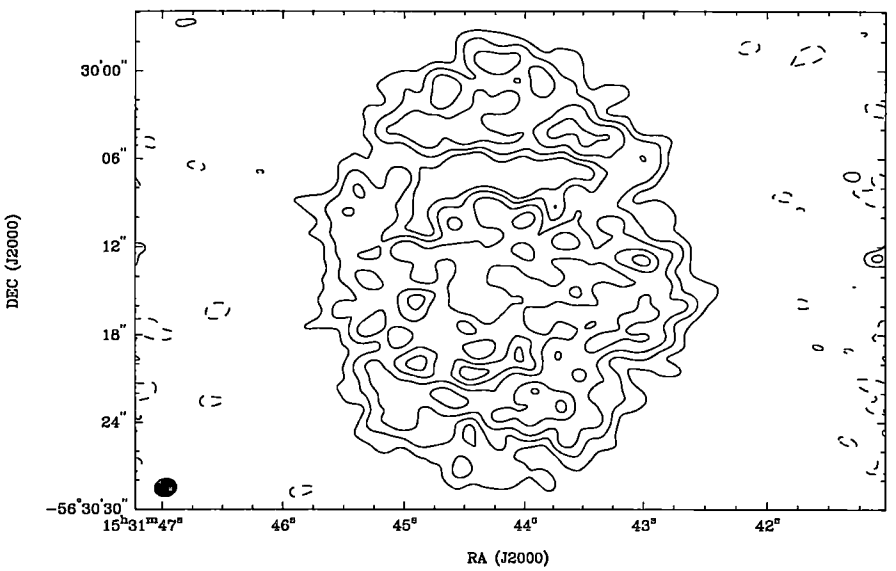

Figure A.2: Radio continuum image of G 323.744−0.253 at 8.6 GHz. The contours are at -8, 8, 16, 32, 64 and 90 per cent of the peak flux density (1.6 mJy beam^{-1}). The integrated flux density of the source 123 mJy. The size of the Gaussian restoring beam is 1.55×1.29 arcsec and is shown on the lower left of the plot.

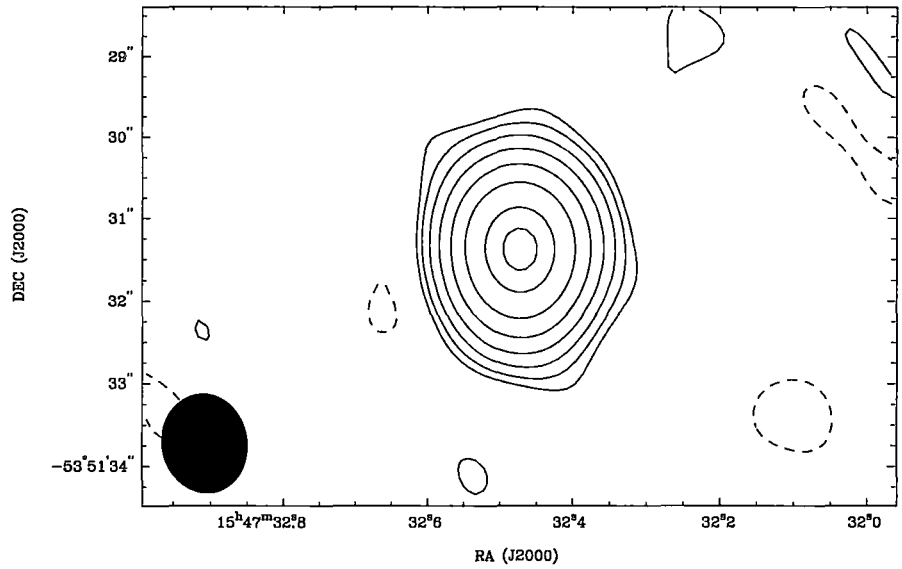

Figure A.3: Radio continuum image of G 327.131+0.526 at 8.6 GHz. The contours are at -1, 1, 2, 4, 8, 16, 32, 64 and 90 per cent of the peak flux density (17.3 mJy beam^{-1}). The integrated flux density of the source 18.4 mJy. The size of the Gaussian restoring beam is 1.21×1.02 arcsec and is shown on the lower left of the plot.

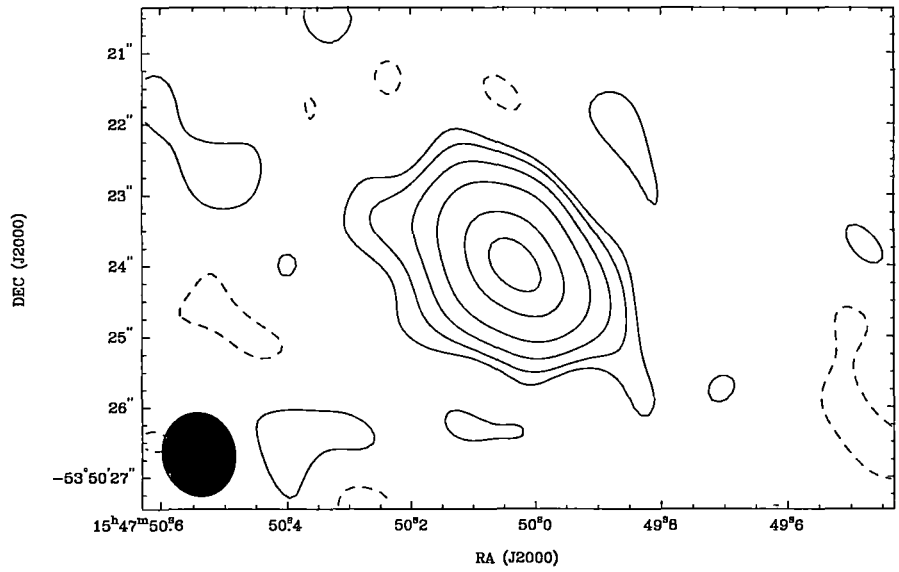

Figure A.4: Radio continuum image of G 327.176+0.514 at 8.6 GHz. The contours are at -4, 4, 8, 16, 32, 64 and 90 per cent of the peak flux density (7.7 mJy beam^{-1}). The integrated flux density of the source 16.8 mJy. The size of the Gaussian restoring beam is 1.21×1.02 arcsec and is shown on the lower left of the plot.

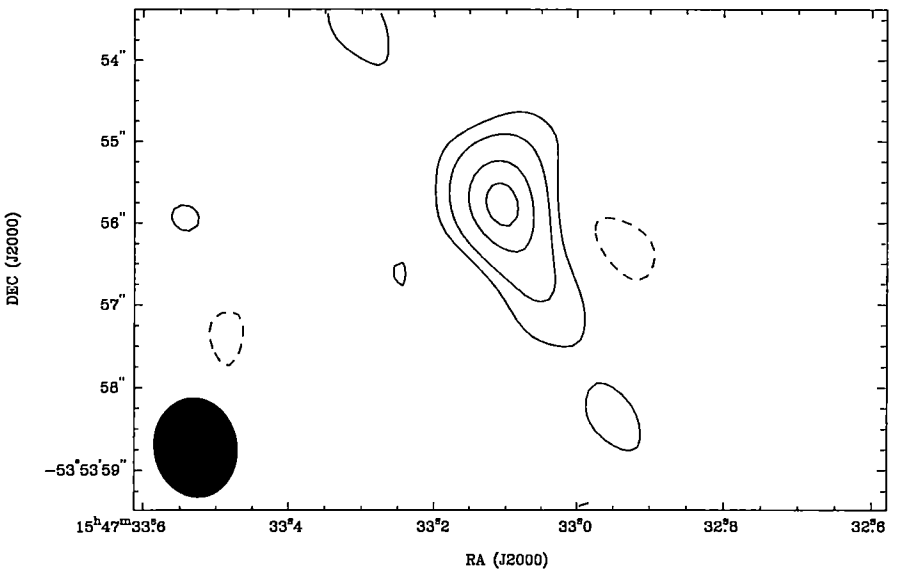

Figure A.5: Radio continuum image of G 327.107+0.493 at 8.6 GHz. The contours are at -16, 16, 32, 64 and 90 per cent of the peak flux density (1.3 mJy beam^{-1}). The integrated flux density of the source 1.4 mJy. The size of the Gaussian restoring beam is 1.21×1.02 arcsec and is shown on the lower left of the plot.

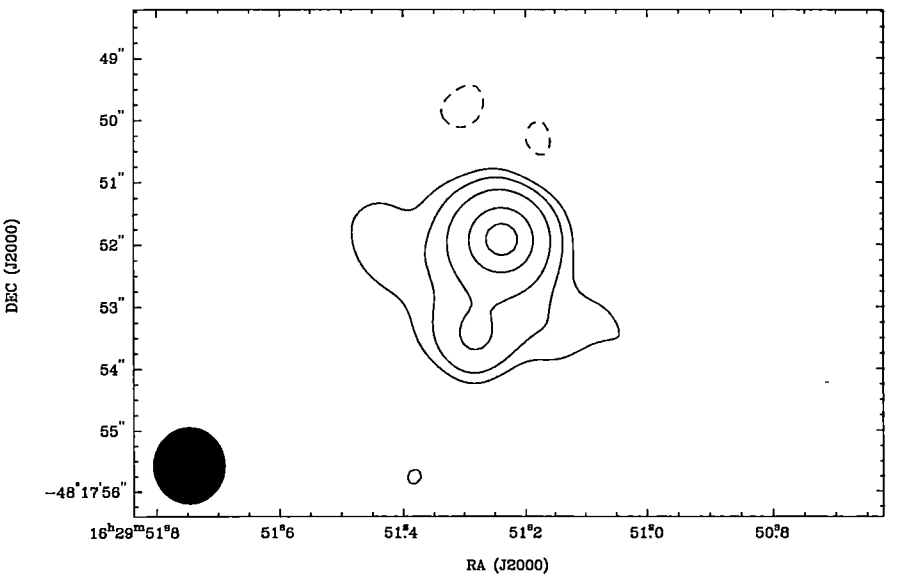

Figure A.6: Radio continuum image of G 335.772+0.143 at 8.6 GHz. The contours are at -8, 8, 16, 32, 64 and 90 per cent of the peak flux density (5.4 mJy beam^{-1}). The integrated flux density of the source 7.8 mJy. The size of the Gaussian restoring beam is 1.27×1.17 arcsec and is shown on the lower left of the plot.

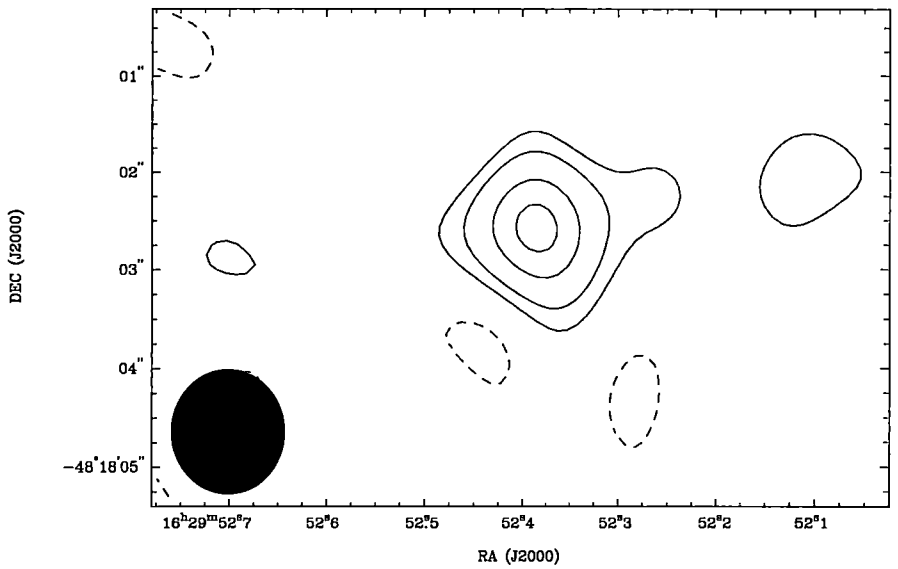

Figure A.7: Radio continuum image of G 335.772+0.139 at 8.6 GHz. The contours are at -16, 16, 32, 64 and 90 per cent of the peak flux density (1.6 mJy beam^{-1}). The integrated flux density of the source 1.3 mJy. The size of the Gaussian restoring beam is 1,27×1.17 arcsec and is shown on the lower left of the plot.

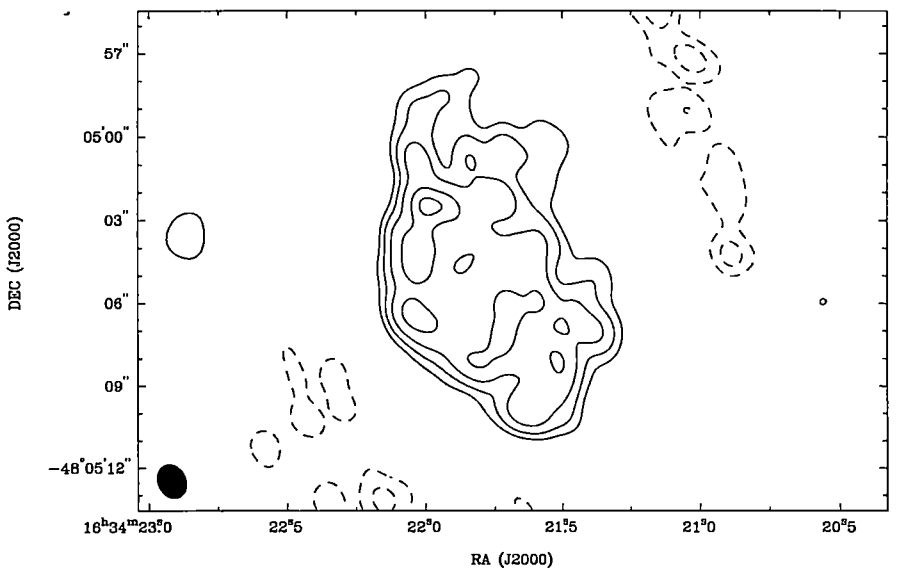

Figure A.8: Radio continuum image of G 336.442−0.260 at 8.6 GHz. The contours are at -8, 8, 16, 32, 64 and 90 per cent of the peak flux density (2.5 mJy beam^{-1}). The integrated flux density of the source 49.9 mJy. The size of the Gaussian restoring beam is 1.29×1.02 arcsec and is shown on the lower left of the plot.

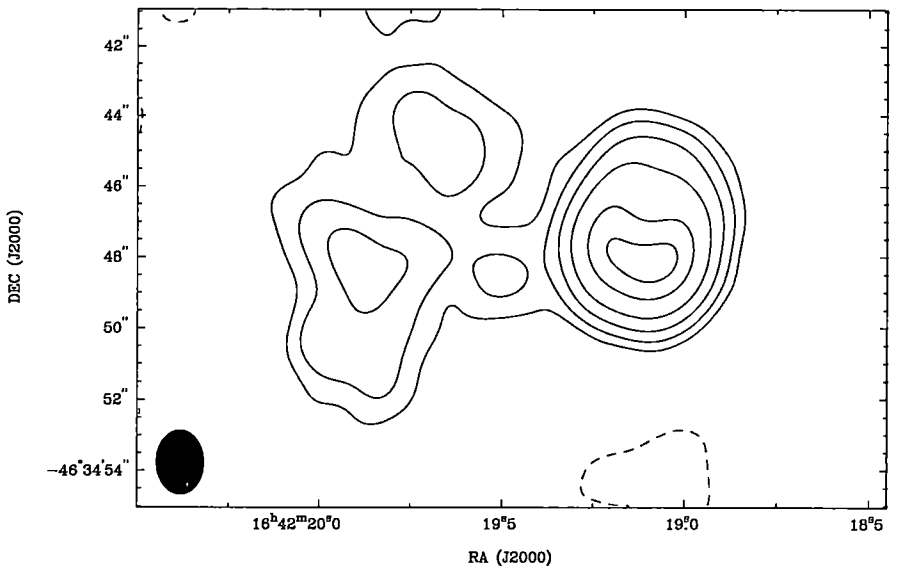

Figure A.9: Radio continuum image of G 338.461−0.258 at 8.6 GHz. The contours are at -1, 1, 2, 4, 8, 16, 32, 64 and 90 per cent of the peak flux density (6.0 mJy beam^{-1}). The integrated flux density of the source 23.9 mJy. The size of the Gaussian restoring beam is 1.82×1.33 arcsec and is shown on the lower left of the plot.

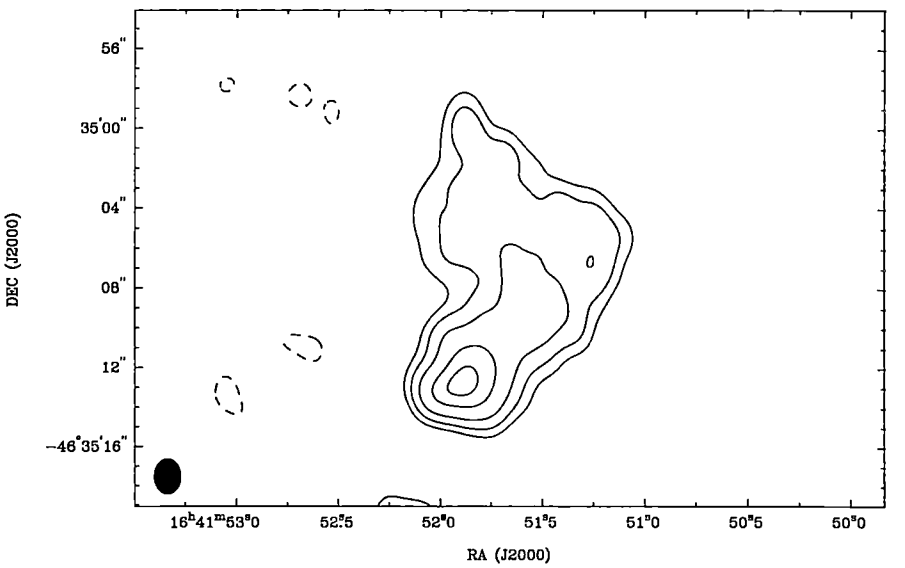

Figure A.10: Radio continuum image of G 338.405−0.205 at 8.6 GHz. The contours are at -8, 8, 16, 32, 64 and 90 per cent of the peak flux density (49.5 mJy beam^{-1}). The integrated flux density of the source 622 mJy. The size of the Gaussian restoring beam is 1.82×1.33 arcsec and is shown on the lower left of the plot.

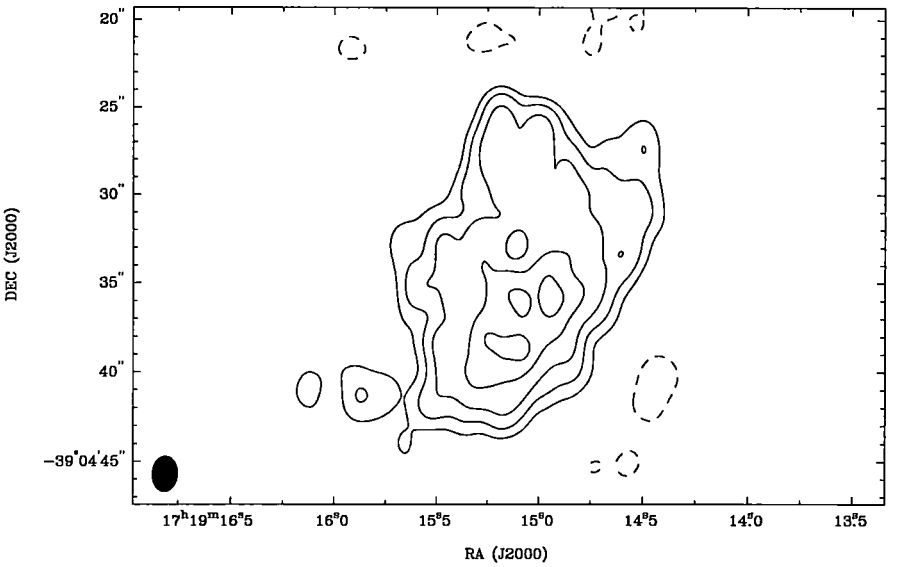

Figure A.11: Radio continuum image of G 348.530−0.972 at 8.6 GHz. The contours are at -8, 8, 16, 32, 64 and 90 per cent of the peak flux density (6.0 mJy beam^{-1}). The integrated flux density of the source 154 mJy. The size of the Gaussian restoring beam is 2.02×1.40 arcsec and is shown on the lower left of the plot.

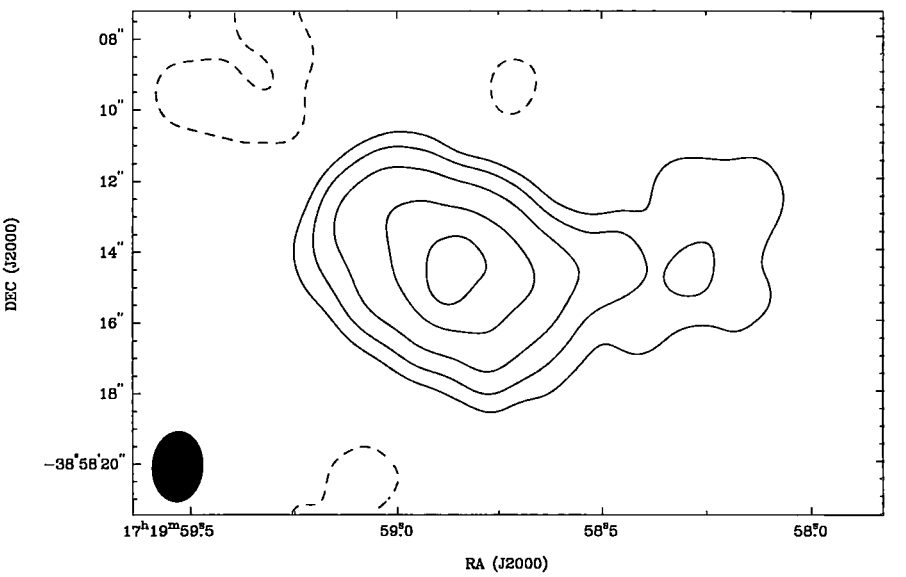

Figure A.12: Radio continuum image of G 348.698−1.027 at 8.6 GHz. The contours are at -8, 8, 16, 32, 64 and 90 per cent of the peak flux density. Because the source was too far offset from the pointing centre to apply a primary beam correction, the flux density of the emission cannot be measured. The size of the Gaussian restoring beam is 2.02×1.40 arcsec and is shown on the lower left of the plot.

References

Aikawa, Y., Umebayashi, T., Nakano, T., and Miyama, S. M.: 1997, *ApJ* **486**, L51

Allen, C. W.: 1973, *Astrophysical quantities*, Athlone Press, London, 3rd Edition

Baan, W.: 1993, in R. Davis and R. Booth (eds.), *Subarcsecond Radio Astronomy*, p. 324, Cambridge Univ. Press, Cambridge, U.K.

Baan, W. A.: 1989, *ApJ* **338**, 804–811

Baan, W. A., Haschick, A., and Henkel, C.: 1992, *AJ* **103**, 728–742

Baan, W. A. and Haschick, A. D.: 1984, *ApJ* **279**, 541–549

Baan, W. A. and Haschick, A. D.: 1987, *ApJ* **318**, 139–144

Baan, W. A., Haschick, A. D., and Henkel, C.: 1989, *ApJ* **346**, 680–689

Baan, W. A., Henkel, C., and Haschick, A. D.: 1987a, *ApJ* **320**, 154–158

Baan, W. A., van Gorkom, J. H., Schmelz, J. T., and Mirabel, I. F.: 1987b, *ApJ* **313**, 102–111

Baan, W. A., Wood, P. A. D., and Haschick, A. D.: 1982, *ApJ* **260**, L49–L52

Baart, E. E. and Cohen, R. J.: 1985, *MNRAS* **213**, 641–655

Barrett, A., Schwartz, R., and Waters, J.: 1971, *ApJ* **168**, L101

Batrla, W., Matthews, H. E., Menten, K. M., and Walmsley, C. M.: 1987, *Nature* **326**, 49–51

Beasley, A. J., Ellingsen, S. P., Claussen, M. J., and Wilcots, E.: 1996, *ApJ* **459**, 600

Beckwith, S. V. W. and Sargent, A. I.: 1993, *ApJ* **402**, 280–291

Beckwith, S. V. W., Sargent, A. I., Chini, R. S., and Guesten, R.: 1990, *AJ* **99**, 924–945

Bloemhof, E. E., Moran, J. M., and Reid, M. J.: 1996, *ApJ* **467**, L117

Bloemhof, E. E., Reid, M. J., and Moran, J. M.: 1992, *ApJ* **397**, 500–519

Bodenheimer, P., Tenorio-Tagle, B., and Yorke, H. W.: 1979, *ApJ* **233**, 85–96

Bottinelli, L., Gouguenheim, L., Le Squeren, A. M., Dennefeld, M., Martin, J. M., and Paturel, G.: 1989, *IAU Circ.* 4928

Bottinelli, L., Gouguenheim, L., Le Squeren, A. M., Dennefeld, M., and Paturel, G.: 1985, *IAU Circ.* **4106**, 1

Bottinelli, L., Gouguenheim, L., Le Squeren, A. M., Martin, J. M., Dennefeld, M., and Paturel, G.: 1986, *IAU Circ.* **4231**, 1

Bottinelli, L., Gouguenheim, L., Le Squeren, A. M., Martin, J. M., Dennefeld, M., and Paturel, G.: 1987, *IAU Circ.* 4357

Braatz, J. A., Wilson, A. S., and Henkel, C.: 1994, *ApJ* **437**, L99–L102

Braatz, J. A., Wilson, A. S., and Henkel, C.: 1996, *ApJS* **106**, 51

Brand, J. and Blitz, L.: 1993, *A&A* **275**, 67

Braz, M. A., Lépine, J., Sivagnanam, P., and Le Squeren, A. M. .: 1990, *A&A* **236**, 479–486
Caswell, J. L.: 1996a, *MNRAS* **283**, 606–612
Caswell, J. L.: 1996b, *MNRAS* **279**, 79–87
Caswell, J. L.: 1997, *MNRAS* **289**, 203–224
Caswell, J. L., Gardner, F. F., Norris, R. P., Wellington, K. J., McCutcheon, W. H., and Peng, R. S.: 1993, *MNRAS* **260**, 425–436
Caswell, J. L. and Haynes, R. F.: 1987, *AuJPh* **40**, 215–238
Caswell, J. L., Kesteven, M. J., Stewart, R. T., Milne, D. K., and Haynes, R. F.: 1992, *ApJ* **399**, L151–L153
Caswell, J. L., Vaile, R. A., and Ellingsen, S. P.: 1995a, *PASA* **12**, 37–53
Caswell, J. L., Vaile, R. A., Ellingsen, S. P., and Norris, R. P.: 1995b, *MNRAS* **274**, 1126–1152
Caswell, J. L., Vaile, R. A., Ellingsen, S. P., Whiteoak, J. B., and Norris, R. P.: 1995c, *MNRAS* **272**, 96–138
Caswell, J. L., Vaile, R. A., and Forster, J. R.: 1995d, *MNRAS* **277**, 210–216
Catarzi, M., Moscadelli, L., and Panella, D.: 1993, *A&ASS* **98**, 127–135
Cesaroni, R., Felli, M., Testi, L., Walmsley, C. M., and Olmi, L.: 1997, *A&A* **325**, 725–744
Chapman, J. M. and Cohen, R. J.: 1985, *MNRAS* **212**, 375–384
Chapman, J. M., Staveley-Smith, L., Axon, D. J., Unger, S. W., Cohen, R. J., Pedlar, A., and Davies, R. D.: 1990, *MNRAS* **244**, 281–290
Chapman, J. W., Cohen, R. J., Pointon, L., Staveley-Smith, L., and Unger, S. W.: 1986, *IAU Circ.* 4180
Cheung, A., Rank, D., Townes, C., Thornton, D., and Welch, W.: 1969, *Nature* **221**, 626–628
Chini, R., Kreysa, E., Mezger, P. G., and Gemuend, H. P.: 1986a, *A&A* **154**, L8–L11
Chini, R., Kruegel, E., and Kreysa, E.: 1986b, *A&A* **167**, 315–324
Chini, R., Kruegel, E., and Wargau, W.: 1987, *A&A* **181**, 378–382
Churchwell, E., Witzel, A., Pauliny-Toth, I., Sieber, W., Huchtmeier, W., and Roland, J.: 1977, *A&A* **54**, 969–971
Churchwell, E., Wolfire, M. G., and Wood, D. O. S.: 1990, *ApJ* **354**, 247–261
Claussen, M. J., Heiligman, G. M., and Lo, K. Y.: 1984, *Nature* **310**, 298–300
Claussen, M. J. and Lo, K. Y.: 1986, *ApJ* **308**, 592–599
Codella, C. and Felli, M.: 1995, *A&A* **302**, 521
Cragg, D. M., Johns, K. P., Godfrey, P. D., and Brown, R. D.: 1992, *MNRAS* **259**, 203–208
De Pree, C. G., Rodriguez, L. F., and Goss, W. M.: 1995, *Rev. Mexicana Astron. Astrofis.* **31**, 39–44
Diamond, P. J., Norris, R. P., Baan, W. A., and Booth, R. S.: 1989, *ApJ* **340**, L49–L52
Dickey, J. M., Planesas, P., Mirabel, I. F., and Kazes, I.: 1990, *AJ* **100**, 1457–1460
Dos Santos, P. M. and Lépine, J. R. D.: 1979, *Nature* **278**, 34
Elitzur, M.: 1992, *ARAA* **30**, 75–112
Elitzur, M. and De Jong, T.: 1978, *A&A* **67**, 323–332

Ellingsen, S.: 1996, *Ph.D. Thesis*, University of Tasmania

Ellingsen, S., McCulloch, P., Diamond, P., and Norris, R.: 1997, in J. Zensus, W. J.M., and G. Taylor (eds.), *IAU Colloquium 164: Radio Emission From Galactic And Extra-Galactic Compact Sources*, pp 106–112, The ASP Conference Series

Ellingsen, S. P., Norris, R. P., Diamond, P. J., McCulloch, P. M., Amy, S. W., Beasley, A. J., Ferris, R. H., Gough, R. G., King, E. A., Lovell, J. E. J., Reynolds, J. E., Tzioumis, A. K., Troup, E. R., Wark, R. M., and Wieringa, M. H.: 1996, in E. A. King (ed.), *Proceedings of the 4th APT Workshop*, pp 106–112, ATNF, Sydney

Ellingsen, S. P., Norris, R. P., and McCulloch, P. M.: 1996a, *MNRAS* **279**, 101–107

Ellingsen, S. P., Norris, R. P., McCulloch, P. M., and Phillips, C. J.: 1998, *MNRAS* in preparation

Ellingsen, S. P., Norris, R. P., Whiteoak, J. B., Vaile, R. A., McCulloch, P. M., and Price, M. G.: 1994a, *MNRAS* **267**, 510–512

Ellingsen, S. P., Von Bibra, M. L., McCulloch, P. M., Norris, R. P., Deshpande, A. A., and Phillips, C. J.: 1996b, *MNRAS* **280**, 378–396

Ellingsen, S. P., Whiteoak, J. B., Norris, R. P., Caswell, J. L., and Vaile, R. A.: 1994b, *MNRAS* **269**, 1019–1024

Forster, J. R. and Caswell, J. L.: 1989, *A&A* **213**, 339–350

Gallimore, J. F., Baum, S. A., O'Dea, C. P., Brinks, E., and Pedlar, A.: 1996, *ApJ* **462**, 740

Garay, G., Moran, J. M., and Rodriguez, L. F.: 1993, *ApJ* **413**, 582–592

Garay, G., Reid, M. J., and Moran, J. M.: 1985, *ApJ* **289**, 681–697

Gardner, F. F. and Whiteoak, J. B.: 1982, *MNRAS* **201**, 13P–15P

Gaume, R. A., Claussen, M. J., De Pree, C. G., Goss, W. M., and Mehringer, D. M.: 1995, *ApJ* **449**, 663–673

Gaume, R. A., Fey, A. L., and Claussen, M. J.: 1994, *ApJ* **432**, 648–655

Gaume, R. A. and Mutel, R. L.: 1987, *ApJS* **65**, 193–253

Gaylard, M. J. and Macleod, G. C.: 1993, *MNRAS* **262**, 43–48

Gaylard, M. J., Macleod, G. C., and Van der Walt, D. J.: 1994, *MNRAS* **269**, 257

Genzel, R., Downes, D., Schneps, M. H., Reid, M. J., Moran, J. M., Kogan, L. R., Kostenko, V. I., Matveenko, L. I., and Ronnang, B.: 1981a, *ApJ* **247**, 1039–1051

Genzel, R., Reid, M. J., Moran, J. M., and Downes, D.: 1981b, *ApJ* **244**, 884–902

Gordon, M. A.: 1988, in G. L. Verschuur and K. I. Kellermann (eds.), *Galactic and extragalactic radio astronomy*, pp 37–94, Springer-Verlag, Berlin and New York, 2nd Edition

Greenhill, L. J., Ellingsen, S. P., Norris, R. P., Gough, R. G., Sinclair, M. W., Moran, J. M., and Mushotzky, R.: 1997, *ApJ* **474**, L103

Greenhill, L. J., Gwinn, C. R., Antonucci, R., and Barvainis, R.: 1996, *ApJ* **472**, L21

Greenhill, L. J., Jiang, D. R., Moran, J. M., Reid, M. J., Lo, K. Y., and Claussen, M. J.: 1995, *ApJ* **440**, 619

Greenhill, L. J., Moran, J. M., Reid, M. J., Gwinn, C. R., Menten, K. M., Eckart, A., and Hirabayashi, H.: 1990, *ApJ* **364**, 513–526
Gwinn, C. R., Moran, J. M., and Reid, M. J.: 1992, *ApJ* **393**, 149–164
Gwinn, C. R., Moran, J. M., Reid, M. J., and Schneps, M. H.: 1988, *ApJ* **330**, 817–827
Habing, H. J., Goss, W. M., Matthews, H. E., and Winnberg, A.: 1974, *A&A* **35**, 1–5
Habing, H. J. and Israel, F. P.: 1979, *ARAA* **17**, 345–385
Haschick, A. D., Baan, W. A., Schneps, M. H., Reid, M. J., Moran, J. M., and Guesten, R.: 1990, *ApJ* **356**, 149–155
Henkel, C., Guesten, R., and Baan, W. A.: 1987, *A&A* **185**, 14–24
Henkel, C., Wouterloot, J. G. A., and Bally, J.: 1986, *A&A* **155**, 193–199
Henning, T., Cesaroni, R., Walmsley, M., and Pfau, W.: 1992, *Astronomy and Astrophysics Supplement Series* **93**, 525–538
Herbst, E.: 1991, *ApJ* **366**, 133–140
Herrnstein, J. R.: 1997, *Ph.D. Thesis*, Harvard University
Herrnstein, J. R., Greenhill, L. J., and Moran, J. M.: 1996, *ApJ* **468**, L17
Herrnstein, J. R., Moran, J. M., Greenhill, L. J., Diamond, P. J., Miyoshi, M., Nakai, N., and Inoue, M.: 1997, *ApJ* **475**, L17
Hillenbrand, L. A., Strom, S. E., Vrba, F. J., and Keene, J.: 1992, *ApJ* **397**, 613–643
Ho, P. T. P., Martin, R. N., Henkel, C., and Turner, J. L.: 1987, *ApJ* **320**, 663
Hofner, P., Kurtz, S., Churchwell, E., Walmsley, C. M., and Cesaroni, R.: 1994, *ApJ* **429**, L85–L88
Hofner, P., Kurtz, S., Churchwell, E., Walmsley, C. M., and Cesaroni, R.: 1996, *ApJ* **460**, 359
Hollenbach, D., Johnstone, D., Lizano, S., and Shu, F.: 1994, *ApJ* **428**, 654–669
Houghton, S. and Whiteoak, J. B.: 1995, *MNRAS* **273**, 1033–1040
Huchtmeier, W.: 1972, *A&A* **17**, 207–214
Hüttemeister, S., Wilson, T. L., Henkel, C., and Mauersberger, R.: 1993, *A&A* **276**, 445–462
Israel, F. P.: 1978, *A&A* **70**, 769–775
Kazes, I. and Baan, W. A.: 1991, *A&A* **248**, L15–L18
Kazes, I., Mirabel, I. F., and Combes, F.: 1988, *IAU Circ.* 4629
Kazes, I., Mirabel, I. F., and Combes, F.: 1989, *IAU Circ.* 4856
Kazes, I., Proust, D., Mirabel, L. F., Combes, F., Balkowski, C., and Martin, J. M.: 1990, *A&A* **237**, L1–L4
Kemball, A. J., Gaylard, M. J., and Nicolson, G. D.: 1988, *ApJ* **331**, L37–L40
Killeen, N. E. B., Staveley-Smith, L., Wilson, W. E., and Sault, R. J.: 1996, *MNRAS* **280**, 1143–1154
Koekemoer, A. M., Henkel, C., Greenhill, L. J., Dey, A., van Breugel, W., Codella, C., and Antonucci, R.: 1995, *Nature* **378**, 697–699
Koo, B.-C., Williams, D. R. D., Heiles, C., and Backer, D. C.: 1988, *ApJ* **326**, 931–940
Lépine, J. R. D. and Marques Dos Santos, P.: 1977, *Nature* **270**, 501
Lin, D. N. C. and Pringle, J. E.: 1990, *ApJ* **358**, 515–524

Lonsdale, C. J., Diamond, P. J., Smith, H. E., and Lonsdale, C. J.: 1994, *Nature* **370**, 117–120
Lovas, F. J.: 1992, *J. Phys. Chem. Ref. Data* **21**, 181–272
Mac Low, M. M. and Elitzur, M.: 1992, *ApJ* **393**, L33–L36
Mac Low, M.-M., van Buren, D., Wood, D. O. S., and Churchwell, E.: 1991, *ApJ* **369**, 395–409
Macleod, G. C.: 1991, *MNRAS* **252**, 36P–38P
Macleod, G. C. and Gaylard, M. J.: 1992, *MNRAS* **256**, 519–527
Macleod, G. C. and Gaylard, M. J.: 1996, *MNRAS* **280**, 868–876
Macleod, G. C., Gaylard, M. J., and Kemball, A. J.: 1993, *MNRAS* **262**, 343–349
Macleod, G. C., Gaylard, M. J., and Nicolson, G. D.: 1992, *MNRAS* **254**, 1P–6P
Mannings, V. and Sargent, A. I.: 1997, *ApJ* **490**, 792+
Martin, J. M., Bottinelli, L., Dennefeld, M., Gouguenheim, L., Handa, T., Le Squeren, A. M., Nakai, N., and Sofue, Y.: 1988a, *A&A* **195**, 71–75
Martin, J. M., Le Squeren, A. M., Bottinelli, L., Gouguenheim, L., and Dennefeld, M.: 1988b, *A&A* **201**, L13–L15
Marvel, K. B.: 1996, *Ph.D. Thesis*, New Mexico State University
McCutcheon, W. H., Wellington, K. J., Norris, R. P., Caswell, J. L., Kesteven, M. J., Reynolds, J. E., and Peng, R. S.: 1988, *ApJ* **333**, L79–L82
McKee, C., Zweibel, E., Goodman, A., and Heiles, C.: 1993, in E. Levy and J. Lunine (eds.), *Protostars and planets III*, pp 327–366, The University of Arizona Press, Tucson and London
Menten, K. M.: 1991a, *ApJ* **380**, L75–L78
Menten, K. M.: 1991b, in A. Haschick and P. Ho (eds.), *Skylines (Proc. Third Haystack Observatory Meeting)*, pp 119–136, ASP, San Francisco
Menten, K. M., Reid, M. J., Moran, J. M., Wilson, T. L., Johnston, K. J., and Batrla, W.: 1988, *ApJ* **333**, L83–L86
Menten, K. M., Reid, M. J., Pratap, P., Moran, J. M., and Wilson, T. L.: 1992, *ApJ* **401**, L39–L42
Mezger, P., Altenhoff, W., Schraml, J., Burke, B., Reifenstein, E., and Wilson, T.: 1967, *ApJ* **150**, L157
Mirabel, I. F., Kazes, I., and Sanders, D. B.: 1988, *ApJ* **324**, L59
Mirabel, I. F., Rodriguez, L. F., and Ruiz, A.: 1989, *ApJ* **346**, 180–183
Mirabel, I. F. and Sanders, D. B.: 1987, *ApJ* **322**, 688–693
Miyoshi, M., Moran, J., Herrnstein, J., Greenhill, L., Nakai, N., Diamond, P., and Inoue, M.: 1995, *Nature* **373**, 127–129
Molinari, S., Brand, J., Cesaroni, R., and Palla, F.: 1996, *A&A* **308**, 573–587
Montgomery, A. S. and Cohen, R. J.: 1992, *MNRAS* **254**, 23P–26P
Moorwood, A. F. M. and Glass, I. S.: 1984, *A&A* **135**, 281–288
Moscadelli, L. and Catarzi, M.: 1996, *Astronomy and Astrophysics Supplement Series* **116**, 211–238
Nakai, N., Inoue, M., Miyazawa, K., and Hall, P.: 1995, *PASJ* **47**, 771–799
Nakai, N. and Kasuga, T.: 1988, *PASJ* **40**, 139–145
Neufeld, D. A. and Maloney, P. R.: 1995, *ApJ* **447**, L17
Neufeld, D. A., Maloney, P. R., and Conger, S.: 1994, *ApJ* **436**, L127
Norris, R. P.: 1984, *PASA* **5**, 514–516

Norris, R. P.: 1985, *MNRAS* **216**, 701–711
Norris, R. P., Baan, W. A., Haschick, A. D., Diamond, P. J., and Booth, R. S.: 1985, *MNRAS* **213**, 821–831
Norris, R. P., Byleveld, S., Diamond, P., Ellingsen S. P., Ferris, R., Gough R.G., Kesteven, M. J., McCulloch, P. M., Reynolds, J. E., Tzioumis, A. K., Takahashi, Y., Troup, E. R., Wellington, K. J., and Phillips, C. J.: 1998, *ApJ* 508
Norris, R. P., Caswell, J. L., Gardner, F. F., and Wellington, K. J.: 1987, *ApJ* **321**, L159–L162
Norris, R. P., Caswell, J. L., Wellington, K. J., McCutcheon, W. H., and Reynolds, J. E.: 1988, *Nature* **335**, 149–151
Norris, R. P., Gardner, F. F., Whiteoak, J. B., Allen, D. A., and Roche, P. F.: 1989, *MNRAS* **237**, 673–681
Norris, R. P., Whiteoak, J. B., Caswell, J. L., Wieringa, M. H., and Gough, R. G.: 1993, *ApJ* **412**, 222–232
Norris, R. P., Whiteoak, J. B., Gardner, F. F., Allen, D. A., and Roche, P. F.: 1986, *MNRAS* **221**, 51P–54P
Palla, F., Brand, J., Comoretto, G., Felli, M., and Cesaroni, R.: 1991, *A&A* **246**, 249–263
Panagia, N.: 1973, *AJ* **78**, 929–934
Panagia, N. and Walmsley, C. M.: 1978, *A&A* **70**, 411–414
Perkins, F., Gold, T., and Salpeter, E.: 1966, *ApJ* **145**, 361–366
Phillips, C., Norris, R., Ellingsen, S., McCulloch, P., Reynolds, J., Gough, R., Tzioumis, A., Gussie, G., Lovell, J., and Wieringa, M.: 1996, in E. King (ed.), *Proceedings of 4th APT Workshop*, pp 113–119, ATNF, Sydney
Plambeck, R. L. and Menten, K. M.: 1990, *ApJ* **364**, 555–560
Plambeck, R. L., Wright, M. C. H., and Carlstrom, J. E.: 1990, *ApJ* **348**, L65–L68
Ponomarev, V. O., Smith, H. A., and Strelnitski, V. S.: 1994, *ApJ* **424**, 976–982
Randell, J., Field, D., Jones, K. N., Yates, J. A., and Gray, M. D.: 1995, *A&A* **300**, 659
Reid, M. J., Haschick, A. D., Burke, B. F., Moran, J. M., Johnston, K. J., and Swenson, G. W., J.: 1980, *ApJ* **239**, 89–99
Reid, M. J. and Moran, J. M.: 1988, in G. L. Verschuur and K. I. Kellermann (eds.), *Galactic and extragalactic radio astronomy*, pp 255–294, Springer-Verlag, Berlin and New York, 2nd Edition
Reid, M. J., Schneps, M. H., Moran, J. M., Gwinn, C. R., Genzel, R., Downes, D., and Roennaeng, B.: 1988, *ApJ* **330**, 809–816
Rodriguez, L. F., Curiel, S., Ho, P. T. P., Torrelles, J. M., and Canto, J.: 1990, *ApJ* **352**, 645–653
Rodriguez, L. F., Curiel, S., Moran, J. M., Mirabel, I. F., Roth, M., and Garay, G.: 1989, *ApJ* **346**, L85–L88
Sagar, R., Piskunov, A. E., Miakutin, V. I., and Joshi, U. C.: 1986, *MNRAS* **220**, 383–403
Sargent, A. I. and Beckwith, S. V. W.: 1994, *Ap&SS* **212**, 181–189
Sault, R. J., Teuben, P. J., and Wright, M. C. H.: 1995, *ADASS* **4**, 433
Schraml, J. and Mezger, P. G.: 1969, *ApJ* **156**, 269–301

Schutte, A. J., van der Walt, D. J., Gaylard, M. J., and Macleod, G. C.: 1993, *MNRAS* **261**, 783

Shepherd, M.: 1997, in P. H. Hunt G. (ed.), *Astronomical Data Analysis Software and Systems VI*, p. 77, The ASP Conference Series

Shu, F., Najita, J., Galli, D., Ostriker, E., and Lizano, S.: 1993, in E. Levy and J. Lunine (eds.), *Protostars and planets III*, pp 3–45, The University of Arizona Press, Tucson and London

Shu, F. H., Adams, F. C., and Lizano, S.: 1987, *ARAA* **25**, 23–81

Shu, F. H., Tremaine, S., Adams, F. C., and Ruden, S. P.: 1990, *ApJ* **358**, 495–514

Sinclair, M. W., Carrad, G. J., Caswell, J. L., Norris, R. P., and Whiteoak, J. B.: 1992, *MNRAS* **256**, 33P

Slysh, V. I., Kalenskii, S. V., Valtts, I. E., and Otrupcek, R.: 1994, *MNRAS* **268**, 464

Smith, C. H., Moore, T. J. T., Aitken, D. K., and Fujiyoshi, T.: 1997, *PASA* **14**, 179–88

Sobolev, A. M., Cragg, D. M., and Godfrey, P. D.: 1997a, *MNRAS* **288**, L39

Sobolev, A. M., Cragg, D. M., and Godfrey, P. D.: 1997b, *A&A* **324**, 211–220

Sobolev, A. M. and Deguchi, S.: 1994, *A&A* **291**, 569–576

Staveley-Smith, L., Allen, D. A., Chapman, J. M., Norris, R. P., and Whiteoak, J. B.: 1989, *Nature* **337**, 625–627

Staveley-Smith, L., Cohen, R. J., Chapman, J. M., Pointon, L., and Unger, S. W.: 1987, *MNRAS* **226**, 689–701

Staveley-Smith, L., Norris, R. P., Chapman, J. M., Allen, D. A., Whiteoak, J. B., and Roy, A. L.: 1992, *MNRAS* **258**, 725–737

Staveley-Smith, L., Unger, S. W., Cohen, R. J., Chapman, J. M., and Pointon, L.: 1986, *IAU Circ.* 4248

Strelnitskii, V. and Syunyaev, R.: 1973, *Sov. Astron.* **16**, 569

Strömgren, B.: 1939, *ApJ* **89**, 526

Tenorio-Tagle, G.: 1979, *A&A* **71**, 59–65

Testi, L., Felli, M., Persi, P., and Roth, M.: 1994, *A&A* **288**, 634–646

Testi, L., Felli, M., Persi, P., and Roth, M.: 1997a, *A&A*, in press

Testi, L., Felli, M., Persi, P., and Roth, M.: 1997b, *A&A*, in press

Thompson, A. R., Moran, J. M., and Swenson, Georg e W., J.: 1986, in *New York, Wiley-Interscience, 1986, 554 p.*

Turner, B. E.: 1985, *ApJ* **299**, 312–333

Unger, S. W., Chapman, J. M., Cohen, R. J., Hawarden, T. G., and Mountain, C. M.: 1986, *MNRAS* **220**, 1P–6P

Val'Tts, I. E., Dzura, A. M., Kalenskii, S. V., Slysh, V. I., Booth, R. S., and Winnberg, A.: 1995, *A&A* **294**, 825–830

van Buren, D., Mac Low, M.-M., Wood, D. O. S., and Churchwell, E.: 1990, *ApJ* **353**, 570–578

van der Walt, D. J., Gaylard, M. J., and Macleod, G. C.: 1995, *Astronomy and Astrophysics Supplement, v.110, p.81* **110**, 81

van der Walt, D. J., Retief, S. J. P., Gaylard, M. J., and Macleod, G. C.: 1996, *MNRAS* **282**, 1085–1095

van Langevelde, H. J., van Dishoeck, E. F., Sevenster, M. N., and Israel, F. P.:

1995, *ApJ* **448**, L123
Walker, R. C., Matsakis, D. N., and Garcia-Barreto, J. A.: 1982, *ApJ* **255**, 128–142
Walsh, A. J., Hyland, A. R., Robinson, G., and Burton, M. G.: 1997, *MNRAS*
Watson, W. D. and Wallin, B. K.: 1994, *ApJ* **432**, L35–L38
Weaver, H. and Williams, R.: 1965, *Nature* **208**, 29–31
Whiteoak, J. B. and Gardner, F. F.: 1974, *ApL* **15**, 211–215
Whiteoak, J. B. and Gardner, F. F.: 1975, *ApJ* **195**, L81
Whiteoak, J. B. and Gardner, F. F.: 1986, *MNRAS* **222**, 513–523
Wilson, T. L., Walmsley, C. M., Jewell, P. R., and Snyder, L. E.: 1984, *A&A* **134**, L7–L10
Wilson, T. L., Walmsley, C. M., Menten, K. M., and Hermsen, W.: 1985, *A&A* **147**, L19–L22
Wood, D. O. S. and Churchwell, E.: 1989a, *ApJ* **340**, 265–272
Wood, D. O. S. and Churchwell, E.: 1989b, *ApJS* **69**, 831–895
Yorke, H. W., Bodenheimer, P., and Laughlin, G.: 1993, *ApJ* **411**, 274–284
Yorke, H. W., Tenorio-Tagle, G., and Bodenheimer, P.: 1983, *A&A* **127**, 313–319
Zuckerman, B., Lilley, A., and Penfield, H.: 1965, *Nature* **208**, 441–443